# A Polyelectrolyte Multilayer Thin Film System for Cell Adhesion, Gene Delivery and Inductive Tissue Engineering Applications

**Christina Holmes, M.A.Sc.**

Biomedical Engineering Department

McGill University

Montreal, Canada

Submitted March 2013

A thesis submitted to McGill University, Faculty of Graduate Engineering and Postdoctoral Studies, in partial fulfillment of the requirements of the degree of doctor of philosophy.

Copyright © Christina Holmes 2013

*To my mother …*

# Abstract

In order for the vast therapeutic potential of tissue engineering to be realized, inductive three-dimensional (3D) scaffolds that can direct cell behaviour and tissue architecture must be developed. Although a variety of strategies which enable scaffold-based biofactor release are under investigation, the processing conditions typically employed restrict the system architectures and mechanical properties that can be produced.

The main objective of this thesis work was to develop an inductive tissue engineering system for *in situ* 3D gene delivery, utilizing the layer-by-layer deposition technique and a model scaffold. Towards that end, a novel polyelectrolyte multilayer film system composed of glycol-modified chitosan (Glyc-CHI) and hyaluronic acid (HA) was developed and analyzed. This biocompatible Glyc-CHI/HA multilayer system was then modified to incorporate gene delivery lipoplexes, composed of plasmid DNA complexed with Lipofectamine2000$^{TM}$, in order to facilitate *in vitro* delivery of a marker gene encoding enhanced green fluorescent protein (EGFP). The system, with and without incoporated gene delivery lipoplexes, was then adapted to be used as a LbL coating on a 3D model porous scaffold system microfabricated from poly(lactic-co-glycolic acid) (PLGA).

The polyelectrolyte multilayer film system developed in this study exhibited a number of novel and useful features. Glyc-CHI/HA films composed of 5 or more bilayers were displayed significantly increased *in vitro* cellular adhesion, growth and viability

compared to corresponding films consisting of the well characterized unmodified chitosan/HA system, while maintaining many similar physical properties. Meanwhile, multilayers incorporating gene delivery lipoplexes achieved *in vitro* transfection efficiencies of up to 20% in NIH3T3 and HEK293 cells, and were able to maintain transfection for at least 7 days. PLGA scaffolds LbL-coated with these Glyc-CHI/HA films supported *in vitro* MC3T3 cell growth and viability for a period of at least 2 weeks at levels similar to, or better than, those achieved in uncoated control scaffolds. A novel imaging technique known as optical coherence phase microscopy (OCPM) was demonstrated to enable *in situ*, non-invasive, label-free imaging of tissue structure and viability within our 3D tissue engineering scaffolds. Finally, coated PLGA scaffolds incorporating gene delivery lipoplexes were found to support scaffold-based *in vitro* transfection of HEK293 cells at levels significantly higher than uncoated scaffolds with surface adsorbed lipoplexes. Overall, this thesis work thus serves as an important first step towards using Glyc-CHI/HA multilayer films for controlled delivery of various therapeutic genes in 2D and 3D inductive tissue engineering applications.

# Résumé

Afin de voir l'important potentiel thérapeutique que représente l'ingénierie tissulaire se réaliser, il faut d'abord voir la réalisation de matrices inductrices tridimensionnelles pouvant régir le comportement des cellules de même que l'architecture des tissus. Bien que différentes stratégies permettant la libération de molécules bioactives en matrice soient à l'étude, les conditions de traitement les plus souvent utilisées restreignent l'architecture du système et les propriétés mécaniques qui pourraient être produites.

Le principal objectif de cette thèse était de développer un système inducteur d'ingénierie tissulaire pour la libération tridimensionnelle *in situ* de gènes à l'aide d'une technique de dépôt couche par couche et d'un modèle matriciel. Vers la fin, un nouveau système de pellicule de polyélectrolytes à couches multiples composé de chitosane modifié au glycol (Glyc-CHI) et d'acide hyaluronique avait été conçu et analysé. Ce système biocompatible à couches multiples de Glyc-CHI/HA a ensuite été modifié pour incorporer des lipoplexes issus de la libération de gènes et composés d'ADN plasmidique complexé avec du Lipofectamine2000$^{MC}$, et ce, afin de faciliter la libération *in vitro* d'un gène marqueur qui encoderait des protéines à fluorescence verte (GFP). Avec ou sans l'incorporation des lipoplexes issus de la libération des gènes, le système a par la suite été adapté pour servir d'enveloppe couche par couche sur un système de modèle matriciel tridimensionnel et poreux microfabriqué à partir de polyacide lactique coglycolique (PLGA).

Le système de pellicule de polyélectrolytes à couches multiples qui a été conçu au cours de cette étude démontrait un certain nombre de nouvelles caractéristiques utiles. Les pellicules de Glyc-CHI/HA composées de 5 bicouches présentaient une adhésion, croissance et viabilité accrues des cellules *in vitro* comparativement à des pellicules similaires formées du système bien connu de chitosan/HA non modifié, tout en conservant de nombreuses propriétés physiques semblables. On a pu observer que des couches multiples incorporant des lipoplexes issus de la libération de gènes parvenaient à atteindre *in vitro* un rendement de transfection de 20 % dans les cellules NIH3T3 et HEK293 et étaient en mesure de maintenir cette transfection pendant au moins 7 jours. Il a également été démontré que les matrices de PGLA enrobées de ces pellicules de Glyc-CHI/HA pouvaient appuyer la croissance et la viabilité *in vitro* de cellules MC3T3 pour une durée minimale de deux semaines, et ce, à des niveaux semblables ou supérieurs à ceux atteints par les matrices témoin non enrobées. Une nouvelle technique d'imagerie nommée microscopie de phase par cohérence optique a permis d'obtenir des images *in situ* non invasives et dépourvues d'étiquettes de la structure et de la viabilité des tissus à l'intérieur de nos matrices tridimensionnelles d'ingénierie tissulaire. Enfin, on a pu observer que les matrices de PLGA enrobées incorporant des lipoplexes issus de la libération de gènes appuient la transfection *in vitro* de cellules HEK293 dans la matrice à des niveaux nettement supérieurs à ceux des matrices non enrobées dont la surface a adsorbé des lipoplexes. En général, la présente thèse est un important premier pas vers l'utilisation de pellicules de Glyc-CHI/HA à couches multiples pour la libération contrôlée de divers gènes thérapeutiques dans les applications inductives bi- et tridimensionnelles de l'ingénierie tissulaire.

## Acknowledgements

This thesis would not be possible without the support of my colleagues, friends and family. First and foremost, I would like to express my deepest gratitude to my supervisor Dr. Maryam Tabrizian. Her guidance, patience and generosity of time and spirit have been invaluable in my personal and academic development. Without her mentorship and tireless encouragement this work would not have been possible.

During my thesis, I had the privilege of working with Dr. Pierre Bagnaninchi at the University of Edinburgh for several months. Learning about his innovative optical coherence phase microscopy system not only helped me with my thesis but also broadened my perspectives. Thanks to his valuable assistance and infectious enthusiasm my research experiences in Scotland were a pure joy.

I am extremely grateful to the Industrial Materials Institute in Boucherville, Quebec for providing me access to the equipment necessary for fabricating the scaffold systems used in this study. I would particularly like to thank Christian De Grandpre for all his help there.

Dr. Heather Durham at the Montreal Neurological Institute graciously allowed me to use her facilities for my bacterial work and plasmid preparation. I would like to thank her and her lab members, especially Dr. Miranda Tradewell, Laura Cooper and Sandra Minotti for their assistance and support.

I would especially like to thank several members, past and present, of the BiomatX group for their invaluable assistance with aspects of my training and project. I would like to thank Dr. Anna Hillberg for her help training me on the QCM-D system and acting as my initial sounding board for all things LbL. I also extend a warm thank you to Line Mongeon for all her help with microscopy and particularly for training me for all those long hours on the AFM. I would like to express my deep appreciation to Dr. Jamal Daoud for his extensive help collaborating on dielectric spectroscopy studies and for his assistance with the Bioplotter system and scaffold design. Additional thanks to Dr. Marinella Sandros and Dr. Cathy Tkaczyk for letting me bounce wacky experimental ideas off of them and offering sane advice. I would also like to thank my summer student Vijitha Sivakumar for her assistance with my DNA release and lipoplex characterization studies. Special thanks to Nadia Morrone and Andrew Pearce for keeping the lab stocked and running over the years. Additionally, I would like to extend my gratitude to Steven Shapka for always ensuring that we never ran out of the essentials and that loose ends in the lab never unravelled. My appreciation also to Pina Sorrini for her administrative wizardry in the department.

To all the members of the BiomatX group, past and present, I would like to express my sincerest appreciation for all of your assistance, moral support, and friendship over the years. My deepest thanks to you all!

I would like to thank the members of my PhD advisory committee, Dr. Christopher Barrett, Dr. Reggie Hamdy, and Dr. Robert Kearney, for all of their helpful advice over the years. I would also like to acknowledge NSERC and FQRNT for the funding that made my work possible.

Finally, I cannot begin to thank my family enough for their unwavering love and support over the years. Words alone cannot express my gratitude to my mother, without whom, I never could have completed my PhD journey.

# Table of Contents

# List of Figures

# List of Tables

# Glossary

| | |
|---|---|
| μCT | Micro-computed x-ray tomography |
| ADSC | Adipose derived stem cell |
| AFM | Atomic force microscopy |
| BCA | Bicinchoninic acid assay |
| BMP | Bone morphogenetic protein |
| BrdU | Bromodeoxyuridine |
| CAD | Computer assisted design |
| CARS | Coherent anti-Stokes Raman scattering |
| CHI | Chitosan |
| CLSM | Confocal laser scanning microscopy |
| ECIS | Electric cell impedance sensing |
| ECM | Extracellular matrix |
| EDC | 1-Ethyl-3-(3-dimethylaminopropyl) carbodiimide |
| EGFP | Enhance green fluorescent protein |
| EIS | Electrical impedance spectroscopy |
| EIT | Electrical impedance tomography |
| ELISA | Enzyme-linked immunosorbent assay |
| FACS | Fluorescent activated cell sorting |
| FDA | Food and drug administration |
| FTIR | Fourier transform infrared |
| GFP | Green fluorescent protein |
| Glyc-CHI | Glycol-chitosan |
| HA | Hyaluronic acid |
| IR | Infrared |
| LbL | Layer-by-layer |
| MPLSM | Multiphoton laser scanning microscopy |
| MRE | Magnetic resonance elastography |
| MRI | Magnetic resonance imaging |
| MSC | Mesenchymal stem cell |
| MTT | 3-(4,5-Dimethylthiazol-2-yl)-2,5-diphenyltetrazolium bromide |
| MW | Molecular weight |
| NMR | Nuclear magnetic resonance |
| OCE | Optical coherence elastography |
| OCPM | Optical coherence phase microscopy |
| OCT | Optical coherence tomography |
| OWLS | Optical waveguide lightmode spectroscopy |
| PAH | Poly(allylamine) |
| PBS | Phosphate buffered saline |
| PGA | Poly(glycolic acid) |
| PE | Polyelectrolyte |
| PEG | Poly(ethylene glycol) |
| PEI | Poly(ethylenimine) |
| PI | Propidium iodide |
| PLA | Poly(lactic acid) |

| | |
|---|---|
| PLGA | Poly(lactic-co-glycolic acid) |
| PLL | Poly(lysine) |
| PSS | Poly(4-sodium styrene sulfonate) |
| QCM-D | Quartz crystal microbalance with dissipation |
| RFP | Red fluorescent protein |
| SAR | Scanning angle reflectometry |
| SEM | Scanning electron microscopy |
| SFF | Solid free from fabrication |
| SHG | Second harmonic generation |
| sNHS | Sulfo- N-hydroxysuccinimide |
| SOCT | Spectroscopic optical coherence tomography |
| TGFβ | Tissue growth factor β |
| TIPS | Thermally induced phase separation |
| TUNEL | Terminal deoxynucleotidyl transferase dedeoxyuridine triphosphate nick end labelling |
| UV-VIS | Ultraviolet-visible spectroscopy |

## Contribution of Authors

This thesis is presented as a collection of manuscripts written by the candidate with the guidance and collaborations of the co-authors. The manuscripts are based on experiments designed and executed by the candidate who was also responsible for data collection and analysis. The design, fabrication and analysis of the multilayer film systems utilized in this thesis and all cell culture work were performed by the candidate. Fabrication of the three dimensional model scaffolds used in this thesis was also performed by the candidate based on a pre-existing design.

Dr. Pierre Bagnaninchi appears as a coauthor on two of the manuscripts in reflection of his role in: designing the optical coherence phase microscopy (OCPM) system utilized to collect some of the data; assistance in performing some of the OCPM scans and analyzing some of the OCPM data; and his involvement in the preparation of the first of the two manuscipts.

Dr. Maryam Tabrizian appears as a coauthor on all manuscripts in reflection of her supervisory role during the execution of the work and her involvement in the preparation of all manuscripts.

# Chapter 1: Introduction

Tissue engineering has emerged over the last two decades as a promising area of research that brings together expertise in biology and materials science to create tissue-specific grafts for organ repair or replacement. In order to maximize therapeutic potential, tissue engineering scaffolds need to go beyond passively providing a temporary mechanical support for cellular ingrowth and must actively guide cell behaviour, phenotype and tissue architecture. Towards this end, a variety of inductive tissue engineering systems that actively release biofactors, such as proteins and genes, are currently under investigation. However, the processing conditions typically employed in scaffold production are restricted to ranges which preserve the activity of the incorporated biomolecules, thus limiting the properties and architectures that can be produced.

Layer-by-layer (LbL) deposition, a simple technique for the fabrication of thin films and coatings, has been extensively used for the 2D controlled release of drugs, bioactive proteins, and plasmid DNA. Employing mild processing conditions and involving the surface assembly of alternating layers of oppositely charged polyelectrolytes, thin LbL coatings can be formed on nearly any 2D or 3D substrate, thus enabling the modification of material surface properties. We thus believe that the use of LbL polyelectrolyte thin films can be expanded to enable the delivery of genes from 3D scaffolds while preserving the properties and architectures of the underlying matrices. The aim of this thesis work, therefore, was to develop a biocompatible polyelectrolyte multilayer film system which enables gene delivery from 3D scaffold systems.

The naturally-derived polysaccharides chitosan (CHI) and hyaluronic acid (HA) have been widely incorporated into multilayer film architectures for a variety of bioapplications, including *in vitro* gene delivery. However, many cell lines exhibit decreased adhesion to thicker CHI/HA films, thus suggesting that cellular transfection from these films may be far from optimal. We thus developed a comparable film system comprised of glycol-modified chitosan (Glyc-CHI) and HA, with the hypothesis that the resulting films would display increased cell adhesion while preserving many of the biocompatible properties of CHI/HA multilayers, thus enhancing transfection efficiency. In order to enable scaffold-based gene delivery, the resulting Glyc-CHI/HA film system, with and without incorporated gene delivery lipoplexes, was then applied as a surface coating on a model 3D tissue engineering scaffold system composed of poly(lactic-co-glycolic acid) (PLGA). Additionally, a novel, non-invasive, label-free imaging technique known as optical coherence tomography (OCT) was evaluated as a tool for assessing cellular adhesion, viability, and proliferation within our LbL-coated scaffold system.

# Chapter 2: Background and Literature Review

## 2.1 Inductive Tissue Engineering

### ***2.1.1 Principles***:

Motivated by a worldwide shortage of donor organs, tissue engineering has emerged over the last two decades as a promising area of research that brings together expertise in biology and materials science to create tissue-specific grafts for organ repair or replacement. The paradigm underlying the field entails the combination of cells and biofactors within a porous, biodegradable supporting material known as a scaffold or matrix (Fig. 2.1). Early research mainly focused on the selection or design of biocompatible materials, methods for the fabrication of scaffold architectures with appropriate mechanical and physical properties, and sourcing of suitable numbers and types of cells. However, tissue engineering requires scaffolds that not only passively provide a temporary mechanical support for cellular ingrowth, but which also actively guide cellular behaviour, phenotype and architecture. Development of inductive 3D scaffolds which localize and control the delivery of protein growth factors and/or genes has thus been a rapidly growing area of investigation.

Natural tissue development, repair and regeneration involve the precise temporal and spatial orchestration of a variety of signalling cascades and cell types. The protein growth factors which play important roles in these signalling pathways have short half-lives and rapid clearance rates when exogenously introduced *in vitro* or *in vivo*. The

timing of therapeutic growth factor delivery is also crucial to optimize tissue induction while avoiding adverse or inhibitory effects (1, 2). Scaffold-based release, therefore, must localize and maintain biofactor concentrations for the timeframe required for optimal *in situ* tissue development, repair or regeneration.

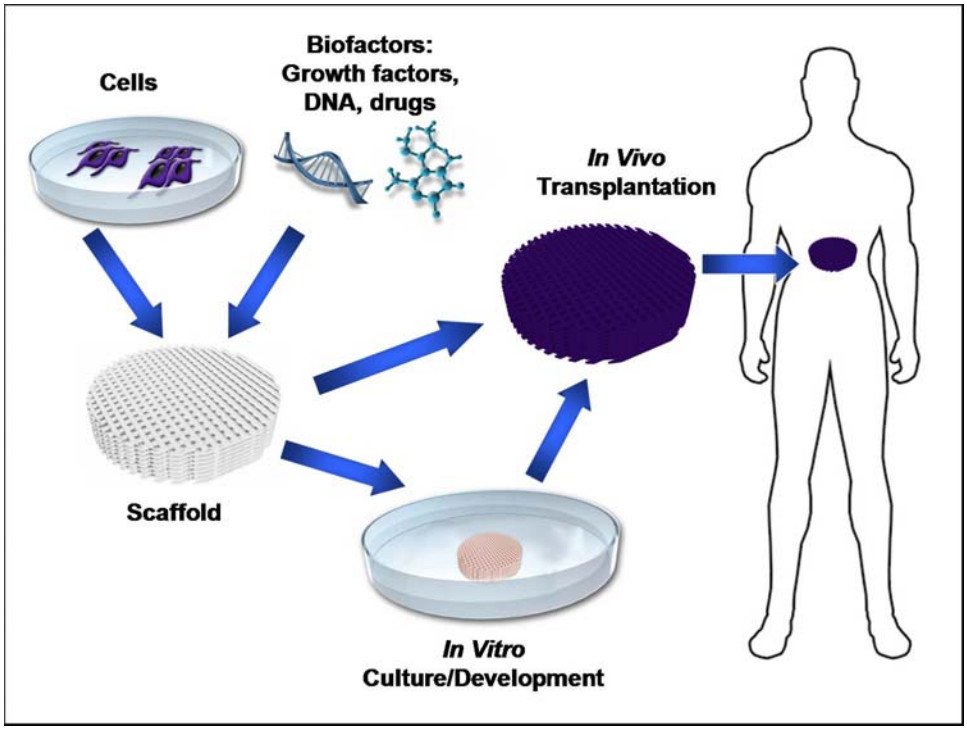


**FIGURE 2.1: The inductive tissue engineering paradigm. Cells and biofactors, such as protein growth factors and DNA, are combined within a porous, biodegradable supporting material known as a scaffold or matrix. The resulting cell-seeded scaffold system can then either be directly transplated *in vivo* or cultured *in vitro* prior to implantation to allow for further tissue development.**

Scaffold-based biofactor release kinetics are governed by both the diffusion rate of the specific molecule through the scaffold system and the degradation rate of the scaffold matrix itself. Thus, the architecture and material employed in inductive scaffold construction must be carefully tailored to the specific tissue and application. Additionally, scaffold processing conditions must be limited to the mild range that

maintains protein conformation, stability and bioactivity (3). In designing an inductive tissue engineering system, it is therefore crucial to consider the materials employed, the scaffold fabrication method and the biofactor incorporation strategy.

### ***2.1.2 Scaffold Materials***:

Materials utilized in scaffold production must fundamentally be "biocompatible", which in the context of tissue engineering means that they must provide a suitable environment that supports appropriate cellular activities for the particular tissue being engineered, while not triggering any undesirable host responses on either a local or systemic level. More specifically, scaffolding materials should be cellular adhesive, biodegradable at an appropriate rate, non-toxic, non-mutagenic, non-immunogenic, processable into a porous matrix and possess suitable mechanical properties. Fortunately, decades of research into implants and controlled drug delivery systems have yielded a wide array of well characterized biodegradable polymers, both naturally-derived and synthetic, which have more recently been investigated for 3D scaffold production (reviewed in (4-9)).

As tissue engineering scaffolds are essentially attempting to mimic the role of the extracellular matrix (ECM), naturally-derived polymers, particularly those proteins and polysaccharides that are themselves components of the ECM, are thus a logical starting point for scaffold design. Ordinarily interacting with and stimulating cells in their native state, naturally-derived polymers are thus intrinsically biocompatible and enzymatically biodegradable, with structures and chemistries that closely mirror the tissue environment. However, the natural origin of these polymers is a double-edged sword leading to batch-

to-batch variability, potential for a xenogenic immune response, or viral and prion contaminants, and high costs associated with purification. Moreover, naturally-derived polymers often have poorer mechanical properties than synthetic materials and can be less amenable to processing. Despite these limitations, natural origin polymers have been used in a wide variety of tissue engineering applications, including in clinical trials and FDA-approved treatments (reviewed in (4, 5, 9)). The most commonly employed naturally-derived tissue engineering polymers can be broadly classified into two main categories: protein-based polymers and polysaccharides.

Proteins, which are essentially polymers consisting of amino acids, constitute the major structural component of most tissues. Fibrous proteins are particularly attractive as tissue engineering materials due to their repetitive secondary and tertiary structures which can create rigidity and thus lead to improved mechanical properties. Of the many protein and amino-acid based polymers investigated in tissue engineering applications, the most widely used are collagen, fibrin, gelatin, elastin, and silk. In addition to animal sourcing, many of these proteins can be produced via recombinant technologies, which enable the control of protein molecular weight and monodispersity, hence eliminating problems with batch-to-batch variations (10-13). More importantly, recombinant techniques allow for precise design of amino acid sequence and the tailoring of protein properties such as biodegradation rate, thus opening the door to novel protein-based polymers which are beginning to be used in tissue engineering scaffolds (13).

Polysaccharides are biopolymers consisting of multiple simple sugar monomers (monosaccharides) joined together via glycosidic bonds. Playing a wide variety of roles *in vivo* from structural to cell signalling, polysaccharides can be obtained from animal, vegetal and microbial sources, and are thus often lower in cost compared to proteins. Polysaccharide physical properties are dependent upon their monosaccharide composition, molecular weight, and structure, i.e. linear vs. branched. The most widely used polysaccharides in tissue engineering are hyaluronic acid, chondroitin sulphate, alginate, chitosan, dextran and starch.

Biodegradable synthetic polymers, although not possessing the inherent biocompatibility of their natural counterparts, provide a variety of advantages for use in tissue engineering. Being synthetic, the chemical and physical properties of these polymers can be precisely controlled with high reproducibility, including biodegradation rate, mechanical stability and processability. Although cell-interacting functional groups can be incorporated into the polymer design, synthetic polymers do not generally interact with cells, nor do they closely resemble the native extracellular matrix. Another important disadvantage is the potential to generate acidic or harmful degradation products *in vivo*. However, the myriad possibilities in design have lead to a vast array of synthetic polymers being employed in scaffolds, including polyesters, polylactones, poly(propylene fumarates), polyanhydrides, polyurethanes, and many others (reviewed in (4, 8)).

Amongst the broad variety of synthetic biodegradable polymers under investigation in the field of tissue engineering, the majority fall within the polyester family. The saturated

aliphatic polyesters poly(lactic acid) (PLA), poly(glycolic acid) (PGA) and poly(lactic-co-glycolic acid) (PLGA) are the most widely utilized, with the latter two employed in devices approved by the Food and Drug Administration (FDA) for human clinical use (14). These polymers degrade *in vivo* via hydrolysis into monomers that can be removed by the existing natural pathways responsible for lactic and glycolic acid removal. The degradation rate of these polymers varies from months to years and depends upon factors such as degree of crystallinity, molecular weight, and copolymerization ratio (3, 9). Although successfully employed in a variety of biomedical applications, many common biodegradable polyesters such as PLA, PGA, and PLGA still exhibit limited mechanical properties and cannot be processed using certain techniques.

While the majority of scaffolds are composed of polymers, certain applications, such as orthopaedic and dental tissue engineering, are better served by the use of scaffolds consisting of ceramics, metals, or composites. Calcium phosphate ceramics, including tricalcium phosphate and hydroxyapatite, and bioactive glasses have been extensively investigated for use in bone tissue engineering due to their superior osteoconductive and osteoinductive properties (reviewed in (15)). However, due to brittleness, poor bioresorbability, and low fracture toughness, ceramic-based scaffolds do face limitations. Polymer-ceramic composite scaffolds combining the advantages of both materials are thus being developed, particularly for osteochondral tissue engineering, with the aim of optimizing mechanical properties and cellular interaction. Interestingly, biodegradable metals, including those based on metals used in orthopaedic implants, have also recently been processed into porous bone tissue engineering scaffolds (16).

### ***2.1.3 Scaffold Fabrication Methods***:

Since structure and function are intricately linked in natural tissues, control of scaffold architecture from the macro- down to the nano- scale is crucial in tissue engineering. The overall architecture of a scaffold will greatly influence construct mechanical properties, biodegradation rate, molecular diffusion, cellular distribution and cell-surface interactions. Alongside selection of the constituent biomaterial(s), two of the key concerns in scaffold design are overall 3D geometry, including micro- and nano- scale surface topography, and porosity, which must be tailored to enable cellular penetration and migration as well as nutrient and waste transport. To date a wide variety of strategies for fabrication of complex, porous, 3D scaffolds have been investigated (reviewed in (17-20)), with recent trends moving towards computer assisted design (CAD) -based manufacturing techniques that allow for precise control of construct architecture (reviewed in (20)).

Hydrogels are one of the mostly widely used classes of 3D matrix for a broad array of tissue engineering applications (reviewed in (21-23)). Consisting of a network of cross-linked hydrophilic natural and/or synthetic polymers, hydrogels are attractive candidates for tissue engineering due to the ease with which they are formed, their highly swollen network structure, their ability to encapsulate cells and growth factors, and their efficient mass transfer properties. Cells, with or without additional biofactors, can be homogenously entrapped within the surrounding matrix during the gelling process, i.e. upon the addition of a chemical or physical cross-linker. Depending upon the properties

of the polymers employed to form the gel, a variety of 'smart' functionalities can also be engineered into the system, such as stimuli (e.g. light, pH, addition of chemicals) - responsive swelling or degradation (reviewed in (24-26)). Used extensively in cell encapsulation, drug delivery, and injectable scaffold applications, hydrogel systems are currently undergoing a number of human clinical trials in applications such as cartilage tissue engineering (27-29). Although possessing the above mentioned advantages, the most significant drawback to hydrogels remains their poor mechanical properties, which has lead to a number of studies into hybrid scaffolds consisting of hydrogels formed within various other scaffold types (30-33).

One of the earliest methods employed in the fabrication of porous polymeric scaffolds is porogen leaching in combination with solvent casting or compression molding (34-36). A porogen, such as biocompatible particulates like salt or sugar, is dispersed within a polymer solution or within a powder-based polymer mixture. Once the scaffold material is set, either via solvent evaporation or heat and pressure, the porogen is leached out of the matrix using an appropriate solvent, thus leaving behind interconnected pores in the size range of the dissolved porogen. Although widely used with a variety of different polymers, this method can give rise to problems in controlling the homogeneity of the dispersed porogen or the degree of pore interconnectivity. The technique generally works best for thin membranes as it can become difficult to completely remove the porogen from thicker constructs. Porogen leaching is also often combined with other fabrication techniques, such as freeze-drying, gas foaming and rapid prototyping, to add an additional scale of porosity.

Freeze-drying and other similar phase separation methods can be used to produce 3D scaffolds with interconnected pores of varying sizes (37-39). In the case of freeze-drying, a polymer is dissolved in an appropriate solvent and mixed with water to form an emulsion which is quickly frozen. The water within this frozen emulsion is then sublimated under low pressure, with the space formerly occupied by ice crystals giving rise to scaffold porosity. Thermally induced phase separation (TIPS) is a similar technique, with a homogenous multi-component system, consisting of a polymer-rich and polymer-poor phase in an easily sublimated solvent, is used in place of a water/polymer emulsion (40-42). In this case, the space left behind by solvent sublimation becomes the pores. In both techniques the degree and size of porosity is controlled by varying the freezing time and other processing parameters (39). Although these techniques are simple and versatile, they result in sponge-like constructs which generally exhibit poor mechanical properties and possibly structural instability upon rehydration. With the TIPS method it can also be difficult to extract all of the solvent, potentially leading to cellular toxicity issues.

Gas foaming is a polymeric scaffold fabrication method that attempts to eliminate the problems associated with harsh organic solvents (43-45). High pressure $CO_2$ is added to dry polymer, e.g. that has been compression molded, dissolving fairly homogenously throughout the matrix. The pressure is then reduced, thus leading the thermodynamically unstable dissolved $CO_2$ to nucleate gas cells which grow and form pores. The resulting

sponge-like scaffolds, however, often exhibit poor pore interconnectivity and often possess a non-porous surface.

Electrospinning is a fabrication method which suits tissue engineering applications where a mesh-like structure would be advantageous, such as connective tissues (46-49). The technique uses high voltage to create an electrically charged jet of polymer melt or solution which is drawn out through a small diameter nozzle. As this charged polymer jet moves towards a charged or grounded collector surface, the solvent evaporates thus forming nanofibres. By controlling the electric field as well as the dispensing and collecting parameters, non-woven nanofibrous mats or membranes with varying fibre diameters can be produced (46). The main challenge still facing this technique is applying it to produce more complex 3D structures.

Rapid prototyping, also referred to as solid free from fabrication (SFF), is an increasingly popular computer-aided technique which allows for complete control over 3D scaffold design (20, 50-52). A digital 3D model of the structure to be produced is generated via CAD software, in some cases linked to medical imaging technologies to yield clinically relevant structures which can even be matched to specific patient defects. The resulting programme is subsequently used by an automated apparatus which manufactures the scaffold by utilizing one of a variety of methods, including: 3D printing, fused deposition modeling, stereolithography, and selective laser sintering (20, 53, 54). They key advantage of these SFF techniques is the precision control of the entire 3D scaffold design, from nano- to macro- scale architecture, to chemistry and mechanical properties.

It also enables the production of unique and complex scaffold geometries which cannot be produced via any other method.

The materials utilized, the fabrication methods employed, and the resulting scaffold architecture help to determine the mechanical properties of an engineered tissue construct. Suitable mechanical properties, that is, those which closely mirror the target tissue, play a vital role in the success of a scaffold system. Within engineered tissues, there is an important mechanical interplay between cells and their surrounding scaffold environment (reviewed in (55)). Scaffold stiffness, for example, can influence cellular adhesion, proliferation and function (56-59); while, cells can exert contractile forces which can deform scaffold architectures (59-62). Thus, it is crucial to select the optimal combination of materials, fabrication methods and scaffold architecture for each specific tissue engineering application.

### ***2.1.4 Biofactor Incorporation and Release Strategies***:

To date, a variety of methods have been explored to incorporate protein growth factors, naked plasmid DNA, adenoviral vectors, lipoplexes, or polyplexes into 3D scaffold systems and control their delivery (reviewed in (63-65)) (Fig. 2.2).

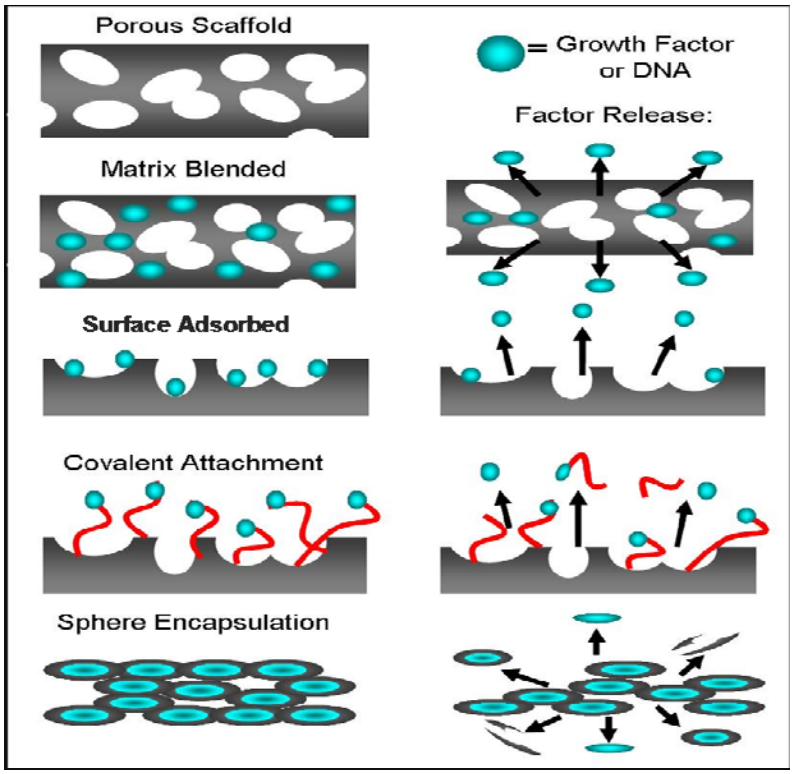


**FIGURE 2.2: Incoportation strategies for producing scaffolds that deliver biofactors, such as protein growth factors and plasmid DNA. Some of the more commonly employed approaches include: directly blending the biofactors with the hydrogel or core scaffold polymers during fabrication; simple surface adsorption of the biofactors onto the scaffold; covalent attachment of the biofactors to the scaffold surface; and encapsulating the biofactors within polymeric microspheres.**

Proteins as well as naked and condensed plasmids can be blended directly into hydrogels or with 'solid scaffold' core polymers via formation of polymer-solvent and biomolecule-water emulsions and subsequent freeze-drying (66), or via gas foaming (67), which eliminates the need for organic solvents. Protein and/or DNA release in these bulk incorporation systems is generally characterized by an initial burst followed by slow release that is controlled by the diffusion and degradation rate of the matrix. Simple, non-specific surface adsorption of proteins, plasmids, polyplexes and lipoplexes via scaffold dipping is also commonly performed (68, 69), although this technique generally results in low levels of protein or gene loading and poor control of release kinetics.

Direct immobilization of proteins and gene delivery vectors to scaffold surfaces, via covalent cross-linking or strategies involving antibody/antigen or biotin/avidin binding, has also been widely investigated (70-73). In designing covalent protein linkage systems, however, one must ensure that the immobilization process does not affect the biological activity of the proteins by blocking active sites or causing denaturation. Additionally, growth factors which require cellular internalization for proper function must only be immobilized via cleavable linkage strategies.

One of the most flexible strategies for the production of controlled delivery scaffold systems involves the use of polymeric micro- or nano-spheres which encapsulate gene delivery vectors or protein growth factors. These factor-loaded spheres can then be aggregated and fused to form 3D scaffolds, blended with the scaffold matrix polymer, or associated with the surface of pre-fabricated scaffolds via adsorption or covalent-cross-linking (74-77). By varying the proteins and or genes that are encapsulated, the polymers used to produce the microsphere shell, and the aggregation or blending strategy, a wide variety of delivery systems can be designed, including those employing sequential and/or zonal release (76, 77). A number of concerns with microsphere fabrication techniques remain, however, such as possible protein denaturation or DNA degradation due to the shear stresses created by sonication during the emulsification process and/or interactions with organic solvents.

Single and multiple protein- and/or gene- releasing scaffold systems have been designed and investigated for a variety of tissue engineering applications, including angiogenesis, bone and cartilage repair, neural and liver regeneration, and wound healing (reviewed in (63, 64)). Current trends in scaffold-based protein and gene delivery are extending beyond controlling dosage and release kinetics to encompass multi-agent delivery and spatially-controlled release. For example, many groups have created concentration gradients of growth factors within hydrogels, with several studies demonstrating the capacity to align neurons and guide axonal extension both *in vitro* and *in vivo* in nerve injury models (78). Meanwhile, zonal protein delivery was demonstrated in an *in vivo* angiogenesis model, with VEGF delivery from one scaffold area resulting in formation of small blood vessels while sequentially delivery of first VEGF and then PDGF in another scaffold zone led to fewer but larger and more mature vessels (79). Spatially patterned gene delivery can also be achieved using various techniques, with one of the most commonly employed strategies being the controlled microfluidic deposition of hydrogels containing different gene delivery vectors (80).

## 2.2. Gene Delivery

***2.2.1 Principles***:

While inductive tissue engineering systems can deliver a variety of biofactors that influence cellular activity, scaffold-based gene delivery offers several potential advantages over release of protein growth factors. In contrast with the challenges that can arise in preserving the 3D structure and bioactivity of proteins, the sequence information of DNA is more easily conserved, thus leading to greater flexibility in the design and application of gene delivery scaffolds. Protein growth factors also tend to exhibit limited half-lives and stability, and are generally more expensive to produce than gene vectors. By inducing host cells to locally produce the growth factors themselves, gene delivery can also provide localized protein expression for longer periods of time and at higher concentrations than exogenous protein delivery. More importantly, the resulting cell-expressed proteins are also far more likely to possess the appropriate conformation, post-translational modifications and thus bioactivity than the recombinant proteins typically released from scaffolds. Furthermore, while inductive tissue engineering via protein delivery is generally limited to cell-surface interacting growth factors, the ability to deliver genes that encode for transcription factors or other intracellular proteins broadens the cellular processes that can be targeted. Finally, tissue-specific gene and thus protein expression can be achieved via use of tissue-specific promoter sequences within the DNA vector.

Like all forms of gene therapy, successful scaffold-based DNA delivery requires the efficient delivery of therapeutically relevant genes to specific cells, the expression of these genes at appropriate levels for the required timeframe, and the minimization of any adverse effects. Naked plasmid DNA can be delivered to cells via a number of physical methods, such as direct nuclear injection, electroporation, ultrasound-facilitated transfer, and hydrodynamic delivery (reviewed in (81)), resulting in successful gene expression. However, viral and non-viral DNA carriers are far more efficient at gene delivery, also known as transfection. Much research effort continues to be devoted to the design and optimization of gene delivery vehicles which can overcome the various biological barriers to transfection.

Any DNA carrier faces a number of challenges along the way to inducing successful gene expression in a cell (reviewed in (82-85)) (Fig. 2.3). The carrier must first protect the DNA from degradation by extracellular nucleases before it can get into the cell. It must also condense the DNA into an appropriate size range for cellular internalization. The carrier vector must then enable cellular uptake, either via targeted pathways, such as receptor mediated endocytosis, or via non-specific means, such as electrostatic or lipophilic interactions with the cellular membrane (86). Once taken up into the cell, the DNA-carrier complex must be transported through the cytoplasm and into the nucleus, escaping the endo-lysosomal pathway along the way if necessary. Inside the nucleus, the carrier must be able to disassociate from the DNA, thus enabling the DNA to be transcribed into proteins. The remaining carrier materials must also ideally be non-toxic and biocompatible.

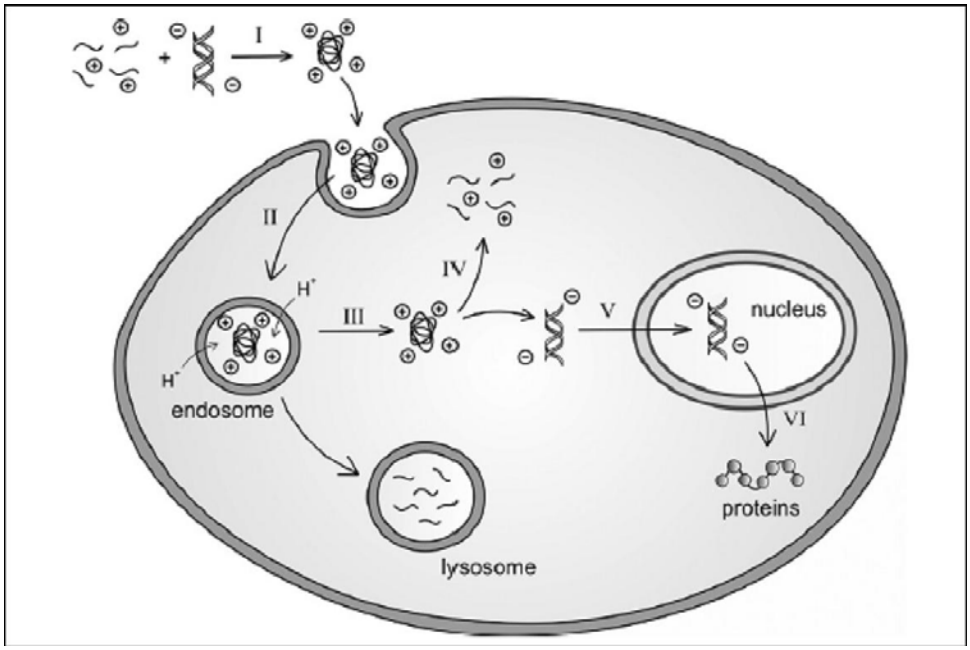


**FIGURE 2.3: Barriers to successful gene delivery and intracellular expression which must be considered in designing a delivery vector. (I) Gene packaging/condensation. (II) Cellular uptake. (III) Endo-lysosomal escape. (IV) Vector release of the gene. (V) Trafficking through the cytoplasm and into the nucleus. (VI) Expression of the gene into a protein. (from: (85))**

The aim of scaffold-based gene release is thus to deliver optimal transfection vectors in a controlled, substrate-mediated manner in order to direct cellular behaviour, function and architecture.

### ***2.2.2 Gene Delivery Vectors***:

A wide variety of viral and non-viral gene delivery vectors have been investigated to date, with several even employed in human clinical trials. As viruses evolved to deliver their genetic material into host cells, viral-based vectors were the first class of carriers to be studied for gene therapy applications (reviewed in (87, 88)). Consisting mainly of RNA or DNA surrounded by a caspid, viral vectors have been modified to be replication-

deficient carriers, with the majority of their genetic material removed to minimize adverse effects. Viral vectors, including those based on adenoviruses, retroviruses, lentiviruses, adeno-associated vectors, and the herpes simplex virus, are the most widely used gene therapy carriers due to their extremely high transfection efficiencies. Indeed, the vast majority of clinical trials employ adenoviral and retroviral vectors to treat a variety of disorders, including immuno-deficiencies, cancer, sickle cell anemia, macular degeneration, heart failure, Alzheimer's disease, and Parkinson's disease (89). However, there are serious concerns about the immunogenicity of various viral vectors, as well as the possibility of mutagenic effects due to random insertion of DNA into the host genome. While different strategies are being employed to modify viral carriers to solve these problems, non-viral DNA delivery vectors have emerged as a viable alternative.

The majority of non-viral gene carriers are cationic in nature and either lipid- or polymer-based, or a hybrid of the two. These cations electrostatically interact with anionic DNA, condensing it into polyplexes or lipoplexes which serve to both protect the DNA from degradation and increase cellular uptake. By varying the ratio of carrier cation groups (e.g. amines) to DNA anionic phosphate groups, also known as the N:P ratio, the resulting DNA polyplex or lipoplex size and surface charge can be optimized to improve transfection efficiency. Although cationic polymer and lipid carriers tend to display significantly lower transfection efficiencies than viral vectors, they are generally easier and cheaper to manufacture, exhibit lower immunogenicity, and offer a greater flexibility in design, particularly for cellular targeting.

Lipid-based gene carriers are the most commonly used form of non-viral vector. Generally consisting of a cationic head group, a hydrophobic domain and a segment linking the two, lipid-based vectors typically exhibit the highest transfection efficiencies amongst non-viral vectors. A wide variety of cationic lipids have been developed for gene delivery (reviewed in (90-93)), with many of them often mixed with a non-charged helper lipid, such as cholesterol or dioleoylphosphatidylethanolamine (DOPE), in order to enhance transfection and/or reduce cytotoxicity. Serving as the 'gold standard' in most transfection studies, Lipofectamine, a commercially available mixture of the polycationic lipid 2,3-dioleyloxy-N-[2(sperminecarboxamido)ethyl]-N,N-dimethyl-1-propanaminium trifluoroacetate (DOSPA) and the neutral lipid dioleoyl phosphatidylethanolamine (DOPE), and its derivatives, such as Lipofectamine2000$^{TM}$, are by far the most widely employed non-viral gene delivery vectors. Able to transfect a wide variety of cell types both *in vitro* and *in vivo* at high efficiency, Lipofectamine has been used in approximately 7% of worldwide gene therapy trials (93). However, Lipofectamine and related lipid-based gene carriers still do not achieve transfection efficiencies as high as viral vectors and cytotoxicity issues remain, particularly as cellular contact time is increased.

A broad variety of synthetic and naturally-derived polymeric vectors have been investigated for gene delivery (reviewed in (82, 85, 94)), including those based on poly(ethylenimine) (PEI), poly(amidoamine), poly(orthester)s, poly(phosphoester)s, poly(lysine) (PLL), cyclodextrin, and chitosan (CHI). With the highest cationic charge density of any polymer, polyethylenimine (PEI) is the most widely studied polymeric

gene delivery vector to date, achieving relatively high transfection efficiencies in a variety of cell lines and primary cell types (95, 96). However, as toxicity remains an issue with PEI and many other synthetic vectors, a number of biodegradable and naturally-derived carriers, including polysaccharide and peptide-based polymers such as chitosan (CHI) and poly(lysine) (PLL), have been studied in the hopes of reducing cytotoxicity and improving biocompatibility (97, 98). By tailoring polymer structure (e.g. linear vs. branched) and molecular weight, as well as the N:P ratio, transfection efficiency can be optimized for specific cell types and gene therapy applications.

Hybrid gene carrier systems combing the best features of polymeric, lipid-based, peptide-based and viral systems have also been widely investigated. For example, viral and lipid-based vectors have been modified with poly(ethylene glycol) (PEG) or other hydrophilic polymers to reduce protein adhesion and thus immune recognition (99, 100). A variety of strategies have also been employed for the surface modification of gene delivery polyplexes, lipoplexes and viral vectors with cell-specific targeting ligands, such as folate, lactose, integrins, transferrin, and aptamers (83, 101, 102). Addition of ligands and polymeric segments that promote endo-lysosomal escape, cytosolic transport, nuclear importation, and vector-DNA dissociation has also been studied for a variety of carriers, particularly polymeric ones (82, 85, 103). Currently, much research is being performed to develop new classes of multifunctional gene delivery vectors, including those that are stimuli- responsive, facilitate intracellular tracking, or enable magnetic or ultrasound assisted delivery (84, 85).

In selecting a gene delivery vector for an inductive tissue engineering application, a number of important factors must be considered. Firstly, whether the target cell population is dividing or non-dividing determines the type of vectors which can be used, since some viral vectors (e.g. retroviral) and many non-viral vectors can only transfect dividing cells. Another concern is the required duration of transgene expression. While many vectors are suitable for transient transfection, which is appropriate if gene expression is only needed for a short-term period, only certain viral vectors (retroviral and lentiviral) can permanently integrate DNA into the host cell genome. Additionally, the immunogenicity of a gene carrier can be a significant issue if sustained release is required, as a more serious immune response can lead to fibrous encapsulation of the inductive scaffold system (104, 105). Most importantly, the stability of the vector will greatly affect the scaffold design and processing conditions that can be employed. Many viral vectors inactivate quickly at room temperature and may be difficult to process with various types of scaffolds, in contrast to non-viral systems which tend to be more stable. Thus the DNA carrier selected is as crucial as the scaffold design to the success of an inductive tissue engineering system.

### ***2.2.3 Substrate-Based Gene Delivery***:

Scaffold- and substrate-based gene delivery offer a number of advantages over traditional solution-based, or 'bolus', transfection. The scaffold itself provides an additional level of protection from systemic degradation and clearance, while localizing transfection to the site of interest, thus minimizing transport and cell targeting issues as well as non-target cell transfection. By concentrating the gene delivery vectors to the vicinity nearest the

cells, substrate-based transfection can also potentially achieve higher transfection efficiencies while simultaneously requiring a lower total amount of DNA. Scaffold-based transfection also provides the potential of sustained gene delivery for longer time frames, as well as an easier means for combined and sequential gene delivery.

Gene-releasing 3D scaffold systems have been investigated for a wide range of tissue engineering applications, including wound healing, angiogenesis, nerve regeneration, and bone, cartilage and tendon repair (reviewed in (106-108)). Naked plasmid DNA, as well as DNA complexed with viral, polymeric and lipid-based carriers have been incorporated within a variety of 3D scaffold types using a number of different methods, as previously overviewed (Chap. 2.1.4). However, strategies involving surface immobilization of DNA and gene delivery vectors raise a number of issues affecting transfection efficiency which merit closer consideration.

Substrate-mediated gene delivery, also referred to as 'reverse transfection' or 'solid-phase transfection', involves the attachment of DNA, with or without a carrier vector, onto a biomaterial surface and is thus utilized not only in tissue engineering applications, but also in medical implant coatings and cellular transfection microarrays (109-111). The key concern in substrate-mediated transfection is balancing immobilization with cellular internalization. The method used to associate the gene delivery vector with the surface must be strong enough to maintain localization, yet not too strong as to prevent cellular uptake and thus transfection. For example, in the case of biotinylated PLL-DNA complexes linked to a neutravidin coated surface, it was found that there is an optimal

amount of biotin functionalization, below and above which transfection efficiency was low. Too much biotin and PLL complexes were not able to be internalized by cells, too little and not enough DNA was localized to the material surface (72).

The context in which surface adsorbed or immobilized gene delivery complexes are presented is also important to substrate-mediated transfection efficiency. The chemistry and topography of the underlying biomaterial surface not only directly affects the DNA loading capacity, but also influences the size and shape of the adsorbed DNA polyplexes or lipoplexes, all of which play a role in transfection efficiency. Material surface features also have a significant effect on cellular adhesion and proliferation, which in turn affect transfection levels, and may even influence the level of cellular endocytosis (112, 113). For example, co-presentation of retroviral and polymeric vectors alongside certain adsorbed proteins, such as fibronectin, has been found to increase surface-mediated transfection (114-116), in some cases without affecting cellular adhesion or spreading (114). It is theorized that this rise in transfection efficiency is due to a change in the route of cellular internalization from clathrin-mediated endocytosis to the caveolin-dependent pathway used for fibronectin uptake (117), thus potentially decreasing edo-lysosomal degradation (118, 119).

A variety of strategies can be employed for the surface-immobilization of gene transfection vectors, including non-specific adsorption (109), encapsulation within a thin polymeric or hydrogel film (110), surface attachment via biotin-streptavidin (72), antibody-antigen conjugate systems (120), or cell-responsive tethering via enzyme-

cleavable linkages (121). Amongst these many methods, layer-by-layer polyelectrolyte deposition has emerged as a simple yet versatile technique which can be utilized with biomaterials of nearly any type, shape or size.

## 2.3 Layer-by-Layer Deposition

### *2.3.1 Principles*:

Employed in a variety of biomedical applications, layer-by-layer (LbL) deposition is a simple and versatile technique used for the fabrication of thin films and coatings. LbL films are produced via the sequential surface assembly of alternating layers of oppositely charged polyelectrolytes and can be formed on nearly any 2D or 3D substrate, thus enabling modification of material surface properties. A wide range of charged species can be incorporated within LbL multilayers, including natural and synthetic polymers, proteins, DNA, drugs, dyes, inorganic nanoparticles, and carbon nanotubes. Film properties such as thickness, mechanical stability, permeability, and surface roughness, chemistry, and wettability can be fine tuned by altering the polyelectrolytes (PEs), layer number, architecture, and fabrication conditions employed. This flexibility makes LbL deposition an attractive method for a diversity of applications, including drug and gene delivery (reviewed in (122-124)).

Developed by Decher and colleagues (125), the general layer-by-layer deposition method is outlined in Fig. 2.4. A charged substrate is immersed in a solution containing an oppositely charged polyelectrolyte (e.g. polycation), which adsorbs onto the surface, thus yielding the first layer and reversing the surface charge. Any unbound polyelectrolyte is then removed via a rinsing step, followed by immersion in another solution consisting of a polyelectrolyte of opposite charge to the first (e.g. polyanion), which forms the second layer. This layer pair, or bilayer, is then rinsed again and the entire cycle is repeated until

the desired number of layers is deposited. Rather than consisting of distinct, strictly structured layers, the resulting LbL films are somewhat "fuzzy" with some layer interpenetration and an overall periodic structure (126, 127). LbL films can not only be formed using the dipping method described above, but can also be produced via spin-coating (128-130), or spray-coating (131-133) of alternating species.

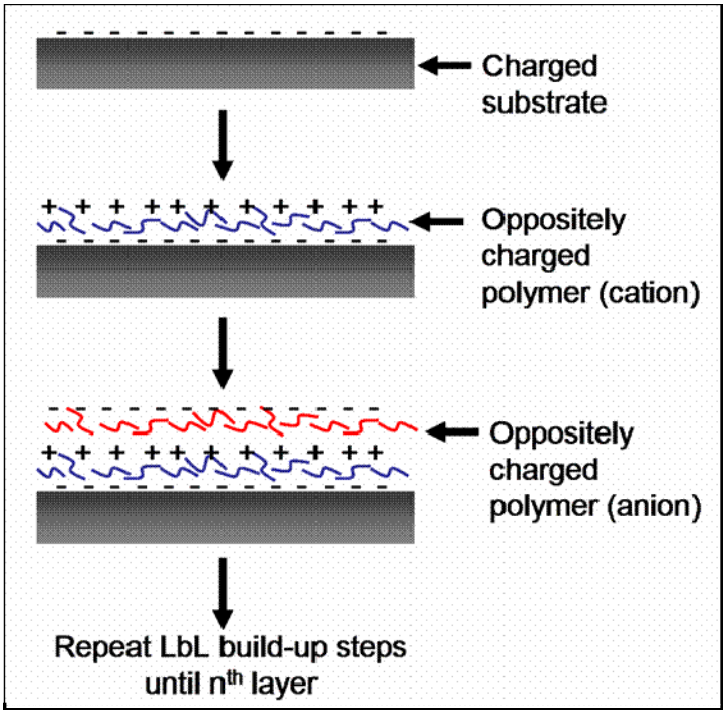


**FIGURE 2.4: Layer-by-Layer deposition process. A polyelectrolyte (in this example, a cation) is deposited onto an oppositely charged substrate, forming the first polymer layer and inverting the surface charge. After a rinsing step, a different oppositely charged polyelectrolyte (in this case, an anion) is deposited, thus forming the second polymer layer and again inverting the surface charge. After a rinsing step, the process is repeated a number of times until the desired number of polymer layers are deposited.**

While a variety of LbL systems have been developed and characterized, the precise mechanisms underlying their formation are only beginning to be understood. Layer-by-layer build-up is believed to be mainly driven by electrostatic interactions; however, the contributions of non-electrostatic forces should not be ignored. Electrostatic forces

alone, for example, cannot account for charge inversion following polyelectrolyte adsorption, as a purely electrostatic interaction would lead to an exact balance of the charge of the underlying layer. Furthermore, in some film systems, inversion of surface charge is not required for polyelectrolyte adsorption (134). Entropic gain, due to the release of water and counterions as oppositely charge polyelectrolytes complex within the film, is theorized to be a key factor in driving film formation (135, 136). Hydrophobic interactions, hydrogen bonding, specific polymer-polymer interactions and other entropic contributions also play important roles in multilayer formation (137). Indeed, many LbL film systems have been designed utilizing non-electrostatic interactions (reviewed in (138)), including hydrogen-bonding (reviewed in (139)), hydrophobic interactions (140), stereo-complexation (141), charge transfer interactions (142), metal-ligand complexation (143), and specific bio-interactions (144-147).

### ***2.3.2 Monitoring LbL Deposition and Film Growth***:

The layer-by-layer build-up of polyelectrolyte films can be investigated using a variety of thin film characterization techniques. In order to analyze a specific multilayer system, film properties, such as surface charge, thickness, mass and structure, are typically evaluated either *in situ* or after each layer deposition step. As surface charge inversion following each polyelectrolyte adsorption step is generally characteristic of LbL build-up, one of the more commonly employed methods for monitoring multilayer film formation involves assessing the surface zeta-potential via streaming potential measurements (148-151).

Changes in film mass and thickness during multilayer fabrication are also essential to film system characterization and can be analyzed through a range of optical and spectroscopic techniques. The majority of these methods measure changes in optical absorbance or reflective spectra in comparison to a bare substrate and use a characteristic film refractive index to determine multilayer thickness. Examples of optical and spectroscopic techniques commonly employed to assess polyelectrolyte multilayer thickness and mass include: ultraviolet-visible spectroscopy (UV-VIS) (152-154), ellipsometry (148, 155, 156), scanning angle reflectometry (SAR) (149, 157), optical waveguide lightmode spectroscopy (OWLS) (157-159), and surface plasmon resonance (SPR) (160-162). These techniques generally employ the assumption that the measured films are optically homogenous and isotropic layers. As this is often not the case, particularly for the first few film layers (150, 159), more than one method is often utilized.

Quartz-crystal microbalance with dissipation (QCM-D) is a widely used alternative method for characterizing LbL film mass and thickness (150, 153, 159, 160, 163, 164). A real-time, high-resolution technique based upon the piezoelectric effect, QCM-D detects mass binding to the surface of electrode-equipped quartz crystals (reviewed in(165)). An alternating electric field is applied to the crystal, thus producing a characteristic resonance frequency which decreases as increasing amounts of mass become bound to the surface. The time-dependent loss of crystal oscillation energy, or dissipation factor, is inversely proportional to the time required for the crystal to stop oscillating once the applied voltage is turned off. This dissipation factor increases as the

amount of mass bound to the crystal sensor increases. Real-time monitoring of changes in frequency and dissipation during multilayer formation on top of quartz sensors thus yields data about the kinetics, mass and thickness of film formation. The thickness of rigid, tightly-bound, purely elastic multilayer films, which are characterized by the observation that frequency changes measured at the fundamental frequency and higher overtones all superimpose well over one another, can be determined by the linear Sauerbrey relationship (166). However, many LbL films display soft, viscoelastic and/or highly hydrated properties which lead to system energy losses and result in a wide spread in QCM-D frequency change measurements recorded at different overtones (164, 167, 168). In these cases, multilayer thickness is related to frequency and dissipation changes through the Voight-Voinova model (169, 170).

Assessment of film structure is another important element of exploring polyelectrolyte multilayer formation. High energy techniques such as x-ray and neutron reflectometry have been used to examine internal multilayer structural features, including layer stratification and degree of layer interpenetration, on a nanometre-scale (127, 171-173). However, as these techniques yield little information about the overall morphology of the film, often require deuteration of the sample, and are expensive and inefficient, atomic force microscopy (AFM) has emerged as the most widely used method for assessing LbL film structure (150, 156, 163, 174-176). Enabling high-resolution characterisation of surface properties such as topography, roughness and mechanical modulus, atomic force microscopy (reviewed in (177)) involves scanning a nano-sized tip, which is attached to a cantilever, over a sample surface. Deflections in the cantilever are detected by reflecting

a laser from the cantilever tip to a photodetector. AFM can be operated in various modes, with the contact and tapping modes being the most commonly employed in characterizing multilayer film morphology and structure. In the contact mode, the tip scans the surface at a low force and is deflected by surface features and forces. Cantilever deflection is monitored and maintained at a constant via a feedback loop to keep the applied force at a preset value. In the tapping mode, the cantilever is vibrated at its resonance frequency whilst tapping the sample surface and a feedback loop maintains constant amplitude. Multilayer film mechanical properties, meanwhile, can be analyzed via AFM nanoindentation studies (178-181).

The wide variety of techniques utilized to analyze LbL film properties reveal important information about the multilayer build-up process. More importantly, these methods allow for the detailed investigation of the many factors influencing LbL film formation, stability and resulting properties.

### ***2.3.3 Film Growth and Influencing Factors***:

The mass and thickness of multilayer films can grow either linearly or "exponentially" with the number of deposited bilayers, depending upon a number of factors. Linearly growing films are generally formed from strong polyelectrolytes with a high charge density, such as poly(4-sodium styrene sulfonate) (PSS) and poly(allylamine) (PAH), which lead to films consisting of relatively immobile polymer chains with only small interdigitations between layers (126, 182, 183). These linear films thus tend to be thinner, more mechanically rigid, and less permeable. Exponential multilayers, by contrast, tend

to be formed from weaker polyelectrolytes, especially biopolymers such as proteins and polysaccharides, and tend to be significantly thicker, more visco-elastic, and somewhat more permeable (184, 185).

"Exponential" multilayer growth, as proposed by the model developed by Lavalle and colleagues (184, 186), appears to be due to diffusion of one or more of the polyelectrolytes into and out of the film system. As an example, consider the poly(lysine) (PLL) and hyaluronic acid (HA) system, where PLL is the freely diffusing polyelectrolyte and HA can only interact with the outermost layers during a deposition step. When a negatively charged HA outer layer is brought into contact with a positively charged PLL solution, the PLL chains not only interact with this layer to adsorb and form PLL-HA complexes, but also diffuse down throughout the film. This free PLL interacts weakly with the film matrix and may even exchange with some of the bound PLL within the film. PLL diffusion into the film stops as the PLL-HA complexes that form at the film surface invert the surface charge thus creating an electrostatic barrier. When a buffer solution is introduced in the rinsing step, some of the free PLL diffuses back out. However, as this diffusion lowers the chemical potential inside the film, which in turn increases the height of the electrostatic barrier to be overcome by the remaining PLL chains, not all the free PLL leaves the film. As the oppositely charged HA solution is brought into contact with the film for the next deposition step, the electrostatic barrier is removed, and some of the free PLL left within the film diffuses out to interact with the HA at the film/solution interface. Thus the HA that adsorbs in this step is not only proportional to the amount of PLL adsorbed in the last step, but is additionally dependent

upon the amount of free PLL that diffuses to the film surface. This, in turn, is related to the total thickness of the film. The mass increase of the film thus increases with total film thickness, becoming “exponential”.

While it is difficult to predict which growth regime will characterize a given polyelectrolyte pair, in general, linear film growth is associated with strongly interacting polyelectrolytes which are highly exothermic, while exponential growth is linked to more weakly interacting polyelectrolytes which are endothermic or weakly exothermic (187, 188). However, most polyelectrolyte systems can be made to transition from linear to exponential growth, or vice versa, given the right conditions. For example, linear films can be made to grow exponentially with an increase in solution salt concentration and many exponentially growing films transition to linear growth once a certain critical number of deposited bilayers is reached (175, 189). Many factors influence the strength of polyelectrolyte interactions and thus whether a film system grows linearly or exponentially, including polymer charge density, the concentration and type of counter ions present in the depositing and rinsing solutions, the deposition time and temperature, solvent quality, and solution pH (174, 175, 190-195).

The presence of salt ions in LbL deposition and rinsing solutions strongly influences the formation and resulting properties of multilayer films. The addition of salt in the deposition solution screens charges on the polyelectrolyte chains, minimizing repulsion interactions within chains and thus leading to chain coiling (175). These coiled chains adsorb in extended ‘loopy’ conformations which allow for greater polyelectrolyte surface

density and thus thicker and rougher films (156, 175). Film thickness tends to increase proportionally to salt concentration, reaching a maximum at an optimal concentration which depends upon the given salt-polyelectrolyte system (191, 196). The species of salt ions used also affects LbL film formation, with multilayer thickness generally varying as Li+<Na+<K+ and F-<Cl-<Br- (190, 197). Generally, ions characterized by smaller and weaker hydration shells interact more strongly with polyelectrolytes, promoting chain coiling and thicker and rougher films (198).

Polyelectrolyte structure, molecular weight and charge density also play important roles in determining multilayer properties. For most polyelectrolyte systems there is a minimum charge density required for LbL film formation (160, 193, 194). Charge density in strong polyelectrolytes is determined by chemical structure alone, while for weak polyelectrolytes, such as polysaccharides and proteins, charge density is also highly dependent upon the solution pH. Generally, fully charged polyelectrolyte chains adsorb in a flat, spread out conformation due to intra-chain repulsion and increased chain-surface interactions, thus leading to thinner films. In this fully charged state, molecular weight appears to have little effect on film thickness for many polyelectrolyte systems (174). Meanwhile, less charged polyelectrolytes tend to coil and adsorb as thicker layers, with increased molecular weight, in this case, leading to thicker films (174, 199).

While the broad range of factors influencing the formation and properties of LbL films may seem daunting, it also provides a great flexibility for multilayer design, enabling fine, nano-scale tuning of film features. By carefully selecting the polyelectrolytes used,

and the layer architecture and preparation conditions employed, multilayer films can be designed for a wide variety of biomedical applications, including modifying cellular and protein adhesion, and tunable drug, protein and gene delivery.

### ***2.3.4 Cellular and Protein Adhesion on LbL Films***:

Protein and cellular adhesion are the first events that occur upon biomaterial implantation, influencing all subsequent host-material interactions, including coagulation, inflammation, and implant integration. Specific promotion or inhibition of protein and cellular surface adhesion is thus crucial for various biomedical applications. Cellular adhesion has been found to be influenced by material surface properties such as chemistry, hydrophobicity/hydrophilicity, topography and mechanical modulus (200). The ability to finely tune film properties thus makes LbL deposition an attractive technique for the fabrication of cell-resistant and cell-promoting films and implant coatings.

Cell adhesion on polyelectrolyte multilayers is dependent upon a wide variety of factors, including the specific cell-type under investigation, the polyelectrolyte species employed, and film properties such as surface roughness, stiffness, swelling behaviour, water content, hydrophobicity/ hydrophilicity, and the charge of the terminating layer (181, 201-207). Although it is difficult to separate the effects of individual factors, generally, increasing layer rigidity tends to increase cellular adhesion. Thin, dense, linearly-growing films, such as PSS/PAH, tend to be more cell-adhesive than thicker, highly hydrated, exponentially growing films, such as those composed of polysaccharides (159,

181, 203, 205). However, when thick viscoelastic films, such as those composed of PLL/HA and CHI/HA, are chemically cross-linked they become more rigid and exhibit increased cell attachment and spreading (180, 204, 208). Similarly, varying the ionic architecture and thus the hydration/swelling behaviour of PAH/PAA films was found to vary fibroblast adhesion properties, with lightly ionically cross-linked films exhibiting more swelling and cytophobicity, while more tightly ionically linked films were cytophilic and more resistant to swelling (205). Thus modulation of film mechanical properties, either during film formation via control of deposition solution pH and ionic strength, or post-assembly via chemical or photo-crosslinking, is one of the most common means of promoting cellular adhesion. Multilayer films can also be made more cell adhesive by adding extracellular matrix proteins, such as collagen, fibronectin, or vitronectin as a terminal layer (209), or by chemically grafting peptide sequences (e.g. RGD) which interact with cell adhesion receptors to the film surface (210, 211).

On the opposite end of the spectrum, multilayer films that resist cellular and protein adhesion have been developed for anti-fouling, immunocamouflage, and anti-thrombogenic applications. Many of these protein-resistant film systems utilize poly(ethylene glycol) (PEG), a highly hydrated polymer used since the 1990s to minimize surface protein adhesion (212), either by depositing a terminating PEG layer at the multilayer surface (213), or by using PEG-grafted polymers within the film construction (214). For example, our group employed the latter strategy to develop a LbL coating consisting of PLL-graft-PEG, alginate, and chitosan-graft-phosphorylcholine that was able to successfully coat and immunocamouflage live red blood cells, preventing

antibody-binding while preserving cell viability and function (215, 216). Various adhesion-resistant, non-PEG based film systems have also been investigated, particularly as anti-thrombogenic coatings. Several groups have shown that LbL polyelectrolyte films containing CHI, HA, albimum, heparin, or dextran can increase the resistance of the underlying substrate to blood coagulation (217-219), while our group has demonstrated that CHI/HA multilayers can be used to coat arterial walls and reduce platelet adhesion (220).

### ***2.3.5 Multilayer Films for Biofactor Delivery***:

The design flexibility of polyelectrolyte multilayers offers a number of advantages for controlled delivery of drugs, growth factors and genes. Biofactors can be incorporated within polyelectrolyte films or capsules as one of the components during LbL deposition, via covalent attachment, or loaded into the film or capsule post-assembly (e.g. via a pH gradient or electrostatic interactions). The loading concentration can be carefully controlled via the number of factor layers integrated within the film, as well as the deposition conditions employed. The mild processing conditions utilized during LbL deposition preserve both the bioactivity of the incorporated factors, for example, maintaining protein growth factor structures close to native conformations (221), as well as the properties of the underlying substrate, thus enabling controlled release from a wider array of materials and architectures. Most importantly, the layered nature of polyelectrolyte films allows for fabrication of multi-stage constructs which enable sequential release of multiple factors.

Depending on the nature of the biofactor to be delivered and the polyelectrolytes employed, factor release can be mediated by passive diffusion through the film, film degradation, or a combination of both. Release of low molecular weight compounds tends to be diffusion controlled with the rate of diffusion dependent upon the internal structure and porosity of the film (123, 222). Delivery of larger species such as proteins, on the other hand, is generally governed by the degradation rate of the film system rather than passive diffusion (223). The delivery kinetics of single or multiple proteins and/or genes from multilayers can thus be controlled via selection of PEs with specific biodegradation rates, for example utilizing hydrolytically or enzymatically degradable polymers, or by varying the number of deposited biomolecule layers, or via altering their respective embedding depths. Chemically cross-linking the polyelectrolyte layers with gluteraldehyde or carbodiimide (224, 225) is another popular strategy for tuning film degradation rate and thus biofactor release. However, these cross-linkers can have cytotoxic effects or potentially alter the structure of the biomolecules being delivered and must therefore be used with care. Alternatively, overall film degradation kinetics can be varied by blending PEs with different degradation rates (226).

Multilayer film diffusion and degradation can also be designed to be stimuli-responsive, enabling environmentally triggered "smart" delivery. As LbL formation, particularly involving weak polyelectrolytes, is highly sensitive to solution pH and ionic strength, films can be designed to respond to changes in their strength, such as the change in pH that occurs between the stomach and intestine. When at least one of the constituent polyelectrolytes is a weak polyacid or base, changes in pH alter the degree of

protonation/deprotonation within the film allowing for control of film permeability and swelling behaviour, and thus biofactor release (227-229). Alternatively, polyelectrolytes that hydrolyze above a critical pH can be employed to enable triggered film degradation (230, 231). Polyelectrolyte films can also be engineered to degrade or become more permeable in response to changes in temperature (232, 233), or the presence of light (234), or mechanical (235, 236), electrochemical (237, 238), and biological (239) stimuli.

Polyelectrolyte multilayer films and capsules have been designed for the delivery of a wide variety of drugs and proteins. Since the first LbL system delivering ibuprofen was developed (240), multilayer systems releasing dexamethasone (241), ampicillin (242), paclitaxel and tamoxifen (243), insulin (244, 245), and many other drugs have been investigated. Protein growth factor delivery for a broad range of biomedical applications has also been explored. For example, delivery of bone morphogenic protein (BMP) -4 and Noggin proteins embedded within PLGA/PLL films can induce or inhibit apopotosis, respectively, in a tooth culture system (246), while delivery of BMP-2 and TGFβ-1 from PLGA/PLL multilayers directed bone and cartilage differentiation of ES cells (247). Meanwhile, our group developed a core-shell nanoparticle system utilizing a LbL coating consisting of chitosan and alginate to successfully deliver BMP-7 *in vivo* enhancing bone regeneration in a rabbit model of distraction osteogenesis (248).

### ***2.3.6 LbL Systems for Gene Delivery***:

Using similar strategies, polyelectrolyte multilayer films and core-shell nanoparticles have also been widely used for gene delivery applications. Naked plasmid DNA, PEI- and cyclodextran- complexed plasmids, and adenoviral vectors have been incorporated into a variety of polyelectrolyte multilayer designs (reviewed in (124)), which have demonstrated successful transfection of many cell lines and primary cell types *in vitro*. Like proteins, DNA does not appear to diffuse readily through multilayer systems, thus necessitating the use of hydrolytically and/or enzymatically degradable polymers, or films engineered to degrade in response to environmental stimuli, as described previously. As in the case of drug and protein delivery, careful selection of the PEs used and the layer architecture and chemistry employed enables both the tailoring of release kinetics and sequential delivery of several different genes (226, 249).

The Voegel and Jessel group has done extensive work on 2D LbL film-based gene delivery, examining numerous different combinations of gene delivery vectors, polyelectrolytes and multilayer architectures for controlled transfection of a variety of cell types. PLL/PGA, CHI/HA, PAH/PSS, and PLL/HA multilayer films have been used to deliver PEI-condensed plasmids (250), pyridylamino cyclodextrin complexed plasmids (249), or adenoviral vectors (251) to several different cell lines (BHK-21, Huh-7, heLA, NIH3T3, COS, CHO) and primary cells (hMFs). While results varied greatly between systems, generally, lower transfection levels were observed when the vector was embedded under greater numbers of PE bilayers, and an increase in the number of vector layers led to an increase in transfection efficiency (249-251). Interestingly, certain polyanions were found to interact with and destabilize PEI-DNA polyplexes, which was

reflected in the observation that Huh-7 cells could only be transfected from CHI/HA films or PLL/PGA and PAH/PSS architectures which sandwiched the PEI-DNA layer between layers of HA (250). Pyridylamino cyclodextrin complexed plasmids embedded within PLL/PLGA multilayers displayed the highest transfection efficiencies for CHO, COS and macrophage cells; in fact, exhibiting efficiencies far greater than those observed with media delivered FUGENE or calcium phosphate control vectors (249). Transfection in this system was not due to passive plasmid release, as there was no significant plasmid release from multilayer films incubated in media for up to 6 days, but appeared to be mediated by direct cellular contact. Most importantly, by varying the film layer architecture (i.e. the order in which the plasmids were embedded) sequential transfection and thus production of different proteins (both nuclear and cytoplasmic) by COS cells could be achieved over a time scale of 2 to 8 hours (249).

As an alternative to embedding viral and non-viral gene delivery vectors within multilayer films, naked plasmid DNA can be directly used as the anionic species for LbL assembly, alongside degradable cationic polymers. For example, Lynn and colleagues built polyelectrolyte multilayers from a synthetic hydrolytically degradable cationic polyamine ("polymer 1") and naked plasmid DNA encoding EGFP or RFP (252), which, used alone or as a stent-coating, could transfect COS cells *in vitro* with efficiencies of ~ 18% and ~4%, respectively (253, 254). Atomic force microscopy and confocal laser scanning microscopy analysis suggested that the DNA/polymer layers re-arranged themselves to present surface-bound condensed DNA nanoparticles ~50-400 nm in diameter (253, 254). Naked plasmid DNA-based LbL multilayers have also been

constructed using chitosan (255), galactosylated chitosan (256), poly(2-aminoethyl propylene phosphate) (257), and reducible hyperbranched poly(amido amine) (258) as the cationic PEs, with similar film surface rearrangements into nanoparticle complexes observed in most cases. As these plasmid-cationic polymer films degrade *in vitro*, these complexes are released, as verified via electrophoresis and TEM (255-257), and are thought to act like other typical cationic gene delivery vectors. Interestingly, the galactosylated chitosan-based films were designed for cell-specific transfection, as the galactose group is a specific ligand for the ASGP-R receptor on hepatocytes. This hepatocyte-specificity was achieved, with films constructed with greater levels of galactose substitution exhibiting an increasing transfection level in HepG2 cells, compared to chitosan alone, and with no increase in transfection shown in 293T kidney cells (256).

The great potential of LbL films for inductive tissue engineering and bioimplants has been recently demonstrated by several groups which have successfully extended multilayer gene delivery to *in vivo* applications. Blacklock and colleagues, for example, have utilized films composed of hyperbranched poly(amido amine) and plasmid DNA encoding secreted alkaline phosphatase (SEAP) to coat thin stainless steel meshes, which, when implanted subcutaneously in rats, demonstrated *in vivo* gene transfection activity via increased secretion of SEAP in the circulation (258). Meanwhile, the Lynn group has applied their previously discussed "polymer 1" system alongside plasmid DNA encoding either EGFP or β-galactosidase as a coating for inflatable embolectomy catheter balloons and has shown that the resulting balloon system was able to transfect cells *in vivo* in a rat

arterial injury model (259). LbL deposition thus holds great promise for enabling the controlled delivery of genes, and other bioactive molecules from three-dimensional scaffold surfaces.

### ***2.3.7 Multilayer Films for Coating of 3D Scaffolds***:

Over the last few years, polyelectrolyte multilayers have begun to be used as surface coatings for inductive 3D tissue engineering scaffold systems. The first studies expanding LbL deposition to tissue engineering applications explored coating 3D polymer scaffolds and hydrogels to improve biocompatibility and cell-adhesion properties. LbL deposition of PEI and gelatin onto poly(DL-lactide) scaffolds, for example, improved *in vitro* MC3T3 cell adhesion (260, 261), while chondroitin sulfate/collagen I multilayers deposited onto poly(L-lactic acid) (PLLA) scaffolds improved *in vitro* chondrocyte attachment, proliferation, and GAG synthesis (262). Similarly, PLL/HA multilayers formed on photo-crosslinked HA hydrogels modified gel swelling and mechanical properties and resulted in increased fibroblast cell adhesion and spreading (263). Using a slightly different approach, the Kotov group formed multilayers consisting of poly(diallyldimethylammonium chloride) and clay nanoparticles on poly(acrylamide) scaffolds to promote cell adhesion, and used the resulting scaffolds for the co-culture of adherent human thymic epithelial cells and non-adherent premyelote monocytes (264).

Inductive tissue engineering systems utilizing LbL films for controlled protein growth factor or gene delivery are also beginning to be developed. For example, electrospun PLLA fibrous mats coated with multilayer films formed of PEI and plasmid DNA

encoding luciferase demonstrated *in vitro* transfection of COS cells, with increasing levels of transfection found with time as well as increased bilayer number (265). Meanwhile, 3D printed β-tricalcium phosphate/polycaprolactone scaffolds were coated with LbL films consisting of a poly (β-aminoester) ("poly 2"), chondroitin sulphate (CS), and BMP-2 in a $[poly2/CS/BMP\text{-}2/CS]_{100}$ architecture, resulting in a system that released approximately 10 μg of BMP-2 protein over a period of 2 weeks (266). When implanted intramuscularly in rats, the inductive LbL scaffold system successfully induced *in vivo* bone formation, as assessed 4 and 9 weeks post-implantation (266). Although these preliminary studies have demonstrated the great promise of LbL assembly for use in inductive 3D scaffolds, much work remains to be done in the detailed scaffold-wide characterization of these films and in extending this technique to more complex scaffold architectures.

## 2.4 Assessing Tissue Growth in Scaffolds

### *2.4.1 Principles*:

Progress in the field of inductive tissue engineering will not only involve the development of scaffold systems that localize and control the delivery of genes and other biofactors, but also requires technologies which can accurately visualize and analyze engineered tissue growth and health in real time and three dimensions (3D). Ideally, these tools will enable non-invasive, repeated measurement of engineered tissue structure and function down to a cellular level, making possible the examination of interactions between cells, biomolecules and scaffolds. Assessment of *in vitro* engineered tissues requires accurate monitoring of tissue growth, morphology, viability and bioactivity over time within 3D constructs. This challenge becomes even greater when one considers the thickness of the tissue constructs, the wide variety of cell types and scaffolding materials involved, and the need for high imaging resolution.

As no one method can currently meet all the criteria required for real-time, non-invasive, label-free, high resolution 3D scaffold imaging, a combination of different techniques is typically used to evaluate various aspects of engineered tissue structure and health. The majority of these procedures are those traditionally associated with conventional tissue biopsy characterization and involve destructive end-point tests, such as histology, immunohistochemistry, and biochemical assays (reviewed in (267)). These traditional techniques generally require the use of staining agents and sample processing, thus proving labour-intensive and expensive, as well as preventing time-course studies. The

few techniques that do allow real-time monitoring, such as confocal microscopy, are either limited in imaging penetration depth to several hundred micrometres and/or require fluorescent labelling. In order to overcome these limitations, a variety of spectroscopy and clinical imaging techniques are currently being adapted and investigated for non-invasive 3D monitoring of tissue engineering constructs (reviewed in (268, 269)).

### ***2.4.2 Histology and Immunohistochemistry Techniques***:

Histology and histochemistry enable the visualization of tissue structural details by utilizing dyes to increase contrast and localize known biomolecules (270). Histological preparation involves sectioning tissue samples into thin slices for staining and subsequent imaging via microscopy. Samples are first flash frozen in liquid nitrogen or chemically fixed using agents such as formalin/formaldehyde, gluteraldehyde, or methanol to preserve tissue structures and molecular information (271). After chemical fixation, tissue samples are dehydrated (e.g. via an ethanol series) and infiltrated with an embedding medium such as paraffin wax or resins. Embedding media provide the tissue with a solid matrix that enables thin sectioning while still being soft enough not to modify tissue structures or damage the cutting blade. During the freezing process, flash frozen tissues are also often immersed in a freezing/embedding solution, such as OCT (Optical Cutting Temperature) medium, which consists of a mixture of polyethylene glycol and polyvinyl alcohol, or a solution of gelatine and sucrose. However, ice itself can act as an embedding medium, enabling cryomicrotome sectioning while causing minimal damage to tissue morphology (271). In both cases, tissue sections approximately 5 to 10 μm in thickness are typically sliced from the sample via microtome or cryomicrotome onto glass slides

for further staining and visualization. Generally, sample fixation combined with paraffin embedding is preferable for traditional histological staining as it maintains overall tissue structure best, while flash freezing is preferable for immunohistochemistry as it better preserves the molecular state of the tissue.

As tissues do not naturally exhibit inherent contrast when observed via traditional light microscopy, numerous histological stains have been developed that enhance contrast and specifically stain various tissue components (270, 271). One of the most widely employed histological stains in tissue microscopy is the dual hematoxylin and eosin stain. Hematoxylin acts like a basic dye and stains acidic or basophilic structures a blue/black colour, such as the cell nucleus, and organelles that contain RNA, like ribosomes and the rough endoplasmic reticulum. Eosin is an acidic dye which is reddish/pink in colour and stains basic or acidophilic structures such as the cytoplasm and extra cellular matrix fibres. Another commonly used stain is Masson's Trichrome, a three colour stain which labels keratins and muscle fibres red, collagen and bone blue/green, cytoplasm pinkish, and nuclei brown/black. A wide variety of other histological stains have been developed to selectively stain tissues, cells and their components, such as Oil Red O and Sudan Black for lipid deposits, Alizarin Red for calcium, and Alcian Blue for mucins and glycosoaminoglycans.

Immunohistochemistry enables more specific identification and visualization of cellular phenotype and tissue constituents than traditional histological staining by utilizing specific antibody-antigen binding. A detection antibody is conjugated to a marker, such

as a fluorophore, enzyme, or colloidal metal, which thus localizes the labelling to cells expressing a specific antigen. This labelled detection antibody can either be the primary antibody which specifically binds to the antigen of interest, or can be a secondary antibody which binds to an unlabeled primary antibody. While direct detection via a primary antibody is the simplest immunohistochemical technique, indirect detection via a labelled secondary antibody is often employed due to enhanced sensitivity and signal (270, 271). In both cases, immersion of samples in a blocking solution, such as the serum of a species unrelated to those of the antibodies and antigens in use, is necessary in order to minimize non-specific antibody binding and background staining. Imaging of the immunohistochemical stain is subsequently performed via light, fluorescence or confocal microscopy depending upon the specific label used and the tissue under investigation.

### ***2.4.3 Microscopy Techniques***:

While conventional light, phase and fluorescent microscopy enable visualization of cells cultured on transparent surfaces and of tissue sections which have been histologically or immunohistochemically stained, the limited penetration depth of these techniques restricts their use largely to 2D applications. Accurate monitoring of *in vitro* engineered tissue structure and function requires imaging of thicker tissue samples and, ideally, 3D sample scanning. Stereological approaches can be applied to stacks of traditional 2D microscopy images taken from consecutive histological slices in order to yield 3D structural information about tissue samples (reviewed in (272)). However, these techniques are limited by loss of information between tissue slices and possible artefacts introduced during sample fixing, embedding, and sectioning. More sophisticated

microscopy techniques, such as confocal, multiphoton and scanning electron microscopy, have thus been employed to image engineered tissues (reviewed in more detail in (268, 269)).

Although confocal laser scanning microscopy (CLSM) provides an imaging resolution similar to that of conventional microscopy, it enables optical depth-sectioning and thus 3D imaging, making it one of the most commonly used techniques to assess engineered tissue structure. The light source used in standard microscopes illuminates the whole sample region in the field of view, thus light interacts with and scatters throughout the sample resulting in detection of light from multiple planes. By contrast, confocal microscopes focus light on a specific point within a sample via a short wavelength laser light source reflected from a dichromatic mirror. The light reflected, scattered or emitted (i.e. due to excitation of a fluorophore within the sample) from this point in the specimen is then collected through a pinhole-sized aperture by a detector. The light source, illuminated sample point, and detector aperture are in an optically conjugate 'confocal' plane, thus allowing for collection of light from this specific focus plane and rejection of light from all other planes (273). The size of the pinhole can be adjusted to regulate the amount of light from other vertical planes that is rejected, thus helping to determine the optical sectioning thickness (or "z resolution") alongside the numerical aperture of the objective lens, wavelength of the excitation and emission light, and refractive index of the sample. Scanning the laser excitation point across the sample plane using a combination of mirrors enables a 2D image to be obtained, while vertical focusing allows

for optional sectioning of the sample. By stacking 2D confocal images, CLSM can produce 3D volume images of the tissue sample.

Reflectance-based confocal microscopy can be performed without the addition of exogenous labels by depending entirely upon endogenous light scattering within the tissue sample. Images of human tissues at subcellular resolution have been achieved using this reflectance-based mode at penetration depths of up to 300 μm (274). However, visualization of internal cellular morphology with high contrast is difficult using reflectance-based confocal imaging, and it is not possible to assess cell viability or function. CLSM imaging with enhanced levels of detail and biochemical information requires the exogenous addition of fluorescence-based dyes and labels, or endogenous expression of fluorescently-modified proteins. Fluorescence-based confocal microscopy is thus often limited by factors such as background autofluorescence from scaffolding materials or tissue constituents, the end-point nature of immunohistochemical labelling, or the need for utilization of genetically modified cells which express fluorescently-labelled proteins. The penetration depth of both modes of confocal imaging depends upon the desired resolution, the optical objectives used, the optical properties of the tissue sample, and the level of signal available for detection. Generally, light penetration into tissue engineering scaffolds, particularly polymeric and composite systems, is somewhat restricted due to the optically dense nature of the overall construct, resulting in typical imaging depths limited to around 100-300 um (269).

Multiphoton laser scanning microscopy (MPLSM) utilizes nonlinear optical adsorption and scattering interactions to enable 2D and 3D imaging at greater penetration depths than confocal microscopy. Maintaining submicron imaging resolutions similar to that of CLSM, MPLSM can achieve penetration depths of up to 1 mm in certain tissues (275, 276), although ranges of about 400-500 μm are more typical (277, 278). A high-energy wavelength-tuneable pulsed laser source is employed in MPLSM to excite fluorescent proteins and dyes within a tissue sample via simultaneous adsorption of two or more near infrared (IR) photons. This nonlinear excitation results in the fluorescently emitted photons having shorter wavelengths, and thus higher energies, than each of the incident photons, allowing for more efficient separation of the excitation and emission spectra of the sample via optical filters. MPLSM does not require the detection pinholes used in CLSM and is therefore characterized by simpler and more efficient signal detection and an improved signal to noise ratio. Another important advantage of MPLSM compared to CLSM is reduced photo-bleaching and photo-damage to samples (279). The main disadvantage to multiphoton imaging is the requirement of an expensive laser system and the need for environmental control (e.g. temperature and humidity) for proper system alignment and operation. Also, as in the case of confocal microscopy, MPLSM still generally requires the use of endogenous fluorescent labels and dyes, or the endogenous cellular expression of fluorescently labelled proteins. In certain cases, however, a variant of multiphoton microscopy known as second harmonic generation (SHG) can be used to image autofluorescence due to a variety of extracellular matrix (ECM) proteins and can thus enable label-free, *in situ* imaging of ECM structures in tissue engineered constructs as well as *in vivo* tissues (reviewed in (280)).

Scanning electron microscopy (SEM), while limited to sample surface imaging, is another commonly used technique in assessing engineered tissue structure. Typically employed to characterize the surface structure of biomaterials and tissue engineering scaffolds pre- and post- cell seeding, SEM imaging can achieve extremely high resolution imaging, on the order of 1 to 5 nm, and magnification ranges of 5 to 250,000 times (281, 282). In place of light, a beam of high energy electrons is used to bombard the sample under vacuum conditions, resulting in the release of secondary electrons, backscattered electrons, x-rays and photons from the surface. These surface emitted species are detected and analyzed to generate a topographical surface image and to reveal information about sample composition and features (282). The sample preparation required for SEM imaging is quite destructive, involving dehydration and surface coating with a metal such as gold to create a surface capable of generating detectable emissions, thus possibly creating processing artefacts and limiting the technique.

### ***2.4.4 Biochemical Assays***:

In addition to imaging macro- and micro-structural details, it is important to evaluate the health and function of engineered tissues. A wide variety of biochemical assays based upon colorimetric, histological and other methods are typically used to analyze cellular viability, proliferation, and phenotype, as well as tissue composition. While bioassay techniques based upon histochemical and immunohistochemical techniques, which work as described above, enable visualization of biochemical information within the tissue structure, colorimetric assays quantify the amount of a particular substance within the

sample. The optical absorbance or fluorescence of a sample solution is measured via a spectrophotometer or fluorimeter, respectively, and is correlated to the concentration of the substance of interest (283). The absorbance or fluorescence of the sample solution varies with concentration either due to the inherent optical properties of the species of interest, such as DNA absorbance at 260 nm, or due to labelling or reaction of the species with an indicator, as in enzyme-linked immunosorbent assays (ELISA), for example, where a protein of interest binds to an enzyme-conjugated antibody (283). By using a calibration curve derived from measurement of a series of solutions of known concentration at the wavelength of maximal adsorption or appropriate fluorescent emission, the sample solution concentration can be determined.

A wide variety of cellular viability and proliferation assays are employed to evaluate tissue growth and health within scaffold systems. Some of the more basic methods enumerate the total number of cells within a tissue sample as a measure of proliferation, typically by utilizing a simple DNA binding dye such as PicoGreen or Hoescht. Picogreen is a fluorescent marker that binds to double-stranded DNA and which is used, following cell lysis, to measure total DNA concentration via fluorimetry (284). Although less sensitive than Picogreen, as it binds to double and single stranded DNA as well as RNA, Hoechst is a cell permeable fluorescent dye which can be used with live or dead cells. Commonly used to label the nucleus of cells in tissue sections, Hoechst staining is widely used in fluorescence and confocal imaging (285). While software can be used to enumerate the number of Hoescht stained cells in microscopy images, Hoescht dye can also be used alongside fluorimetry as a colorimetric means of determining total DNA

content within a sample. Alternatively, many popular colorimetric and histochemical assays utilize cellular metabolic activity, membrane integrity, or DNA damage as a means of evaluating cellular viability (reviewed in (286)).

Cellular reduction of tetrazolium salts such as MTT, XTT and WST-1 into formazan dyzes is the most commonly used method for determining the number of metabolically active cells within a sample (287-290). MTT, or 3-(4,5-dimethylthiazol-2-yl)-2,5-diphenyltetrazolium bromide, for example, is metabolized within cells to form insoluble purple fomazan crystals, which can be solubilised following cell lysis and used to assess the number of viable cells by measuring sample adsorbance via spectrophotometry and comparison to a standard curve (287, 288). While MTT requires cell lysis and thus can only be used as an end point assay, XTT and WST-1 produce water-soluble formazan crystals and can thus be used for repeated measures (289, 290). In all cases calibration is crucial, as metabolic activity can vary between cell types and with time for any given cell type thereby making direct correlations with viable cell numbers difficult. Thus colorimetric metabolic assays are best for comparisons with a control population.

Live/Dead staining is a popular histochemical method for evaluation of cellular viability within tissue sections (291, 292). As its name suggests, the technique uses two fluorescent dyes to separately label live and dead cells and is imaged via fluorescence or confocal microscopy. Membrane permeable calcein AM is cleaved by metabolically active cells to form the fluorescent form of calcein which emits at approximately 500 nm. Ethidium bromide is non-cell-permeable and thus only enters dead or damaged cells

where it binds to nucleic acids and fluoresces at around 530 nm. Since calcein labelling depends upon metabolically viable cells, Live/Dead staining cannot be used with embedded and sectioned tissue samples.

Sophisticated DNA labelling techniques such as BrDU incorporation and TUNEL staining can be used to visualize and assess cellular proliferation and apoptosis, respectively, within tissue engineered constructs. Bromodeoxyuridine (BrdU) is a synthetic analogue to deoxythymidine and can be incorporated in its place within DNA during cellular proliferation. The presence of BrdU within cells which have proliferated can be visualized via immunohistochemical staining using labelled anti-BrdU antibodies (293, 294). Late stage cellular apoptosis is characterized by DNA damage which can be assessed via terminal deoxynucleotidyl transferase (TdT) dUTP nick end labeling (TUNEL) (295, 296). In TUNEL staining, the enzyme TdT mediates the incorporation of modified dedeoxyuridine triphosphate (dUTP) at DNA double strand breaks. These modified dUTPs can be conjugated directly to labelling fluorophores or to molecules which can be detected via antibody-antigen or biotin-streptavidin interactions, thus enabling immunohistochemical labelling of apoptotic cells.

Evaluating the expression and distribution of specific phenotypic and functional markers and tissue constituents, such as extracellular matrix proteins, is also crucial in the assessment of *in vitro* engineered tissues. The majority of these expression assays utilize variations of immunolabelling methods based upon antibody-antigen binding interactions. For example, immunohistochemistry coupled with microscopy techniques

can be employed to visualize the distribution of a panel of different protein species within a given tissue section. Meanwhile, the amounts of specific proteins within a tissue sample can be quantified using either enzyme-linked immunosorbent assays (ELISA), as mentioned above, or immunoblotting, which involves immunolabelling of proteins which have been separated by size via gel electrophoresis (297). The number of cells within a tissue expressing a given set of markers can also be quantified using immunolabelling coupled with fluorescent activated cell sorting (FACS).

FACS is a flow cytometry technique which measures the light scattering properties of individual cells within a fluid stream (298, 299). Cells suspended in a stream of 'sheath' fluid are carried to a flow cell where they are illuminated with a laser beam. Light scattering from these cells is detected by forward and side scattering detectors, termed FSC and SSC, respectively, and is used to determine the size and complexity of the cell. Fluorescence emitted from cells labelled with fluorescently-conjugated antibodies or cells modified to endogenously express fluorescent proteins can also be detected and used to quantify the number of cells expressing certain markers. FACS can also be used to separate cells based on their fluorescence and light scattering properties, by breaking the fluid stream into a series of small droplets containing single cells, electrostatically charging these droplets, and using charged deflector plates to deflect the droplets into separate collectors. Although extremely useful for quantifying the number of cells expressing and co-expressing a wide variety of markers, FACS analysis requires cells to be dissociated from their scaffold and tissue, thus limiting the technique to destructive, end-point testing.

While the colorimetric, histochemical and immunoassays discussed above provide a wealth of information about cellular viability, proliferation and marker expression, they are also somewhat limited in their applications to analysis of tissue engineering constructs. The majority of these assays are destructive end point tests that require the addition of exogenous labels and stains as well as time consuming sample processing and calibration curves. In an attempt to overcome these limitations, there has recently been a move towards combining non-invasive spectroscopy techniques, which provide viability and/or biochemical data, with non-destructive microscopy and clinical imaging techniques.

### ***2.4.5 Spectroscopy Techniques***:

A variety of spectroscopy techniques have been investigated for monitoring tissue viability and biochemical information. Appealing due to their non-invasive nature and lacking the need for the use of exogenous labels, these spectroscopy methods are only beginning to be explored for imaging of 3D tissue engineered constructs. Often these techniques are combined with more conventional microscopy or clinical imaging systems, enabling the biochemical data obtained via spectroscopy to be mapped to structural images of the tissue. To date, the most commonly studied spectroscopy techniques for biomedical applications include Fourier transform infrared (FT-IR) spectroscopy, Raman spectroscopy and its variant coherent anti-Stokes Raman scattering (CARS), and dielectric spectroscopy (reviewed in (268, 300-303)).

Fourier transform infrared (FT-IR) spectroscopy enables the non-invasive, label-free examination of tissue samples on a molecular level (reviewed in (300)). FT-IR spectrometers employ a broadband IR light source and a Michelson interferometer to reflect light from, or transmit light through, a sample and into detector. The IR light is adsorbed by chemical bonds within the sample, producing adsorption spectra which are distinctive of the specific molecules present. IR spectra from each point within a sample are collected and a Fourier transform of the signals from the time to the frequency domain is performed. The resulting data are analyzed and used to determine the chemical composition of the sample.

By coupling FT-IR spectrometry with a scanner and either focal plane array detection or linear array detection, 2D and 3D FT-IR image maps of sample chemistry can be produced. FT-IR spectroscopy has been used to map the chemical composition of various tissue sections, including those from tumours (304), bone (305), skin (306), intestine (307), and liver (308). Using serial tissue sections and software, 3D multivariate image maps can be created, as has been demonstrated for bone (309) and cervical tissue (310). Although showing promise as a tool for assessing biochemical composition of tissue engineering constructs, FT-IR spectroscopy is limited by its thin penetration depth of several microns and the strong IR absorbance of water which can obstruct the signal related to certain cellular components in some conditions. FT-IR imaging in tissue engineering applications may thus be restricted to use with sectioned samples.

Similar to FT-IR spectroscopy, Raman spectroscopy utilizes the scattering interactions of near-IR light to yield information about the chemical composition of a tissue sample (reviewed in (301, 302)). In Raman spectroscopy, near-IR light from a laser is focused through a series of mirrors onto the sample where it excites molecules and looses energy. This interaction with the molecules within the sample causes a proportion of the light to shift in frequency (a 'Raman shift'). The non-shifted fraction of the scattered light is filtered out by a notch filter and the remaining Raman-shifted light from the sample is passed on to the detector. Analysis of the shifted signal reveals chemical information about the sample, since each chemical bond in a molecule results in distinctive frequency shifts in photons.

Raman spectroscopy, like FT-IR, has been used to produce 2D and 3D maps of tissue chemical composition using sections from a variety of tissue and organs, including bone, skin, lung, breast, muscle, nervous and epithelial tissues (reviewed in (301, 302)). When coupled with optical microscopy, the superior resolution of Raman microspectroscopy enables single cell and sub-cellular analysis, facilitating discrimination between different cell states, such as differentiation, viability, or cancer phenotype. Raman spectroscopy provides a number of advantages over FT-IR since it is not affected by the presence of water and can offer superior spatial resolution due to the shorter wavelength lasers used (~ 1 μm for Raman compared to ~ 10 μm for FT-IR) (311, 312). However, Raman spectroscopy is limited by its low sensitivity thus requires high powered laser sources and longer acquisition times which, in some cases, can be detrimental to live cell imaging.

Several methods to enhance Raman spectroscopy have been explored, with coherent anti-Stokes Raman scattering (CARS) emerging as the most widely used. CARS is a non-linear version of Raman spectroscopy which greatly enhances sensitivity by using three laser light beams, referred to as the probe, pump and Stokes beams, to illuminate the sample. The frequencies of the pump and Stokes beams must be tuned such that the difference between the two corresponds to the vibrational transition frequency of the molecule trying to be detected. If this vibrational resonance frequency is achieved, the target molecules in the probe volume (i.e. the focal point of the pump and Stokes beams) vibrate coherently, scattering the probe beam and resulting in an enhanced coherent signal with a higher frequency than the probe beam and much greater intensity than can be achieved with spontaneous linear Raman scattering (302, 303). Although limited by a low penetration depth around 100 μm and requiring high concentrations of the molecule of interest for detection, CARS has been used to map the chemical composition of a number of tissues and cells, finding a particular niche in detecting lipids (reviewed in (302, 303)). Most importantly, preliminary studies coupling CARS with SHG two-photon microscopy have demonstrated 3D label-free, non-invasive imaging of cells in hydrogel-like scaffolds (313, 314). The two-photon SHG mode was used to image the cellulose fibrous scaffolds, while the CARS mode was used to image MC3T3 murine pre-osteoblasts (314) or human smooth muscle cells (313) seeded in these scaffolds by using lipid as their chemical marker.

In contrast to the previously discussed techniques which use optical spectra to obtain biochemical information, electrical impedance spectroscopy (EIS) uses the dielectric

properties of cells and tissues to assess morphological and physiological properties in a real-time, label-free, non-invasive manner. Also known as dielectric spectroscopy, EIS applies a defined alternating current to tissue samples and measures their frequency-dependent changes in complex electrical impedance. The bioimpedance of cells and tissues is determined by the extracellular environment (e.g. ECM proteins), the capacitance of cellar membranes, and intracellular resistance. Indeed, cells consist of a conducting cytoplasm surrounded by a thin insulating membrane and can thus be modeled as an equivalent circuit composed of an effective membrane capacitance ($C_m$) and intra- and extra-cellular resistances ($R_i$ and $R_e$). Cells within a tissue therefore act as a network of capacitors and resistors which affect the overall impedance measurement. The dielectric properties of cells and tissues display frequency dependence, with low frequencies (<10 kHz) governed by membrane capacitance and thus yielding information reflecting cellular size and shape, and frequencies between 10 kHz and 100 MHz serving to short-circuit the membrane capacitance, allowing the external electric field to penetrate into the cell interior and yield data reflecting intracellular properties.

Electrical impedance spectroscopy has been applied in a variety of biomedical applications and is starting to be explored in tissue engineering. Cellular adhesion, proliferation, differentiation and apoptosis on 2D electrode surfaces can be monitored using a variation on the EIS technique known as electric cell-substrate impedance sensing (ECIS) (315-320). Meanwhile, EIS can also be used to monitor 3D tissue growth and differentiation (321, 322). More importantly, electrical impedance tomography (EIT) is a technique that couples EIS to an array of electrode detectors in order to measure tissue

bioimpedance at various points and thus create 2D and 3D tissue impedance maps, and has found a variety of clinical applications (323-326). Impedance spectroscopy is only beginning to be applied to tissue engineering applications and to date has been used to characterize scaffold structure (327) and to monitor cellular proliferation and differentiation in porous scaffold systems (328-330).

### ***2.4.6 Clinical Imaging Techniques***:

Recently, clinical imaging modalities have progressed from a non-invasive means of visualizing macroscale tissue morphology and anatomy towards higher resolution microscale imaging, with many even enabling tissue functional assessment. Although often offering poorer resolution than many of the microscopy techniques discussed above, clinical imaging techniques provide much greater imaging penetration depths and are often label-free, thus making them attractive methods for assessing engineered tissue structure. More importantly, many of these adapted clinical imaging tools can yield quantitative information about tissue viability, chemistry and mechanical properties. Amongst the clinical techniques currently being adapted for imaging of tissue engineering systems, the most widely employed are micro-computed x-ray tomography (μCT), magnetic resonance imaging (MRI), and optical coherence tomography (OCT).

Widely used in tissue engineering scaffold characterization, x-ray micro-computed tomography (μCT) acquires high-resolution cross-sectional images based upon the physical density of materials, which are then used to generate 3D images and make quantitative measurements of structural properties (reviewed in (331-333)). In μCT,

samples are irradiated by an x-ray beam which is attenuated as it passes through the sample and into the detector. From the detector measurements, the x-ray paths are determined and a 2D image map of attenuation coefficients, which corresponds to material density, is generated (334). These 2D maps are then used to reconstruct a 3D image of the sample. Depending upon the system and set-up employed, μCT image resolution varies from less than 1 μm to 50 μm, with higher resolutions generating larger data sets and requiring longer imaging times (335). In the field of tissue engineering, μCT is mainly used to image 3D scaffold structure and to quantify scaffold surface area, porosity, pore size distribution and volume fractions (281, 336, 337). μCT imaging is limited by the x-ray attenuation properties of the materials under investigation and is thus generally not used to image scaffolds containing cells, with the exception of those in bone tissue engineering, where mineralized bone provides high contrast (338-340). However, the addition of exogenous contrast agents such as osmium tetroxide and silicon-based Microfil has enabled some other tissues to be imaged such as vasculature and nervous tissues (341-344). Although extremely useful for scaffold structural characterization and the assessment of tissue engineered bone, μCT imaging is mostly restricted to end-point analysis in most areas of tissue engineering due to its use of ionizing radiation and need for contrast agent enhancement.

Magnetic resonance imaging (MRI) provides 3D, non-invasive, deep tissue, high resolution imaging both *in vitro* and *in vivo* and is thus increasingly being applied to tissue engineering (reviewed in (345)). MRI measures changes in proton spin within the water of tissues inside a strong magnetic field, using a series of radiofrequency pulses

and magnetic field gradients to manipulate proton spin behaviour and for spatial localization. These measurements detect differences in tissue hydration, the state of tissue water (e.g. freely diffusing vs. protein-bound), and nuclear magnetic resonance (NMR) relaxation times which are then mapped into MR images revealing tissue structure (346). Imaging resolutions of less than 100 μm can be achieved with MRI systems using 7-14 Tesla magnets and high magnetic field strengths, enabling tissue visualization down to nearly the cellular level (347-349). Addition of exogenous paramagnetic and superparamagnetic contrast agents can not only enhance intrinsic tissue contrast and track pre-labelled cells, but can also be used to map the biochemical and physiological state of tissues through the use of more sophisticated contrast agents (reviewed in (350)), such as those designed to be cell-permeable, ligand-targeted, or enzyme-responsive.

MRI has been used to visualize and analyze tissue growth, composition and health in a variety of *in vitro* tissue engineering systems, including those aimed at regenerating bone, cartilage, bladder, and pancreas tissue (348, 351-354). More importantly, MRI is an invaluable technique for monitoring *in vivo* scaffold implantation and integration (355, 356), and has even been used in human clinical trials to assess scaffold-mediated cartilage repair (357). MRI can also be used to map the mechanical properties of tissues and tissue engineered constructs via magnetic resonance elastography (MRE) (reviewed in (358)). In MRE, a low frequency mechanical shear wave, generated by an electromechanical actuator, is applied to a tissue sample in synchronization with a phase contrast MRI pulse sequence (359). The resulting shear wave images are analyzed and

used to map tissue elasticity in 2D and 3D. To date, MRE has been used to assess changes in mechanical properties of tissue engineered bone and fat during *in vitro* development (348, 360), and is beginning to be applied *in vivo* (358). The main limitation in applying MRI techniques for tissue engineering assessment remains the high cost of imaging systems. The need for contrast agents, which may have cytotoxic effects, for enhanced contrast and biochemical imaging also presents a few restrictions, although label-free MRI techniques for assessing cellular viability within scaffolds are currently under investigation (361).

Optical coherence tomography (OCT) is a label-free, non-invasive, real time imaging technique which uses interferometry and differences in the light scattering properties of materials to generate 2D and 3D depth-resolved tissue images (362). In OCT, a low coherence near-IR light source is split into two paths, one directed onto the sample and the other to a reference mirror, via a beam splitter. Light scattered by the sample arm is recombined with light from the reference arm and the resulting interference signal is detected and analyzed. By transversely scanning the sample beam, a 2D image map of backscattered light intensity, and thus tissue contrasts, can be formed and used to generate 3D images. Typical OCT imaging resolution is around 10-15 um at tissue penetration depths of several millimetres (363, 364). However, by utilizing high numerical aperture objectives in an OCT variant known as optical coherence phase microscopy (OCPM), imaging resolution can be enhanced to enable single cell mapping and the detection of nanometer-level detail (365, 366).

In tissue engineering, OCT imaging and its variants have shown great promise in enabling both structural and functional tissue assessment (reviewed in (367)). OCT has been used to characterize scaffold architecture and porosity (368, 369) as well as to monitor tissue seeding, growth, migration and structure within hydrogels and scaffold systems (367, 368, 370, 371). One OCT variant, spectroscopic OCT (SOCT), which measures the depth-resolved spectra of the light scattered back from the sample, is under investigation as a method for distinguishing between different cell types within scaffolds (348). Meanwhile, the mechanical properties of engineered tissues can also be assessed via another variation on OCT known as optical coherence elastography (OCE) (372). In OCE, mechanical stimulation is applied to tissue samples in synchronization with OCT imaging in order to map tissue elasticity.

Several complementary imaging techniques, including MPLSM and Raman spectroscopy, have been coupled to OCT in order to map biochemical and physiological data to engineered tissue structure (367, 373). These complementary methods also serve to enhance the optical contrast between cells and their surrounding scaffold materials. Poor cell-scaffold contrast in certain systems is one of the main limitations in the application of OCT imaging to tissue engineering. A number of label-free OCT strategies are also currently under investigation to enhance cell-scaffold contrast, including the monitoring of phase and/or intensity speckle fluctuations associated with cell viability (374, 375), which will be further explored in this work.

# Chapter 3: Project Hypothesis and Objectives

## 3.1 Project Hypothesis:

Layer-by-layer (LbL) deposition can be used to enable localized gene delivery from the surface of three-dimensional (3D) scaffolds in a manner that preserves the underlying properties of the scaffold system.

## 3.2 Main Project Objective:

The main objective of this thesis work was to develop an inductive tissue engineering system for *in situ* 3D gene delivery, utilizing the layer-by-layer deposition technique and a model scaffold system. Towards that end, we designed, produced, characterized, and evaluated a biocompatible glycol-chitosan/hyaluronic acid (Glyc-CHI/HA) polyelectrolyte multilayer film system that facilitated *in vitro* delivery of a marker gene encoding enhanced green fluorescent protein (EGFP) from a porous, polymeric scaffold system composed of poly(lactic-co-glycolic acid) (PLGA).

## 3.3 Project Sub-Objectives:

1. Characterize the physical and cellular adhesion properties of 2D glycol-chitosan/ hyaluronic acid (Glyc-CHI/HA) multilayer films (Chapter 5).

2. Demonstrate that lipoplex-based gene delivery vectors can be incorporated within glycol-chitosan/ hyaluronic acid multilayer films and successfully transfect several cell lines *in vitro* (Chapter 6, Appendix 2).

3. Validate that optical coherence tomography (OCT) is a useful technique for imaging tissue growth and viability within our porous tissue engineering scaffold system (Chapter 7).

4. Demonstrate that LbL deposition can be used to coat a model 3D porous, polymeric scaffold and that this coating can support *in vitro* cell adhesion, growth and viability (Chapter 8).

5. Demonstrate that LbL deposition, incorporating a layer of gene delivery lipoplexes, onto our model 3D porous scaffold can be used to successfully transfect cells *in vitro*, utilizing EGFP plasmids (Chapter 8).

# Chapter 4: Inductive Scaffold System Design

## 4.1 Polyelectrolyte Multilayer Film System:

Although a wide variety of natural and synthetic polyelectrolytes have been utilized in the production of LbL films for use in biomedical applications, protein and gene delivery generally requires the use of biodegradable polyelectrolytes (Chap. 2.3.5). We thus chose to use the biodegradable polysaccharides glycol-modified chitosan (Glyc-CHI) and hyaluronic acid (HA) to form polyelectrolyte multilayer films in which to embed our gene delivery vectors (Fig. 4.1).

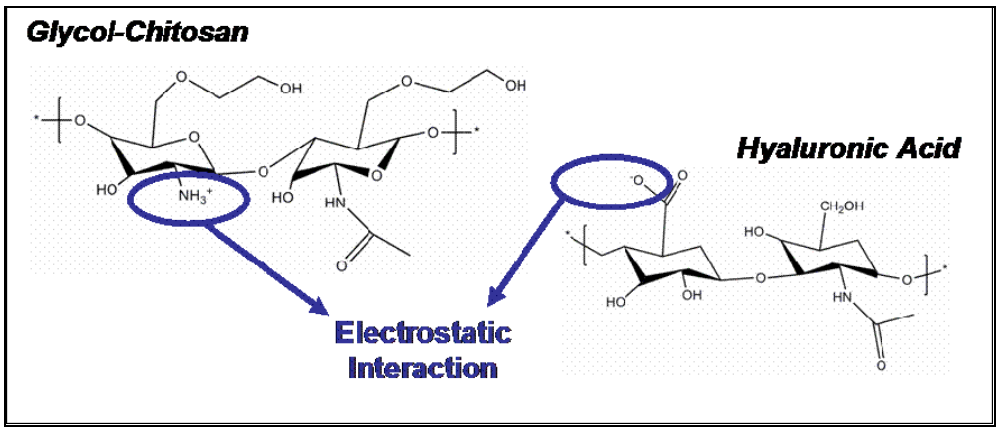


**FIGURE 4.1: Structures of glycol-chitosan (Glyc-CHI) and hyaluronic acid (HA). Glyc-CHI and HA form mulialyer films via electrostatic layer-by-layer deposition. The electrostatic interactions are believed to be between the protonated amine groups in glycol-chitosan and the deprotonated carboxyl group on hyaluronic acid.**

The linear polysaccharides chitosan (CHI) and hyaluronic acid (HA) constitute one of the most widely-studied multilayer film systems, with applications in drug and gene delivery, as well as in antithrombogenic and antibacterial coatings (159, 220, 250, 251, 376).

Hyaluronic acid is a polyanion found in the extracellular matrix, which plays an important role in mediating tissue hydration and water transport (27). Chitosan, derived from the deacetylation of chitin, which is commonly found in the shells of marine crustaceans and the cell walls of fungi, is a polycation that exhibits antibacterial properties and high mucoadhesion (377). Studies have demonstrated successful *in vitro* cellular transfection from 2D CHI/HA multilayer films using both adenoviral and PEI-condensed vectors (249, 250). However, studies have indicated that many cell lines exhibit decreased adhesion to CHI/HA multilayer films, particularly as the number of bilayers are increased (208), thus suggesting transfection from these films may be far from optimal. While chemical cross-linking via EDC and sulfo-NHS has been shown to significantly increase chondrosarcoma cell attachment on CHI/HA multilayers (208), not all chemical cross-linkers enhance cellular adhesion in this system (378). More importantly, chemical cross-linking of multilayer films may limit the gene release kinetic profiles that can be produced.

Work with water-soluble phosphorylcholine-modified chitosan has indicated significantly improved bone marrow cellular adhesion properties on cast films, compared to unmodified chitosan (379). Commercially available glycol-modified chitosan (Glyc-CHI) is also water soluble and has been widely employed in drug and gene delivery (380, 381), and is beginning to be used in tissue engineering applications (382, 383). In the first portion of this study we demonstrated that Glyc-CHI/HA polyelectrolyte multilayers exhibited improved cell adhesion properties that we believed would further enhance film-based transfection efficiency (Chap. 5).

## 4.2 Gene Delivery Vectors:

In order to enhance transfection efficiencies from our LbL-films, we originally used poly(ethylenimine) (PEI) as our gene delivery vector, since it is one of the most efficient and widely studied cationic polymeric transfection reagents (Chap. 2.2.2). PEI-based polyplexes have been used to transfect many different cell lines, in numerous scaffold-based gene delivery designs (384), and have also been explored for 2D gene delivery from multilayer films (250), thus making them a highly attractive choice for the purposes of our study. However, after performing extensive film-based transfection studies in NIH3T3 cells, we found lower than desired transfection efficiencies (less than 5%, Appendix 2). Thus we switched our delivery vector to the commercially available, lipid-based Lipofectamine2000$^{TM}$ reagent. A proprietary formulation, Lipofectamine2000$^{TM}$ is one of the most widely used gene delivery vectors due to its high transfection efficiency, the high level of gene expression produced, and the broad range of cell lines that it can transfect (Chap. 2.2.2).

## 4.3 Scaffold Material and Fabrication Method:

As the bulk material for our model scaffold we decided to use poly (lactic-co-glycolic acid) (PLGA). PLGA is a synthetic, biocompatible, biodegradable polyester commonly used in a number of tissue engineering and controlled drug release applications, including some approved by the FDA (385). As a copolymer, the degradation rate and mechanical

properties of PLGA can be tuned by varying the ratio of glycolide to lactide units, making it one of the most widely used polymers for the production of a variety of scaffold systems (Chap. 2.1.2).

Our porous PLGA scaffolds are produced by the solid free form fabrication technique (Chap. 2.1.3), via the BioPlotter system (EnvisionTec, Gladbeck, Germany), using a protocol previously developed in our lab (33). The Bioplotter is a rapid prototyping system involving the computerized 3D layer-by-layer deposition of polymer strands, via a syringe pump, into a 3D scaffold structure (386, 387) (Fig. 4.2). The system enables precise control over the architecture, porosity and pore size range produced.

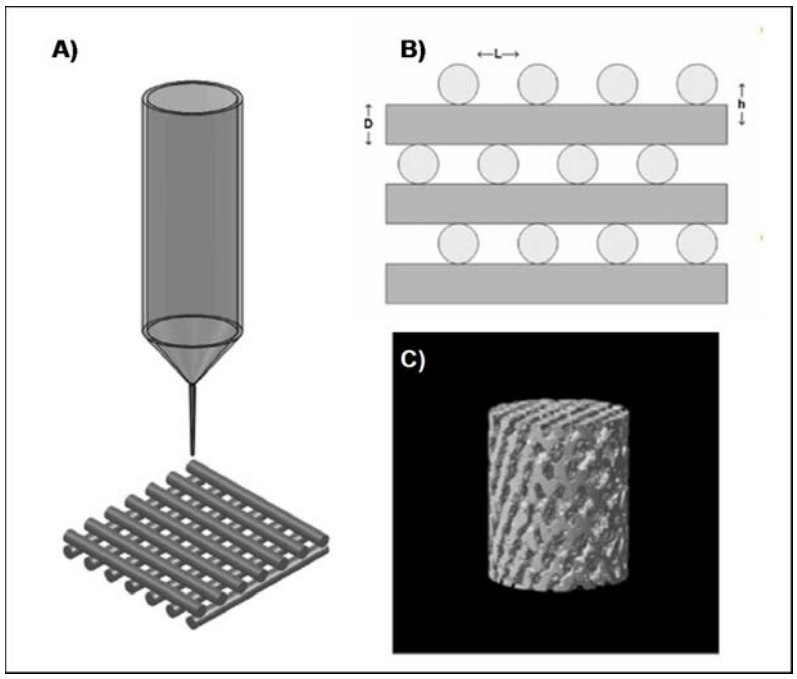


**FIGURE 4.2: Schematic depicting the scaffold fabrication process and resulting scaffold structure. A) The Bioplotter deposition process utilizing a syringe pump. B) Cross-sectional representation of deposited PLGA strands with diameter (D), strand thickness (h), and layer spacing (L). C) MicroCT image of a representative scaffold, with L= 300 µm. (Figure adapted from (330)).**

## 4.4 Overall System Design:

Porous scaffolds composed of poly(lactic-co-glycolic acid) (PLGA) were immersed into alternating cationic and anionic polyelectrolyte solutions of glycol-chitosan (Glyc-CHI) and hyaluronic acid (HA), in order to build up polyelectrolyte layers on the scaffold surface. A layer of lipoplexes containing plasmid DNA encoding enhanced green fluorescent protein (EGFP) was embedded within these films to enable *in vitro* transfection. (Fig. 4.3)

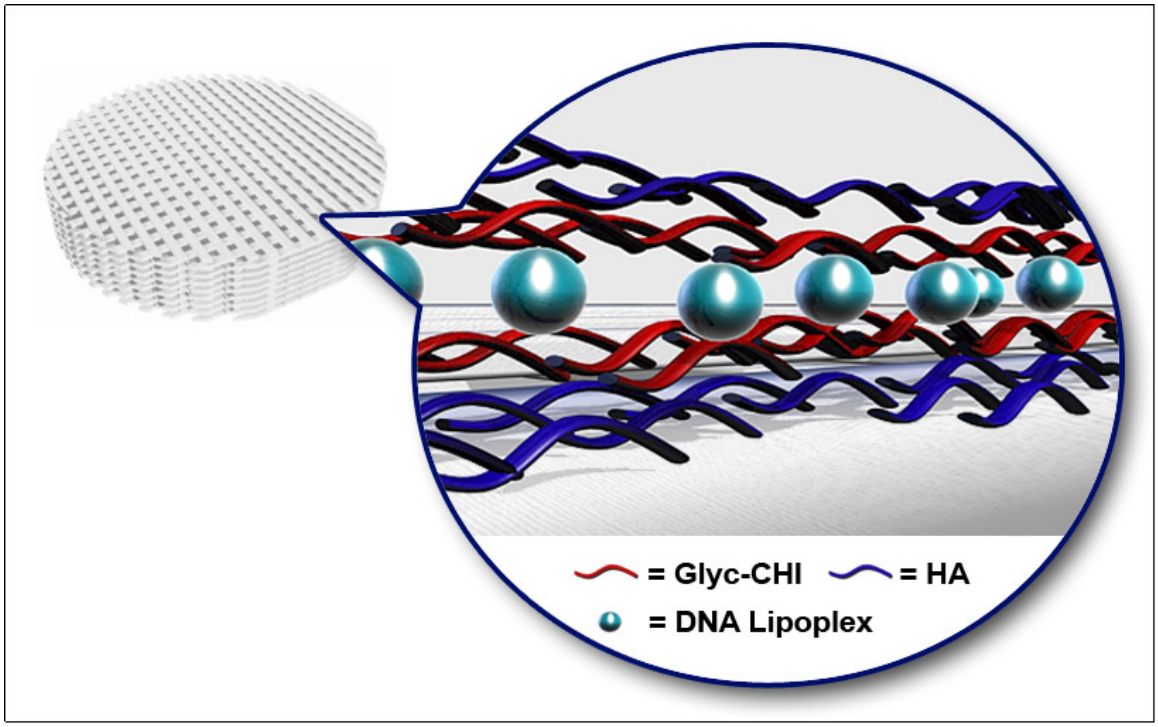


**FIGURE 4.3: Outline of the overall design for the inductive tissue engineering system developed in this study. Polylelectrolyte multilayer films, composed of glycol-chitosan (Glyc-CHI) and hyaluronic acid (HA), which incorporate gene delivery lipoplexes are LbL-coated onto microfabricated PLGA scaffolds.**

# Chapter 5: Glycol-Chitosan/Hyaluronic Acid Multilayer Films Exhibit Enhanced Cellular Adhesion Properties

In order to meet the first sub-objective of this thesis project, the formation and physical and cellular adhesion properties of 2D layer-by-layer films composed of glycol-modified chitosan (Glyc-CHI) and hyaluronic acid (HA) were characterized. We hypothesized that polyelectrolyte multilayer films consisting of Glyc-CHI and HA would exhibit improved cellular adhesion compared to corresponding films consisting of unmodified chitosan. Film deposition was monitored by quartz crystal microbalance (QCM), while film roughness and hydration properties where characterized via atomic force microscopy (AFM) and water contact angle measurement, respectively. Total serum protein adsorption to the films was assessed via the BCA protein assay. MC3T3-E1 murine pre-osteoblast adhesion and viability were analyzed via light microscopy and the MTT assay, respectively.

The results of this work are presented in the following manuscript entitled "Enhanced MC3T3 Pre-osteoblast Viability and Adhesion on Polyelectrolyte Multilayer Films Composed of Glycol-Modified Chitosan and Hyaluronic Acid" which was published by the Journal of Biomedical Materials Research Part A in 2011.

Following the manuscript, the results of similar studies evaluating murine embryonic fibroblast (NIH 3T3) cell and human embryonic kidney (HEK293) cell adhesion and viability are presented.

**Enhanced MC3T3 Pre-osteoblast Viability and Adhesion on Polyelectrolyte Multilayer Films Composed of Glycol-Modified Chitosan and Hyaluronic Acid**

Christina A. Holmes[1,3] and Maryam Tabrizian[1,2,3,*]

[1]Department of Biomedical Engineering, [2]Faculty of Dentistry, and [3]Centre for Biorecognition and Biosensors, Duff Medical Science Building, 3775 University Street, McGill University, Montreal, H3A 2B4, Canada

*Corresponding author: maryam.tabrizian@mcgill.ca

## 5.1 Abstract

Layer-by-layer (LbL) polyelectrolyte (PE) films made of the naturally derived polysaccharides chitosan (CHI) and hyaluronic acid (HA) constitute a well-studied system for the development of cell-responsive biointerfaces. However, many cell lines exhibit decreased adhesion to CHI/HA multilayer films, particularly as the number of bilayers is increased. Here our group demonstrates that films composed of glycol-modified chitosan (glyc-CHI) exhibit significantly improved MC3T3 pre-osteoblast adhesion and viability compared to corresponding films consisting of unmodified CHI. These differences in cellular adhesion are likely due to differences in surface topography and roughness, as measured via AFM, as well as in film chemistry and the water-solubility of the cation, since both types of films exhibited similar: thickness, as measured via QCM and AFM; wettability, as measured via contact angle; and serum protein adsorption, as measured via the BCA assay.

## 5.2 Introduction

Amongst the wide variety of surface modification techniques, electrostatic layer-by-layer (LbL) deposition has emerged as a simple and versatile method for tailoring cell-material interactions. Varying the polylectrolytes (PEs) selected and the conditions employed during their deposition can produce LbL films with a broad range of physio-chemical properties, thus enabling a diverse array of biomedical applications, including drug and gene delivery, biosensing, cell encapsulation, and bioactive implant coatings (122, 123, 388). The investigation of LbL multilayers composed of naturally derived polymers, such as polysaccharides, proteins and nucleic acids, has been of particular interest due to their excellent biocompatibility.

The linear polysaccharides chitosan (CHI) and hyaluronic acid (HA) constitute one of the most widely-studied PE film systems, with applications in drug and gene delivery, as well as in antithrombogenic and antibacterial coatings (159, 220, 250, 251, 376). Hyaluronic acid is a polyanion found in the extracellular matrix, which plays an important role in mediating tissue hydration and water transport (27). Chitosan, derived from the deacetylation of chitin, which is commonly found in the shells of marine crustaceans and the cell walls of fungi, is a polycation that exhibits antibacterial properties and high mucoadhesion (377). Although biocompatible, LbL films composed of CHI and HA have been found to exhibit decreased cellular adhesion as the number of bilayers is increased (159, 378). This cell resistant trend extends to most LbL film systems containing biopolymers, including: polylysine, heparin, gelatin, alginate, and

dextran (389), although a few studies have shown naturally-derived PE coatings to improve cellular adhesion to synthetic polymeric scaffolds (260-262).

Cell adhesion on PE multilayers depends not only upon the specific polymers employed, but upon physical film properties such as surface roughness, stiffness, swelling behavior, water content, hydrophobicity/ hydrophilicity, and potentially the charge of the terminating layer (180, 204, 205, 389). Although it has been difficult to separate the impact of individual factors, generally, increasing layer rigidity tends to increase cellular adhesion. Chemical cross-linking of multilayer films composed of CHI/ HA or polylysine (PLL) and HA, for example, was found to increase film stiffness (as measured by AFM indentation) as well as the attachment and spreading of chondrosarcoma and smooth muscle cells (180, 204). However, we have found in previous work that not all chemical cross-linkers enhance cellular adhesion, with some, such as genipin, decreasing it even further (378). Furthermore, cross-linking multilayer films generally decreases their biodegradation rate and may thus limit their use in certain drug delivery applications.

Recent work with cast films composed of water-soluble phosphorylcholine-modified chitosan (Pc-CHI) has indicated significantly improved bone marrow cellular adhesion properties in comparison to unmodified CHI (379). Meanwhile, initial studies of LbL films composed of Pc-CHI and HA have demonstrated biocompatibility (215, 390). The more commercially available glycol-modified chitosan (Glyc-CHI) also exhibits significantly improved water solubility and biocompatibility, features that have led to its wide deployment in drug delivery systems, as well as in gene therapy and tissue

engineering applications (380-383). We were therefore interested in whether LbL films composed of Glyc-CHI and HA would exhibit enhanced cellular adhesion in comparison to analogous unmodified CHI multilayers, whilst preserving their biocompatible and other favorable properties, thus expanding possible biomedical applications.

Here we investigate the formation, physio-chemical properties, and cellular adhesion profiles of PE multilayers composed of water-soluble Glyc-CHI and HA, and compare these to corresponding CHI/HA films. Film deposition was monitored by dissipative quartz crystal microbalance (QCM-D), while film roughness and hydration properties were characterized via atomic force microscopy (AFM) and water contact angle measurement, respectively. Total serum protein adsorption as well as MC3T3-E1 murine pre-osteoblast adhesion and viability on top of these films were then analyzed. Our results indicate that Glyc-CHI/HA multilayer films displayed significantly increased cellular adhesion and viability at higher bilayer numbers, compared to corresponding umodified-CHI/HA control films, predominately due to differences in surface topography, roughness and film chemistry.

## 5.3 Materials and Methods

***5.3.1 Polyelectrolyte solutions***:

Hyaluronic Acid (HA) with a molecular weight of 74 kDa was purchased from Lifecore Biomedical (Chaska, MN, USA). Chitosan (CHI) with a molecular weight of approximately 91 kDa (via GPC) and Glycol-Chitosan (Glyc-CHI) with a molecular weight of approximately 80 kDa (via GPC) were purchased from Sigma-Aldrich. All solutions were prepared at a concentration of 2 mg/ml in 0.1 M NaCl buffer (with the exception of CHI, which was prepared in 0.1 M NaCl, 0.1% acetic acid buffer), adjusted to pH 6.0, and filtered through a 0.22 μm PES stericup filtration unit (Milipore).

***5.3.2 LbL Assembly of Films*:**

Sodium dodecyl sulphate (SDS) and sodium chloride (NaCl, purity ~99%) were purchased from Sigma-Aldrich; cell culture cover glasses (15 mm, round) were obtained from Fisher Scientific. Prior to film deposition, cover glasses were cleaned in 10 mM SDS for three hours, rinsed in distilled water three times, treated with 0.1 N HCl overnight and thoroughly rinsed in distilled water. LbL build up was achieved using the pipette approach, wherein 300 μl of each polymer was deposited directly onto the cover glass, beginning with the polycation (CHI or Glyc-CHI). After the polymer was allowed to adsorb for 20 min, the polymeric films were rinsed three times in 0.1 M NaCl buffer. Then the polyanion, HA, was added, allowed to adsorb for 20 min and rinsed three times. This was repeated at each step of LbL deposition in order to form $[CHI/HA]_N$, $[CHI/HA]_NCHI$, $[Glyc\text{-}CHI/HA]_N$ and $[Glyc\text{-}CHI/HA]_NGlyc\text{-}CHI$ films, where N = 3, 5 and 10 bilayers.

***5.3.3 Monitoring In Situ Film Build-Up and Thickness***:

LbL film build-up for $[Glyc\text{-}CHI/Ha]_{10}$ Glyc-CHI films was monitored *in situ* by QCM-D, using a Q-Sense D 300 unit (Q-sense, Sweden). Changes in frequency ($\Delta f$) and energy dissipation ($\Delta D$) were measured at the fundamental frequency of the crystal (f = 5 MHz) as well as at the third, fifth, and seventh overtones (15, 25, and 35 MHz, respectively). Polyelectrolyte films were formed by injecting 400 µl of the polyelectrolyte solution (Glyc-CHI or HA) into the measuring cell, allowing 10 min for adsorption, followed by rinsing with 2000 µl of 0.1 M NaCl solution. This procedure continued until 10 bilayers were deposited, with an additional terminating layer of Glyc-CHI. The film thickness was calculated from the frequency and energy dissipation data using QTools software and the Voigt-based viscoelastic model proposed by Voinova et al (169, 170). For these calculations, the polyion film density was assumed to be 1.2 $g/cm^3$ and the 0.1 M NaCl buffer fluid density and viscosity were assumed to be 1.004 $g/cm^3$ and 9.03 x $10^{-4}$ kg/ms, respectively (391).

***5.3.4 Atomic Force Microscopy*:**

The topography of $[Glyc\text{-}CHI/HA]_N$Glyc-CHI and $[CHI/HA]_N$CHI films, where N = 3 and 5 bilayers, was imaged by atomic force microscopy (AFM) in both "dry" and "wet" conditions using the Nanoscope III (Digital Instruments, USA) system in the tapping mode. Prior to "dry" analysis, all samples were rinsed three times in distilled water, allowed to soak for 30 min to ensure removal of NaCl from the film surface, and dried with nitrogen. "Dry" images were acquired in air at ambient temperature using a silicon probe with a nominal spring constant of 40 N/m and a nominal radius of curvature of 35

μm (model RTESP, Veeco, USA). In the case of "wet" analysis, samples were analyzed within a multimode fluid cell (model MTFML, Veeco) filled with 0.1 M NaCl solution (pH 6), using a silicon nitride probe with a nominal spring constant of 0.3 N/m and a nominal radius of curvature of 20 μm (model NP, Veeco). In both conditions, a 10 μm x 10 μm area was scanned at a rate of 1 Hz using the minimum amount of force required to obtain steady images. Mean RMS surface roughness and maximum film feature height were calculated using Nanoscope v 5.12r5 software on a 5 μm by 5 μm area.

In order to determine the thickness of $[Glyc\text{-}CHI/HA]_N Glyc\text{-}CHI$ and $[CHI/HA]_N CHI$ films, where N = 3 and 5 bilayers, AFM scratch tests were performed. Briefly, holes were created in the films by repeatedly scanning a 5 μm x 5 μm area, lowering the set point to nearly its minimum value and increasing the scan rate to 30 Hz. The newly exposed area was then imaged by increasing the scan size and returning to normal parameters.

***5.3.5 Contact Angle Analysis***:

Prior to analysis, all samples were rinsed three times in distilled water, allowed to soak for 30 min to ensure removal of NaCl from the film surface, and dried with nitrogen. The wettability of the film surfaces was monitored by determining the contact angle of a 1 μL deionized water droplet using a video contact angle measuring system (VCA 2500, AST, Billerica, Ma).

***5.3.6 Protein Adsorption***:

For protein adsorption studies, $[CHI/HA]_N$, $[CHI/HA]_NCHI$, $[Glyc\text{-}CHI/HA]_N$ and $[Glyc\text{-}CHI/HA]_NGlyc\text{-}CHI$ films, where N = 3, 5 and 10 bilayers, were built as described above in 24 well tissue culture plates (Falcon), sterilized with 70% (v/v) ethanol for one hour and then washed in the following ethanol series for 30 min each: 50%, 20% and 10%. To ensure complete removal of the ethanol, substrates were then washed three times (20 min each wash) in 1 x sterile PBS buffer, pH 7.4. It should be noted that during the washing and media equilibration steps, all of the substrates, including the controls, were treated in the same manner. 500 µl of complete cell culture media (alpha minimum essential medium (ά-MEM, Gibco, Invitrogen Corporation) supplemented with 10% fetal bovine serum (FBS, Gibco, Invitrogen), 1% penicillin/streptomycin (Invitrogen), 0.2 mM L-ascorbic acid (Sigma) and 2 mM L-glutamine (Sigma)) was then added to each of the wells at 37°C in a humidified atmosphere of 5% $CO_2$. Controls included uncoated glass slides, empty wells, and multilayer films incubated in 1 x sterile PBS buffer.

After 2 hours, the media was removed and the films were rinsed twice in 1 x PBS buffer. The adsorbed proteins were desorbed by incubation in 500 µL of 10 mM SDS solution on a shaking table for 1 hour at room temperature. The concentration of total proteins within the SDS solutions was determined via the bicinchoninic acid (BCA) method using a micro BCA protein assay reagent kit (Pierce, IL, USA) according to the instructions of the manufacturer. Analysis was performed with a µQuant™ microplate spectrophotometer (Bio-Tek Instruments, Winooski, VT) at an absorbance of 562 nm.

Each protein concentration was calibrated using a concurrently produced standard curve using the bovine serum albumin provided with the assay kit.

### ***5.3.7 Cellular Adhesion and Viability*:**

Mouse pre-osteoblast MC3T3-E1 (subclone 14) cells were supplied by American Type Culture Collection (ATCC, Manassas, VA), and grown in alpha minimum essential medium (ά-MEM, Gibco, Invitrogen Corporation) supplemented with 10% fetal bovine serum (FBS, Gibco, Invitrogen), 1% penicillin/streptomycin (Invitrogen), 0.2 mM L-ascorbic acid (Sigma) and 2 mM L-glutamine (Sigma) and incubated at 37°C in a humidified atmosphere of 5% $CO_2$.

Similar to the protein adhesion experiments, $[CHI/HA]_N$, $[CHI/HA]_NCHI$, $[Glyc\text{-}CHI/HA]_N$ and $[Glyc\text{-}CHI/HA]_NGlyc\text{-}CHI$ films, where N = 3, 5 and 10 bilayers, within 24 well tissue culture plates (Falcon), were sterilized with 70% (v/v) ethanol for one hour, washed in a 50%, 20% and 10% ethanol series for 30 min each, and washed three times for 20 min each in 1 x sterile PBS buffer. 500 µl of the appropriate media was then added to each of the wells and left to equilibrate for an hour at 37°C in a humidified atmosphere of 5% $CO_2$. Again, all of the substrates, including the controls, were treated in the same manner.

After trypsinization, cells were spun down at 1000 rpm for 5 min, re-suspended in fresh media, and the cell concentration was determined using a hemocytometer. A seeding

population of 2 x $10^4$ cells (in a volume of 500 µl) was added to each of the wells and incubated at 37°C in a humidified atmosphere of 5% $CO_2$ for 48 hours.

For analysis of cellular adhesion, culture media was removed, samples were rinsed once in PBS and images at 10 x and 20 x magnification were acquired with a stereoscopic zoom microscope (SMZ1500, Nikon) equipped with a digital camera (DXM1200F, Nikon) operated with the ACT-1 software. A minimum of 4 fields per sample was imaged and cell numbers were determined by manual count with the assistance of ImageJ software.

In order to analyze cellular viability, media was removed, samples were rinsed once in PBS, and 300 µL of serum-free, phenol-red-free ά-MEM media (Gibco, Invitrogen) was added to each well. The number of viable cells in each well was determined using the Vybrant MTT Cell Proliferation Assay Kit (Invitrogen), which is based upon the conversion of MTT (3-(4,5-Dimethylthiazol-2-yl)-2,5-diphenyltetrazolium bromide) to a strongly pigmented formazan product by live cells, according to manufacturer instructions. Analysis was performed with a µQuant™ microplate spectrophotometer (Bio-Tek Instruments, Winooski, VT) at an absorbance of 570 nm.

### ***5.3.8 Statistics*:**

Statistical analyses of data were performed using the software package SPSS/PASW Statistics v18.0 (SPSS Inc., Chicago, IL). All data are presented as mean ± STD. The significance level was set at $p < 0.05$. As most data either failed the Shapiro-Wilk test for normality and/or the Levene's test for homogeneity of variance, or were of small sample

size, Kruskal-Wallis non-parametric analyses were performed. In the case of contact angle data, a two-way ANOVA test with a Student Neuman-Keul's posthoc test, was also performed for comparison.

## 5.4 Results and Discussion

### ***5.4.1 Glyc-CHI/HA Film Build-up and Surface Characterization*:**

As cellular adhesion to polyelectrolyte multilayers is dependent upon a combination of chemical and physical surface properties, Glyc-CHI/HA film build-up, thickness, topography, roughness, and surface wettability were characterized in detail. Frequency shifts (Δf/v) and changes in energy dissipation (ΔD) over time for the build-up of [Glyc-CHI/HA]$_{10}$Glyc-CHI multilayer films, as monitored via QCM-D, are presented in Fig. 5.1. As each polyelectrolyte was injected into the system, a decrease in frequency was observed corresponding to an increase in film mass, thus indicating layer-by-layer deposition. The normalized frequency shift (-Δf/v) data at each bilayer number (Fig. 5.2) indicates a non-linear growth regime (184), with higher bilayer numbers (8$^{th}$ onwards) displaying an increased growth rate. Similarly, larger dissipation changes were seen at higher bilayer numbers, thus indicating that Glyc-CHI/HA films became more viscoelastic as they grew (Fig. 5.1). Rinses with 0.1 M NaCl buffer between polyelectrolyte deposition steps could also be identified as small upturns in the frequency curve and downturns in the dissipation curve, suggesting small amounts of polymer desorption. Measurements were performed at the fundamental frequency of the crystal, 5 MHz, as well as at its third, fifth and seventh overtones (15, 25 and 35 MHz, respectively). However, as higher bilayer numbers (8$^{th}$ and above) were deposited, the thickness and viscoelasticity of the films rendered the QCM-D system unable to continue higher frequency measurements.

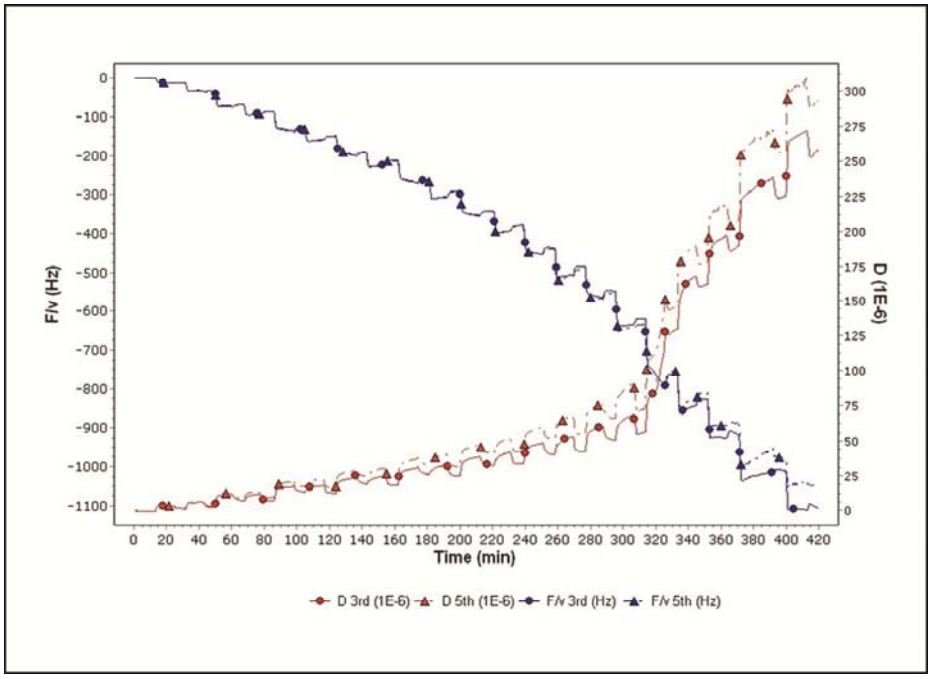


**FIGURE 5.1: Plots of change in dissipation (ΔD, right axis) and QCM frequency shifts (Δf/v, left axis) over time during the deposition of a [Glyc-CHI/HA]$_{10}$Gly-CHI film. Frequency was monitored at the third (solid lines, circles) and fifth (dashed lines, triangles) overtones of the fundamental frequency, corresponding to 15 and 25 MHz, respectively. Data presented is for one representative experiment; results from other experimental runs (n = 5) are consistent.**

The viscoelastic nature of the Glyc-CHI/HA films, as indicated by the large dissipation changes and spread in frequency data for different overtones, renders the Sauerbrey equation (166), which directly relates frequency shift data to mass adsorbed for rigid films, invalid for this system. Instead, the Voigt-based viscoelastic model (169, 170) was applied to the frequency and dissipation data measured at the third and fifth overtones, again displaying non-linear film growth, yielding [Glyc-CHI/HA]$_{10}$Glyc-CHI multilayers approximately 250-350 nm thick (Fig. 5.2). These results are consistent with those for multilayer films composed of unmodified-CHI and HA, which have been found to display non-linear growth that borders on the "exponential" using a variety of techniques including QCM-D, OWLS, SPR, and ellipsometry (159, 378, 390). Previous QCM-D

analysis demonstrated $[CHI/HA]_{10}CHI$ films, formed at the same pH and ionic strength and using HA of the same molecular weight and 91 kDa unmodified CHI, to be comparable in thickness, at approximately 300-400 nm thick (as calculated via the Voigt model), and to display increasing viscoelasticity with bilayer number (378).

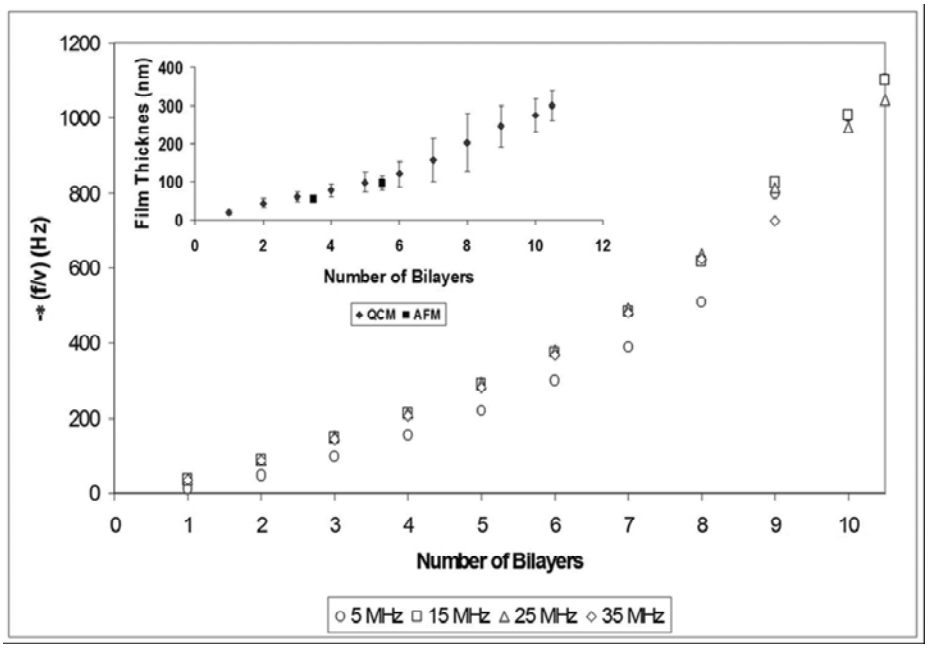


**FIGURE 5.2: Normalized frequency shift (Δf/v) data for each bilayer number (i.e., $[Glyc-CHI/Ha]_N$). Frequency was monitored at the fundamental frequency (circles) and its third (squares), fifth (triangles), and seventh (diamonds) overtones, corresponding to 5, 15, 25, and 35 MHz, respectively. Data presented is for one representative experiment. Inset: Approximate film thickness with increasing bilayer number. Multilayer thickness increased with successive polymer layer deposition resulting in $[Glyc-CHI/Ha]_{10}$Glyc-CHI multilayers ~ 250–350 nm thick. Data presented is the average of three representative experiments.''QCM'' thickness (diamonds) was determined by applying the Voigt-based viscoelastic model to frequency shift (Δf/v) and dissipation(ΔD) data recorded via QCM at the third and fifth overtones (i.e., 15 and 25 MHz, respectively). ''AFM'' thickness (squares) was obtainedvia the AFM scratch test method under wet conditions (n = 9).**

Looking at the plot of approximate film thickness (Fig. 5.2) for each Glyc-CHI/HA bilayer reveals larger variations between experiments in the 7 to 9 bilayer range. Previous studies characterizing the growth and properties of unmodified CHI/HA films indicated a

threshold range, between 7 and 9 bilayers, where films transition from patchy island-like surfaces to more uniform and smooth films (159, 378, 390). This transition has been found to depend upon the molecular weight of the CHI and HA employed and the conditions of build-up (199). It is thus believed that the larger experimental variations observed for Glyc-CHI/HA films in this 7 to 9 bilayer range are due to slight variations in where this transition occurs from run-to-run of QCM-D analysis.

As QCM-D is an indirect means by which to determine multilayer thickness, atomic force microscopy (AFM) scratch tests were also performed on three and five bilayer films as a more direct method. Briefly, in the presence of 0.1 M NaCl solution (pH=6) a small area of each film was repeatedly scanned at high frequency under "hard" tapping conditions, thus creating a hole, the height of which was directly measured. Scratching [Glyc-CHI/HA]$_3$Glyc-CHI and [Glyc-CHI/HA]$_5$Glyc-CHI multilayers yielded average thicknesses of 54 nm ± 6 nm and 94 nm ± 18 nm, respectively, in good agreement with the values calculated via QCM-D and the Voigt model (Fig. 5.2, inset). The thickness of [CHI/HA]$_3$CHI and [CHI/HA]$_5$CHI films was also evaluated via the scratch test and found to be similar to corresponding Glyc-CHI multilayers at 56 nm ± 11 nm and 92 nm ± 20 nm, respectively ($\chi^2$= 0.09, $p > 0.92$). Although difficulty obtaining good quality images prevented the scratch test from being performed in these conditions for films composed of 10 bilayers, we anticipate the QCM-D-determined thicknesses to be in a similar range.

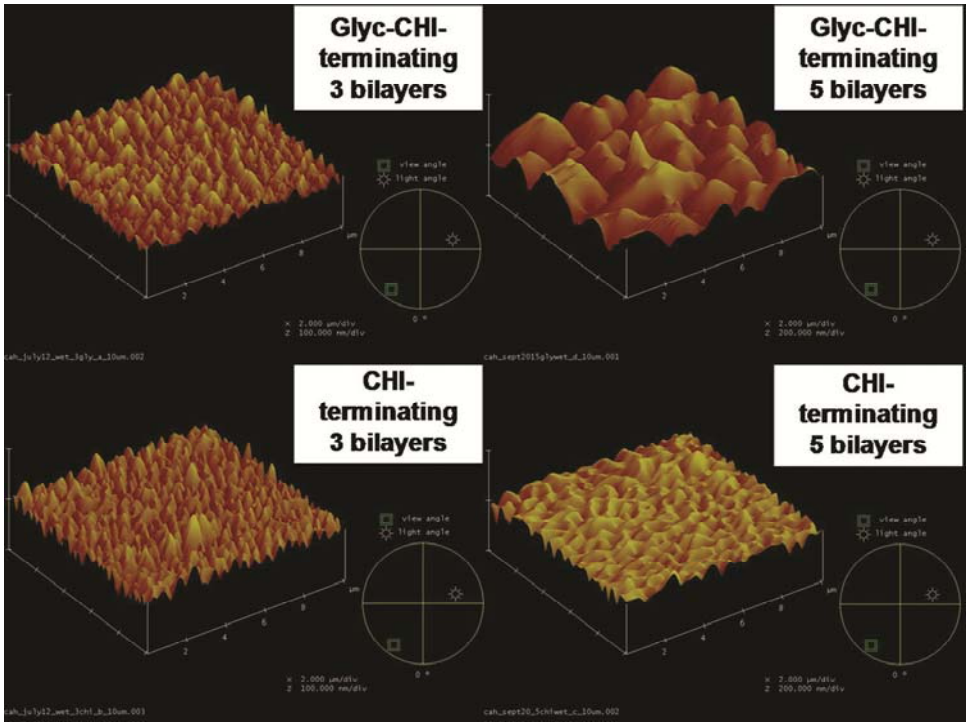


**FIGURE 5.3: AFM imaging of multilayer surface topography of: (top, left) [Glyc-CHI/HA]$_3$Glyc-CHI; (top, right) [Glyc-CHI/HA]$_5$Glyc-CHI; (bottom, left) [CHI/HA]$_3$CHI; and (bottom, right) [CHI/HA]5CHI films in the presence of 0.1M NaCl solution. Scan size = 10 µm, Z-range = 100 nm for three bilayer films (left) and 200 nm for five bilayer films (right).**

Tapping mode AFM analysis of dried [Glyc-CHI/HA]$_N$Glyc-CHI and [CHI/HA]$_N$CHI multilayer films, where N = 3, 5 and 10, indicated little difference between systems in topography or surface roughness (Table 5.1). By contrast, AFM analysis of these same films in the presence of 0.1 M NaCl solution (pH=6) revealed that, while three bilayer surfaces were similar, five bilayer films composed of Glyc-CHI exhibited a significantly higher RMS surface roughness in comparison to corresponding unmodified CHI controls. Examining films composed of three bilayers (Fig. 5.3 left, top and bottom), one observes that both film systems display a similar surface topography composed of many small island-like structures with maximum heights of approximately 68 nm ± 14 nm for Glyc-CHI/HA and 85 nm ± 19 nm for CHI/HA, corresponding to comparable rms surface

roughness values of 11 nm ± 3 nm and 11 nm ± 3 nm, respectively. At five bilayers (Fig. 5.3 right, top and bottom), the islands appear to coalesce into longer wave-like features, which, although displaying similar maximum heights in the case of CHI/HA (89 nm ± 18 nm), are significantly larger for Glyc-CHI/HA (118 nm ± 19 nm; $\chi^2 = 11.46$, $p < 0.01$). This increase in feature height, in turn, leads to increased rms surface roughness for $[\text{Glyc-CHI/HA}]_5\text{Glyc-CHI}$ films (25 nm ± 5 nm) both compared to $[\text{CHI/HA}]_5\text{CHI}$ multilayers (13 nm ± 3 nm; $\chi^2 = 4.36$, $p \leq 0.04$), and three bilayer Glyc-CHI films ($\chi^2 = 11.46$, $p \leq 0.001$). When films reached ten bilayers in thickness, good quality AFM images became difficult to obtain in either wet or dry conditions due to the viscoelasticity of the films, however, both types of multilayers appeared to be smoother (data not shown).

The AFM results presented here reflect trends from previous studies, with CHI/HA films growing from isolated polymer islands which enlarge and coalesce into smoother surfaces somewhere around bilayer 10 (159, 378, 390). Notably, the observed increase in surface roughness for five bilayer Glyc-CHI/HA films echoes the analysis of multilayers composed of HA and another water-soluble CHI-derivative, phosphorylcholine-modified-CHI (Pc-CHI), which were also found to be rougher than their analogous CHI/HA surfaces (390). However, while Glyc-CHI/HA films were found to be similar in thickness and viscoelasticity to their CHI/HA counterparts, multilayers composed of Pc-CHI proved to be thicker due to increased film hydration, which also translated into greater film viscoelasticity (390). Intriguingly, while the difference between the "wet" and "dry" maximum feature heights decreased between three and five bilayer CHI/HA

films, it increased in the case of the Glyc-CHI/HA system, suggesting an increase in water-uptake and film swelling, also reminiscent of Pc-CHI surfaces.

| Film Composition | Static Contact Angle ( θe) | Wet Surface Roughness RMS (nm) | Dry Surface Roughness RMS (nm) | Wet Maximum Feature Height (nm) | Dry Maximum Feature Height (nm) |
|---|---|---|---|---|---|
| $[CHI/HA]_3CHI$ | 43 ± 3 | 11 ± 3 | 5 ± 2 | 85 ± 19 | 53 ± 18 |
| $[Glycol\text{-}CHI/HA]_3$ Glycol-CHI | 40 ± 3 | 11 ± 3 | 5 ± 1 | 68 ± 14 | 45 ± 16 |
| $[CHI/HA]_5CHI$ | 47 ± 2 | 13 ± 3 | 9 ± 4 | 89 ± 18 | 80 ± 16 |
| $[Glycol\text{-}CHI/HA]_5$ Glycol-CHI | 54 ± 3 | 25 ± 5 | 10 ± 2 | 118 ± 19 | 55 ± 6 |
| $[CHI/HA]_{10}CHI$ | 53 ± 4 | NA | NA | NA | NA |
| $[Glycol\text{-}CHI/HA]_{10}$ Glycol-CHI | 64 ± 4 | NA | NA | NA | NA |

**TABLE 5.1: Surface Characterization of $[Glycol\text{-}CHI/HA]_N Glycol\text{-}CHI$ and $[CHI/HA]_N CHI$ Multilayer Films, where N = 3, 5, 10.**
**All data presented are from three separate experiments (n = 9), with the exception of three bilayer dry surface roughness and dry maximum feature height data, which are from two separate experiments (n = 6). Kruskal–Wallis test statistics for contact angle data: Glyc-CHI versus CHI ($\chi^2 = 2.13$, $p < 0.13$); differences in number of bilayers ($\chi^2 = 34.01$, $p \leq 0.001$). Kruskal–Wallis test statistics for ''dry'' RMS roughness data: Glyc-CHI versus CHI ($\chi^2 = 0.37$, $p = 0.58$); differences in number of bilayers ($\chi^2 = 11.05$, $p \leq 0.001$). Kruskal–Wallis test statistics for ''dry'' max height data: Glyc-CHI versus CHI ($\chi^2 = 3.64$, $p \leq 0.06$); differences in number of bilayers ($\chi^2 = 5.47$, $p \leq 0.02$). Kruskal–Wallis test statistics for ''wet'' RMS roughness data: Glyc-CHI versus CHI ($\chi^2 = 4.36$, $p \leq 0.04$); differences in number of bilayers ($\chi^2 = 11.46$, $p \leq 0.001$). Kruskal–Wallis test statistics for ''wet'' max height data: Glyc-CHI versus CHI ($\chi^2 = 0.23$, $p \leq 0.64$); differences in number of bilayers ($\chi^2 = 11.46$, $p \leq 0.01$).**

The static water contact angle of both Glyc-CHI/HA and CHI/HA films increased along with bilayer number (Table 5.1), thus indicating that both types of multilayers became more hydrophobic as they grew ($\chi^2 = 34.01$, $p < 0.01$). While no statistically significant differences were observed between Glyc-CHI and unmodified CHI films using the Kruskal-Wallis test ($\chi^2 = 2.30$, $p < 0.13$), at five and ten bilayers Glyc-CHI/HA films displayed slightly higher contact angles, which were significant when analyzed via two-way ANOVA ($p < 0.001$), thus suggesting they tend to be somewhat more hydrophobic than corresponding CHI/HA multilayers. The increase in film hydrophobicity with layer number was consistent with previous results for the unmodified CHI/HA system (378). However, the slight increase in Glyc-CHI-based film hydrophobicity compared to

unmodified CHI was interesting in light of the previously mentioned implied increase in Glyc-CHI/HA film swelling properties, as well as the improved hydrophilicity of Glyc-CHI itself.

### ***5.4.2 Protein Adsorption*:**

Since *in vivo* protein adsorption plays a key role in mediating cell-surface interactions, analysis of whether the small increase in Glyc-CHI/HA film hydrophobicity translated into differences in total serum protein adsorption was performed (Fig. 5.4). After a 2-hour incubation in serum-containing media, no significant differences in total protein adsorption were observed between films consisting of Glycol-CHI or corresponding ones composed of unmodified CHI ($\chi^2 = 1.68,\ p < 0.20$). Furthermore, no differences were found between films consisting of 3, 5 or 10 bilayers for either polyelectrolyte system ($\chi^2 = 0.60,\ p > 0.70$), or between films terminating in anionic HA or cationic Glyc-CHI or CHI ($\chi^2 = 2.01,\ p < 0.16$). Although hydrophobic multilayers are generally reported to adsorb more proteins than hydrophilic surfaces (392), the fact that the observed hydrophobicity increase for higher bilayer Glyc-CHI films was not large enough to be statistically significant is likely the reason that it was not reflected in the protein adhesion data. Meanwhile, the lack of differences in total adsorbed proteins between films with opposite terminating layer charges (i.e. cation vs. anion) may be due to the wide variety of different proteins and ionic species contained in fetal bovine serum, or due to layer interpenetration which is often found in exponentially growing films.

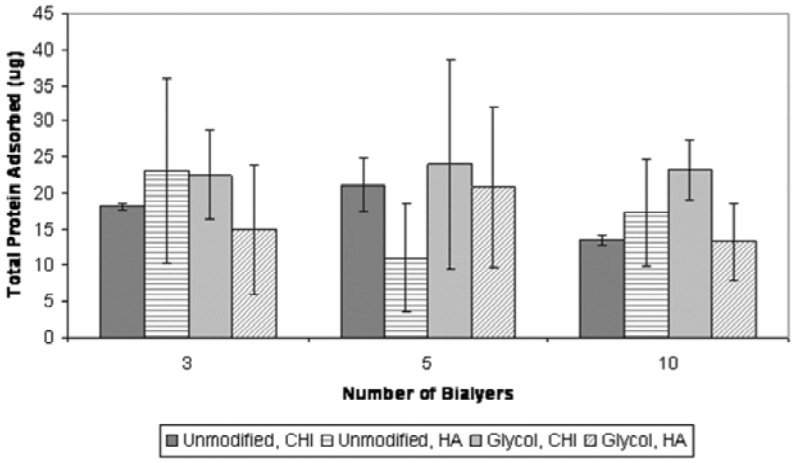


**FIGURE 5.4: Total protein adsorption to $[Glyc\text{-}CHI/HA]_N Glyc\text{-}CHI$ and $[CHI/HA]_N CHI$ multilayer films, where N = 3, 5, 10 after 2 h incubation in complete media containing 10% fetal bovine serum. The amount of protein was determined via the BCA total protein assay. Data presented if from three separate experiments (n = 9). Kruskal–Wallis test statistics for: Glyc-CHI versus CHI ($\chi^2 = 1.68$, $p < 0.20$); cation terminating versus anion terminating: ($\chi^2 = 2.01$, $p < 0.16$); differences in number of bilayers ($\chi^2 = 0.60$, $p > 0.74$).**

### ***5.4.3 Cellular Adhesion and Viability*:**

Glyc-CHI/HA multilayer films composed of 5 or more bilayers displayed significantly higher MC3T3 cell adhesion ($\chi^2 = 40.20$, $p < 0.001$) and viability ($\chi^2 = 54.70$, $p < 0.001$) compared to corresponding films formed of unmodified CHI. MC3T3 cellular adhesion after 48 hours growth on cationic- and anionic-terminating layers of either Glyc-CHI/HA or unmodified CHI/HA films consisting of 3, 5 or 10 bilayers was imaged via light microscopy (Fig. 5.5) and quantified via computer-assisted manual count (Fig. 5.6 top). As previously reported (208, 378), films composed of unmodified CHI displayed cellular adhesion comparable to glass control surfaces at 3 bilayers, however, as the film thickness increased to 5 and 10 bilayers, cellular adhesion dramatically decreased (Fig. 5.6 top).

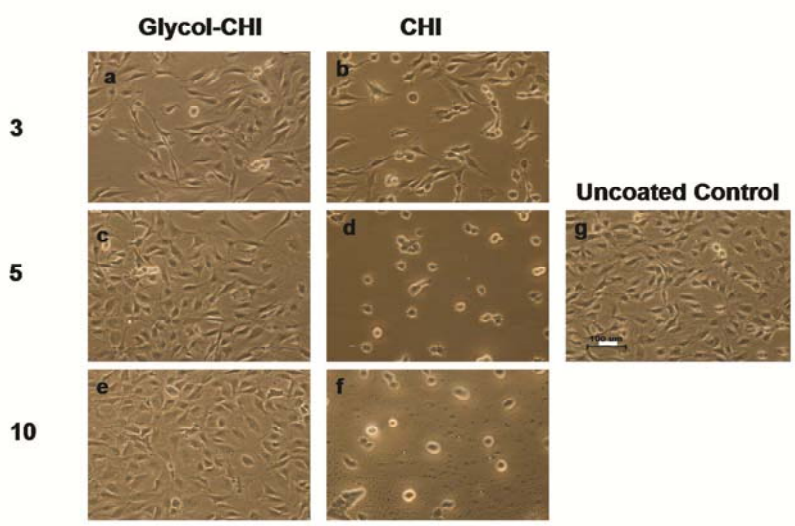


**FIGURE 5.5: Representative bright-field images of MC3T3 cell adhesion after 48 h on $[Glyc\text{-}CHI/HA]_N Glyc\text{-}CHI$ (a, c, e) and $[CHI/HA]_N CHI$ films (b, d, f), where N = 3(a,b), 5(c,d), or 10(e,f) bilayers. Results for films terminating in an HA layer ($[CHI/HA]_N$) are consistent with those presented here. A control image (g) of MC3T3 cell adhesion on uncoated glass slides, with scale bar of 100 μm, is presented for comparison. All images obtained with a 20 x objective.**

A closer look at cell morphology at 5 and 10 bilayers (Fig. 5.5D, F) revealed that MC3T3 cells did not spread but remained rounded, often growing in clusters. We speculated previously, that the good cell adhesion observed on 3 bilayer CHI/HA films (Fig. 5.5B) was actually due to incomplete coverage of the underlying glass substrate caused by the patchy nature of the film at that stage of growth (378). By contrast, films composed of Glyc-CHI did not display a decrease in cellular adhesion with increased thickness, with high levels of cellular adhesion, comparable to control glass surfaces, observed at 3, 5 and 10 bilayers (Fig. 5.6 top). The morphology of MC3T3 cells on Glyc-CHI/HA films also indicated a well spread phenotype at all bilayer numbers tested (Fig. 5.5A, C, E). MTT assays similarly conducted after 48 hours of MC3T3 growth on $[Glyc\text{-}CHI/HA]_N$ and $[CHI/HA]_N$ multilayer films, where N = 3, 5, 10 bilayers (Fig. 5.6 bottom), clearly reflect the adhesion data, with Glyc-CHI/HA films displaying significantly higher

MC3T3 cell viability at 5 or more bilayers, compared to corresponding unmodified CHI films ($\chi^2 = 54.70$, $p < 0.001$). No differences in either cell adhesion or viability were observed between cationic or anionic terminating layers within each PE system ($\chi^2 = 0.04$, $p > 0.80$; and $\chi^2 = 1.60$, $p > 0.21$).

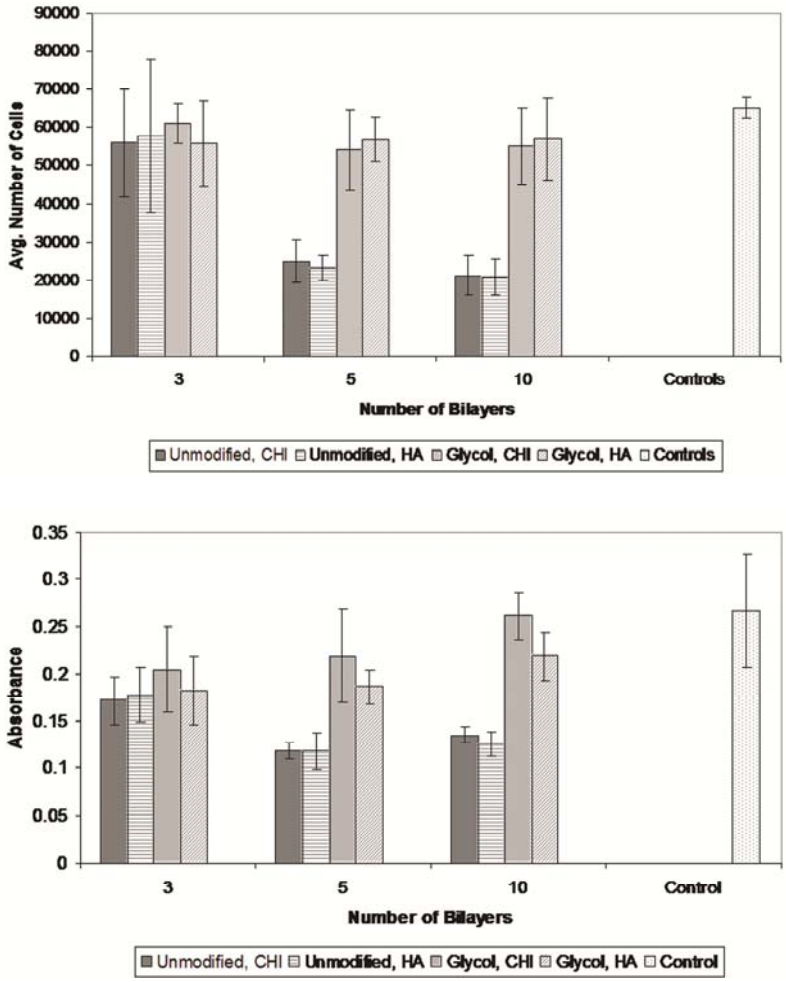


**FIGURE 5.6: Quantification of MC3T3: (top) cell adhesion and (bottom) viability after 48 h on $[Glyc\text{-}CHI/HA]_N$ and $[CHI/HA]_N$ films terminating in either HA or CHI, where N = 3, 5, or 10 bilayers. Top: Average cell numbers were determined via manual count of representative microscopy images using ImageJ software. MC3T3 adhesion on uncoated glass slides is presented as a control. Kruskal–Wallis test statistics for: Glyc- CHI versus CHI ($\chi^2 = 40.20$, $p < 0.001$); cation terminating versus anion terminating: ($\chi^2 = 0.04$, $p > 0.80$); differences in number of bilayers ($\chi^2 = 14.86$, $p < 0.001$). Bottom: Average cell viability measured as absorbance via the MTT assay. Data presented in each case is from three separate experiments (n = 9). Kruskal–Wallis test statistics for: Glyc-CHI versus CHI ($\chi^2 = 54.70$, $p < 0.001$); cation terminating versus anion terminating: ($\chi^2 = 1.60$, $p > 0.21$); differences in number of bilayers ($\chi^2 = 6.62$, $p < 0.04$).**

The observed increase in rms surface roughness and differences in film topography displayed by five bilayer Glyc-CHI/HA films, compared to corresponding films composed of unmodified CHI, may play a role in underlying the significant increase in cellular adhesion and viability, as both types of multilayers exhibited similar thickness, viscoelasticity, and total serum protein adsorption. Numerous studies have examined the effects of surface roughness and topography on cellular adhesion; however, overall trends tend to be material and cell type specific. Even within a given material-cell system it has proved difficult to separate the individual contributions of roughness from the pattern and distribution of the surface topographical features themselves, or from the changes in surface chemistry or wettability that result from the methods used to create the roughness variations. In the case of the MC3T3-E1 preosteoblasts used here, for example, there appears to be a material-specific threshold roughness, above which cellular adhesion and/or proliferation is dramatically reduced (393, 394). Differences in film surface roughness, however, are only one contributing factor to the differences in MC3T3 cell adhesion and viability, as the increase in roughness within the Glyc-CHI system between three and five bilayers was not accompanied by a significant change in cell numbers.

Although many studies have related cell adhesion to the hydrophobicity/hydrophilicity of biomaterial surfaces (395), it is somewhat uncertain whether the small (maximum 10 degrees), non-statistically significant increase in Glyc-CHI/HA film hydrophobicity contributed much to the large observed increase in cellular adhesion and viability. Indeed, the slight film hydrophobicity increase was not reflected in significant differences in total serum protein adhesion, which has been found to play an important role in cell adhesion

(396). It is possible that the actual protein species adsorbed differed between films composed of Glyc-CHI and unmodified CHI and thus contributed to enhanced cellular adhesion. However, significant differences in the types of protein adsorbed by multilayers ending in cationic and anionic PEs would be intuitively expected, and there were no significant cell adhesion differences observed between films terminating in HA vs. Glyc-CHI or CHI within either film system.

PE films composed of HA and another water-soluble CHI-derivative, phosphorylcholine-modified-CHI (Pc-CHI), have demonstrated biocompatibility (215, 390). Similar to Glyc-CHI/HA films, Pc-CHI/HA films were found to be rougher than their analogous CHI/HA films, while, in contrast, Pc-CHI films also displayed an increased thickness due to increased film hydration, which also translated into greater film viscoelasticity (390). Although differences between "wet" and "dry" AFM feature heights do suggest an increase in Glyc-CHI film water content, at least at five bilayers, compared to CHI/HA controls, the similarities in the Glyc-CHI vs. CHI film viscoelasticity and thickness, coupled with slightly greater surface hydrophobicity indicate that direct study of Glyc-CHI/HA film hydration and swelling should be performed. Initial screening has suggested that Pc-CHI/HA multilayers also exhibit enhanced cellular adhesion (data not shown), which is likely due to the presence of the Pc groups, as PE films tend to display decreased cellular adhesion with increasing thickness, hydration and viscoelasticity (205). Although differing in some physical properties, films composed of HA and either Glyc-CHI or Pc-CHI both display improved cellular adhesion compared to corresponding multilayers composed of unomodfied CHI. This suggests that the water-solubility of

chitosan derivatives may play a role in underlying the increased film cytocompatibility. Overall, Glyc-CHI/HA films are distinctive in providing many similar physical properties to the widely employed CHI/HA system, while greatly enhancing cellular adhesion and viability, thereby enabling a wider variety of biomedical applications.

## 5.5 Conclusions

Glycol-CHI/HA multilayer films composed of 5 or more bilayers displayed significantly higher cell adhesion and viability compared to corresponding films formed of unmodified CHI. These differences in cell adhesion are likely due to a combination of differences in surface topography, roughness, and chemistry, since both types of films exhibited similar: thickness and viscoelasticity, as measured via QCM; wettability, as measured via contact angle; and serum protein adsorption, as determined via the BCA assay. Enhanced cellular adhesion and viability, alongside the preservation of many of the physical properties of the commonly employed CHI/HA system, thus make water soluble Glyc-CHI/HA films an attractive candidate for a wide variety of applications in drug and gene delivery, as well as in implant and tissue engineering coatings.

## 5.6 Acknowledgements

The authors would like to thank A. Hillberg and L. Mongeon for technical training and S. Shapka for performing Gel Permeation Chromatography analyses. This work was funded by a National Science and Engineering Research Council of Canada Discovery Grant, the Canadian Institutes of Health Research, and Le Fonds Québécois de la Recherche sur la Nature et les Technologies (through the Centre for Biorecognition and Biosensors). C A. Holmes is supported by a National Science and Engineering Research Council of Canada Graduate Scholarship.

## 5.7 NIH3T3 and HEK293 Cell Adhesion and Viability on Glyc-CHI/HA Multilayers

In order to assess whether the improved cellular adhesion and viability observed on Glyc-CHI/HA multilayer films was cell-specific, we extended our published work with MC3T3 pre-osteoblasts to include both NIH3T3 murine embryonic fibroblast cells and HEK293 human embryonic kidney cells (ATCC, Manassas, VA). Cellular adhesion and viability were investigated via light microscopy and the MTT assay, respectively. Similar to our previous findings, NIH3T3 fibroblasts also exhibited increased adhesion (Fig. 5.7) and viability (Fig. 5.8) on Glyc-CHI/HA multilayer films composed of higher numbers of bilayers, compared to corresponding umodified-CHI/HA control films ($\chi^2$ = 52.18, p <0.001).

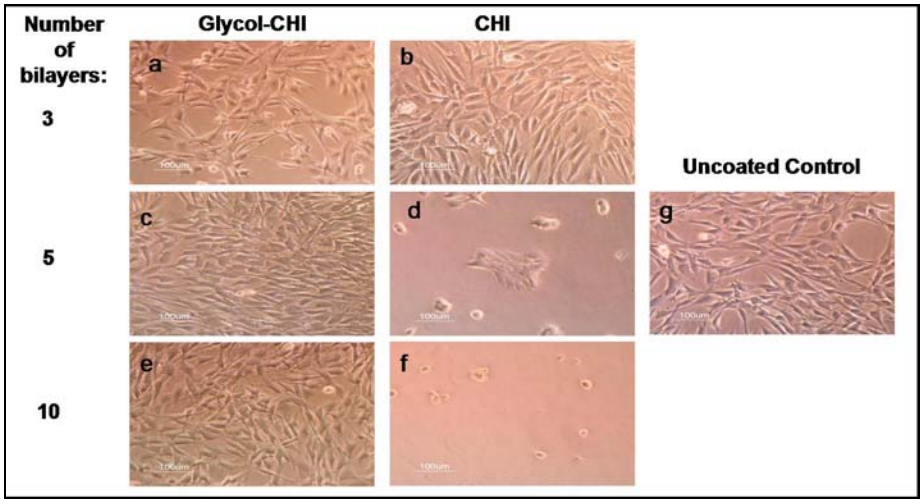


**FIGURE 5.7: Representative bright-field images of NIH3T3 cell adhesion after 48 hours on $[Glyc\text{-}CHI/HA]_N Glyc\text{-}CHI$ (a,c,e) and $[CHI/HA]_N CHI$ films (b,d,f), where N = 3(a,b), 5(c,d), or 10(e,f) bilayers. Results for films terminating in an HA layer ($[CHI/HA]_N$) are consistent with those presented here. A control image (g) of NIH3T3 cell adhesion on uncoated glass slides, with scale bar of 100 µm, is presented for comparison.**

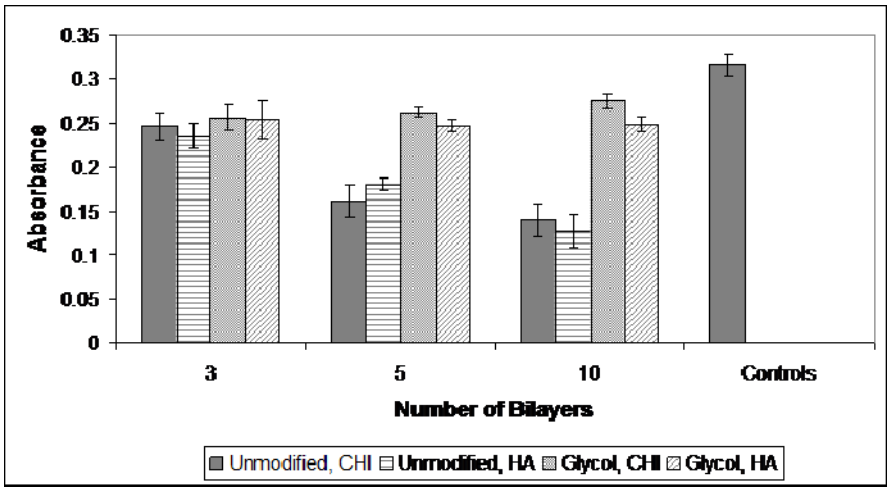


**FIGURE 5.8: NIH3T3 cell viability, as determined via the MTT assay, after 48 hours on: $[CHI/HA]_N$CHI ("Unmodified, CHI"); $[CHI/HA]_N$ ("Unmodified, HA"); $(Glyc\text{-}CHI/HA)_N$glyc-CHI ("Glycol, CHI"); and $[Glyc\text{-}CHI/HA]_N$ ("Glycol, HA") multilayer films, where N= 3, 5 or 10 bilayers. Data presented is from 3 separate experiments (n=9). NIH3T3 adhesion on uncoated glass slides is presented as a control. Kruskal–Wallis test statistics for: Glyc- CHI versus CHI ($\chi^2$ = 52.18, p <0.001); cation terminating versus anion terminating: ($\chi^2$ = 2.09, p =0.148); differences in number of bilayers ($\chi^2$ = 10.27, p = 0.006).**

Initial studies suggest that HEK293 cells exhibited a well spread morphology on Glyc-CHI/HA multilayer films composed of 3, 5 or 10 bilayers, similar to glass controls. By contrast, HEK293 cells seeded on corresponding umodified-CHI/HA films tend to adhere in patches and exhibit a more rounded morphology (Fig. 5.9). Interestingly, these significant differences in cell morphology did not translate into an expected increase in viability on Glyc-CHI/HA films (Fig. 5.10). Surprisingly, the MTT assay revealed no differences in viability for 3 and 5 bilayer films, while for 10 bilayer films a slight increase in HEK293 viability on umodified-CHI/HA compared to Gly-CHI/HA films was observed ($\chi 2 = 4.95$, $p = 0.026$).

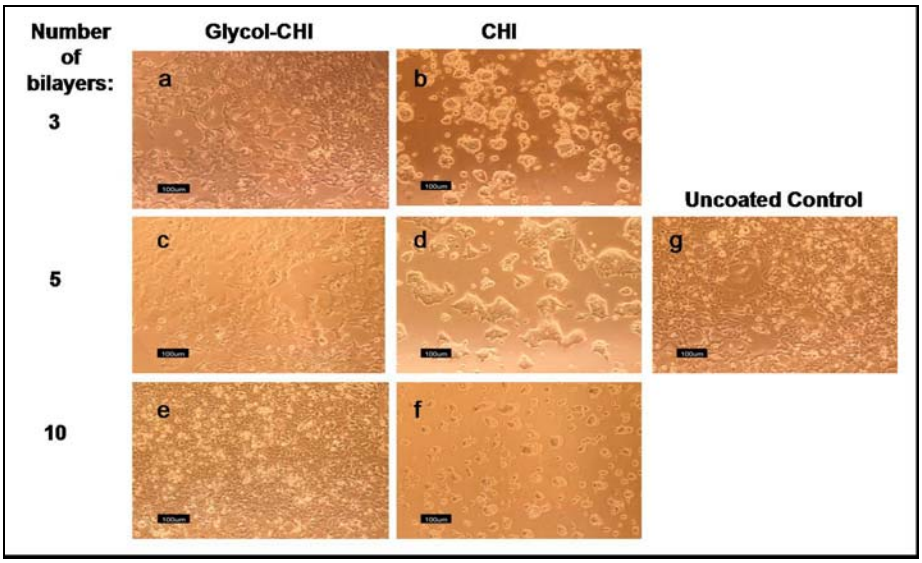


**FIGURE 5.9: Representative bright-field images of HEK293 cell adhesion after 48 hours on $[Glyc\text{-}CHI/HA]_N$Glyc-CHI (a,c,e) and $[CHI/HA]_N$CHI films (b,d,f), where N = 3(a,b), 5(c,d), or 10(e,f) bilayers. Results for films terminating in an HA layer ($[CHI/HA]_N$) are consistent with those presented here. A control image (g) of HEK293 cell adhesion on uncoated glass slides, with scale bar of 100 µm, is presented for comparison.**

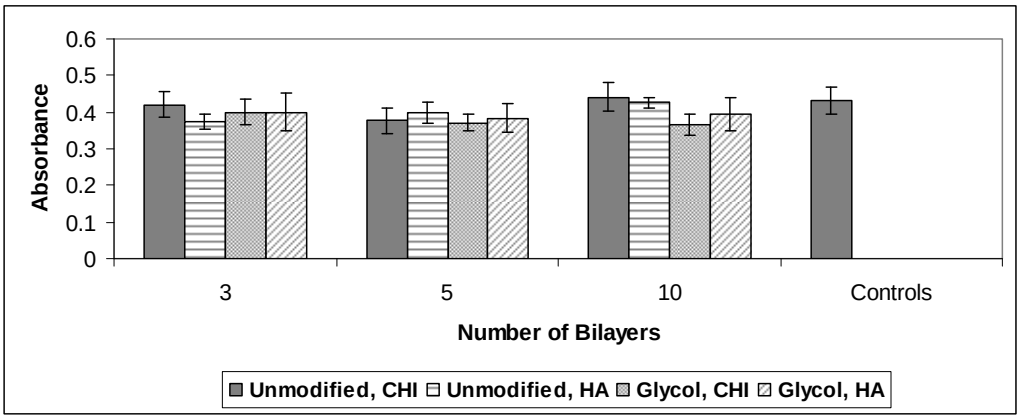


**FIGURE 5.10: HEK293 cell viability, as determined via the MTT assay, after 48 hours on: $[CHI/HA]_N$CHI ("Unmodified, CHI"); $[CHI/HA]_N$ ("Unmodified, HA"); $(Glyc\text{-}CHI/HA)_N$glyc-CHI ("Glycol, CHI"); and $[Glyc\text{-}CHI/HA]_N$ ("Glycol, HA") multilayer films, where N= 3, 5 or 10 bilayers. Data presented is from 2 separate experiments (n=6). HEK293 adhesion on uncoated glass slides is presented as a control. Kruskal–Wallis test statistics for: Glyc- CHI versus CHI ($\chi^2 = 4.95$, p = 0.026); cation terminating versus anion terminating: ($\chi^2 = 0.07$, p =0.787); differences in number of bilayers ($\chi^2 = 4.65$, p = 0.098).**

This significant difference between morphology and MTT-measured viability in HEK293 cells may be due a number of factors. It is possible that there are larger numbers of tightly

packed cells present within the rounded cell clusters than one would visually estimate on CHI/HA films. Perhaps the better spread HEK293 cells on Glyc-CHI/HA films take up more room and thus give the illusion of there being more cells. It is also possible that the HEK293 cells are more metabolically active on unmodified CHI films, or that they are less metabolically active on Glyc-CHI films.

Overall, however, HEK293 cells on Glyc-CHI/HA films did not exhibit reduced viability compared to corresponding films composed of unmodified-CHI. More importantly, HEK293 cells displayed a more typical, well-spread morphology and more homogenous surface coverage on Glyc-CHI/HA films, compared to the patchy, rounded clusters on unmodified-CHI films. Thus, although not exhibiting increased viability for all cell types, Glyc-CHI/HA films remain a promising candidate for gene delivery applications.

# Chapter 6: Glycol-Chitosan/Hyaluronic Acid Films with Embedded Gene Delivery Lipoplexes Enable Successful *In Vitro* Gene Delivery

As part of the second sub-objective of this thesis work, lipoplexes containing plasmid DNA were embedded within Glyc-CHI/HA polyelectrolyte films. Prior to embedding, the size and surface charge of lipoplexes, formed by complexing Lipofectamine2000$^{TM}$ and plasmid DNA encoding the fluorescent marker gene EGFP, were characterized via dynamic light scattering and zeta potential analysis, respectively. These lipoplexes were then adsorbed on top of, or within, Glyc-CHI/HA LbL films of varying architectures and the resulting film morphology was assessed via atomic force microscopy (AFM) and scanning electron microscopy (SEM). The *in vitro* transfection efficiency and cytotoxicity of these multilayer films was then assessed for NIH3T3 murine embryonic fibroblast and HEK293 human embryonic kidney cells via fluorescence microscopy and fluorescence activated cell sorting (FACS) analysis.

The results of this work are presented here in the manuscript entitled "Substrate-mediated gene delivery from glycol-chitosan/hyaluronic acid polyelectrolyte multilayer films" which was accepted by the American Chemical Society's journal Applied Materials and Interfaces in 2013 and is currently in press.

Substrate-mediated gene delivery from glycol-chitosan/hyaluronic acid polyelectrolyte multilayer films.

Christina A. Holmes[1] and Maryam Tabrizian[1,2*]

[1]Department of Biomedical Engineering and [2]Faculty of Dentistry, Duff Medical Science Building, 3775 University Street, McGill University, Montreal, H3A 2B4, Canada
*Corresponding author: maryam.tabrizian@mcgill.ca

## 6.1 Abstract

Substrate-mediated transfection is one of the key strategies for localized gene delivery. Layer-by-layer (LbL) polyelectrolyte deposition is a promising technique which enables controlled delivery of a number of biofactors, including nucleic acids. Here, we embed lipoplexes containing plasmid DNA within polyelectrolyte multilayers composed of glycol-chitosan (Glyc-CHI) and hyaluronic acid (HA) in order to produce a film system that enables localized, surface-based transfection. The topography and morphology of the resulting multilayers were characterized after lipoplex adsorption and during subsequent film build-up via AFM and SEM, respectively. DNA embedding efficiency and release were then examined. Lipoplex-containing Glyc-CHI/HA films were found to successfully transfect NIH3T3 fibroblasts and HEK293 kidney cells *in vitro*, maintaining transfection levels of approximately 20% for a period of at least 7 days.

## 6.2 Introduction

Spatial control of gene delivery is an essential feature of many biomedical applications, including inductive tissue engineering, medical implant coatings, and cellular transfection microarrays. One main approach to localized gene transfer, termed "substrate-mediated gene delivery" (72) or "reverse-transfection" (110), involves the immobilization of DNA and carrier vectors onto a biomaterial surface, as opposed to the traditional "bolus" transfection method of adding the DNA and vector to an aqueous media. A variety of strategies can be employed to surface-immobilize gene transfection vectors, including non-specific adsorption (109), surface attachment via biotin-streptavidin (72) and antibody-antigen conjugate systems (120), or encapsulation within a thin polymeric or hydrogel film (110). Amongst these many methods, layer-by-layer polyelectrolyte deposition has emerged as a simple yet versatile technique which can be utilized with biomaterials of nearly any type, shape or size.

Layer-by-layer (LbL) deposition involves the sequential surface assembly of alternating layers of oppositely charged polyelectrolytes (PEs)(127), and has been widely used for the controlled release of drugs, bioactive proteins, and genes (reviewed in (122)). Naked plasmid DNA, PEI- and cyclodextran- complexed plasmids, and adenoviral vectors have been incorporated into a variety of polyelectrolyte multilayer designs (reviewed in (124)) and have been successfully used to transfect cells *in vitro* and *in vivo* (258, 259). Careful selection of the PEs used and the layer architecture and chemistry employed enables both

the tailoring of release kinetics and sequential delivery of several different genes (226, 249).

Plasmid DNA itself is often directly used as the anionic PE for LbL assembly, alongside degradable cationic polymers. For example, Lynn and colleagues built PE multilayers from a synthetic hydrolytically degradable cationic polyamine ("polymer 1") and naked plasmid DNA encoding EGFP or RFP (252), which, used alone or as a stent-coating, could transfect cells *in vitro* (253) and *in vivo* (259). AFM analysis suggested that the DNA/polymer layers re-arranged themselves to present surface-bound condensed DNA nanoparticles (253). Naked plasmid DNA-based LbL multilayers have also been constructed using chitosan (255), galactosylated chitosan (256), poly(2-aminoethyl propylene phosphate) (257), poly(ethylimine) (397), and reducible hyperbranched poly(amido amine) (258) as the cationic PEs, with similar film surface rearrangements into nanoparticle complexes observed in most cases. As these plasmid-cationic polymer films degrade, these complexes are released, as verified via electrophoresis and TEM (256, 257), and are thought to act like other typical cationic gene delivery vectors.

Alternatively, plasmids pre-complexed with a viral or non-viral gene carrier vector can also be incorporated within multilayer films for controlled, substrate-mediated transfection. The Voegel and Jessel groups, for example, have done extensive work using PLL/PGA, CHI/HA, PAH/PSS, and PLL/HA multilayer films to deliver PEI-condensed plasmids (250), pyridylamino cyclodextrin complexed plasmids (249), or adenoviral vectors (251) to several different cell lines as well as primary cells. While results varied

greatly between systems, generally, lower transfection levels were observed when the vector was embedded under greater numbers of PE bilayers, and an increase in the number of vector layers led to an increase in transfection efficiency (249-251).

Few studies to date have attempted to incorporate DNA-lipoplexes within LbL PE films, even though lipid-based DNA carriers are the most widely used non-viral vectors. Several other strategies have been used to immobilize DNA-lipoplexes to biomaterial surfaces, with most studies focusing on surface adsorption (109, 119, 398) or physical incorporation within cast films (399, 400). As a coating enabling stent-based gene delivery, Yaumuchi and coworkers have used LbL deposition to assemble alternating layers of DNA-containing lipoplexes and naked plasmid DNA on top of self assembled monolayers of carboxylic acid-terminated alkanethiol. The resulting multilayers were able to successfully transfect HEK293 and HUVEC cells *in vitro* with EGFP at high efficiencies, with continued EGFP expression for a period of over 9 days in the case of films composed of 5 layers (401). While this film system shows promise, it uses a high concentration of DNA in production and is limited in the types of release profiles it can yield. It would thus be of great interest to incorporate DNA-containing lipoplexes within a biocompatible PE film, rather than composing the multilayer itself entirely of DNA and lipoplexes.

As gene delivery vectors do not diffuse readily through most LbL multilayer systems, it is crucial to select PEs that allow for controlled film dissolution under physiological conditions. The biodegradable, naturally-derived polysaccharides chitosan (CHI) and

hyaluronic acid (HA) have been incorporated into multilayer film architectures for a variety of bioapplications, including successful *in vitro* transfection when incorporating adenoviral or PEI-condensed vectors (249, 250). However, studies have indicated that many cell lines exhibit decreased adhesion to CHI/HA multilayer films, particularly as the number of layers are increased (208), thus suggesting transfection from these films may be far from optimal. We have recently developed an alternative film system utilizing glycol-modified chitosan (Glyc-CHI), and have demonstrated that Glyc-CHI/HA films exhibit significantly improved cellular adhesion compared to corresponding films consisting of unmodified chitosan, while maintaining many of their physical properties (402). Here we embed lipoplexes containing plasmid DNA within Glyc-CHI/HA multilayers, characterize the topography, morphology and release profile of the resulting LbL films, and use them to successfully transfect NIH3T3 fibroblasts and HEK293 kidney cells *in vitro*.

## 6.3 Materials and Methods

### ***6.3.1 Materials***:

Hyaluronic Acid (HA) with a molecular weight of 74 kDa was purchased from Lifecore Biomedical (Chaska, MN, USA). Glycol-Chitosan (Glyc-CHI) with a molecular weight of approximately 80 kDa (via GPC) was purchased from Sigma-Aldrich. The plasmid encoding enhanced green fluorescent protein (pEGFP-C3) was acquired from Clontech (CA, USA). Lipofectamine 2000TM and subcloning efficiency DH5α competent E. coli cells were obtained from Invitrogen (CA, USA). NIH3T3 mouse embryonic fibroblast cells and HEK293 human embryonic kidney cells were supplied by American Type Culture Collection (ATCC, VA, USA). Sodium dodecyl sulphate (SDS) and sodium chloride (NaCl) were purchased from Sigma-Aldrich; cell culture cover glasses (15 mm, round) were obtained from Fisher Scientific.

### ***6.3.2 Plasmid Amplification and Purification***:

The 4.7 kb plasmid encoding enhanced green fluorescent protein (pEGFP-C3), driven by a human cytomegalovirus promoter (CMV) and containing a kanomycin resistance gene, was amplified in DH5α cells in the presence of kanomycin. Plasmid purification was performed using a Plasmid Maxi Prep Kit (Quiagen, CA, USA) according to manufacturer instructions, and the resulting plasmid DNA (pDNA) was re-suspended in MillQ water. The pDNA concentration and purity was measured using a UV spectrophotometer at 260 and 280 nm.

### *6.3.3 Formation and Characterization of DNA Lipoplexes*:

All lipoplexes were prepared at room temperature in a 0.1 M NaCl buffer solution, adjusted to pH 6.0 and filtered through a 0.22 μm PES stericup filtration unit (Milipore), at a ratio of 2 μL of Lipofectamine 2000TM to 1 μg of pEGFP. Briefly, two solutions of equal volume (150 μL in the case of film formation, and 500 μL in the case of particle characterization) were prepared, one containing either 1, 2, 4, or 6 μg of pEGFP DNA, and the other containing 2, 4, 8 or 12 μL of Lipofectamine 2000$^{TM}$ (i.e. at a ratio of 2 μL of lipid to 1 μg of plasmid), and left to stand for 10 min. These two solutions were then combined and incubated at room temperature for 15 minutes, before immediate use in the formation of films or for lipoplex characterization.

The hydrodynamic diameter and polydispersity of the DNA lipoplexes were determined via low angle dynamic light scattering (DLS) at room temperature at a 90$^{o}$ angle (90Plus, Brookhaven Instruments, NY, USA), while lipoplex surface charge was characterized via zeta potential measurement (ZetaPALS, Brookhaven Instruments, NY, USA). DLS and zeta measurements were performed in a 0.1 M NaCl buffer solution, pH ~6.0.

### *6.3.4 LbL Assembly of Films*:

Both Glyc-CHI and HA polyelectrolyte solutions were prepared at a concentration of 2 mg/mL in 0.1 M NaCl buffer, adjusted to pH 6.0, and filtered through a 0.22 μm PES stericup filtration unit (Milipore). Prior to film deposition, cover glasses were cleaned in 10 mM SDS for three hours, rinsed in distilled water three times, treated with 0.1 N HCl overnight and thoroughly rinsed in distilled water. LbL build up was achieved using the

pipette approach, wherein 300 µl of each polymer solution was deposited directly onto the cover glass, beginning with the polycation (Glyc-CHI). After the polymer was allowed to adsorb for 10 min, the polymeric films were rinsed twice in 0.1 M NaCl buffer. Then the polyanion, HA, was added, allowed to adsorb for 10 min and rinsed twice. This was repeated at each step of LbL deposition until 5 bilayers of film, with an additional terminating layer of Glyc CHI, i.e. $[Glyc\text{-}CHI/HA]_5Glyc\text{-}CHI$, was formed. Next, 300 µL of DNA-Lipoplex solution, containing 2, 4, or 6 µg of pEGFP, was added to the films, allowed to adsorb for 2 hours, and rinsed once in 0.1 M NaCl buffer. These DNA lipoplex containing films were then either used as is, or covered with a further 2 or 4 bilayers and a terminating layer of Glyc-CHI, thus forming: $[Glyc\text{-}CHI/HA]_5Glyc\text{-}CHI$-Lipo or "surface adsorbed" films; $[Glyc\text{-}CHI/HA]_5Glyc\text{-}CHI\text{-}Lipo\text{-}[Glyc\text{-}CHI/HA]_2Glyc\text{-}CHI$ or "two overlying bilayer" films; and $[Glyc\text{-}CHI/HA]_5Glyc\text{-}CHI\text{-}Lipo\text{-}[Glyc\text{-}CHI/HA]_4Glyc\text{-}CHI$ films or "four overlying bilayer" films, respectively.

### ***6.3.5 Atomic Force Microscopy***:

The topography of DNA lipoplex containing Glyc-CHI/HA films was imaged by atomic force microscopy (AFM) in "wet" conditions using the Nanoscope III (Digital Instruments, USA) system in the tapping mode. Samples were analyzed within a multimode fluid cell (model MTFML, Veeco) filled with 0.1 M NaCl solution (pH 6), using a silicon nitride probe with a nominal spring constant of 0.3 N/m and a nominal radius of curvature of 20 µm (model NP, Veeco). A 20 µm x 20 µm area was scanned at a rate of 1 Hz using the minimum amount of force required to obtain steady images. Mean RMS surface roughness was calculated using Nanoscope v 5.12r5 software.

### ***6.3.6 Scanning Electron Microscopy***:

DNA lipoplex-containing film morphology was characterized with a Hitachi S-4700 field emission gun scanning electron microscope (FEG-SEM). Prior to imaging, film samples were dehydrated in an increasing series of ethanol solutions (30 – 100 % in water); with a 10 min incubation for each step in the series. Samples were then critically point dried in $CO_2$ and gold-palladium-coated, via sputter coating under an argon atmosphere, prior to SEM analyses.

### ***6.3.7 Quantification of DNA Film Content and Release***:

DNA lipoplex containing Glyc-CHI/HA films were formed on cover glasses placed within 24 well tissue culture plates (Falcon) and incubated in 1 x PBS solution, pH= 7.4, at 37°C in a humidified atmosphere of 5% $CO_2$. The supernatant was removed and replaced with fresh PBS solution each day. The amount of DNA within the supernatant was measured via the Quant-iT PicoGreen assay (Molecular Porbes, Invitrogen) according to manufacturer specifications. Briefly, an equal volume of 0.2 % w/v heparin sulphate (Sigma) solution in 2 x TE buffer was added to the supernatant solution (final concentration of 0.1% w/v heparin in 1 x TE buffer) in order to decomplex the plasmid from the lipoplex, thus allowing the Picogreen stain access to the DNA. Fluorescence was then measured using a fluorescent plate reader (Flx800, Bio-Tek Instruments, VT, USA) using excitation and emission wavelengths of ~480 nm and ~520 nm, respectively. A series of DNA standards in 0.1% w/v heparin, 1 x TE buffer was produced and measured for reference.

In order to indirectly measure the quantity of DNA embedded within the Glyc-CHI/HA films, the plasmid content of the lipoplex solution before and after deposition, as well as the DNA concentration of the rinsate was measured via the Picogreen assay as described above.

### ***6.3.8 Cell Culture and Transfection***:

NIH3T3 mouse embryonic fibroblast cells, and HEK293 human embryonic kidney cells (ATCC) were grown in Dulbecco's minimum essential medium (DMEM, ATCC) supplemented with 10% fetal calf serum (FCS, ATCC) and 1% penicillin/streptomycin (Invitrogen) and incubated at 37°C in a humidified atmosphere of 5% $CO_2$.

$[Glyc\text{-}CHI/HA]_5Glyc\text{-}CHI\text{-}Lipo$,$[Glyc\text{-}CHI/HA]_5Glyc\text{-}CHI\text{-}Lipo\text{-}[Glyc\text{-}CHI/HA]_2Glyc\text{-}CHI$, and $[Glyc\text{-}CHI/HA]_5Glyc\text{-}CHI\text{-}Lipo\text{-}[Glyc\text{-}CHI/HA]_4Glyc\text{-}CHI$ films, containing 2, 4, or 6 μg of pEGFP, were built in 24 well tissue culture plates (Falcon), as described above with a few modifications. After the first three bilayers of film were formed (i.e. $[Glyc\text{-}CHI/HA]_3$), samples were sterilized with 70% (v/v) ethanol for 30 min and then washed in the following ethanol series for 15 min each: 50%, 20% and 10%. To ensure complete removal of the ethanol, substrates were then washed three times (5 min each wash) in 0.1 M NaCl buffer, pH 6. Film deposition then continued under sterile conditions and using sterile solutions, with a polyelectrolyte deposition time of 20 min employed for the first sterile bilayer (i.e. the 4th bilayer), and 10 min used for all subsequent bilayers. It should be noted that during the washing and media equilibration steps, all of the substrates, including the controls, were treated in the same manner.

After film formation, NIH3T3 or HEK293 cells were prepared for seeding. Cells were trypsinized and spun down at 1000 rpm for 5 min, re-suspended in fresh media, and the cell concentration was determined using a hemocytometer. A seeding population of 5 x $10^4$ cells (in a volume of 500 µl) was added to each of the wells and incubated at 37°C in a humidified atmosphere of 5% $CO_2$ for 2, 4 or 7 days, with media exchange being performed every 2 days. As a positive control, bolus transfections were performed on cells seeded on $[Glyc\text{-}CHI/HA]_5Glyc$ films. Briefly, 25 µL solutions containing either 2 µg of pEGFP or 4 µL of Lipofectamine 2000TM were prepared separately in 0.1 M NaCl buffer (pH= 6.0), combined and incubated at room temperature for 15 min., and added to the seeded cells. Negative controls consisted of cells seeded on $[Glyc\text{-}CHI/HA]_5Glyc$ films, and cells seeded on $[Glyc\text{-}CHI/HA]_5Glyc\text{-}CHI\text{-}Lipo^*\text{-}[Glyc\text{-}CHI/HA]_2Glyc\text{-}CHI$ films, where the lipoplexes were formed with blank plasmid DNA in place of pEGFP.

### ***6.3.9 Fluorescence Microscopy***:

Fluorescent images of transfected cells after 2, 4 or 7 days were acquired with a stereoscopic zoom microscope (SMZ1500, Nikon) equipped with a high pressure mercury lamp (C-SHG1, Nikon; USA), the appropriate set of filters for fluorescein (FITC) excitation and emission, and a digital camera (DXM1200F, Nikon) operated with the ACT-1 software.

### ***6.3.10 Fluorescent Activated Cell Sorting Analysis***:

Cellular transfection efficiency and cytotoxicity after 2, 4 or 7 days was assessed via fluorescent activated cell sorting (FACS). After removing the media, samples were rinsed once in PBS and cells were trypsinized for 5 min (0.05% trpsin-EDTA, Invitrogen). Next, 1 mL of 2% FBS in PBS was added to each well and cells were spun down at 250 x g for 5 min. Cells were then re-suspended in 300 µl of 2% FBS in PBS, transferred into FACS tubes, and 3 µl of 40 µg/mL propidium iodide (PI) was added to each sample. Samples were then directly FACS analyzed using the BD FacsCalibur system (BD Biosciences, USA), equipped with a 488 nm argon laser to excite both PI and GFP, with 10,000 cells per sample assessed. FACS data was subsequently analyzed for GFP and PI expression using FlowJo software (Treestar Inc., OR, USA), using appropriate gates and controls.

### ***6.3.11 Statistics***:

Statistical analyses of data were performed using the software package SPSS/PASW Statistics v18.0 (SPSS Inc., Chicago, IL). All data are presented as mean ± STD. The significance level was set at $p < 0.05$. As most data either failed the Shapiro-Wilk test for normality and/or the Levene's test for homogeneity of variance, or were of small sample size, Kruskal-Wallis non-parametric analyses were performed.

## 6.4 Result and Discussion

### *6.4.1 Lipoplex and Film Characterization*:

The size, surface charge and polydispersity of the lipoplexes used in this study, formed from the complexation of plasmid DNA encoding enhanced green fluorescent protein (pEGFP) with Lipofectamine2000$^{TM}$, are presented in Table 6.1. Increasing the amount of DNA increased the resulting lipoplex size, from 360 ± 59 nm in diameter for 2 μg of plasmid to 754 ± 59 nm for 6 μg, while the polydispersity index remained fairly constant. All lipoplexes exhibited a net negative surface charge, around -40 mV, and were thus subsequently sandwiched between polycationic Glyc-CHI layers when forming LbL films.

| Amount of DNA (μg) | Avg. Particle Diameter (nm) | Avg. Zeta Potential (mV) | Avg. Polydispersity Index |
|---|---|---|---|
| 2 | 360 ± 59 | -44 ± 4 | 0.25 ± 0.01 |
| 4 | 585 ± 54 | -46 ± 1 | 0.31 ± 0.01 |
| 6 | 754 ± 59 | -38 ± 3 | 0.30 ± 0.01 |

**TABLE 6.1: Physical characterization of pEGFP containing lipoplexes. Lipoplexes were formed at a ratio of 2 μL of Lipofectamine2000$^{TM}$ to 1 μg of plasmid using the indicated amount of DNA. The size and polydispersity of the resulting complexes were determined via low angle dynamic light scattering (DLS), while particle surface charge was characterized via zeta potential measurement. Data presented is from 3 separate experiments (n = 9).**

Previous studies of DNA-Lipofectamine2000$^{TM}$ complexes have yielded both negatively charged (109, 400, 403) and positively charged (404) particles, broadly ranging in hydrodynamic diameter from 100-1000 nm (400, 403-405). The observed wide variety in

lipoplex properties, including those seen in this study, are mainly due to differences in the conditions employed for particle formation, including: the size, type and amount of plasmid used; the ratio of lipid to DNA utilized; the volume and properties of the solution in which they are complexed (e.g. presence of serum and/or ionic species such as calcium, pH); and complexation time.

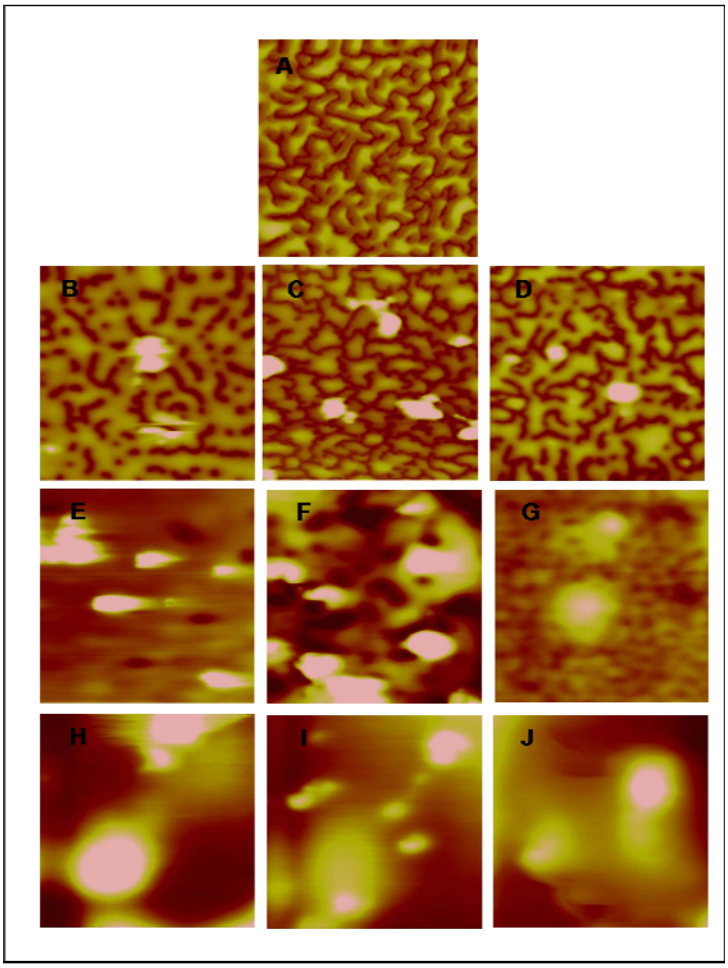


**FIGURE 6.1: AFM imaging of the surface topography of lipoplex-contaning polyelectrolyte films constructed using 2 µg (B,E,H), 4 µg (C,F,I) or 6 µg (D,G,J) of pEGFP DNA. Lipoplexes formed using the indicated amounts of DNA were adsorbed on the surface of [Glyc-CHI/HA]$_5$Glyc-CHI films (B,C,D), and then covered with a further 2 film bilayers (E,F,G), or 4 film bilayers (H,I,J). A close-up scan of a [Glyc-CHI/HA]$_5$Glyc-CHI film without any adsorbed lipoplexes is presented for comparison (A). Scan size = 20 µm (B-J), Z-range = 250 nm (A, C), 350 nm (B,D-F,H,I), or 450 nm.**

Atomic force microscopy (AFM) images of surface adsorbed (Fig. 6.1 B-D), two bilayer overlying (Fig. 6.1 E-G) and four bilayer overlying (Fig. 6.1 H-J) films revealed that DNA lipoplexes tended to adsorb upon the multilayer surface (Fig. 6.1 A) as large (averaging 2-3 μm) aggregates of varying size, as opposed to individual particles with sizes similar to the effective hydrodynamic diameters determined via DLS analysis. In the case of the surface adsorbed films, the AFM images also clearly displayed the structure of the underlying film, visible underneath and surrounding the large adsorbed particles, which was similar to that of bare [Glyc-CHI/HA]$_5$Glyc-CHI films (Fig. 6.1 A) and to that observed in our previous studies (402). As the DNA-lipoplexes were covered with an increasing number of bilayers (centre and right), the areas surrounding the particles gradually appear smoother.

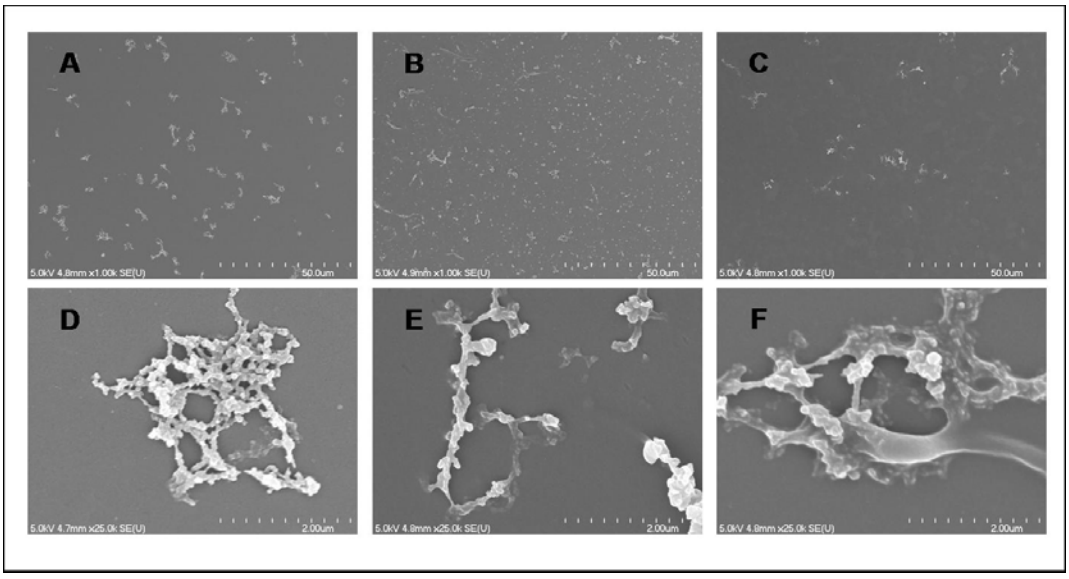


**FIGURE 6.2: SEM images of film morphology of polyelectrolyte films constructed using 4 μg of pEGFP at 1,000 times (A-C) and 25,000 times (D-F) magnification. Lipoplexes were adsorbed on the surface of [Glyc-CHI/HA]$_5$Glyc-CHI films (A,D), and then covered with a further 2 film bilayers (B,E), or 4 film bilayers (C,F).**

This coating over of the surface-bound lipoplexes is more apparent on scanning electron microscopy (SEM) images (Fig. 6.2). SEM of PE multilayers formed with 4 μg of DNA revealed that DNA-Lipofectamine2000$^{TM}$ complexes adsorbed on the film surface as clusters of smaller particles of varying size, often joined together via strand-like structures (Fig. 6.2 A, D). These details of particle structure become less distinct as the lipoplexes are covered with a further 2 (Fig. 6.2 B,E) and then 4 (Fig. 6.2 C, F) bilayers of PE film. The clustered globule-like appearance of the surface adsorbed DNA-Lipofectamine2000$^{TM}$ complexes observed here is very similar to that seen via SEM for comparable particles composed of DNA and various lipids (406, 407).

The presence of large lipoplex aggregates forming on the PE film surface is not entirely surprising due to the long particle adsorption time used. DNA-lipid complexes are often known to form aggregates with time after preparation, particularly at high concentrations, which is one of the reasons they are prepared fresh before use (408). Indeed, our lipoplexes formed using 4 μg of DNA were found to aggregate in solution from an average diameter of 585 ± 54 nm, to approximately 1081 ± 18 nm after one hour, and to around 1291 ± 48 nm after two hours. Interactions between the lipid portion of the DNA complexes and the underlying PE layer may also contribute to aggregation or lipoplex deformation at the film surface. Previous studies of unilamellar lipid vesicles embedded within PGA/PAH films similarly showed vesicle fusion or aggregation into structures much larger (400-1000 nm) than those of individual vesicles in solution (200 nm) (409).

### *6.4.2 Lipoplex Embedding Efficiency and DNA Release*:

By measuring the DNA concentration, via the PicoGreen assay, of the lipoplex solution before and after deposition, as well as the DNA concentration of the rinsate, the actual pEGFP content within the PE films was indirectly determined. Films formed with 2 μg of plasmid were found to contain 712 ± 44 ng of DNA, representing an embedding efficiency of 32%, while those built with 4 μg and 6 μg contained 1259 ± 175 ng (31%), and 1271 ± 417 ng (21%), respectively. The electrostatically-mediated adsorption of lipoplexes thus appears to saturate at approximately 600 ng/cm$^2$ of DNA for this Glyc-CHI/HA film system. In comparison, previous work examining surface adsorption of DNA-Lipofectamine2000$^{TM}$ complexes to tissue culture plastic found that 2 hours of incubation yielded a DNA surface density of around 200-300 ng/cm$^2$, which rose significantly to approximately 4 μg/cm$^2$ after 24 hrs of adsorption (109). As in our study, the adsorbed DNA density was found to depend upon the quantity of DNA used, however, in direct contrast to our results, lower amounts of incubated plasmid (0.5 vs 2 μg) resulted in greater overall DNA density and loading efficiency (109). Yaumuchi and coworkers, meanwhile, achieved a DNA surface density of under 300 ng/cm$^2$ for the LbL deposition of 3 layers of lipoplexes, which were alternated with 2 layers of free plasmid, in their stent coating study (401).

DNA release from "2 μg", "4 μg" and "6 μg" [Glyc-CHI/HA]$_5$Glyc-CHI-Lipo, [Glyc-CHI/HA]$_5$Glyc-CHI-Lipo-[Glyc-CHI/HA]$_2$Glyc-CHI, and [Glyc-CHI/HA]$_5$Glyc-CHI-Lipo-[Glyc-CHI/HA]$_4$Glyc-CHI films incubated in PBS, pH = 7.4, at 37$^o$C was measured each day for a period of one week (Fig. 6.3). All films were found to be fairly stable, with

less than 5% of embedded DNA released cumulatively by day 7 for any film type. Unsurprisingly, in the case of maximally loaded "4 μg" and "6 μg" films, less DNA was released when the lipoplexes were embedded within 2 or 4 bilayers than when the lipoplexes were simply adsorbed onto the surface. These results bear resemblance to previous studies, where ~6% of DNA from the lipoplexes adsorbed to tissue culture plastic were released in PBS over one week (109), and less than 10% of adsorbed DNA was released in PBS for a single layer of lipoplexes in the stent coating study (401).

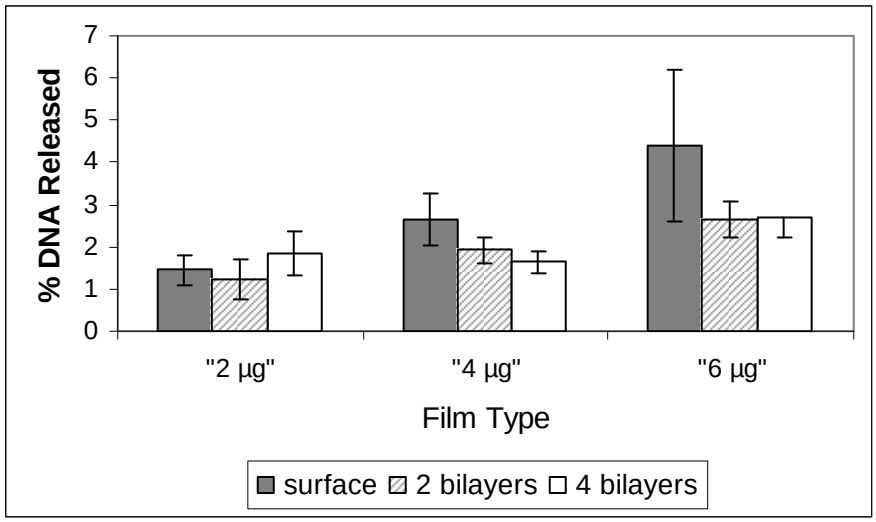


**FIGURE 6.3: Cumulative DNA released over 7 days for Glyc-CHI/HA films constructed using 2 μg, 4 μg or 6 μg of pEGFP and with the following architectures: [Glyc-CHI/HA]$_5$Glyc-CHI-Lipo (filled), or [Glyc-CHI/HA]$_5$Glyc-CHI- Lipo[Glyc-CHI/HA]$_N$Glyc-CHI films, where N=2 (lines) or 4 (empty). DNA released into the PBS supernatant was measured via the Picogreen assay each day and the cumulative amount released over 7 days was calculated and compared to the amount of DNA embedded within each film. Data presented represents the mean ± STD for 3 separate experiments. (n=9)**

### ***6.4.3 Transfection Efficiency and Cytotoxicity***:

Initial 48 hr transfection studies performed using NIH3T3 fibroblast cells revealed a significant difference in transfection efficiency as the amount of DNA used to construct the film varied ($\chi^2$= 26.277, p<0.001). More specifically, an increase in transfection efficiency was observed between "2 μg" and "4 μg" films, but no significant increase for

"6 µg" films, with a maximum transfection efficiency of approximately 14% (Fig 6.4A). These results closely reflect the observed saturation in DNA content between "4 µg" and "6 µg" films, as mentioned above. Films constructed using 4 µg of un-complexed plasmid DNA exhibited less than 1% transfection efficiency (data not shown).

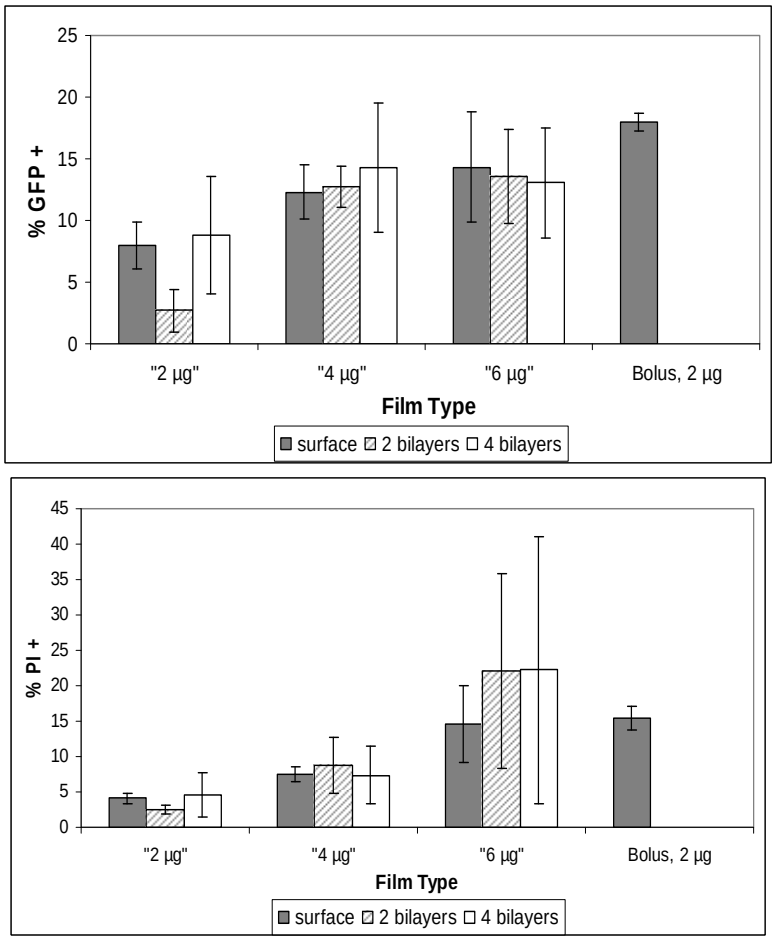


**FIGURE 6.4: NIH3T3 transfection efficiency (top) and death (bottom) after 48 hrs of growth on $[Glyc\text{-}CHI/HA]_5Glyc\text{-}CHI\text{-}Lipo[Glyc\text{-}CHI/HA]_NGlyc\text{-}CHI$ films, where N=0 (filled), 2 (lines) or 4 (empty). Lipoplexes were formed from the indicated amount of pEGFP. Data presented represent the mean percentage of GFP-expressing (A) or PI-staining (B) cells, as determined via fluorescent activated cell sorting, ± STD for 3 separate experiments. (n=9). (Stats, for amount of DNA: $\chi^2$= 26.277, p<0.001 for GFP, $\chi^2$= 40.130, p<0.001 for PI; for No. of bilayers: $\chi^2$= 1.552, p=0.460 for GFP; $\chi^2$= 0.35, p=0.983 for PI)**

Film cytotoxicity was also found to increase along with the amount of DNA used to construct the films ($\chi^2$= 40.130, p<0.001), with a maximum of 22% of cells staining for PI (Fig 6.4B). This continued increase in cytotoxicity, even after DNA saturation is achieved, may be due to a possible increase in lipid content between "4 μg" and "6 μg" films. Interestingly, overall there was no significant difference between films where the lipoplexes were simply surface adsorbed or films with 2 or 4 overlying bilayers ($\chi^2$= 1.552, p=0.460 for GFP; $\chi^2$= 0.35, p=0.983 for PI). However, when solely examining films constructed using 2 μg of pEGFP, a decrease in transfection efficiency when surface adsorbed lipoplexes were covered with 2 bilayers was observed, which recovered to initial levels when covered with 4 bilayers.

Positive controls, consisting of NIH3T3 cells seeded on $[Glyc\text{-}CHI/HA]_5Glyc\text{-}CHI$ films and bolus transfected with lipoplexes prepared with 2 μg of DNA, yielded a transfection efficiency of approximately 18% and 23% PI staining. It is important to note that our bolus transfection conditions involved cell-lipoplex contact in serum-containing media for the entire 48 hour experimental period. This likely accounts for the lower transfection efficiency and higher cytotoxicity observed here in comparison to typical bolus transfection studies which involve 4-8 hours of contact in serum-free media.

Higher transfection efficiencies were observed for HEK293 cells 48 hours post transfection (Fig 6.5A and 6.5B). Again the amount of DNA employed in constructing the film had a significant effect ($\chi^2$= 32.890, p<0.001), with an increase in transfection efficiency observed between "2 μg" and "4 μg" films, and no significant increase for "6

μg" films. However, this time a maximum transfection efficiency of over 20% was observed.

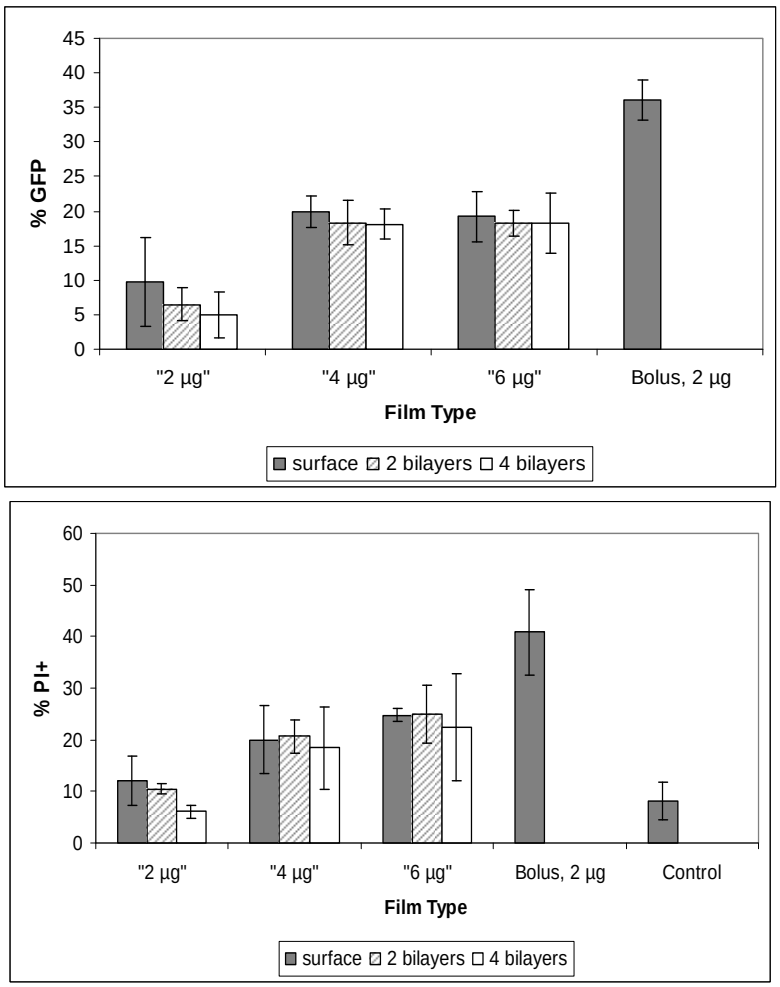


**FIGURE 6.5: HEK293 transfection efficiency (top) and death (bottom) after 48 hrs of growth on $[Glyc\text{-}CHI/HA]_5Glyc\text{-}CHI\text{-}Lipo[Glyc\text{-}CHI/HA]_NGlyc\text{-}CHI$ films, where N=0 (filled), 2 (lines) or 4 (empty). Lipoplexes were formed from the indicated amount of pEGFP. Data presented represent the mean percentage of GFP-expressing (A) or PI-staining (B) cells, as determined via fluorescent activated cell sorting, ± STD for 2 separate experiments. (n=6). (HEK293 stats, for amount of DNA: $\chi^2$= 32.890, p<0.001 for GFP, $\chi^2$= 28.104, p<0.001 for PI; for No. of bilayers: $\chi^2$= 2.402, p=0.301 for GFP; $\chi^2$= 1.373, p=0.503 for PI)**

A similar increase in film cytotoxicty alongside increasing amounts of incubated DNA was also exhibited (Fig 6.5B), with a maximum of 25% of cells staining for PI ($\chi^2$=

28.104, $p<0.001$). Also similar to results for NIH3T3 fibroblasts, no significant differences between films with zero, 2 or 4 overlaying bilayers were generally observed ($\chi^2= 2.402$, $p=0.301$ for GFP; $\chi^2= 1.373$, $p=0.503$ for PI), with the exception of films constructed with 2 μg of DNA. However, in this case, the transfection efficiency and cytoxicity decreased with the addition of overlaying bilayers. Bolus transfected HEK293 cell controls yielded a transfection efficiency of approximately 36% alongside 41% PI staining. Again the lower bolus transfection efficiency and higher cytotoxicity observed compared to typical bolus experiments is likely due to the extended period of cell contact.

Given that the transfection efficiencies exhibited by HEK293 cells were higher than those observed for NIH3T3 cells, all transfection studies of further time points were conducted solely with HEK293 cells. Also, since no significant increase in transfection efficiency was observed between "4 μg" and "6 μg" films, we present time course transfection data for "4 μg" films only.

Examining film-based transfection 2, 4 and 7 days post transfection via fluorescence microscopy suggests an increase in the number of GFP expressing cells with time (Figure 6.6). When the actual transfection efficiency is measured via FACS analysis (Fig 6.7, left), this increase in transfection efficiency is found to be significant ($\chi^2= 6.908$, $p=0.032$), although smaller (~4% maximum difference between day 2 and 7) than apparent from microscopy. Likewise, cytotoxicty, as indicated by the number of PI staining cells (Fig 6.7, right), was found to be maximal (up to ~8% difference between days 2 and 7) for all film types on day 7 ($\chi^2= 17.397$, $p<0.001$). This increase in

cytotoxicity over time may be due to the prolonged contact time between the lipoplexes and the cells.

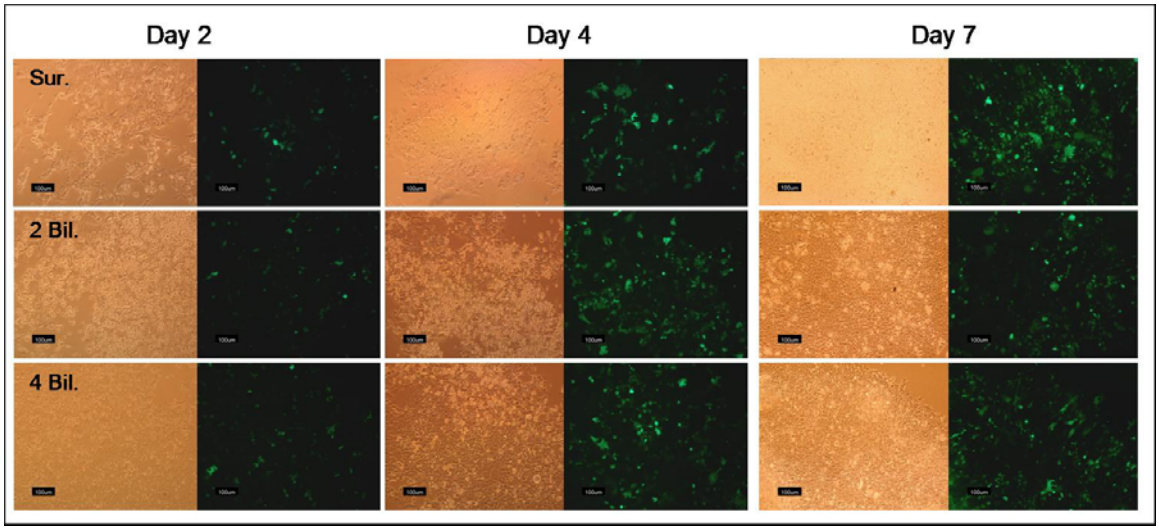


**FIGURE 6.6: Representative bright field and fluorescence microscopy images of HEK293 cells after 2 (left), 4 (centre) and 7 (right) days on polyelectrolyte films constructed using 4 µg of pEGFP, and with the following architectures: [Glyc-CHI/HA]$_5$Glyc-CHI- Lipo (top), or [Glyc-CHI/HA]$_5$Glyc-CHI- Lipo[Glyc-CHI/HA]$_N$Glyc-CHI films, where N=2 (centre) or 4 (bottom).**

While covering the lipoplexes with layers of PE film might intuitively be expected to somewhat delay transfection, this effect was not observed. Instead, although there was little difference on day 2 post-transfection, by days 4 and 7 the transfection efficiency was found to be lower as the number of overlying film bilayers increased, with the greatest difference observed on day 7 ($\chi^2$= 9.191, p=0.01). These observed reductions in transfection efficiency were small (maximum ~6% between no covering layers and 4 covering bilayers), yet unexpected. Meanwhile, overall the number of overlying bilayers was found to have no statistically significant effect on cytotoxicity ($\chi^2$= 4.260, p=0.119), even though on day 7 films with 4 covering bilayers appear to show ~7% less PI than films with no covering bilayers.

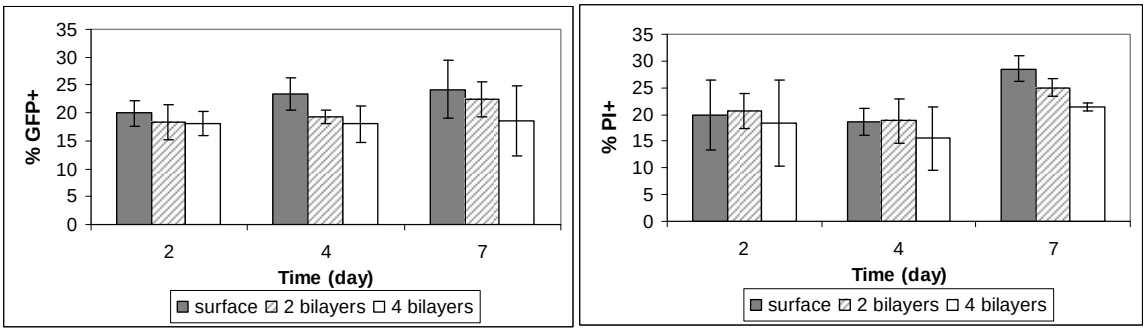


**FIGURE 6.7: HEK293 transfection efficiency (left) and death (right) over time on [Glyc-CHI/HA]$_5$Glyc-CHI- Lipo[Glyc-CHI/HA]$_N$Glyc-CHI films, where N = 0 (filled), 2 (lines), or 4 (empty). Lipoplexes were formed from 4 µg of pEGFP. Data presented represent the mean percentage of GFP-expressing (top) or PI-staining (bottom) cells, as determined via fluorescent activated cell sorting, ± STD (n = 6). (Stats for No. of bilayers: $\chi^2$= 9.191, p=0.01 for GFP, $\chi^2$= 4.260, p=0.119 for PI; for day: $\chi^2$= 6.908, p=0.032 for GFP, $\chi^2$= 17.397, p<0.001 for PI)**

The small but significant decrease in transfection efficiency observed with increasing bilayer coverage for day 4 and 7 post transfection could be due to a combination of factors. For example, any destabilizing interactions between the lipoplexes and PE layers are likely to be greater as the number of overlying bilayers is increased and this effect may further be exacerbated with time. It is also possible that lower amounts of plasmid DNA were actually embedded in films with higher numbers of covering bilayers, since the increased number of washing steps during preparation could have leached out DNA. The lack of anticipated time delay in transfection with increasing film coverage, on the other hand, may be due to an insufficient number of overlying bilayers or the time period we chose to observe. For comparison, sequential transfection of COS cells was achieved over a time scale of 2 to 8 hours in an influential study which embedded two cyclodextrin complexed plasmids, one encoding EGFP and the other a nuclearly expressed protein, within PLGA/PLL films (249). The film architecture employed in that case sandwiched each plasmid layer between 5 bilayers of film, similar to our 4 overlying bilayer films,

thus suggesting that in our study we may have looked too late to detect any differences in transfection kinetics between our films with surface adsorbed vs. embedded lipoplexes.

As has been found in other studies (223), the transfection observed from our lipoplex containing films appears to be mediated via direct cellular contact and/or interaction with the film rather than lipoplex diffusion. This is suggested by the observed stability of our films in PBS over a period of over one week, as well as preliminary studies conducted in serum-free media. In these experiments, lipoplex containing Glyc-CHI/HA films were incubated in serum-free media for 2 days. When the collected supernatant from this period of incubation was added to control HEK293 cells grown on tissue culture plastic, no transfection was observed (data not shown). However, when HEK293 cells were seeded on the remaining films, successful substrate-mediated transfection was achieved, albeit at lower efficiencies than those observed on fresh films (data not shown).

The transfection efficiencies achieved by our lipoplex film system may at first glance appear lower than those obtained by both the previously mentioned tissue culture plastic-adsorbed lipoplex study (109) and the LbL-based lipoplex stent coating study (401), which yielded transfection efficiencies of ~30% in NIH3T3 cells, and ~80% in HEK293 cells, respectively. However, it is difficult to directly compare these results with ours due to the differing analysis methods used. In the former study, for example, the plasmid that was delivered encoded for luciferase and thus transfection was assessed via a luminometer (109). In the latter case, although an analogous gene encoding GFP was used, transfection efficiency was measured via randomized manual count of fluorescent

microscopy images (401), which may somewhat overestimate the number of GFP positive cells and does not take into account autofluoresence. However, in our work FACS analysis, a far more accurate technique for quantifying both transfection efficiency and cell death within the same samples, was employed. Additionally, the maximal ~80% transfection observed in the LbL stent coating study was for 5 layer films which contain 3 layers of lipoplexes and 2 layers of plasmid DNA (401). When only a single layer of lipoplexes was used, a transfection efficiency similar to that observed here, ~20%, was found. This suggests that increasing the number of lipoplex-containing layers in our LbL film system might also significantly increase the transfection efficiency that can be achieved. Finally, while transfection for the LbL stent coating system peaked at day 3 post-transfection and gradually decreased with time (401), our system was able to maintain transfection levels (or even increase them slightly) over at least 7 days.

## 6.5 Conclusions

In this study we have successfully incorporated lipoplexes containing plasmid DNA within Glyc-CHI/HA polyelectrolyte multilayer films. We have further demonstrated that this lipoplex film system can be used to transfect both NIH3T3 fibroblasts and HEK293 kidney cells *in vitro*, with the transfection efficiency varying depending on the cell type. Films supported transfection for a period of at least 7 days, with a small but statistically significant increase in efficiency and cytotoxcity observed over time. While the number of overlying film bilayers had no significant effect on transfection efficiency or cytotoxicity at 2 days post-transfection, by day 7 there was a small but significant decrease in transfection observed as the adsorbed lipoplexes were covered by greater number of bilayers. Future work with this film system will focus on incorporating more plasmid layers and varying the films architecture in order to achieve sequential gene delivery of multiple genes and a wider variety of transfection kinetic profiles. The lipoplex-containing Glyc-CHI/HA film system could easily be adapted to serve as a coating for stents, orthopaedic implants or 3D tissue engineering scaffolds, thus making it an attractive candidate for use in a variety of gene delivery applications.

## 6.6 Acknowledgements

The authors would like to thank L. Mongeon for assistance with SEM imaging, V. Sivakumar for assistance with DNA release studies, and Dr. H. Durham for access to bacterial work facilities. This work was funded by a National Science and Engineering

Research Council of Canada Discovery Grant, and the Canadian Institutes of Health Research Regenerative Medicine Grant. C A. Holmes is supported by a National Science and Engineering Research Council of Canada Graduate Scholarship.

# Chapter 7: Optical Coherence Phase Microscopy for Non-Invasive, Label-Free Monitoring of Tissue Structure and Viability in 3D Tissue Engineering Scaffolds

One of the main challenges in developing inductive tissue engineering systems is assessing cellular growth and health within 3D scaffolds in a non-destructive manner. As a sub-objective of this thesis work, we validated that optical coherence tomography (OCT) could be used to image tissue structure and viability within our scaffold systems. OCT is a label-free, non-invasive, clinical imaging technique which is beginning to be applied to tissue engineering applications, mainly for structural imaging. However, we and others have begun to develop variations on OCT imaging in order to enable functional imaging. In a previous study, we demonstrated that phase fluctuations associated with cell viability can be recorded via optical coherence phase microscopy (OCPM). Here we build upon those results to demonstrate that OCPM can enable *in situ*, non-invasive, label-free imaging of tissue structure and viability within 3D scaffolds. We image two cell types seeded within two distinct scaffold systems with different architectures. We compare fluctuation imaging results with those of fixed cells and with viability assessments made via fluorescent live/dead labelling.

The results of these studies are presented in the following manuscript entitled "Optical coherence phase microscopy enables label-free monitoring of tissue growth and viability in tissue engineering scaffolds" which was accepted in 2012 by the Journal of Tissue Engineering and Regenerative Medicine, and is currently in press.

**Optical coherence phase microscopy enables label-free monitoring of tissue growth and viability in tissue engineering scaffolds**

Holmes, Christina, [1] Tabrizian, Maryam[1, 2], and Bagnaninchi Pierre O.[3]

[1] Department of Biomedical Engineering, [2]Faculty of Dentistry, McGill University, Montreal, H3A 2B4, Canada, [3]MRC Centre for Regenerative Medicine, University of Edinburgh, Edinburgh, EH16 4SB, Scotland

## 7.1 Abstract

As the field of tissue engineering continues to progress, there is a deep need for non-invasive, label-free imaging technologies which can monitor tissue growth and health within thick 3D constructs. Amongst the many imaging modalities under investigation, optical coherence tomography (OCT) has emerged as a promising tool, enabling non-destructive *in situ* characterization of scaffolds and engineered tissues. However, the lack of optical contrast between cells and scaffold materials using this technique remains a challenge. In this communication, we show that mapping the optical phase fluctuations resulting from cellular viability allows for the distinction of live cells from their surrounding scaffold environment. Viability imaging was performed via a common-path Optical Coherence Phase Microscope (OCPM); an OCT modality which has been shown to be sensitive to nanometer level fluctuations. More specifically, we examined the development of human adipose derived stem cells and/or murine pre-osteoblasts within two distinct scaffold systems; commercially available alginate sponges and custom microfabricated poly(D,L-lactic-co-glycolic acid) fibrous scaffolds. Cellular viability is demonstrated as an endogenous source of contrast for OCPM, enabling real-time, label-free monitoring of 3D engineered tissue development.

## 7.2 Introduction

The development of non-invasive, label-free 3D imaging technologies is vital to the future progress of tissue engineering and regenerative medicine. Assessment of *in vitro* engineered tissues requires accurate monitoring of tissue growth, morphology, viability and bioactivity over time within 3D constructs. This challenge becomes even greater when one considers the thickness of the tissue constructs, the need for high imaging resolution, and the wide variety of cell types and scaffolding materials involved. As no one method can currently meet all these criteria, a combination of different techniques is typically used to evaluate various aspects of engineered tissue structure and health (269). The majority of these procedures are destructive end-point tests, such as histology, scanning electron microscopy (SEM), immunohistochemistry, and metabolic assays. These require the use of staining agents and sample processing and sectioning, thus preventing time-course studies and requiring numerous samples at great cost. The few techniques that do allow for real-time monitoring, such as confocal microscopy, are either limited in imaging penetration depth to a few hundred micrometres and/or require fluorescent labelling.

Optical coherence tomography (OCT) is an interferometric imaging modality (362, 363) that has emerged as a promising tool for 3D monitoring of engineered tissues. Achieving micrometre scale resolution at millimetre scale penetration depths, OCT has been established as a clinical standard in ophthalmology (410), with further medical applications under investigation in the areas of dermatology, oncology and cardiology

(411, 412). Operating under a similar principle as ultrasound imaging, with the exception of measuring delays in backscattered light instead of sound, OCT enables non-invasive, real-time, label-free imaging both *in vitro* and *in vivo* (412).

In the field of tissue engineering, OCT has been used to characterize scaffold architecture and porosity as well as to assess cell seeding, growth, and migration within hydrogels and scaffolds (367, 369-371, 413). However, with the exception of optically clear hydrogels, no clear optical contrast exists between cells and surrounding scaffold materials via OCT imaging.

One OCT variant, known as spectral domain optical coherence phase microscopy (OCPM), can achieve quantitative phase contrast images that enable single cell mapping and the detection of nanometer-level fluctuations (366). Recently, we developed a common-path optical coherence phase microscopy system with a sensitivity that enabled the recording of phase fluctuations associated with cell viability in 2D and 3D (374). Similarly, Dunkers *et al.* (375) monitored cell viability with optical coherence microscopy via measurement of intensity speckle fluctuation. Finally, Nolte and collegues used digital holographic optical coherence imaging to record optical fluctuations in multicellular tumour spheroids and demonstrated that these fluctuations arise from cellular and intracellular motility (414, 415).

Here we demonstrate that the optical fluctuations arising from live cells can be used as an endogeneous source of contrast between cells and surrounding scaffold materials. We

performed OCPM fluctuation imaging in 3D for a variety of engineered tissues, utilizing two distinct scaffold systems with different architectures and two cell types. Our results show that fluctuation imaging enables label-free, non-invasive monitoring of cell growth and viability within various polymeric scaffold systems.

## 7.3 Materials and Methods

### *7.3.1 Optical Coherence Phase Microscopy (OCPM)*:

The OCPM system used in this study (Fig 7.1A) was in a common path set-up, utilizing a strong reflection within the sample arm as a reference, rather than a separate reference arm as in a conventional Michelson interferometer. This resulted in an increase in phase stability as common noise was rejected more efficiently. The system, as described previously (374), was based upon a commercial OCT engine (Callisto, Thorlabs) with a superluminescent diode (SLD) light source centred around 930 nm with a FWHM bandwidth of 90 nm, providing a tissue resolution of approximately 5 μm. The light was coupled out of the OCT engine into a single mode fibre and collimated onto a pair of galvanometers for raster scanning. The custom laser scanning head (LSH) was attached to an inverted microscope (SPi95, Brunel) and delivered to a custom scanning lens. A spectrum was measured at each x,y point of the sample at a rate of 1200 spectra per second, with 500 A scans collected in the x direction. Fast fourier transforms of the spectra yielded both intensity and phase information along the depth, z. Intensity data were used to perform in-depth microstructural imaging. In addition, we recorded phase fluctuation measurements by collecting several successive B scans at the same location, and the maximum and standard deviation of the first time derivative of the phase, i.e. time fluctuations, were analysed over the acquisition time interval.

### ***7.3.2 Scaffolds and Cell Seeding*:**

Cell growth and viability were imaged and analyzed in two polymeric scaffolds systems with very different architectures. One was a commercially available alginate sponge, Algimatrix (Gibco), with a pore size range of 50-200 μm. The other was a custom microfabricated fibrous poly(D,L-latctic-co-glycolic acid) scaffold, described previously (33), with a layered mesh-like structure and an average pore size of approximately 260 μm. Two different cell types were employed in these scaffold-seeding experiments: human adipose derived stem cells (ADSCs, Invitrogen) cultured in low serum MesenPRO RS media supplemented with 2mM L-glutamine and MesenPRO RS growth supplements (Invitrogen); and murine MC3T3-E1 pre-osteoblasts (ATCC) grown in alpha minimum essential medium supplemented with 10% fetal bovine serum, 1% penicillin/streptomycin and 2 mM L-glutamine (Invitrogen). Both cell lines were incubated at 37°C in a humidified atmosphere of 5% $CO_2$ until seeded onto scaffolds.

Algimatrix scaffolds in 96 well tissue culture plates were conditioned overnight in ADSC media and statically seeded with ADSCs, according to manufacturer protocols, at a density of 3 x $10^5$ cells/scaffold in a volume of 100 μL of ADSC media supplemented with 10% (v/v) Algimatrix Firming Buffer (Gibco). After 10 min of incubation, a further 100 μL of ADSC media without firming buffer was added to each well. The next day, the cell-seeded scaffolds were transferred to a non-adherent 24 well plate and 1 mL of fresh ADSC media was added.

Meanwhile, PLGA scaffolds were sterilized prior to cell seeding via immersion in 70% ethanol for 30 min, followed by two rinses in phosphate buffered saline and subsequent UV irradiation for 30 min. PLGA scaffolds in non-adherent 24 well plates were also conditioned overnight in either ADSC or MC3T3 media and subsequently seeded with either ADSCs or MC3T3s at a density of 1 x $10^6$ cells/scaffold in a volume of 50 μL of the appropriate media. After 4 hours of incubation, a further 1.5 mL of the appropriate media was added to each well. The following day, cell-seeded scaffolds were transferred to a fresh non-adherent 24 well plate and 1.5mL of fresh media was added. Both types of scaffolds were cultured for a period of at least 7 days with media exchanges performed every other day.

### ***7.3.3 Live/Dead Staining and Confocal Microscopy*:**

In order to confirm that the cells scanned via OCPM were viable, day 7 MC3T3-seeded PLGA scaffolds were stained with calcein-AM and ethidium homodimer-1 (LIVE/DEAD® Viability/Cytotoxicity Kit, Invitrogen, Canada) to label live and dead cells, respectively. Live/dead cell imaging was performed using a Zeiss LSM 510 confocal microscope.

## 7.4 Results and Discussion

Cell growth and viability within PLGA and AlgiMatrix scaffolds were monitored over time via OCPM scans performed every other day. 3D images of a 1 $mm^3$ volume of scaffold morphology were produced by acquiring successive cross sectional 2D scans via laser scanning. Looking only at the 3D light intensity images of MC3T3 growth in PLGA scaffolds on day 1 (Fig 7.1B) and day 7 (Fig 7.1C), changes in construct morphology over time are evident.

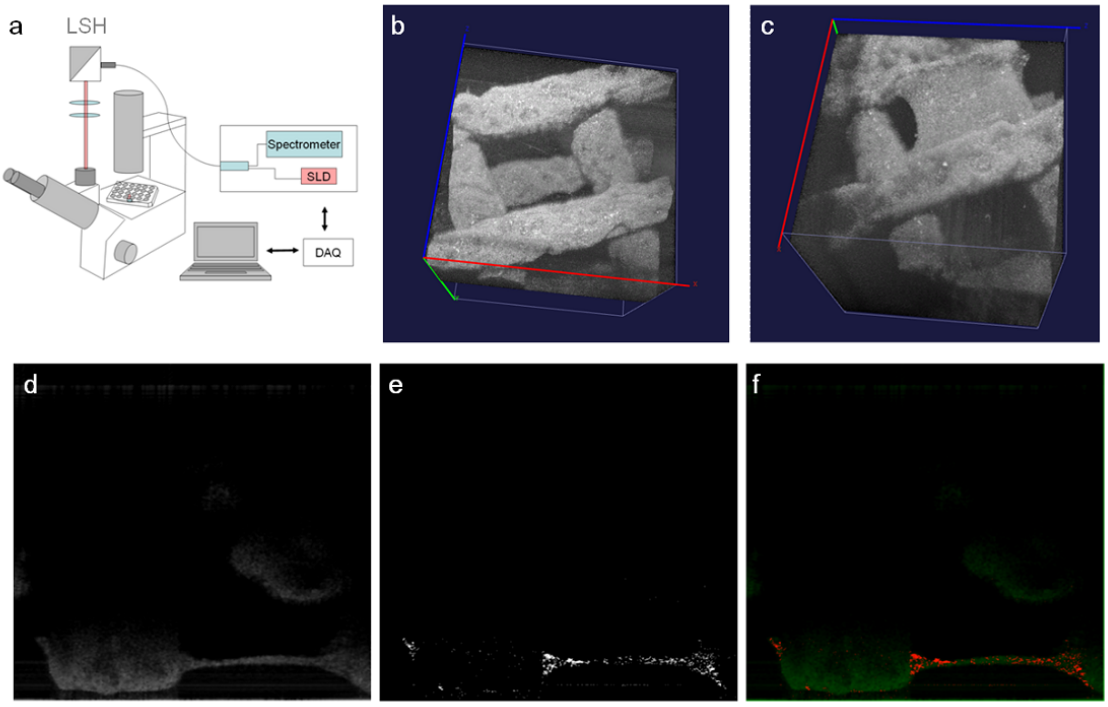


**FIGURE 7.1: a) Schematic of the optical coherence phase microscope (OCPM) in inverted mode. OCPM produces 1$mm^3$ 3D pictures of scaffolds by acquiring successive cross sectionional images by laser scanning from beneath the sample. b) A PLGA printed scaffold seeded with MC3T3 cells at day 1 and c) day 7. At day 7 cells started to create a tissue-like structure. d) Corresponding 1mm x 1mm cross-sectional image in intensity mode. No contrast was observed between the cells and the scaffold. e) Phase fluctuation imaging highlighted the cell layer. f) Cell viability imaging is produced by combining the intensity on the green channel and phase fluctuation imaging mode on the red channel. Cell vitality is an endogenous source of contrast that enables label-free and noninvasive monitoring of live cells within 3D scaffolds.**

On the first day, the underlying mesh-like 3D structure of the fibrous scaffold is quite clear. In places one can even discern the micro-porosity, due to salt-leaching, within the polymeric strands themselves. Meanwhile, at this early time point it is difficult to distinguish the pre-osteoblast cells from the polymeric strands on which they are growing, as the image contrast between the two is low. The cells at this stage are mostly apparent as small bulges around the strands.

By contrast, at day 7 the gaps between polymer strands are becoming filled with tissue sheets and projections, indicating substantial cell growth. Although there is much higher tissue volume at this stage, when one observes a 2D cross-sectional light intensity scan of the same scaffold (Fig 7.1D), there is still very low contrast between the cells and the polymeric material, making it particularly difficult to discern the cells where they are attached to the strands. The phase fluctuation scans of that same region of the scaffold (Fig. 7.1E), however, render the cell layer apparent. By overlaying the intensity image (green channel, Fig. 7.1F) and the phase fluctuation image (red channel, Fig. 7.1F), we can map cell viability to tissue morphology without the need for additional instrumentation or contrast agents. Cellular viability within day 7 MC3T3-seeded PLGA scaffolds was confirmed via live/dead staining and confocal microscopy. A representative Z-stack series of images (Fig. 7.2) indicates that, while there is some cell death within these scaffolds, most pre-osteoblasts remained viable.

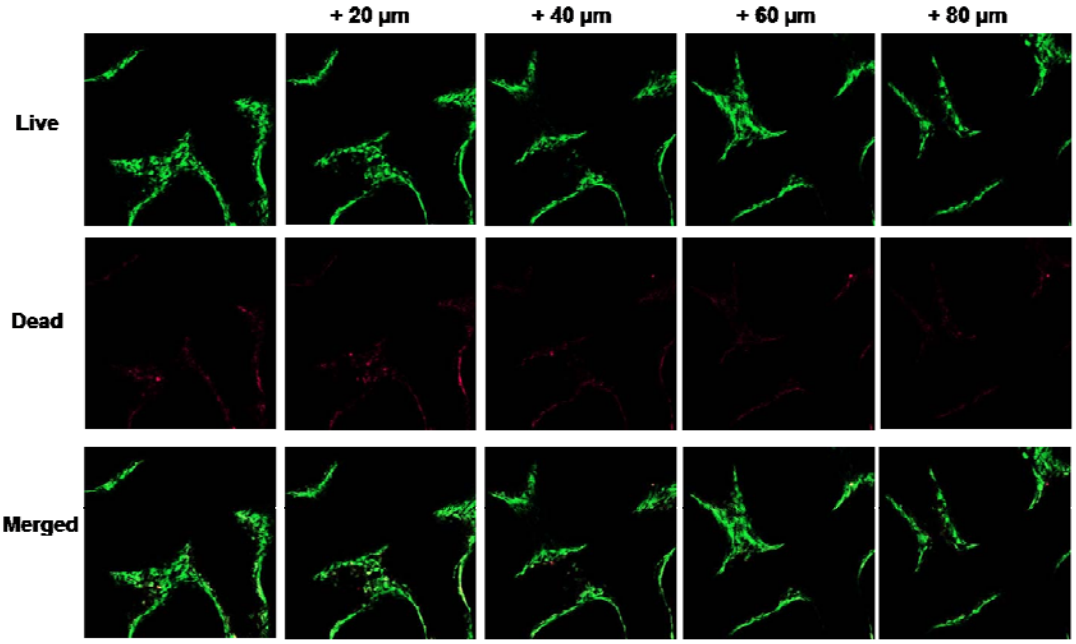


**FIGURE 7.2: Live/Dead (calcein/ethidium) confocal z-stack images (increasing in depth as indicated from left to right) of MC3T3 cells after 7 days growth on PLGA printed scaffolds. Scaffolds were imaged from beneath the sample to a depth of around 100 µm using a 10 x objective. Scan size approximately 1 mm x 1 mm.**

Using ADSCs, we have previously shown that the phase fluctuations recorded via OCPM likely correspond to nanometre-scale micromotion associated with viable cells (374). In order to confirm that these findings were not cell type dependent, we compared PLGA scaffolds containing live and dead MC3T3 pre-osteoblasts. Cell-seeded scaffolds were scanned on day 14 both before (Fig. 7.3 C, G, K) and after (Fig. 7.3 D, H, L) fixation. Light intensity scans of scaffold morphology showed little distinction between live (Fig. 6.3 C) and fixed (Fig. 7.3 D) cells. Phase fluctuation images, however, highlighted significant differences with live cells (Fig. 7.3 G) displaying strong fluctuation signals, while fixed cells (Fig 3H) showed only residual noise. Overlaying the images (Fig. 7.3 K, L), it is apparent that cellular viability itself serves as an endogenous source of contrast that enables label-free monitoring of live cells within 3D scaffolds.

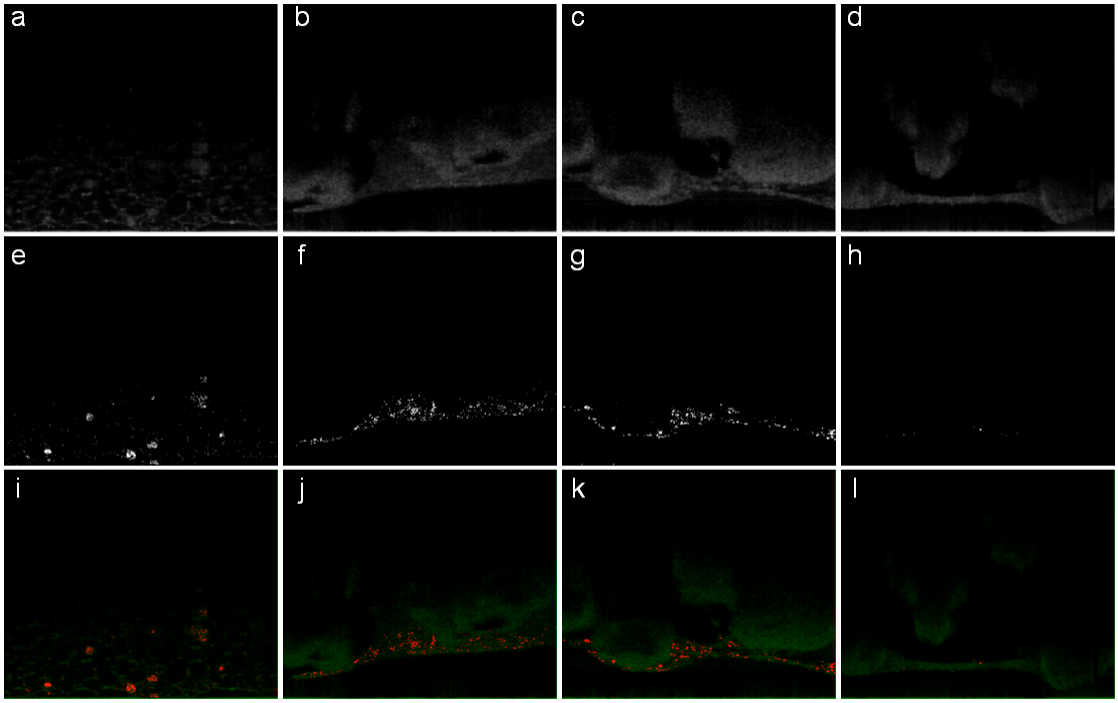


**FIGURE 7.3: OCPM intensity imaging (a-d) of live adipose derived stem cells cultured in Algimatrix (a), a commercial alginate porous scaffold, and in microplotted PLGA scaffolds (b) and compared to live (c) and fixed (d) MC3T3 cells in PLGA scaffolds, which clearly displayed the in-depth microstructure of the cell scaffold constructs. *A priori* knowledge of the blank scaffold structure enables an estimation of the cell distribution. The corresponding phase fluctuation imaging (e-h) highlighted specific areas of the culture that were found to correspond to live cell distribution, distinguishing it from the fixed scaffold (h) where only residual noise was observed. This was clearly confirmed by cell fluctuation mapping (i-l) demonstrating the potential of OCPM for label free and live imaging of tissue engineering structures. All images are 1 mm x 1 mm.**

To further demonstrate the flexibility of fluctuation imaging, we imaged ADSCs seeded on our PLGA scaffolds (Fig. 7.3 B, F, J) as well as on architecturally and mechanically different Algimatrix matrices (Fig. 7.3 A, E, I). The ADSCs produced a thicker tissue within the PLGA scaffolds than the MC3T3 cells had, as was apparent in both the light intensity (Fig. 7.3 F) and phase fluctuation (Fig. 7.3 J) scans. As observed via the light intensity image (Fig. 7.3A), the morphology of the AlgiMatrix scaffold was significantly

different from the PLGA scaffolds, appearing sponge-like with thin interconnected walls. Similar to the other system, the light intensity contrast between the cells and matrix material was low, with the cells mainly distinguishable as brighter clusters within the pores. Again, it is the phase fluctuation image that emphasizes the location of the live cells (Fig. 7.3 E), with the alginate material of the scaffold itself providing little to no signal. Combining phase fluctuation and light intensity scans in either engineered tissue (Fig. 7.3 I, J) once more illustrates the promise of fluctuation imaging to provide non-invasive, real-time, label-free mapping of cell viability to overall 3D tissue morphology.

As indicated by Figure 7.1 B and C, 3D OCPM scans offer the capability of quantifying changes in tissue volume and cell–to-scaffold volume ratio over time provided initial scans of un-seeded scaffolds are performed. However, the estimated changes in total cell volume will also include any non-viable cells within the tissue. By contrast, fluctuation imaging allows for the quantification of viable cell volume over time without the need for prior blank scaffold scanning, as the scaffolding material itself yields only a residual noise signal which can be corrected.

## 7.5 Conclusions

Overall, we have demonstrated that fluctuation imaging, as achieved by our optical coherence phase microscopy (OCPM) system, creates an endogenous cell to scaffold contrast that enables real-time, non-invasive, label-free mapping of cellular viability to 3D tissue morphology. We have further demonstrated that this system can be used in a variety of engineered tissue systems by monitoring pre-osteoblasts and adipose derived stem cells in two distinct scaffold systems composed of different polymers and possessing dissimilar architectures. These results, alongside the capability for quantification of viable cellular volume, highlight the great potential of motility imaging as a tool for monitoring 3D tissue growth and health within complex tissue engineered constructs.

## 7.6 Acknowledgements

Pierre O. Bagnaninchi gratefully acknowledges support from the research councils UK for his fellowship and funding from EPSRC (EP/G030871/1). This research was also supported by a Le Fonds Québécois de la Recherche sur la Nature et les Technologies travel grant, a National Science and Engineering Research Council of Canada Discovery Grant, and a Canadian Institutes of Health Research Regenerative Medicine Grant.

# Chapter 8: Glycol-Chitosan/Hyaluronic Acid Film-Based Coatings Support Cell Growth and Viability on 3D Polymeric Scaffolds and Enable Scaffold-Based Gene Delivery

As the final phase of this thesis work, the glycol-chitosan/hyaluronic acid film system was extended for use in inductive tissue engineering systems. First we demonstrated that Glyc-CHI/HA films could be successfully deposited onto a 3D model, porous scaffold system microfabricated from poly(lactic-co-glycolic acid) (PLGA). We then confirmed that these LbL-coated scaffolds could successfully support *in vitro* cell adhesion, growth and viability for a period of at least two weeks via live/dead staining coupled with confocal microscopy and optical coherence phase microscopy (OCPM). Lipoplexes, formed by complexing Lipofectamine2000$^{TM}$ and plasmid DNA encoding the fluorescent marker gene EGFP, were then incorporated within the LbL coating in order to enable scaffold-based gene delivery. The *in vitro* transfection efficiency and cytotoxicity of these coated scaffolds was then assessed for HEK293 human embryonic kidney cells via fluorescence microscopy and fluorescence activated cell sorting (FACS) analysis, and compared that that of uncoated control scaffolds with surface adsorbed lipoplexes.

The results of this work are presented here in the manuscript entitled "Glycol-chitosan/hyaluronic acid polyelectrolyte multilayer coatings for tissue engineering and scaffold-based non-viral gene delivery" which will be submitted in 2013 to the journal Biomaterials.

**Polyelectrolyte film-based coatings consisting of glycol-chitosan and hyaluronic acid support cell growth and viability on 3D polymeric scaffolds and enable scaffold-based gene delivery**

Holmes, Christina,[1] Bagnaninchi Pierre O.[3] and Tabrizian, Maryam*[1,2],

[1] Department of Biomedical Engineering, [2]Faculty of Dentistry, McGill University, Montreal, H3A 2B4, Canada, [3]MRC Centre for Regenerative Medicine, University of Edinburgh, Edinburgh, EH16 4SB, Scotland

## 8.1 Abstract

Although a variety of delivery strategies are being explored in the field of inductive tissue engineering, the milder processing conditions typically required often restrict the range of scaffold properties and architectures that can be produced. Layer-by-layer (LbL) deposition is a simple technique which can overcome many of these limitations and has been extensively used for controlled release of proteins, drugs, and genes from microcapsules and 2D films. Here we demonstrate that a polyelectrolyte multilayer film system composed of glycol-chitosan (Glyc-CHI) and hyaluronic acid (HA) can be used to coat 3D microfabricated polymeric tissue engineering scaffolds. These LbL coated scaffolds are shown to support *in vitro* cell adhesion, growth, and viability for a period of at least two weeks at levels similar to or higher than uncoated controls. These polyelectrolyte multilayer coatings were then further adapted for non-viral gene delivery applications via incorporation of gene delivery lipoplexes. Scaffold-based delivery of the EGFP marker gene was successfully demonstrated *in vitro* in HEK293 cells for Glyc-CHI/HA coated scaffolds, which exhibited significantly higher transfection efficiencies than uncoated control scaffolds with surface adsorbed lipoplexes. These results show the great potential of glycol-chitosan/hyaluronic acid polyelectrolyte multilayer films for a variety of gene delivery and inductive tissue engineering applications.

## 8.2 Introduction

In order for the vast therapeutic potential of tissue engineering to be realized, three-dimensional (3D) scaffolds that can direct cell behaviour and tissue architecture must be realized. Scaffold-based gene delivery offers several potential advantages as an approach to inductive tissue engineering. Compared to systemic gene therapy approaches, gene-releasing scaffolds localize transfection to the cells directly in the implant area, increase transfection efficiency, and prolong vector delivery (416). Meanwhile, conserving DNA sequence information is easier than preserving the 3D structure of protein growth factors, thus leading to greater flexibility in scaffold design parameters. Additionally, by inducing host cells to locally produce growth factors, the resulting proteins are more likely to possess the appropriate conformation and post-translational modifications, and thus greater bioactivity, than the recombinant proteins typically released from scaffolds. Furthermore, the ability to deliver genes that encode for transcription factors and other intracellular proteins, as well as the capability to achieve tissue-specific expression, broadens the cellular processes that can be targeted.

To date, a wide variety of methods have been explored to control scaffold-based delivery of naked plasmids, or DNA incorporated within adenoviral vectors, lipoplexes, or polyplexes (reviewed in (64, 65)). Bulk scaffold incorporation of naked and condensed plasmids can be achieved via gas foaming (417, 418), encapsulation within hydrogels (419), electrospinning (420), thermally induced phase separation (421), or the inclusion of DNA-loaded polymeric micro- or nano-spheres (77, 422). These techniques generally result in systems characterized by an initial burst release of DNA followed by slower

release that is controlled by the diffusion and degradation rate of the matrix. Alternatively, non-specific surface adsorption of gene delivery vectors onto scaffold surfaces is also commonly performed, with surfaces often modified in order to encourage vector-surface interactions (69). However, these strategies generally lead to low levels of gene loading and poor control of release kinetics. In order to provide more control over the DNA release rate, direct immobilization of gene delivery vectors to scaffold surfaces via covalent cross-linking, or approaches involving antibody/antigen or biotin/avidin binding are also under investigation (73, 120, 423).

Layer-by-layer (LbL) deposition, a technique which involves the sequential surface assembly of alternating layers of oppositely charged polymers, i.e. polyelectrolytes (PEs) (127), has been widely used for the controlled release of drugs, bioactive proteins, and genes from 2D films and microcapsules (122). Naked plasmid DNA, PEI- and cyclodextran- complexed plasmids (249, 250), and adenoviral vectors (251) have been incorporated into a variety of polyelectrolyte multilayer designs (further reviewed in (124)), which have demonstrated successful *in vitro* transfection. While results vary greatly between systems, generally, lower transfection levels were observed when the vector was embedded under greater numbers of PE layers, and an increase in the number of vector layers led to an increase in transfection efficiency. Careful selection of the PEs used and the layer architecture and chemistry employed enables both the tailoring of release kinetics and sequential delivery of several different genes (226, 249, 424).

As a technique that can be used with materials of nearly any type, shape or size, LbL deposition is beginning to be employed in 3D tissue engineering applications. The deposition of PE multilayers onto 3D synthetic polymer scaffolds has been characterized for several systems, with a few studies extending to scaffold-based delivery of biofactors. LbL deposition of PEI and gelatin onto PLLDA scaffolds, for example, improved *in vitro* MC3T3 cell adhesion (260, 261), while chondroitin sulfate/collagen multilayers deposited onto PLLA scaffolds improved *in vitro* chondrocyte attachment, proliferation, and GAG synthesis (262). Similarly, PLL/HA multilayers formed on photo-crosslinked HA hydrogels modified gel swelling and mechanical properties and resulted in increased fibroblast cell adhesion and spreading (263). Meanwhile, 3D printed β-tricalcium phosphate/polycaprolactone scaffolds were coated with LbL films consisting of a poly (β-aminoester) ("poly 2"), chondroitin sulphate (CS), and BMP-2, resulting in a system that successfully induced *in vivo* bone formation when implanted intramuscularly in rats (266). Most importantly, electrospun poly(L-lactic acid) fibrous mats coated with multilayer films formed of PEI and plasmid DNA encoding luciferase demonstrated *in vitro* transfection of COS cells, with increasing levels of transfection found with an increased number of layers (265). LbL deposition thus holds great promise for enabling the controlled delivery of genes, and other bioactive molecules from three-dimensional scaffold surfaces, with the added advantage of preserving bulk material properties and hence enabling a wider array of scaffold properties to be produced.

We previously developed a polyelectrolyte film system consisting of glycol-modified chitosan (Glyc-CHI) and hyaluronic acid (HA) which exhibited significantly improved

cellular adhesion compared to the well-studied unmodified chitosan/HA system, while maintaining many of the advantageous physical properties (402). This Glyc-CHI/HA film system was then adapted to incorporate gene delivery lipoplexes and was shown to successfully transfect cells *in vitro* for a period of at least one week (Chap. 5). Here we demonstrate that Glyc-CHI/HA polyelectrolyte multilayers can be used to coat 3D polymeric tissue engineering scaffolds microfabricated from poly(lactic-co-glycolic acid) (PLGA) (33). Pre-osteoblast cell adhesion, growth and viability in these LbL coated scaffolds was assessed via live/dead staining coupled with confocal microscopy and compared to uncoated control scaffolds. Viability and overall tissue growth within coated and uncoated scaffolds were also monitored using optical coherence phase microscopy (OCPM); a novel, non-invasive, label-free imaging technique, which we have previously demonstrated can map viability via phase fluctuations arising from cellular motility (374)(Chap. 6). Finally, we incorporated gene delivery lipoplexes, consisting of Lipofectamine2000$^{TM}$ and plasmid DNA encoding enhanced green fluorescent protein (EGFP), within these scaffold coatings and assessed their *in vitro* transfection efficiency and cytotoxicity in the HEK293 model cell line. Comparisons with uncoated control scaffolds with surface-adsorbed lipoplexes were also performed.

## 8.3 Materials and Methods

### *8.3.1 Materials*

Hyaluronic Acid (HA) with a molecular weight of 74 kDa was purchased from Lifecore Biomedical (Chaska, MN, USA). Glycol-Chitosan (Glyc-CHI) with a molecular weight of approximately 80 kDa (via GPC) was purchased from Sigma-Aldrich. Poly(DL-lactide-co-glycolide) acid (PLGA; 85 Mole% DL-lactide, 15 Mole% glycolide) with a molecular weight ranging from 92 -142 kDa was obtained from Lakeshore Biomaterials ( USA). Mouse pre-osteoblast MC3T3-E1 (subclone 14) cells and HEK293 human embryonic kidney cells were supplied by American Type Culture Collection (ATCC, Manassas, VA).

The plasmid encoding enhanced green fluorescent protein (pEGFP-C3) was acquired from Clontech (CA, USA). Lipofectamine2000$^{TM}$ and subcloning efficiency DH5α competent E. coli cells were obtained from Invitrogen (CA, USA).

### *8.3.2 Scaffold Fabrication*

Three-dimensional (3D) scaffolds were fabricated from poly(DL-lactide-co-glycolide) acid (PLGA) using an XYZ bioplotter system (Envisiontec, Germany), as previously described (33, 386, 387). The PLGA was dissolved in methyl ethyl ketone (Sigma) at a 1:1 ratio of PLGA to solvent and subsequently mixed with 15% w/w sodium chloride (NaCl), sieved to yield a particle size distribution of 53-63 nm. The PLGA solution was transferred to the plotting cartridge and was dispensed layer by layer, forming a $0^o/90^o$

strand structure 40 x 40 mm-wide and 3.6 mm-thick using a CAD file as a template. 250 μm-diameter dispensing tips were used to yield a strand diameter (D) of 150 μm at a dispensing speed of 165 mm/s (425). The layers were overlaid to give a strand thickness of 120 μm and a layer spacing distance of 300 μm. Individual scaffolds were punched from the initial scaffold brick using a biopsy punch, yielding scaffold discs 8 mm in diameter and 3.6 mm-thick. Resulting scaffolds were previously found to exhibit a porosity of approximately 53% and an average pore size around 260 μm in the dry state (33). These scaffolds were then immersed in water overnight in order to leach out the salt particles, air-dried for 24 h, and vacuum-dried for 48 h to allow for the complete evaporation of the solvent/water.

### ***8.3.3 Preparation of FITC-labelled Glyc-CHI***

All steps were performed under light protection conditions and adapted from Son et al, 2003. Glycol-chitosan and FITC were dissolved in 0.5 M sodium carbonate buffer at a concentration of 10 mg/mL and 5 mg/mL, respectively. The FITC solution was added drop-wise to the glycol-chitosan and stirred overnight at room temperature. The resulting solution was dialyzed against MillQ water using a snakeskin membrane (MWCO 12,000) for 3 days. The dialyzed solution was then freeze-dried for 2 days.

### ***8.3.4 Quartz Crystal Microbalance with Dissipation***

All polyelectrolyte solutions were prepared at a concentration of 2 mg/mL in 0.1 M NaCl buffer, pH=6.0, and filtered sterile. Layer-by-layer (LbL) film build-up for [Glyc-CHI/Ha]$_5$ Glyc-CHI films was monitored *in situ* on crystals spin-coated with PLGA via

quartz crystal microbalance with dissipation (QCM-D), using a Q-Sense D 300 unit (Q-sense, Sweden). Changes in frequency (Δf) and energy dissipation (ΔD) were measured at the fundamental frequency of the crystal (f = 5 MHz) as well as at the third, fifth, and seventh overtones (15, 25, and 35 MHz, respectively). Polyelectrolyte films were formed by injecting 400 µl of the polyelectrolyte solution (Glyc-CHI or HA) into the measuring cell, allowing 10 min for adsorption, followed by rinsing with 2000 µl of 0.1 M NaCl solution. This procedure continued until 5 bilayers were deposited, with an additional terminating layer of Glyc-CHI. The film thickness was calculated from the frequency and energy dissipation data using QTools software and the Voigt-based viscoelastic model proposed by Voinova et al (170). For these calculations, the polyion film density was assumed to be 1.2 g/cm$^3$ and the 0.1 M NaCl buffer fluid density and viscosity were assumed to be 1.004 g/cm$^3$ and 9.03 x $10^{-4}$ kg/ms, respectively (391).

### ***8.3.5 Polyelectrolyte Multilayer Film Coating of Scaffolds***

All polyelectrolyte solutions were prepared at a concentration of 2 mg/mL in 0.1 M NaCl buffer, pH=6.0, and filtered sterile. Prior to coating, scaffolds were immersed in a 70% ethanol solution for 30 min, rinsed twice in phosphate buffered saline (PBS) and then UV sterilized for 30 min. Scaffolds were then immersed overnight in 1.5 mL of Gly-CHI solution within 24 well tissue culture plates (Falcon), and rinsed twice in 0.1 M NaCl buffer (pH = 6.0). Up to 3 scaffolds at a time were then transferred into a sterile 10 mL syringe for further rinsing and layer-by-layer deposition. Use of the syringe entirely immersed the scaffolds in liquid and allowed for the easy removal of any air bubbles. In order to rinse or deposit a given polyelectrolyte, 1.5 mL/scaffold of the relevant solution

was aseptically drawn into the syringe via a needle. The needle was then removed, the syringe was inverted and any air was manually evacuated. The scaffold was then left to immerse in the polyelectrolyte solutions for 10 min per step, with two rinsing steps in between deposition of subsequent HA or Glyc-CHI layers. This process was repeated until [Glyc-CHI/HA]$_5$Glyc-CHI films were coated onto the PLGA scaffolds.

### ***8.3.6 Preparation of Gene Delivery Scaffolds***

Gene delivery lipoplexes ("Lipo") were prepared as at room temperature in a 0.1 M NaCl buffer solution adjusted to pH 6.0, at a ratio of 2 μL of Lipofectamine 2000$^{TM}$ to 1 μg of pEGFP. Briefly, two solutions of equal volume (25 μL) were prepared, one containing either 4, 8 or 12 μg of pEGFP DNA, and the other containing 8, 16 or 24 μL of Lipofectamine 2000$^{TM}$, and left to stand for 10 min. These two solutions were then combined and incubated at room temperature for 15 minutes, before immediate use in the formation of scaffold coatings.

Gene delivery scaffolds were produced via LbL-coating of PLGA scaffolds in manner similar to that described above. After deposition of [Glyc-CHI/HA]$_5$Glyc-CHI films, coated PLGA scaffolds were transferred to sterile 24-well suspension culture plates and gene delivery lipoplexes in a total volume of 50 μL were allowed to adsorb for 2 hours. Each scaffold was then rinsed twice in 0.1 M NaCl buffer solution and aseptically transferred back into 10 mL syringes for further layer-by-layer deposition. Scaffolds were thus coated with [Glyc-CHI/HA]$_5$Glyc-CHI-Lipo-[Glyc-CHI/HA]$_2$Glyc-CHI films. Gene

delivery lipoplexes were similarly adsorbed onto uncoated PLGA scaffolds as controls for comparison.

### ***8.3.7 Cell Culture and Scaffold Cell Seeding***

Mouse pre-osteoblast MC3T3-E1 cells were grown in alpha minimum essential medium (ά-MEM, Gibco, Invitrogen Corporation) supplemented with 10% fetal bovine serum (FBS, Gibco, Invitrogen), 1% penicillin/streptomycin (Invitrogen), 0.2 mM L-ascorbic acid (Sigma) and 2 mM L-glutamine (Sigma). HEK293 human embryonic kidney cells were grown in Dulbecco's minimum essential medium (DMEM, ATCC) supplemented with 10% fetal calf serum (FCS, ATCC) and 1% penicillin/streptomycin (Invitrogen). All cells were incubated at 37°C in a humidified atmosphere of 5% $CO_2$.

Prior to coating and cell seeding, uncoated scaffolds were immersed in a 70% ethanol solution for 30 min, rinsed twice in phosphate buffered saline (PBS) and then UV sterilized for 30 min. Coated scaffolds were prepared as mentioned above and transferred to non-adherent, 24-well suspension culture plates (Greiner Bio-one, VWR). Each scaffold was seeded with 1 x $10^6$ MC3T3 cells or 2 x $10^6$ HEK293 cells in a volume of 50 μL, which was manually pipetted onto the scaffold, and incubated at 37°C in a humidified atmosphere of 5% CO2. After 4 hours, 1.5 mL of the appropriate culture medium was added.

### *8.3.8 Evaluation of Cell Seeding Efficiency*

In order to estimate MC3T3 cell seeding efficiency after 24 hours, scaffolds were transferred to fresh wells, lightly rinsed in PBS, and trypsinized for 10 minutes. Fresh media was then adeed and scaffolds were repeatedly flushed via manual pipetting in order to dislodge remaining cells. The resulting cell suspensions were spun down at 1000 rpm for 5 min, as were the scaffolds. The resulting pellets were re-suspended in serum-free, phenol-red-free ά-MEM media (Gibco, Invitrogen) and recombined in a total volume of 500 μL as the 'seeded' fraction. The cells which did not adhere to the scaffolds, i.e. those from the original wells, were also collected via trypsinization, spun down at 1000 rpm for 5 min, and re-suspended in 500 μL of serum-free, phenol-red-free ά-MEM media as the 'non-adherent' fraction. The number of viable cells in each fraction was determined using the Vybrant MTT Cell Proliferation Assay Kit (Invitrogen) according to manufacturer instructions. Analysis was performed with a μQuant™ microplate spectrophotometer (Bio-Tek Instruments, Winooski, VT) at an absorbance of 570 nm. The seeding efficiency was then determined by comparing the adsorbances of both fractions.

### *8.3.9 Live/Dead Staining and Confocal Microscopy*

In order to confirm that MC3T3 cells within the scaffolds were viable, both coated and uncoated PLGA scaffolds were stained with calcein-AM and ethidium homodimer-1 (LIVE/DEAD® Viability/Cytotoxicity Kit, Invitrogen, Canada) at various time points to label live and dead cells, respectively. Live/Dead cell staining was performed according to manufacturers' instructions. Scaffold imaging was performed using a Zeiss LSM 510

confocal microscope. A series of z-stack images covering a penetration depth of approximately 100 μm was collected for a minimum of three regions per scaffold, with at least three scaffolds imaged per condition and time point. Estimation of the fraction of live and dead cells within the scaffolds was performed via z-stack optical sectioning analysis and measurement using ImageJ software (National Institutes of Health, NIH).

### *8.3.10 Fluorescence Microscopy*

Fluorescent images of scaffolds coated with fluorescently-labelled Glyc-CHI and of transfected HEK293 cells grown for 48 hours on coated and uncoated scaffolds were acquired with a stereoscopic zoom microscope (SMZ1500, Nikon) equipped with a high pressure mercury lamp (C-SHG1, Nikon; USA), the appropriate set of filters for fluorescein (FITC) and/or enhanced green fluorescent protein (EGFP) excitation and emission, and a digital camera (DXM1200F, Nikon) operated with QCapturePro 7 software.

### *8.3.11 Optical coherence phase microscopy (OCPM)*

The custom optical coherence phase microscope (OCPM) system used in this study was in a common path set-up, utilizing a strong reflection within the sample arm as a reference, rather than a separate reference arm as in a conventional Michelson interferometer. This resulted in an increase in phase stability as common noise was rejected more efficiently. The system, as described previously (374), was based upon a commercial OCT engine (Callisto, Thorlabs) with a superluminescent diode (SLD) light

source centred around 930 nm with a FWHM bandwidth of 90 nm, providing a tissue resolution of approximately 5 μm. The light was coupled out of the OCT engine into a single mode fibre and collimated onto a pair of galvanometers for raster scanning. The custom laser scanning head (LSH) was attached to an inverted microscope (SPi95, Brunel) and delivered to a custom scanning lens. A spectrum was measured at each x,y point of the sample at a rate of 1200 spectra per second, with 500 A scans collected in the x direction. Fast Fourier transforms of the spectra yielded both intensity and phase information along the depth, z. Intensity data were used to perform in-depth microstructural imaging. In addition, we recorded phase fluctuation measurements by collecting several successive B scans at the same location, and the maximum and standard deviation of the first time derivative of the phase, i.e. time fluctuations, were analysed over the acquisition time interval.

### ***8.3.12 Estimation of Scaffold DNA Content and Release***

PLGA scaffolds coated in $[Glyc\text{-}CHI/HA]_5Glyc\text{-}CHI\text{-}Lipo\text{-}[Glyc\text{-}CHI/HA]_4Glyc\text{-}CHI$ films, where lipoplexes were formed using 4 μg of plasmid DNA and 8 μL of Lipofectamine2000™, and uncoated control scaffold with surface adsorbed lipoplexes were placed within 24-well suspension culture plates (Greiner Bio-One) and incubated in 1 x PBS solution, pH = 8.4, at 37°C in a humidified atmosphere of 5% $CO_2$. The supernatant was removed and replaced with fresh PBS solution every second day for a period of one week. The amount of DNA within the supernatant was measured via the Quant-iT PicoGreen assay (Molecular Porbes, Invitrogen) according to manufacturer specifications. Briefly, an equal volume of 0.2 % w/v heparin sulphate (Sigma) solution

in 2 x TE buffer was added to the supernatant solution (final concentration of 0.1% w/v heparin in 1 x TE buffer) in order to decomplex the plasmid from the lipoplex, thus allowing the Picogreen stain access to the DNA. Fluorescence was then measured using a fluorescent plate reader (brand) using excitation and emission wavelengths of ~480 nm and ~520 nm, respectively. A series of DNA standards in 0.1% w/v heparin, 1 x TE buffer was produced and measured for reference.

In order to measure the quantity of DNA adsorbed onto/within the coated and uncoated scaffolds, the plasmid content of the lipoplex solution before and after deposition, as well as the DNA concentration of the rinsate was measured via the Picogreen assay as described above.

### ***8.3.13 Fluorescent Activated Cell Sorting Analysis***

HEK293 cellular transfection efficiency and cytotoxicity after 2, 4 or 7 days was assessed via fluorescent activated cell sorting (FACS). After removing the media, samples were rinsed once in PBS and cells were trypsinized for 5 min (0.05% trpsin-EDTA, Invitrogen). Next, 1 mL of 2% FBS in PBS was added to each well and cells were spun down at 250 x g for 5 min. Cells were then re-suspended in 300 µl of 2% FBS in PBS, transferred into FACS tubes, and 3 µl of 40 µg/mL propidium iodide (PI) was added to each sample. Samples were then directly FACS analyzed using the BD FacsCalibur system (BD Biosciences, USA), equipped with a 488 nm argon laser to excite both PI and GFP, with 10,000 cells per sample assessed. FACS data was subsequently analyzed for

GFP and PI expression using FlowJo software (Treestar Inc., OR, USA), using appropriate gates and controls.

### ***8.3.14 Statistics***

Statistical analyses of data were performed using the software package SPSS/PASW Statistics v18.0 (SPSS Inc., Chicago, IL). All data are presented as mean ± STD. The significance level was set at $p < 0.05$. As most data either failed the Shapiro-Wilk test for normality and/or the Levene's test for homogeneity of variance, or were of small sample size, Kruskal-Wallis non-parametric analyses were performed. In the case of OCPM phase fluctuation data, which passed both normality and homogeneity of variance tests, a two-way ANOVA test was performed, as well as independent sample T-tests for comparison.

## 8.4 Results

### *8.4.1 Polyelectrolyte Multilayer Coating of Three Dimensional PLGA Scaffolds*

Prior to scaffold coating, quartz crystal microbalance with dissipation (QCM-D) *in situ* monitoring of Glyc-CHI/HA film build-up was performed on PLGA-spin coated sensors to ensure the suitability of the multilayer system for the scaffold material substrate. Frequency shifts (Δf/v) and changes in energy dissipation (ΔD) over time for the build-up of $[\text{Glyc-CHI/HA}]_5\text{Glyc-CHI}$ multilayer films are presented in Fig. 8.1. As each polyelectrolyte was injected into the system, a decrease in frequency was observed corresponding to an increase in film mass, thus indicating layer-by-layer deposition. The overall pattern of film growth on the PLGA substrate closely resembled that observed previously on bare quartz-crystals (402). However, film thickness, as determined via the Voight model (170), was found to be slightly greater at approximately 160 nm compared to around 120 nm on bare quartz crystals, suggesting that the difference in substrate material had some effects. Overall, these results indicated that layer-by-layer deposition of polyelectrolyte films on scaffolds composed of PLGA would be feasible.

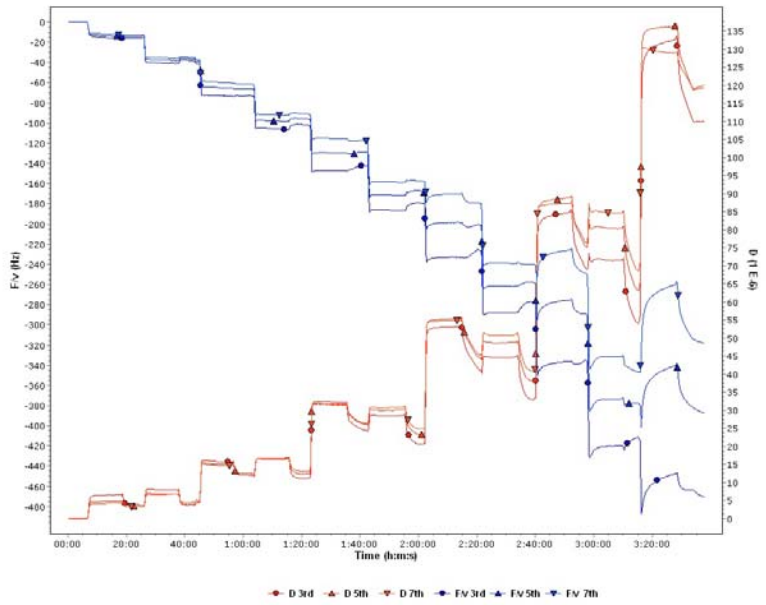


**FIGURE 8.1: Plots of change in dissipation (ΔD, right axis) and QCM frequency shifts (Δf/v, left axis) over time during the deposition of a [Glyc-CHI/HA]$_5$Gly-CHI film on a PLGA-coated QCM-D sensor. Frequency was monitored at the third (circles), fifth (upright triangles) and seventh (inverted triangles) overtones of the fundamental frequency, corresponding to 15 MHz, 25 MHz and 35 MHz, respectively. Data presented is for one representative experiment.**

The porous PLGA scaffolds used in this study (Fig. 8.2.A) were produced by the solid free form fabrication technique, via the BioPlotter system, as previously described (33). In order to monitor build-up of Glyc-CHI/HA films on these 3D scaffolds, Glyc-CHI was FITC-labelled and the fluorescent intensity of the scaffolds after deposition of every cationic layer was measured via a fluorescent spectrophotometer (Fig. 8.2.C). As anticipated, the fluorescent intensity generally increased with increasing bilayer number as [FITC-Glyc-CHI/HA]$_5$FITC-Glyc-CHI films were deposited onto the PLGA scaffolds (Fig. 8.2.B), thus suggesting successful scaffold coating. This coating remained fairly stable for a period of at least one week in 0.1 M NaCl buffer, as confocal imaging at this point revealed no apparent differences in fluorescent staining (data not shown).

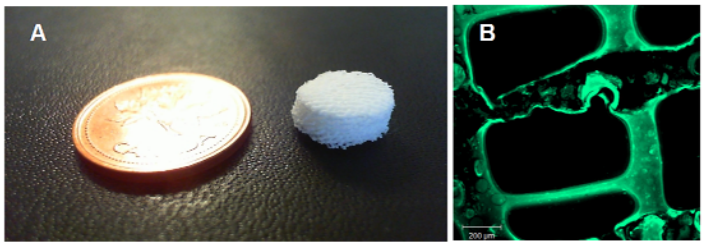


C)

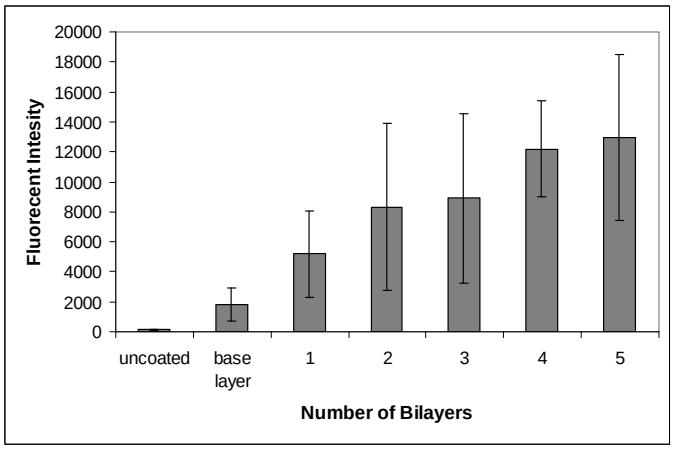


**FIGURE 8.2: Layer-by-layer deposition of FITC-Glyc-CHI/HA films on 3D PLGA Scaffolds. (A) Photo of the microfabricated PLGA scaffolds prior to coating beside a penny for scale. (B) Representative confocal microscopy image of the PLGA scaffold coated in a [FITC-Glyc-CHI/HA]$_5$FITC-Glyc-CHI film. (C) Increase in FITC intensity with increasing film bilayer number as scaffolds are coated. Data presented represents 2 separate experiments (n=6)**

### *8.4.2 Cell Seeding and Growth within Scaffolds*

In order to assess cellular adhesion, growth, and viability, scaffolds coated with [Glyc-CHI/HA]$_5$Glyc-CHI films and uncoated control scaffolds were seeded with MC3T3 pre-osteoblasts and assessed using a variety of techniques. Cell adhesion for both coated and uncoated scaffolds was assessed 24 hours post-seeding via the MTT assay, by comparing the fractions of scaffold-adherent (after trypsinization) and non-adherent viable cells. No significant differences were observed in the total number of viable adherent cells, as measured via MTT adsorbance, or in the estimated seeding efficiency, with

approximately 59 ± 6% of preosteoblasts seeding on LbL coated scaffolds compared to 61 ± 9% on uncoated controls. The MTT determined seeding efficiencies likely underestimated total cellular adhesion, as not all cells could be removed from either coated or uncoated scaffolds via trypsinization. Indeed, both scaffolds exhibited some residual MTT staining post-trypsinization indicating remaining viable cells. Thus subsequent assessments of cellular growth and viability within scaffolds were made via live/dead cell staining or optical coherence microscopy.

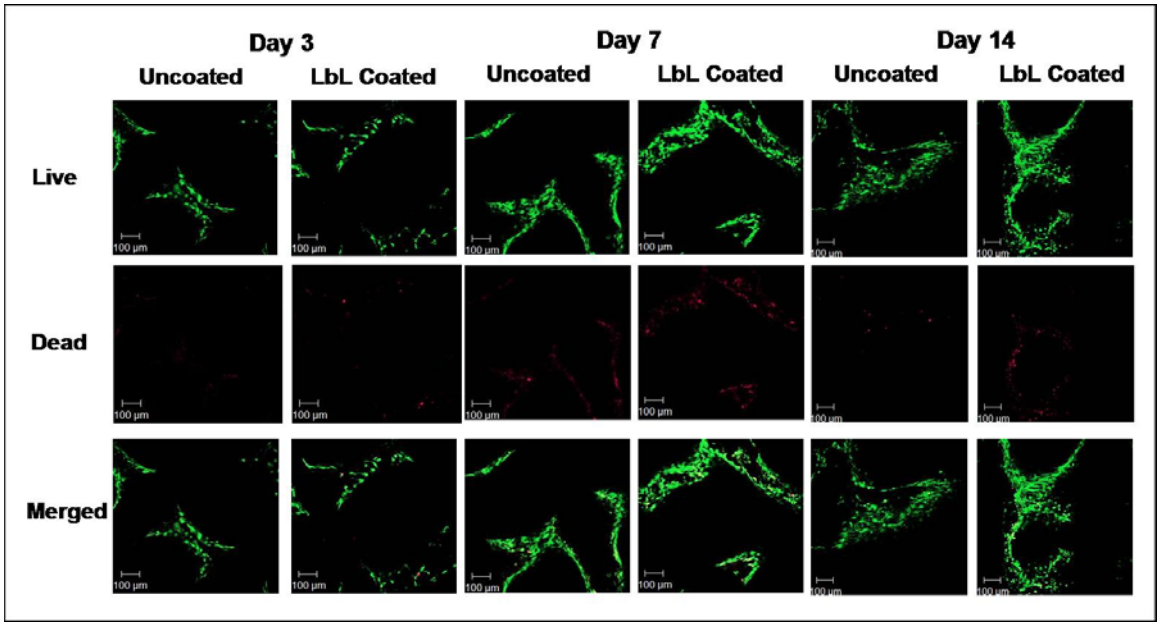


**FIGURE 8.3: Representative live/dead (calcein AM/ethidium bromide) confocal images of MC3T3 cells grown on scaffolds coated with [Glyc-CHI/HA]$_5$Glyc-CHI films and on uncoated control scaffolds at the indicated time points. Scan size approximately 1 mm x 1 mm. (top) Live, calcein-stained, images. (middle) Dead, ethidium bromide-stained, images. (bottom) Merged images of the two channels.**

MC3T3 cell growth and viability on LbL coated and uncoated scaffolds was evaluated at 3, 7, and 14 days post-seeding via Live/Dead (i.e. calcein AM/ethidium bromide) staining and confocal microscopy (Fig. 8.3). Imaging revealed that cells mainly grew along the scaffold strands for the first week, with the observed increase in viable cells from day 3

(Fig. 8.3 left), to 7 (Fig. 8.3 centre) indicating successful proliferation. By week two (Fig. 8.3 right), cells had further proliferated, expanding to fill the spaces between strands with denser tissue-like structures. Although some cell death was apparent, especially at day 7, the majority of cells in both scaffold systems appeared to be viable. At first glance, no significant differences between coated and uncoated scaffolds were clear from the images at any of the time points, apart from an apparent slight increase in PI-staining in coated scaffolds on day 14. ImageJ software was thus employed to perform estimates of the percentage area within the scaffolds that contained live and dead cells, using a series of z-stack images acquired over a 100 μm penetration depth at several points within each scaffold. Results of ImageJ analysis (Fig. 8.4) suggested that, while there were no differences for the first week, by week two LbL coated scaffolds seemed to exhibit a greater viable cell area than uncoated controls. This difference appears to be due to a lack of significant proliferation between day 7 and 14 for uncoated scaffolds, in contrast with coated scaffolds.

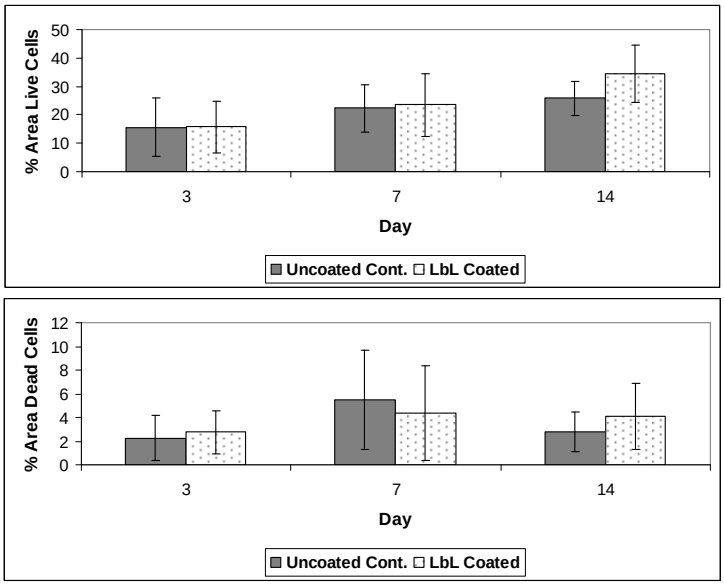


**FIGURE 8.4: Proportion of scaffold area estimated to contain live MC3T3 cells (top) or dead cells (bottom) as determined via ImageJ software analysis of live/dead stained z-stack confocal images. Analyzed z-stacks were made up of 5 images (approximately 1 mm x 1 mm), spaced 20 µm apart, representing a total penetration depth of around 100 µm. Data presented as mean ± STD (n=6).**

Confocal image analysis of scaffold cell volume is limited by its semi-quantitative nature, making it difficult in this case to make definitive conclusions as to whether the small (~ 10%) calculated increase in live cell area was indeed indicative of a significant difference in cell growth between coated and uncoated scaffolds. Additionally, live/dead staining is destructive, necessitating the assessment of different scaffolds at each time point, which could mask experiment-to-experiment variations. We thus sought to confirm our findings using an alternative method for monitoring cell growth and viability within coated and uncoated scaffolds. To this end we employed optical coherence phase microscopy to monitor cell growth over time within the same scaffolds.

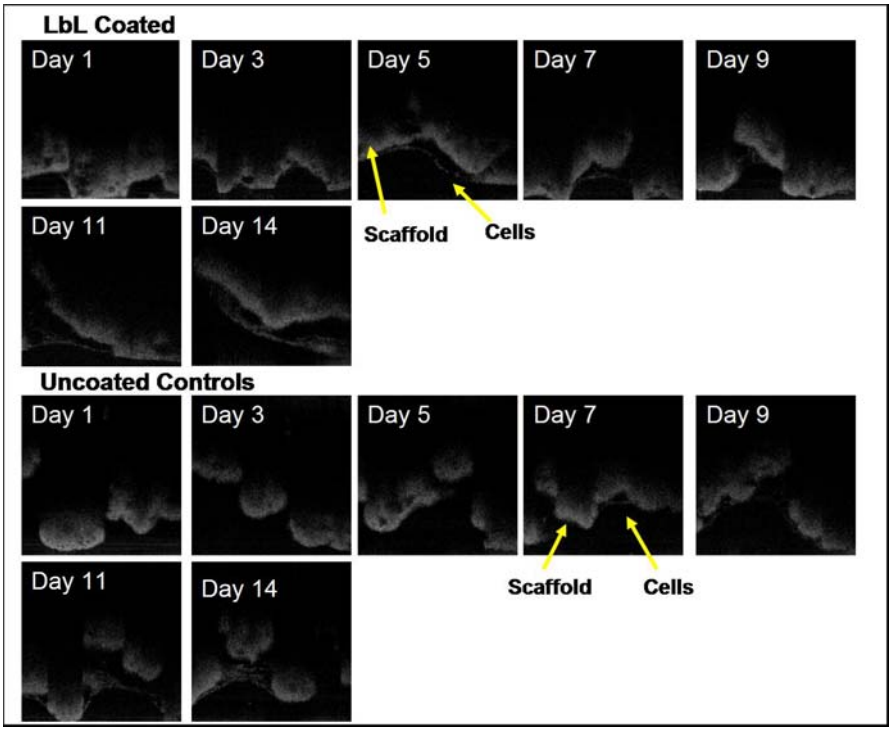


**FIGURE 8.5: Representative optical coherence phase microscopy (OCPM) cross-sectional images of MC3T3 cell growth on both LbL-coated scaffolds (top) and uncoated controls (bottom) at the time points indicated. All images are of a small representative 1mm x 1mm region within the scaffold, and represent an imaging penetration depth of 1mm. Yellow arrows indicate the dense scaffold strands and the thinner cell structures in representative images.**

Optical coherence phase microscopy (OCPM) imaging was performed every second day for a period of two weeks on coated and uncoated scaffolds seeded with MC3T3 pre-osteoblasts in order to non-invasively monitor tissue growth. Representative cross-sectional images of overall construct morphology over time for each scaffold system are presented in Fig. 8.5. The polymeric scaffold strands are evident within the OCPM intensity images as large, optically dense structures. In both scaffold systems 24 hours post-seeding, it is difficult to optically distinguish between cells growing on the surface of these strands and the scaffold material itself. For the LbL-coated scaffolds, by day 3 cells begin to become more evident, appearing as a very thin coating around the strand surface (bottom left corner of the image). By day 5, this cell layer has become clearly

distinguishable in LbL coated scaffolds (see arrows), continuing to grow and thicken around and between scaffold strands over the two week culture period, thus indicating cell proliferation and tissue growth. By contrast, in uncoated control scaffolds the thin cell layer only begins to become distinguishable from the surrounding scaffold material by day 7 (see arrows), developing and thickening over the second week of culture.

As a means of assessing cellular viability within these same coated and uncoated scaffolds, OCPM motility imaging was performed at selected time points (Fig. 8.6). Phase fluctuations arising from cellular motility (374) indicated the presence of viable cells within both LbL coated and uncoated control scaffolds at each tested time point (Fig. 8.6, middle). These viable cell fluctuations mapped well to the cell structures observed via OCPM intensity images (Fig. 8.6 merged), suggesting that a similar correlation likely holds in previous intensity images. Quantification of phase fluctuation density was performed for coated and uncoated scaffolds on days 7 and 9, as the scaffold strand area within images at these time points was found to be similar enough between all conditions that any observed changes would be due to cells alone. Analysis of live cell area as determined from OCPM phase fluctuation data (Fig. 8.7) indicated that, while there were no significant differences at day 7, by day 9 coated scaffolds exhibited a greater live cell area than uncoated controls ($t= 3.512$, $df = 28$, $p = 0.002$ (two-tailed)). These results agreed with our previous analysis via live/dead staining, thus suggesting that by week 2 of culture, coated scaffolds support increased cell growth compared to uncoated controls.

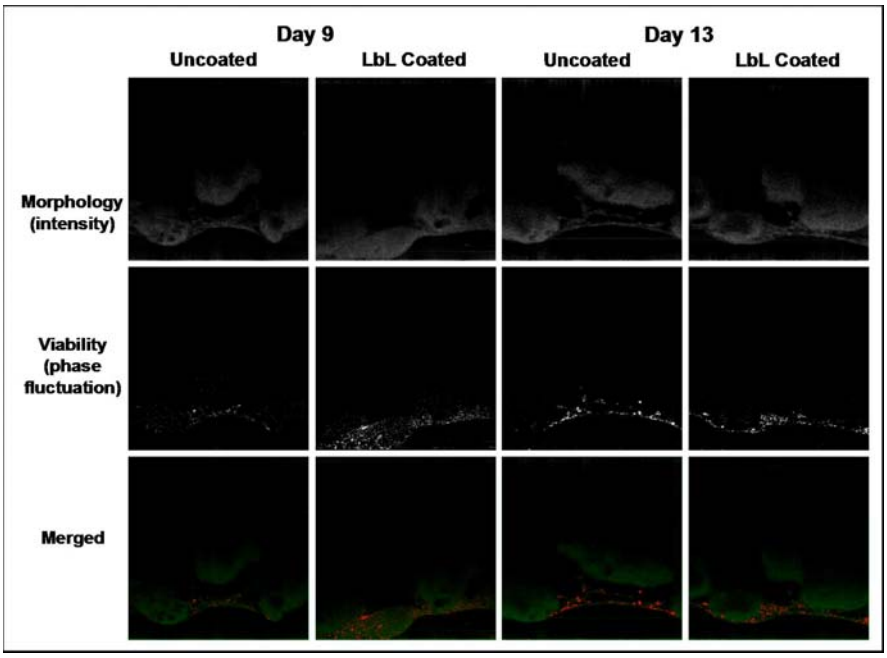


**FIGURE 8.6: Representative OCPM images of MC3T3 cell morphology and viability on LbL coated scaffolds and uncoated controls at the indicated time points. OCPM intensity images (top) revealed the in-depth microstructure of the sample. Phase fluctuation imaging (middle), originating from cell motility, highlighted areas with viable cells. Combined imaging (bottom), with the intensity channel in green and phase fluctuations in red, maps cell viability to overall construct structure. All images are approximately 1mm x 1mm.**

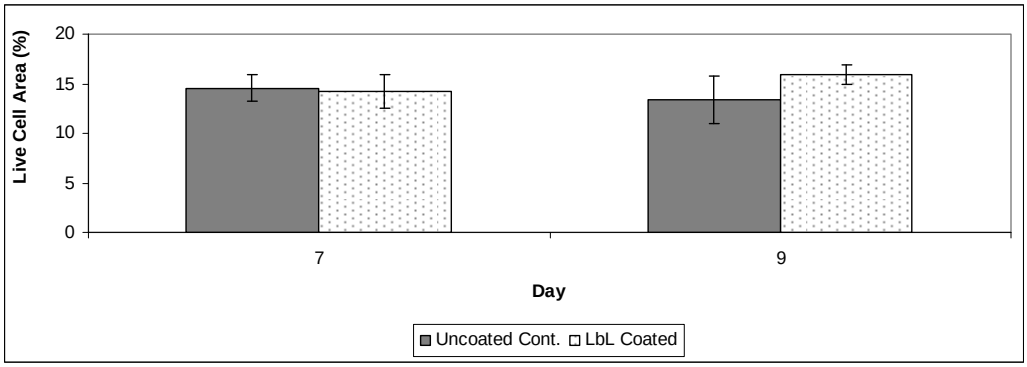


**FIGURE 8.7 Proportion of scaffold area estimated to contain live MC3T3 cells as determined via analysis of phase fluctuation OCPM imaging. A total of 5 representative areas (with images approximately 1 mm x 1 mm) were analyzed per scaffold, with 3 scaffolds analyzed per day and per condition. Data presented as mean ± STD. Two-way ANOVA analysis revealed no significant main effects for day ($F = 0.171$, $p = 0.681$) or for coating vs. uncoated ($F = 3.647$, $p = 0.061$). However a significant interaction effect was observed ($F = 5.907$, $p = 0.018$). Subsequent T-test analysis for coated vs. uncoated scaffolds on day 2 indicated a significant difference ($t= 3.512$, $df = 28$, $p = 0.002$ (two-tailed)).**

### *8.4.3 Scaffold-Based Gene Delivery*

As Glyc-CHI/HA coatings had been found to successfully support cell growth and viability on 3D scaffolds, they were then tested for their ability to enable scaffold-based gene delivery. PLGA scaffolds were again coated with [Glyc-CHI/HA]$_5$Glyc-CHI films to which negatively charged gene delivery lipoplexes, formed with either 4, 8 or 12 μg of plasmid DNA encoding EGFP, were adsorbed. These lipoplex-containing scaffolds were further LbL coated until [Glyc-CHI/HA]$_5$Glyc-CHI-Lipo-[Glyc-CHI/HA]$_2$Glyc-CHI films were formed. Lipoplexes were also adsorbed onto uncoated PLGA scaffolds as controls.

By measuring the DNA concentration, via the PicoGreen assay, of the lipoplex solution before and after deposition as well as the DNA concentration of the rinsate, the DNA loading efficiency within the coated and uncoated scaffolds was indirectly estimated (see Table 8.1). In all cases, LbL coated scaffolds were estimated to have higher initial DNA loading efficiencies than uncoated control scaffolds, thus suggesting that electrostatically-mediated adsorption of lipoplexes onto coated scaffolds with a terminating layer of Glyc-CHI appeared to be more efficient than simple surface adsorption onto PLGA. However, the estimated loading efficiency of coated scaffolds likely somewhat overestimated the overall amount of DNA within the scaffold, as it is possible that the further processing steps involved in LbL deposition removed some of the initially adsorbed DNA.

| DNA Concentration within Lipoplexes | Estimated DNA Loading Efficiency (%) : | |
|---|---|---|
| | Uncoated Scaffolds | Coated Scaffolds |
| 4 µg | 68 ± 10 | 75 ± 9 |
| 8 µg | 67 ± 7 | 93 ± 7 |
| 12 µg | 68 ± 4 | 94 ± 2 |

**Table 8.1: Estimated DNA loading efficiency onto LbL coated PLGA scaffolds and uncoated control scaffolds. Lipoplexes formed using either 4, 8 or 12 µg of plasmid DNA and 8, 16, or 24 µL of Lipofectamine2000™, respectively, were adsorbed onto coated and uncoated scaffolds. The concentration of DNA before and after adsorption (including the rinsate) was measured via the PicoGreen assay and the resulting initial loading efficiency was calculated. Data presented as average ± standard error (n=6).**

DNA release in phosphate buffered saline (PBS) from coated and uncoated scaffolds, both containing lipoplexes formed using 4 µg of plasmid, was measured every second day for a period of one week (Fig 8.7). As a means of accounting for any DNA that might have been lost in coated scaffolds post-lipoplex adsorption during further LbL deposition, the percentage of DNA released from each scaffold system was calculated in relation to the lower amount of DNA adsorbed onto uncoated scaffolds. Surprisingly, neither coated nor uncoated scaffolds exhibited a significant burst release of DNA over the first 24 hours. Overall, LbL coated scaffolds exhibited very little DNA release, with minimal amounts measured at any given time point and a total of less than 10% released by day 7. By contrast, uncoated control scaffolds generally displayed an increasing amount of DNA release with time, with over 50% of adsorbed DNA released by day 7. These results further suggest that the electrostatically-mediated adsorption of lipoplexes onto LbL coated scaffolds formed a stronger association than the non-specific adsorption of lipoplexes onto uncoated PLGA scaffolds.

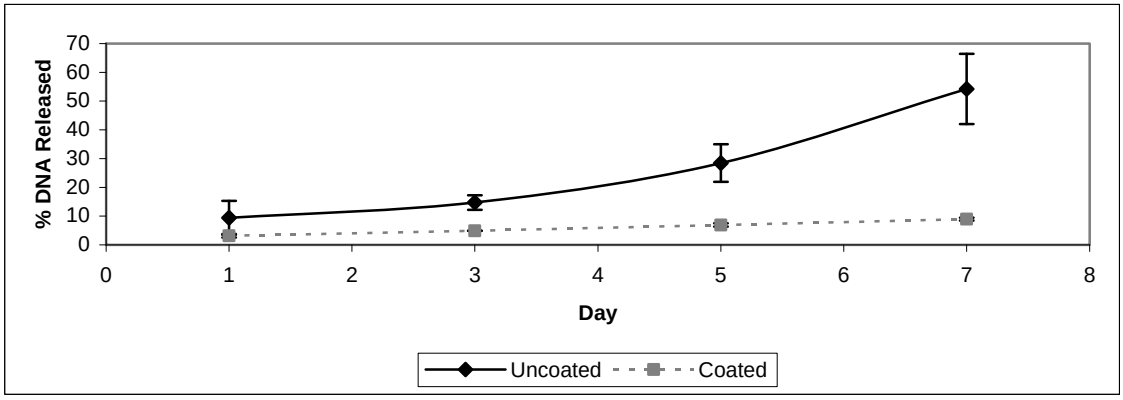


**FIGURE 8.8: DNA release over time from LbL coated PLGA scaffolds and uncoated control scaffolds. Both types of scaffold contained lipoplexes formed using 4 μg of plasmid DNA and were incubated in PBS, pH = 7.4 at 37°C. The supernatant was collected at the indicated time points and the DNA concentration was measured via the PicoGreen assay and normalized to the amount of DNA estimated to be loaded onto uncoated control scaffolds. Data presented as average ± standard error (n = 3).**

In order to determine *in vitro* transfection efficiency, coated and uncoated scaffolds containing lipoplexes formed with 4, 8 or 12 μg of plasmid DNA were seeded with HEK293 cells. Although poorly adherent to both uncoated and coated scaffolds (Appendix 3), HEK293 cells were used as they are one of the most widely employed cell lines in transfection assessment studies. After 48 hours, enhanced green fluorescent protein (EGFP) expression was evaluated via fluorescence microscopy (Fig. 8.10) and FACS analysis (Fig. 8.9 top), while cytotoxicity was measured via propidium iodide (PI) staining and FACS analysis (Fig. 8.9 bottom). In all cases, LbL coated scaffolds exhibited significantly higher transfection efficiencies than uncoated scaffolds ($\chi^2$=9.424, p=0.002). Interestingly, while increasing the amount of DNA contained in the adsorbed lipoplexes resulted in increased transfection efficiency for uncoated scaffolds, this was not the case for coated scaffolds, where transfection efficiency peaked for 8 μg scaffolds but decreased for 12 μg. The enhanced transfection efficiency observed for coated scaffolds was associated with higher cytotoxicity compared to uncoated controls ($\chi^2$=

19.348, p<0.001). This dual increase in both transfection efficiency and cytoxicity for LbL coated scaffolds reinforces the earlier observations of a higher estimated loading efficiency in comparison with uncoated scaffolds. Furthermore, the observations that coated scaffolds exhibited increased transfection efficiency yet little DNA release in PBS suggest that transfection in LbL-coated scaffolds was mediated by cell-coating interactions rather than diffusive release.

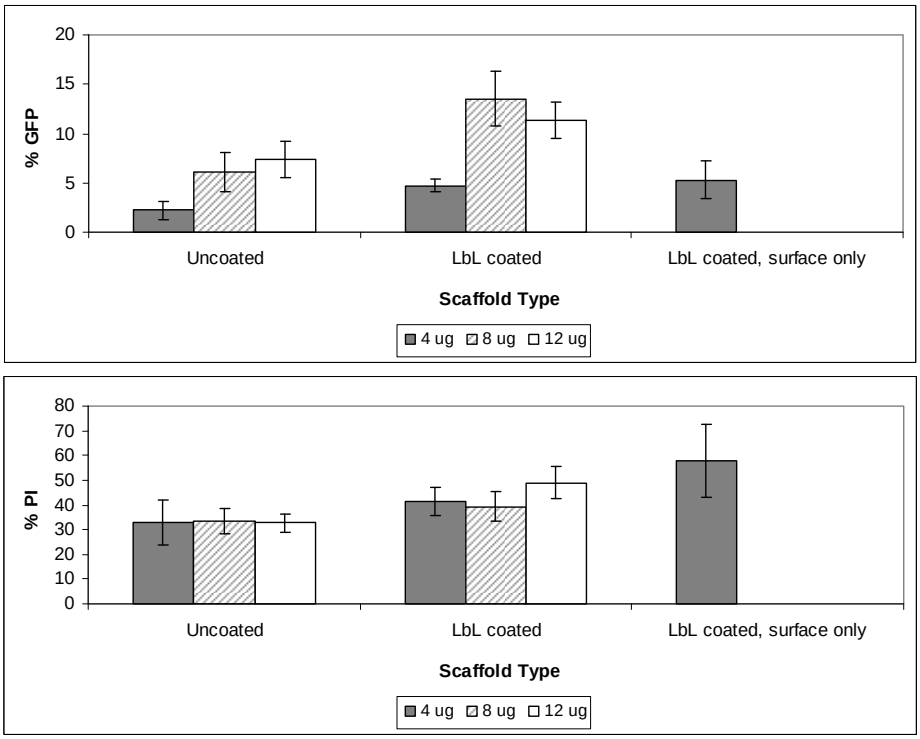


**FIGURE 8.9: HEK293 transfection efficiency (top) and death (bottom) after 48 hrs of growth on scaffolds coated with [Glyc-CHI/HA]$_5$Glyc-CHI-Lipo[Glyc-CHI/HA]$_2$Glyc-CHI films and on uncoated control scaffolds with adsorbed lipoplexes. Lipoplexes were formed from the indicated amount of pEGFP. In the case of lipoplexes formed with 4 µg of DNA, coated scaffolds with surface adsorbed lipoplexes (i.e. scaffolds with [Glyc-CHI/HA]$_5$Glyc-CHI-Lipo films) were also studied. Data presented represent the mean percentage of GFP-expressing (top) or PI-staining (bottom) cells, as determined via fluorescent activated cell sorting, ± STD (n=6). (Stats, for amount of DNA: $\chi^2$= 19.351, p<0.001 for GFP, $\chi^2$= 2.441, p=0.295 for PI; for coated vs. non-coated: $\chi^2$= 9.424, p=0.002 for GFP; $\chi^2$= 19.348, p<0.001 for PI)**

Preliminary studies were also conducted to determine whether the additional film layers overlying the adsorbed lipoplexes were necessary, using coated scaffolds and lipoplexes

consisting of 4 μg of plasmid DNA. While coated scaffolds with surface adsorbed lipoplexes (i.e. $[Glyc\text{-}CHI/HA]_5Glyc\text{-}CHI\text{-}Lipo$ scaffolds) exhibited no significant differences in transfection efficiency compared to those with embedded lipoplexes (i.e. $[Glyc\text{-}CHI/HA]_5Glyc\text{-}CHI\text{-}Lipo[Glyc\text{-}CHI/HA]_2Glyc\text{-}CHI$ scaffolds ($\chi^2$=3.103, p=0.078), they did display significantly increased cytotoxicity ($\chi^2$=5.026, p=0.025). These results suggested that the film layers covering the adsorbed DNA lipoplexes were required to minimize the known cytotoxic effects associated with higher concentrations of lipid-based gene carriers (426, 427). Thus, in subsequent experiments using lipoplexes formed from higher concentrations of DNA, coated scaffolds without overlying film layers were not studied.

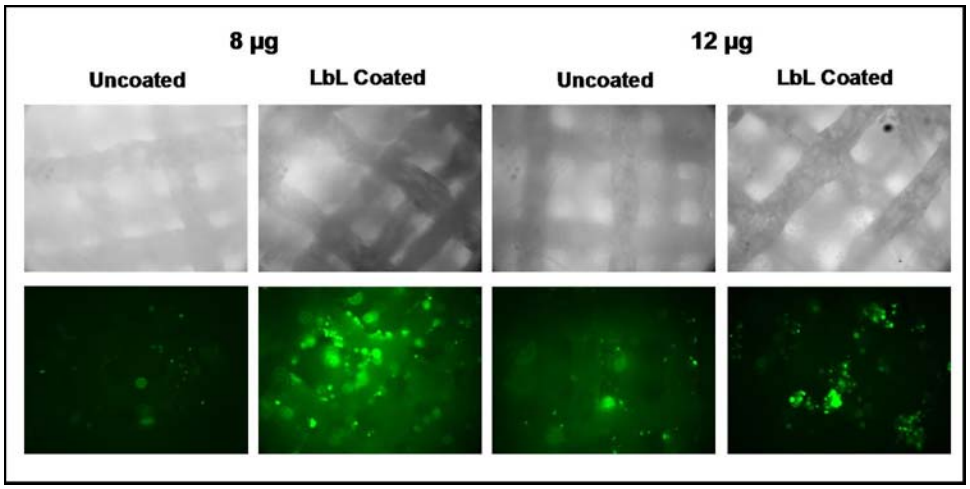


**FIGURE 8.10: Representative bright field (top) and fluorescence microscopy (bottom) images of HEK293 cells after 48 hours growth on coated and uncoated scaffolds containing lipoplexes formed with the indicated amount of plasmid DNA. All images taken with a 10 x objective.**

As previously mentioned, HEK293 cells are known to be weakly adherent (428-430) and were found to adhere poorly to uncoated and coated scaffolds in our initial OCPM studies (see Appendix 3). Therefore, the non-adherent fractions of HEK293 cells remaining 24

hours post scaffold-seeding were kept and their transfection was also assessed. While there was no significant effect on transfection efficiency overall ($\chi^2$= 1.649, =0.199), generally, the non-adherent fraction exhibited decreased transfection in the case of uncoated control scaffolds and slightly increased transfection in the case of 4 μg and 12 μg coated scaffolds. Meanwhile, in all cases the non-adherent fraction displayed significantly reduced cytotoxicity ($\chi^2$= 26.204, $p<0.001$). The observed lower cytotoxicity is likely due to the non-adherent fraction being in contact with the gene delivery lipoplexes for a shorter time period, thus reducing the cytotoxic effects associated with high concentrations of lipofectamine and longer exposure times (427). However, the trends in transfection are somewhat surprising in light of the lack of DNA release observed in PBS for coated scaffolds and the high amount of plasmid release for uncoated scaffolds. It is possible that the slight increases in transfection efficiency for the non-adherent fraction of cells from coated scaffolds is associated with the lower cytotoxicity, as fewer of the transfected cells may have died than with the adherent fraction. Alternatively, the presence of cells on the scaffolds likely mediates quicker DNA release from coated scaffolds than was observed in PBS buffer. There is also the strong probability that the majority of the cells were transfected during the initial 4 hour seeding period where all the cells were in contact with the scaffolds. Future studies will more closely examine the mechanisms and kinetics governing coated scaffold-based transfection.

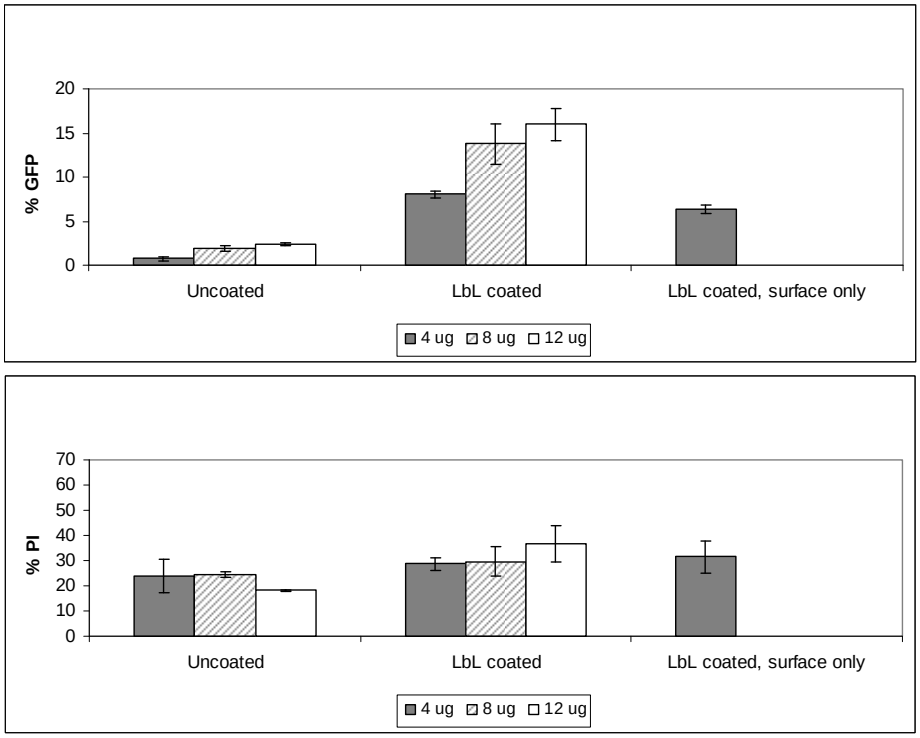


**FIGURE 8.11 Transfection efficiency (top) and death (bottom) of non-adherent HEK293 cells 48 hrs post seeding on scaffolds coated with $[Glyc\text{-}CHI/HA]_5Glyc\text{-}CHI\text{-}Lipo[Glyc\text{-}CHI/HA]_2Glyc\text{-}CHI$ films and on uncoated control scaffolds with adsorbed lipoplexes. Lipoplexes were formed from the indicated amount of pEGFP. Data presented represent the mean percentage of GFP-expressing (top) or PI-staining (bottom) cells, as determined via fluorescent activated cell sorting, ± STD (n=6). (Stats, for amount of DNA: $\chi^2$= 6.777, =<0.034 for GFP, $\chi^2$= 0.957, p=0.620 for PI; for coated vs. non-coated: $\chi^2$= 26.274, p<0.001 for GFP; $\chi^2$= 14.062, p<0.001 for PI; for amount of adherent vs non-adherent: $\chi^2$= 1.649, =0.199 for GFP, $\chi^2$= 26.204, p<0.001 for PI)**

## 8.5 Discussion

The results of this study serve as an important first step in demonstrating the utility of the Glyc-CHI/HA polylelectrolyte film system for enabling gene delivery from 3D tissue engineering scaffolds. The electrostatically-mediated adsorption of gene delivery lipoplexes in the LbL coating unsurprisingly lead to higher loading efficiency, lower DNA release in PBS, and higher transfection efficiency in coated scaffolds compared to uncoated controls with non-specifically adsorbed lipoplexes. Indeed, groups have previously used simple surface coatings of charged polymers such as gelatine in order to increase electrostatic adsorption of non-viral gene delivery vectors to scaffolds and thus enhance loading and transfection efficiency (431). However, our results indicated that additional film layers overlying the lipoplexes can serve an important role in reducing cytotoxic effects; an effect which may also apply to other gene delivery vectors. More importantly, the multilayer nature of our Glyc-CHI/HA film system allows for more design flexibility than a simple surface coating. Future studies, for example, will examine varying the overlying film architecture in order to alter the release kinetics of the gene delivery lipoplexes in order to produce different transfection profiles.

Although the maximum transfection efficiency achieved in this study (~14%) is significantly lower than that achieved by other scaffold systems designed for non-viral gene delivery (432-435), it is important to note that many of these alternative gene delivery scaffold systems are based on hydrogels, which exhibit limited mechanical

properties and architectures, or for systems where non-viral vectors are directly blended with scaffold materials, which also restricts the range of scaffold architectures that can be produced. LbL deposition, by contrast, can be used to coat a wide variety of shapes and materials, thereby enabling gene delivery from scaffolds and implants with a broader range of architectures while preserving their underlying mechanical properties. Additionally, by increasing the number of lipoplex-containing layers in our LbL film system the transfection efficiency that can be achieved will likely be significantly increased. This was found to be the case in a 2D study with films that consisted of plasmid DNA and DNA-containing lipoplexes, where increasing the number of lipoplex-containing layers from 1 to 3 yielded an approximately four-fold increase in transfection efficiency (401).

The main advantage of biocompatible multilayer films for non-viral gene delivery, such as the Glyc-CHI/HA system presented here, is their vast flexibility in both design and application. For example, the Lynn group has utilized LbL films constructed from a synthetic hydrolytically degradable cationic polyamine and plasmid DNA to coat stents and inflatable embolectomy catheter balloons, and has even demonstrated that the balloon system was able to transfect cells *in vivo* in a rat arterial injury model (254, 259). We therefore intend to similarly extend the Glyc-CHI/HA film system presented here to coat other 3D tissue engineering systems (e.g. scaffolds with different architectures and consisting of different materials), as well as medical devices such as stents and orthopaedic implants.

## 8.6 Conclusions

Multilayer films consisting of glycol-chitosan (Glyc-CHI) and hyaluronic acid (HA) were employed to coat 3D tissue engineering scaffolds microfabricated from PLGA. These LbL coated scaffolds were shown, via live/dead staining and optical coherence phase microscopy, to support *in vitro* cell adhesion, growth and viability for a period of at least two weeks at levels similar to or better than uncoated control scaffolds. Gene delivery lipoplexes were then successfully incorporated within the Glyc-CHI/HA film coatings, and were demonstrated to enable scaffold-based transfecion at levels significantly higher than uncoated scaffolds with surface adsorbed lipoplexes. Future work with this film system will focus on optimizing film architectures in order to further improve transfection efficiency, produce a wider variety of transfection kinetic profiles, achieve sequential gene delivery of multiple plasmids, and explore the coating of alternative scaffold systems and medical implants. Overall, polyelectrolyte multilayer films consisting of glycol-chitosan and hyaluronic acid show great promise for a wide variety of 3D gene delivery and tissue engineering applications.

## 8.7 Acknowledgements

This research was supported by a Le Fonds Québécois de la Recherche sur la Nature et les Technologies travel grant, a National Science and Engineering Research Council of Canada Discovery Grant, and a Canadian Institutes of Health Research Regenerative Medicine Grant. P. O. Bagnaninchi would also like to acknowledges support from the research councils UK for his fellowship and funding from EPSRC.

# Chapter 9: Conclusions and Perspectives

The overall aim of this thesis work was to demonstrate that layer-by-layer deposition can be used to enable localized gene delivery from the surface of 3D scaffolds in a manner that preserves the underlying properties of the system. To this end, a biocompatible polyelectrolyte multilayer film system consisting of glycol-chitosan (Glyc-CHI) and hyaluronic acid (HA) was developed and evaluated. Glyc-CHI/HA multilayers were characterized and analyzed, both with and without incorporated gene delivery lipoplexes, as 2D stand-alone films and as coatings for a model 3D polymeric scaffold system. Here we review each of the sub-objectives of this thesis study (Chap. 4.3) and present a brief summary of the findings observed from their achievement.

## 9.1 Summary of Objectives and Achievements

### ***9.1.1 Characterization of the physical and cellular adhesion properties of 2D glycol-chitosan/ hyaluronic acid (Glyc-CHI/HA) multilayer films***

The LbL build-up of polyelectrolyte films consisting of glycol-chitosan and hyaluronic acid was successfully demonstrated by quartz crystal microbalance with dissipation (QCM-D). Resulting Glyc-CHI/HA multilayers composed of 5 or more bilayers were found to support increased *in vitro* cell adhesion, growth and viability compared to corresponding films composed of unmodified chitosan for MC3T3 pre-osteoblasts and NIH3T3 fibroblasts. These differences in cellular adhesion were likely due to differences in surface topography and roughness, as measured via AFM, as well as in film chemistry and the water-solubility of the cation, since both types of films exhibited similar: thickness, as measured via QCM and AFM; wettability, as measured via contact angle; and serum protein adsorption, as measured via the BCA assay. (Chap. 5)

### ***9.1.2 Incorporation of lipoplex-based gene delivery vectors within Glyc-CHI/HA multilayer films and in vitro characterization of resulting film-based transfection and cytotoxicity***

Gene delivery lipoplexes, composed of plasmid DNA encoding EGFP complexed with Lipofectamine2000$^{TM}$, were successfully incorporated within Glyc-CHI/HA films. The topography and morphology of the resulting multilayers were characterized after lipoplex adsorption and during subsequent film build-up via AFM and SEM, respectively. Lipoplex containing Glyc-CHI/HA films were found to successfully transfect NIH3T3

fibroblasts and HEK293 kidney cells *in vitro*, via FACS analysis. In HEK293 cells transfection levels of approximately 20% were achieved and maintained for a period of at least 7 days. Transfection from these Glyc-CHI/HA films appeared to be mediated by cell-film interactions rather than diffusion, as multilayers exhibited little DNA release in PBS. (Chap. 6)

### ***9.1.3 LbL deposition of Glyc-CHI/HA films onto model 3D porous, polymeric scaffolds and characterization of subsequent cell adhesion, growth, and viability***

Glyc-CHI/HA films were successfully coated onto a 3D model porous scaffold system microfabricated from poly(lactic-co-glycolic acid) (PLGA). The resulting coated scaffolds were shown to support *in vitro* MC3T3 cell growth and viability in these scaffolds, via live/dead staining and optical coherence phase microscopy, for a period of at least 2 weeks. Qualitative and quantitative measurements indicated that cell growth and viability in LbL coated scaffolds appeared to be similar to, or better than, that achieved in uncoated control scaffolds. (Chap. 8)

### ***9.1.4 Incorporation of gene delivery lipoplexes within LbL coatings on 3D porous scaffolds and characterization of subsequent scaffold-based transfection and cytotoxicity***

Gene delivery lipoplexes were incorporated within Glyc-CHI/HA films coated onto 3D PLGA scaffolds and were found to support scaffold-based *in vitro* transfection of HEK293 cells at levels significantly higher than uncoated scaffolds with surface adsorbed

lipoplexes. Scaffold-based transfection from these Glyc-CHI/HA coatings again appeared to be mediated by cell-film interactions rather than diffusion, as coated scaffolds exhibited little DNA release in PBS. (Chap. 8)

### ***9.1.5 Demonstration that optical coherence phase microscopy (OCPM) can be used for imaging tissue growth and viability within porous tissue engineering scaffold systems***

We showed that OCPM enabled *in situ*, non-invasive, label-free imaging of tissue structure and viability within 3D tissue engineering scaffolds. We imaged two cell types, MC3T3 pre-osteoblasts and adipose derived stem cells (ADSCs), seeded within two distinct scaffold systems with different architectures, including our model porous scaffold system microfabricated from poly(lactic-co-glycolic acid) (PLGA). We compared fluctuation imaging results with those of fixed cells and with viability assessments made via fluorescent live/dead labelling. Cellular viability was mapped to tissue morphology, via measurement of optical phase fluctuations arising from cellular motility, and was found to provide an endogenous source of contrast for OCPM, thus enabling label-free viability imaging within 3D engineered tissues.

## 9.2 Discussion and Future Work

While the majority of the goals of this thesis were attained, many issues remain to be addressed in future studies. Some of these concerns are discussed below, including: questions arising from 2D studies of film formation and properties; issues with lipoplex incorporation; problems that arise in moving from 2D to 3D LbL systems; and some of the possible limitations of the overall LbL-based inductive tissue engineering system.

### *9.2.1 Remaining Questions Regarding 2D Film Formation and Properties*

While a broad range of factors are known to influence the formation and properties of LbL films (as discussed in section 2.3.2), only one set of formation conditions was employed in our studies of Glyc-CHI/HA multilayers (PE concentration 2mg/mL, in 0.1 M NaCl, pH=6.0). It would thus be of great interest to explore the effects of pH, ionic strength, and molecular weight on the build-up of Glyc-CHI/HA films and their resulting physical and cellular adhesion properties. For example, in multilayers composed of unmodified chitosan and hyaluronic acid, higher molecular weights were found to be related to increased film thickness and an earlier onset of the steep "exponential" phase of film growth (199). Meanwhile, high salt concentrations were associated with rapid CHI/HA multilayer growth and very low salt concentrations resulted in difficulties in film formation (159).

Another physical property of Glyc-CHI/HA films that was not explored in this work, but would be of fundamental importance in many biomedical applications, is the film

biodegradation rate. Future studies of multilayer degradation in various biologically relevant media (e.g. serum-containing media, enzymes such as hyaluronidase and chitinase) and in the presence of cells should be performed. Chemical cross-linking of Glyc-CHI/HA films, such as via genipin or EDC-sNHS chemistry, and its subsequent effects on film degradation and physical properties should also be explored, as it has been for the well-characterized CHI/HA system (208, 436).

In evaluating cellular adhesion, growth and viability on Glyc-CHI/HA films, weakly adherent HEK293 human embryonic kidney cells were found to behave differently than strongly adherent MC3T3 murine pre-osteoblasts and NIH3T3 murine embryonic fibroblasts. While the latter two cell types displayed significantly increased adhesion and viability on Glyc-CHI/HA films when compared to corresponding unmodified CHI films, HEK293 cells displayed no viability differences, despite exhibiting increased cell spreading on Glyc-CHI multilayers. These cell-specific variations suggest that adhesion and viability of additional cell lines should be screened on Glyc-CHI/HA films in future studies.

In order to better understand cellular adhesion on Glyc-CHI/HA films, initial studies of cellular adhesion kinetics were performed via electric cell impedance sensing (Appendix 1). Results indicated that while NIH3T3 and MC3T3 cell adhesion on [Glyc-CHI/HA]$_{10}$Glyc-CHI films reached levels comparable to uncoated controls, the rate of this adhesion was slower and cell density dependent. This observed delay in cellular adhesion influenced our subsequent scaffold seeding protocol. In order to increase cell

seeding efficiency we thus chose an initial low volume adhesion time of 4 hours prior to addition of excess media. Delayed cellular adhesion may also have effects on the application of Glyc-CHI/HA films as implant coatings and should thus be further studied.

### ***9.2.2 Gene Delivery Lipoplex Incorporation Issues***

The incorporation of gene delivery lipoplexes within Glyc-CHI/HA multilayers involved the adsorption of negatively charged lipoplexes onto a 5 bilayer film with an additional terminating cationic Glyc-CHI layer. This adsorption step, believed to be electrostatically mediated, was performed over a 2 hour time period in order to assure maximal lipoplex loading. However, we also theorized that this long incubation time contributed to lipoplex aggregation and thus the adsorption of lipoplexes on the film surface as large clusters (Chap. 6.4.1). A more detailed study of lipoplex adsorption kinetics and the effects of adsorption time on resulting film structure, DNA loading efficiency, and *in vitro* transfection should thus be performed. Furthermore, the mechanisms underlying lipoplex adsorption should be explored in more detail. For example, whether adsorption is dominated by electrostatic attraction could be assayed by comparing films formed with lipoplexes adsorbed onto Glyc-CHI vs. HA terminating layers.

One of the main limitations of our study was the indirect method used to assess DNA loading efficiency within both films and scaffolds. More direct assessment of DNA content via measurement of UV adsorption at ~ 260 nm was attempted using three types of spectrophotometers. However, in all cases, background readings and/or low sensitivity rendered UV measurements ineffective. Direct quantification of film DNA content was

also attempted via enzymatic film degradation and subsequent measurement via the Picogreen assay or UV adsorption. However, this method also led to high background readings that obscured DNA measurements via either technique. Pre-labelling of DNA with a fluorescent or other tagging molecule was ruled out due to the possibility that the presence of the tag would alter the complexation of plasmid DNA with Lipofectamine2000$^{TM}$ and thus result in lipoplexes with different properties than those formed with unlabelled DNA. Future studies utilizing radio-labelled plasmid DNA, which will likely have less effect on complexation, are thus recommended to more accurately measure DNA content.

Interestingly, we initially aimed to incorporate gene delivery polyplexes, consisting of plasmid DNA complexed with polyethylemine (PEI), rather than lipoplexes within our Glyc-CHI/HA films. One of the most efficient and widely studied polymeric transfection reagents, PEI-based polyplexes have been used in previous PE multilayer film systems to achieve successful *in vitro* transfection (250). However, after performing extensive film-based transfection studies in NIH3T3 cells, using a variety of N:P ratios, we found lower than desired transfection efficiencies (less than 5%, see tables in Appendix 2). Whether this significantly reduced transfection in comparison to lipoplexes was due solely to inherent differences in carrier transfection efficiency, or whether polyplexes interacted with Glyc-CHI/HA films in a manner which limited transfection remains a question to be explored.

One of the main motivations for the development of the Gly-CHI/HA film system was the belief that the poor cellular adhesion properties of unmodified CHI/HA films limited their gene delivery efficiency. Although Glyc-CHI/HA films consisting of 5 or more bilayers exhibited significantly improved cellular adhesion and viability compared to corresponding films composed of unmodified chitosan, we never directly compared gene delivery from CHI/HA films to that from the Glyc-CHI/HA films. In moving from pure Glyc-CHI/HA multilayers to those incorporating gene delivery lipoplexes, the overall structure and topography of the films was altered. While it would be extremely difficult to separate the effects of film topography from those arising from the presence of the lipoplexes themselves, it is possible that these changes in film structure do not preserve the significant enhancement in cellular adhesion and viability. Transfection efficiency from lipoplex-containing CHI/HA films should thus be assessed and compared to that from the Glyc-CHI/HA films presented here.

Finally, as previously discussed (Chap. 6.5), future work exploring various alterations to lipoplex-containing Glyc-CHI/HA film architecture and their effects on gene delivery is highly recommended. For example, more plasmid layers should be incorporated to enhance film transfection efficiency. Addition of more overlying layers and/or subsequent film crosslinking should also be examined as means to alter transfection kinetics. Furthermore, embedding multiple genes at different film depths should be investigated in order to facilitate sequential delivery.

### *9.2.3 Concerns in Transitioning Between 2D and 3D LbL Systems*

An underlying film consisting of 5 Glyc-CHI/HA bilayers was chosen for lipoplex adsorption and scaffold coating because initial experiments (Chap. 5) indicated that these films were approximately 100 nm thick and would thus provide a good base covering. It was also hypothesized that 5 bilayers would be sufficient to account for the effects of the underlying substrate on LbL adsorption, which particularly affects the formation of the first few layers (437). It would be interesting to further test this assumption by examining 2D and 3D lipoplex adsorption on thinner and thicker underlying films. For example, finding the minimum number of underlying layers required in order to enable efficient lipoplex loading and high levels of substrate-based transfection would be of great benefit.

One of the main concerns in moving from 2D to 3D LbL deposition are the effects of the underlying substrate on multilayer formation and properties. Substrate chemistry and charge density are well known to effect LbL formation (437, 438). These effects were clearly observed here via QCM-D analysis, where 5 bilayer Glyc-CHI/HA films formed on quartz crystals coated with PLGA were found to be thicker than those adsorbed on uncoated crystals (Chap 8.4.1). The shape and topography of the underlying substrate may also have some influence on PE multilayer formation. For example, recent studies of LbL deposition in confined geometries and on nanoporous topographies have revealed differences in overall film thickness compared to films formed on flat substrates (439-442). The underlying PLGA scaffold structure, including the porous topography of the scaffold strands due to salt leaching, may thus have had some effect on the properties of the Glyc-CHI/HA film coating. It will be difficult to determine whether there are indeed

significant differences in the properties of Glyc-CHI/HA multilayers in 2D film form compared to in 3D coating form. However, some overall film vs. coating properties could be assessed in future studies to gain some insight into possible differences. For example, variations in film biodegradation rate or cell seeding efficiency over time (as a means of assessing cellular adhesion kinetics) could be evaluated.

Another important issue in the LbL-coating of 3D scaffolds is what effects, if any, the coating has on underlying scaffold properties. The micro-printed, porous PLGA scaffolds employed in our study were previously found to have an average porosity of ~ 54 %, an average pore size of ~ 261 μm, and an average strand diameter of ~ 112 μm, via μCT analysis (33). In comparison, our 5 bilayer Glyc-CHI/HA film coating was estimated to be approximately 160 nm thick (Chap 8.4.1), representing a mere 0.06 % change in pore size and a tiny 0.14 % increase in strand thickness. While the actual thickness of the scaffold coating may be somewhat larger, given these estimates, it remains highly unlikely that the multilayer coating would change pore size or strand diameter by more than 1%. Thus, the LbL-coating of 5 bilayers of our Glyc-CHI/HA film system onto this PLGA scaffold did not appear to significantly alter the underlying scaffold architecture. Additionally, given the thinness of these coatings in comparison to the underlying scaffold structure, the mild processing conditions used in their formation, and the relatively soft nature of un-crosslinked polysaccharide multilayers (180, 204, 443), it is highly improbable that they have significantly changed the overall mechanical properties of the underlying scaffold system. However, in order to definitively confirm these

theories, future studies analyzing both the mechanical modulus and architectural details of the scaffold system before and after LbL-coating should be conducted.

Some important differences between 2D Glyc-CHI/HA films and their 3D scaffold coating counterparts are already apparent. For example, 3D scaffold coatings exhibited a significant increase in estimated DNA loading efficiency (~75-94%) compared to 2D films (~20-32%). This enhancement in loading efficiency could have been due to the larger surface area to volume ratio for scaffolds, where the total volume of the lipoplex solution was 50 μL, compared to films, where a 300 μL volume was used for deposition. Increased interaction between the lipoplexes and the 3D geometry of the scaffold could have also have contributed to improved adsorption. Whether variations in the properties of the base film coating existed between 2D films and 3D coatings and contributed to differences in lipoplex adsorption also remains a question. By contrast, little difference was seen in the overall percentage of DNA released in PBS for films (less than 5%) and scaffolds (less than 10%).

Interestingly, the observed increase in loading efficiency did not translate into increased *in vitro* transfection efficiency. The maximum HEK293 transfection efficiency achieved in 3D scaffolds was significantly lower (~14%) than that observed on 2D films (~25%). This reduction in transfection efficiency could be due to the poor HEK293 adhesion seen on scaffolds, possible variations in the properties of 2D films vs. 3D coatings, or inherent differences in cellular transfection efficiency due to the change from a 2D to a 3D environment (444).

### *9.2.4 Limitations in 3D Scaffold Analysis and OCPM Imaging*

One of the main challenges in this thesis work was the assessment of tissue growth, morphology and viability within our 3D polymeric scaffold systems. Attempts at scaffold sectioning and immunostaining were fraught with problems. Scaffolds were initially embedded within a combination of sucrose and OCT media, flash frozen, and cryosectioned via a cryo-microtome according to typical protocols (Chap. 2.4.2). However, cryosections of our polymeric scaffolds failed to adhere to glass slides (with and without pre-treatment) making subsequent immunostaining unfeasible. Impregnating scaffolds with a gelatine solution prior to flash freezing enabled scaffold cryosections to adhere to pre-treated glass slides, however, it also affected the structure of the tissue growing between scaffold strands. Thus, live/dead staining of unsectioned scaffolds was performed in place of immunostaining, with scaffolds being re-positioned and flipped to assess different regions.

Although optical coherence phase microscopy did enable non-invasive, label-free, real-time monitoring of tissue morphology and viability within our 3D scaffolds, a number of limitations to the technique remain. The average OCPM image penetration depth achieved with our scaffolds was less than 1 mm, which, although significantly greater than the ~ 200 – 300 μm possible with confocal microscopy, was still not as deep as we had hoped. More importantly, quantification of the volume of viable cells within scaffolds via phase fluctuation motility data was extremely difficult. Subtle variations in the overall morphology of the imaged regions, for example due to differences in

background or number of strands captured within the imaging field, complicated the quantification and comparison of viable cell volumes between different days and different scaffolds. Much future work will need to be done in establishing scanning protocols and imaging analysis programs to enable more accurate comparisons between systems.

An array of additional studies should also be performed to assess the 3D distribution of various factors. For example, lipoplex distribution within coated and uncoated scaffolds could be examined via use of a lipid-specific dye. Localization of GFP-expressing transfected cells and dead cells throughout scaffolds could also be performed via PI and nuclear staining combined with fluorescent confocal imaging. Attempts could also be made to try and assess the thickness or morphology of the LbL scaffold coating at different locations within the scaffold via sectioning coupled with SEM imaging or other analysis methods.

### ***9.2.5 Possible System Limitations and More Future Work***

The most important next steps in further developing Glyc-CHI/HA coatings for scaffold-based gene delivery involve shifting towards delivery of functional genes, assessment of more clinically relevant cell lines, and moving towards *in vivo* animal studies. One promising avenue of study would be adapting the system for application in bone tissue engineering. Scaffold coatings could be used to deliver plasmid DNA encoding bone morphogenetic protein 2 or 7 (BMP-2 or BMP-7) to either MC3T3 murine pre-osteoblasts, human or murine adipose derived stem cells (ADSCs), or human or murine

mesenchymal stem cells (MSCs) and the *in vitro* differentiation of these cells into mature, bone-forming osteoblasts could be assessed. Ectopic bone formation within these BMP-gene delivering scaffolds could then be assessed *in vivo*, with and without pre-seeded MSCs, via subcutaneous implantation in mice or rats. As a wide variety of gene delivery bone tissue engineering systems have been investigated, this application would provide a useful means of functionally assessing the advantages and disadvantages of our LbL scaffold coating system.

Demonstrating that the Glyc-CHI/HA film system can be extended to coat scaffolds with different architectures and composed of various materials is another crucial area for future work. The ability to coat porous polymeric scaffolds with widely different structures, such as those produced via electrospinning, freeze-drying, or gas foaming, should be assessed. Deposition of Glyc-CHI/HA films on hydrogels, ceramic composite scaffolds, and metallic meshes should also be examined. More significantly, the use of Glyc-CHI/HA multilayers as biomedical implant coating for stents, dental implants and orthopaedic applications should also be explored.

Should functional tests prove promising; a number of practical issues will need to be addressed in modifying Glyc-CHI/HA LbL film coatings for clinical scaffold-based gene delivery applications. The overall preparation time for our 3D scaffold coatings is currently too long (approximately 7 hours) for realistic "off the shelf" use. Minimal lipoplex adsorption times which enable high transfection efficiencies will need to be determined. Whether scaffolds can be pre-coated, either entirely or in part (e.g. the film

coating underlying the lipoplexes), and stored will also need to be explored. More importantly, transfection efficiencies and kinetic delivery profiles will need to be optimized via variations in film architecture. Although a number of questions and challenges remain, overall this thesis work represents an important first step towards using Glyc-CHI/HA multilayer films for controlled delivery of various therapeutic genes in 2D and 3D tissue engineering applications.

# References


1. Uludag H, D'Augusta D, Golden J, Li J, Timony G, Riedel R, et al. Implantation of recombinant human bone morphogenetic proteins with biomaterial carriers: A correlation between protein pharmacokinetics and osteoinduction in the rat ectopic model. Journal of biomedical materials research. 2000;50(2):227-38. Epub 2000/02/19.

2. Sakano S, Hasegawa Y, Murata Y, Ito T, Genda E, Iwata H, et al. Inhibitory effect of bFGF on endochondral heterotopic ossification. Biochemical and biophysical research communications. 2002;293(2):680-5. Epub 2002/06/11.

3. Tessmar JK, Gopferich AM. Matrices and scaffolds for protein delivery in tissue engineering. Advanced drug delivery reviews. 2007;59(4-5):274-91. Epub 2007/06/05.

4. Gunatillake PA, Adhikari R. Biodegradable synthetic polymers for tissue engineering. European cells & materials. 2003;5:1-16; discussion Epub 2003/10/17.

5. Malafaya PB, Silva GA, Reis RL. Natural-origin polymers as carriers and scaffolds for biomolecules and cell delivery in tissue engineering applications. Advanced drug delivery reviews. 2007;59(4-5):207-33. Epub 2007/05/08.

6. Mano JF, Silva GA, Azevedo HS, Malafaya PB, Sousa RA, Silva SS, et al. Natural origin biodegradable systems in tissue engineering and regenerative medicine: present status and some moving trends. Journal of The Royal Society Interface. 2007;4(17):999-1030.

7. Velema J, Kaplan D. Biopolymer-based biomaterials as scaffolds for tissue engineering. Advances in biochemical engineering/biotechnology. 2006;102:187-238. Epub 2006/11/09.

8. Cheung H-Y, Lau K-T, Lu T-P, Hui D. A critical review on polymer-based bio-engineered materials for scaffold development. Composites Part B: Engineering. 2007;38(3):291-300.

9. Nair LS, Laurencin CT. Biodegradable polymers as biomaterials. Progress in Polymer Science. 2007;32(8–9):762-98.

10. Olsen D, Yang C, Bodo M, Chang R, Leigh S, Baez J, et al. Recombinant collagen and gelatin for drug delivery. Advanced drug delivery reviews. 2003;55(12):1547-67.

11. McMillan RA, Conticello VP. Synthesis and Characterization of Elastin-Mimetic Protein Gels Derived from a Well-Defined Polypeptide Precursor. Macromolecules. 2000;33(13):4809-21.

12. Woodhouse KA, Klement P, Chen V, Gorbet MB, Keeley FW, Stahl R, et al. Investigation of recombinant human elastin polypeptides as non-thrombogenic coatings. Biomaterials. 2004;25(19):4543-53.

13. Werkmeister JA, Ramshaw JAM. Recombinant protein scaffolds for tissue engineering. Biomedical materials. 2012;7(1):012002.

14. Lee J-W, Gardella J. Surface perspectives in the biomedical applications of poly(a-hydroxy acid)s and their associated copolymers. Analytical and Bioanalytical Chemistry. 2002;373(7):526-37.

15. Habraken WJ, Wolke JG, Jansen JA. Ceramic composites as matrices and scaffolds for drug delivery in tissue engineering. Advanced drug delivery reviews. 2007;59(4-5):234-48. Epub 2007/05/05.

16. Yusop AH, Bakir AA, Shaharom NA, Abdul Kadir MR, Hermawan H. Porous biodegradable metals for hard tissue scaffolds: a review. International journal of biomaterials. 2012;2012:641430. Epub 2012/08/25.

17. Tsang VL, Bhatia SN. Three-dimensional tissue fabrication. Advanced drug delivery reviews. 2004;56(11):1635-47. Epub 2004/09/08.

18. Liu C, Xia Z, Czernuszka JT. Design and Development of Three-Dimensional Scaffolds for Tissue Engineering. Chemical Engineering Research and Design. 2007;85(7):1051-64.

19. Weigel T, Schinkel G, Lendlein A. Design and preparation of polymeric scaffolds for tissue engineering. Expert review of medical devices. 2006;3(6):835-51. Epub 2007/02/07.

20. Hollister SJ. Porous scaffold design for tissue engineering. Nature materials. 2005;4(7):518-24. Epub 2005/07/09.

21. Zhu J, Marchant RE. Design properties of hydrogel tissue-engineering scaffolds. Expert review of medical devices. 2011;8(5):607-26. Epub 2011/10/27.

22. Seliktar D. Designing cell-compatible hydrogels for biomedical applications. Science. 2012;336(6085):1124-8. Epub 2012/06/02.

23. Geckil H, Xu F, Zhang X, Moon S, Demirci U. Engineering hydrogels as extracellular matrix mimics. Nanomedicine. 2010;5(3):469-84.

24. Soppimath KS, Aminabhavi TM, Dave AM, Kumbar SG, Rudzinski WE. Stimulus-Responsive “Smart” Hydrogels as Novel Drug Delivery Systems*. Drug Development and Industrial Pharmacy. 2002;28(8):957-74.

25. Bawa P, Pillay V, Choonara YE, Toit LCd. Stimuli-responsive polymers and their applications in drug delivery. Biomedical materials. 2009;4(2):022001.

26. Kopeček J, Yang J. Hydrogels as smart biomaterials. Polymer International. 2007;56(9):1078-98.

27. Kogan G, Soltes L, Stern R, Gemeiner P. Hyaluronic acid: a natural biopolymer with a broad range of biomedical and industrial applications. Biotechnology letters. 2007;29(1):17-25. Epub 2006/11/09.

28. Burdick JA, Prestwich GD. Hyaluronic Acid Hydrogels for Biomedical Applications. Advanced Materials. 2011;23(12):H41-H56.

29. Spiller KL, Maher SA, Lowman AM. Hydrogels for the repair of articular cartilage defects. Tissue engineering Part B, Reviews. 2011;17(4):281-99. Epub 2011/04/23.

30. Ekaputra AK, Prestwich GD, Cool SM, Hutmacher DW. The three-dimensional vascularization of growth factor-releasing hybrid scaffold of poly (ε-caprolactone)/collagen fibers and hyaluronic acid hydrogel. Biomaterials. 2011;32(32):8108-17.

31. Abed A, Deval B, Assoul N, Bataille I, Portes P, Louedec L, et al. A biocompatible polysaccharide hydrogel-embedded polypropylene mesh for enhanced tissue integration in rats. Tissue engineering Part A. 2008;14(4):519-27. Epub 2008/03/29.

32. Shim J-H, Kim JY, Park M, Park J, Cho D-W. Development of a hybrid scaffold with synthetic biomaterials and hydrogel using solid freeform fabrication technology. Biofabrication. 2011;3(3):034102.

33. Daoud JT, Petropavlovskaia MS, Patapas JM, Degrandpre CE, Diraddo RW, Rosenberg L, et al. Long-term in vitro human pancreatic islet culture using three-dimensional microfabricated scaffolds. Biomaterials. 2011;32(6):1536-42. Epub 2010/11/26.

34. Chen G, Ushida T, Tateishi T. Development of biodegradable porous scaffolds for tissue engineering. Materials Science and Engineering: C. 2001;17(1–2):63-9.

35. Mikos AG, Thorsen AJ, Czerwonka LA, Bao Y, Langer R, Winslow DN, et al. Preparation and characterization of poly(l-lactic acid) foams. Polymer. 1994;35(5):1068-77.

36. Murphy WL, Dennis RG, Kileny JL, Mooney DJ. Salt fusion: an approach to improve pore interconnectivity within tissue engineering scaffolds. Tissue engineering. 2002;8(1):43-52. Epub 2002/03/12.

37. Hou Q, Grijpma DW, Feijen J. Preparation of interconnected highly porous polymeric structures by a replication and freeze-drying process. Journal of Biomedical Materials Research Part B: Applied Biomaterials. 2003;67B(2):732-40.

38. Ho M-H, Kuo P-Y, Hsieh H-J, Hsien T-Y, Hou L-T, Lai J-Y, et al. Preparation of porous scaffolds by using freeze-extraction and freeze-gelation methods. Biomaterials. 2004;25(1):129-38.

39. O'Brien FJ, Harley BA, Yannas IV, Gibson L. Influence of freezing rate on pore structure in freeze-dried collagen-GAG scaffolds. Biomaterials. 2004;25(6):1077-86.

40. Shin KC, Kim BS, Kim JH, Park TG, Nam JD, Lee DS. A facile preparation of highly interconnected macroporous PLGA scaffolds by liquid–liquid phase separation II. Polymer. 2005;46(11):3801-8.

41. Gong Y, Ma Z, Gao C, Wang W, Shen J. Specially elaborated thermally induced phase separation to fabricate poly(L-lactic acid) scaffolds with ultra large pores and good interconnectivity. Journal of Applied Polymer Science. 2006;101(5):3336-42.

42. Hua FJ, Kim GE, Lee JD, Son YK, Lee DS. Macroporous poly(L-lactide) scaffold 1. Preparation of a macroporous scaffold by liquid–liquid phase separation of a PLLA–dioxane–water system. Journal of biomedical materials research. 2002;63(2):161-7.

43. Di Maio E, Mensitieri G, Iannace S, Nicolais L, Li W, Flumerfelt RW. Structure optimization of polycaprolactone foams by using mixtures of CO2 and N2 as blowing agents. Polymer Engineering & Science. 2005;45(3):432-41.

44. Mooney DJ, Baldwin DF, Suh NP, Vacanti JP, Langer R. Novel approach to fabricate porous sponges of poly(d,l-lactic-co-glycolic acid) without the use of organic solvents. Biomaterials. 1996;17(14):1417-22.

45. Xu Q, Ren X, Chang Y, Wang J, Yu L, Dean K. Generation of microcellular biodegradable polycaprolactone foams in supercritical carbon dioxide. Journal of Applied Polymer Science. 2004;94(2):593-7.

46. Nair LS, Bhattacharyya S, Laurencin CT. Development of novel tissue engineering scaffolds via electrospinning. Expert Opinion on Biological Therapy. 2004;4(5):659-68.

47. Xu CY, Inai R, Kotaki M, Ramakrishna S. Aligned biodegradable nanofibrous structure: a potential scaffold for blood vessel engineering. Biomaterials. 2004;25(5):877-86.

48. Li W-J, Laurencin CT, Caterson EJ, Tuan RS, Ko FK. Electrospun nanofibrous structure: A novel scaffold for tissue engineering. Journal of biomedical materials research. 2002;60(4):613-21.

49. Ji W, Sun Y, Yang F, van den Beucken JJ, Fan M, Chen Z, et al. Bioactive electrospun scaffolds delivering growth factors and genes for tissue engineering applications. Pharmaceutical research. 2011;28(6):1259-72. Epub 2010/11/23.

50. Kochan D, Kai CC, Zhaohui D. Rapid prototyping issues in the 21st century. Computers in Industry. 1999;39(1):3-10.

51. Cheah CM, Chua CK, Leong KF, Chua SW. <i>Development of a Tissue Engineering Scaffold Structure Library for Rapid Prototyping. Part 1: Investigation and Classification</i>. The International Journal of Advanced Manufacturing Technology. 2003;21(4):291-301.

52. Pfister A, Landers R, Laib A, Hübner U, Schmelzeisen R, Mülhaupt R. Biofunctional rapid prototyping for tissue-engineering applications: 3D bioplotting versus 3D printing. Journal of Polymer Science Part A: Polymer Chemistry. 2004;42(3):624-38.

53. Hutmacher DW, Sittinger M, Risbud MV. Scaffold-based tissue engineering: rationale for computer-aided design and solid free-form fabrication systems. Trends in Biotechnology. 2004;22(7):354-62.

54. Leong KF, Cheah CM, Chua CK. Solid freeform fabrication of three-dimensional scaffolds for engineering replacement tissues and organs. Biomaterials. 2003;24(13):2363-78.

55. Dado D, Levenberg S. Cell-scaffold mechanical interplay within engineered tissue. Seminars in cell & developmental biology. 2009;20(6):656-64. Epub 2009/07/15.

56. Levenberg S, Huang NF, Lavik E, Rogers AB, Itskovitz-Eldor J, Langer R. Differentiation of human embryonic stem cells on three-dimensional polymer scaffolds. Proceedings of the National Academy of Sciences of the United States of America. 2003;100(22):12741-6. Epub 2003/10/17.

57. Engler AJ, Sen S, Sweeney HL, Discher DE. Matrix elasticity directs stem cell lineage specification. Cell. 2006;126(4):677-89. Epub 2006/08/23.

58. Hadjipanayi E, Mudera V, Brown RA. Close dependence of fibroblast proliferation on collagen scaffold matrix stiffness. Journal of tissue engineering and regenerative medicine. 2009;3(2):77-84. Epub 2008/12/04.

59. Levy-Mishali M, Zoldan J, Levenberg S. Effect of scaffold stiffness on myoblast differentiation. Tissue engineering Part A. 2009;15(4):935-44. Epub 2008/09/30.

60. Bell E, Ivarsson B, Merrill C. Production of a tissue-like structure by contraction of collagen lattices by human fibroblasts of different proliferative potential in vitro. Proceedings of the National Academy of Sciences of the United States of America. 1979;76(3):1274-8. Epub 1979/03/01.

61. Pins GD, Collins-Pavao ME, Van De Water L, Yarmush ML, Morgan JR. Plasmin triggers rapid contraction and degradation of fibroblast-populated collagen lattices. The Journal of investigative dermatology. 2000;114(4):647-53. Epub 2000/03/25.

62. Dikovsky D, Bianco-Peled H, Seliktar D. Defining the role of matrix compliance and proteolysis in three-dimensional cell spreading and remodeling. Biophysical journal. 2008;94(7):2914-25. Epub 2008/01/08.

63. Chung HJ, Park TG. Surface engineered and drug releasing pre-fabricated scaffolds for tissue engineering. Advanced drug delivery reviews. 2007;59(4-5):249-62. Epub 2007/05/08.

64. Storrie H, Mooney DJ. Sustained delivery of plasmid DNA from polymeric scaffolds for tissue engineering. Advanced drug delivery reviews. 2006;58(4):500-14. Epub 2006/06/09.

65. De Laporte L, Shea LD. Matrices and scaffolds for DNA delivery in tissue engineering. Advanced drug delivery reviews. 2007;59(4-5):292-307. Epub 2007/05/22.

66. Whang K, Goldstick TK, Healy KE. A biodegradable polymer scaffold for delivery of osteotropic factors. Biomaterials. 2000;21(24):2545-51. Epub 2000/11/09.

67. Nam YS, Yoon JJ, Park TG. A novel fabrication method of macroporous biodegradable polymer scaffolds using gas foaming salt as a porogen additive. Journal of biomedical materials research. 2000;53(1):1-7. Epub 2000/01/15.

68. Lee H, Cusick RA, Browne F, Ho Kim T, Ma PX, Utsunomiya H, et al. Local delivery of basic fibroblast growth factor increases both angiogenesis and engraftment of hepatocytes in tissue-engineered polymer devices. Transplantation. 2002;73(10):1589-93. Epub 2002/06/04.

69. Jang JH, Bengali Z, Houchin TL, Shea LD. Surface adsorption of DNA to tissue engineering scaffolds for efficient gene delivery. Journal of biomedical materials research Part A. 2006;77(1):50-8. Epub 2005/12/15.

70. Patel N, Padera R, Sanders GHW, Cannizzaro SM, Davies MC, Langer R, et al. Spatially controlled cell engineering on biodegradable polymer surfaces. The FASEB Journal. 1998;12(14):1447-54.

71. Kang I-K, Kwon OH, Lee YM, Sung YK. Preparation and surface characterization of functional group-grafted and heparin-immobilized polyurethanes by plasma glow discharge. Biomaterials. 1996;17(8):841-7.

72. Segura T, Shea LD. Surface-tethered DNA complexes for enhanced gene delivery. Bioconjugate chemistry. 2002;13(3):621-9. Epub 2002/05/16.

73. Segura T, Chung PH, Shea LD. DNA delivery from hyaluronic acid-collagen hydrogels via a substrate-mediated approach. Biomaterials. 2005;26(13):1575-84. Epub 2004/11/04.

74. Hu Y, Hollinger JO, Marra KG. Controlled release from coated polymer microparticles embedded in tissue-engineered scaffolds. Journal of drug targeting. 2001;9(6):431-8. Epub 2002/02/02.

75. Richardson TP, Peters MC, Ennett AB, Mooney DJ. Polymeric system for dual growth factor delivery. Nature biotechnology. 2001;19(11):1029-34. Epub 2001/11/02.

76. Suciati T, Howard D, Barry J, Everitt NM, Shakesheff KM, Rose FR. Zonal release of proteins within tissue engineering scaffolds. Journal of materials science Materials in medicine. 2006;17(11):1049-56. Epub 2006/11/24.

77. Saul JM, Linnes MP, Ratner BD, Giachelli CM, Pun SH. Delivery of non-viral gene carriers from sphere-templated fibrin scaffolds for sustained transgene expression. Biomaterials. 2007;28(31):4705-16. Epub 2007/08/07.

78. Moore K, MacSween M, Shoichet M. Immobilized concentration gradients of neurotrophic factors guide neurite outgrowth of primary neurons in macroporous scaffolds. Tissue engineering. 2006;12(2):267-78. Epub 2006/03/22.

79. Chen RR, Silva EA, Yuen WW, Mooney DJ. Spatio-temporal VEGF and PDGF delivery patterns blood vessel formation and maturation. Pharmaceutical research. 2007;24(2):258-64. Epub 2006/12/28.

80. Houchin-Ray T, Whittlesey KJ, Shea LD. Spatially patterned gene delivery for localized neuron survival and neurite extension. Molecular therapy : the journal of the American Society of Gene Therapy. 2007;15(4):705-12. Epub 2007/02/15.

81. Wells DJ. Gene therapy progress and prospects: electroporation and other physical methods. Gene therapy. 2004;11(18):1363-9. Epub 2004/08/06.

82. De Laporte L, Cruz Rea J, Shea LD. Design of modular non-viral gene therapy vectors. Biomaterials. 2006;27(7):947-54. Epub 2005/10/26.

83. Putnam D. Polymers for gene delivery across length scales. Nature materials. 2006;5(6):439-51. Epub 2006/06/02.

84. Wang T, Upponi JR, Torchilin VP. Design of multifunctional non-viral gene vectors to overcome physiological barriers: Dilemmas and strategies. International journal of pharmaceutics. 2012;427(1):3-20.

85. Wong SY, Pelet JM, Putnam D. Polymer systems for gene delivery—Past, present, and future. Progress in Polymer Science. 2007;32(8–9):799-837.

86. Khalil IA, Kogure K, Akita H, Harashima H. Uptake Pathways and Subsequent Intracellular Trafficking in Nonviral Gene Delivery. Pharmacological Reviews. 2006;58(1):32-45.

87. Kootstra NA, Verma IM. Gene therapy with viral vectors. Annual review of pharmacology and toxicology. 2003;43:413-39. Epub 2002/10/03.

88. Zhang X, Godbey WT. Viral vectors for gene delivery in tissue engineering. Advanced drug delivery reviews. 2006;58(4):515-34. Epub 2006/06/10.

89. Sheridan C. Gene therapy finds its niche. Nature biotechnology. 2011;29(2):121-8. Epub 2011/02/09.

90. Liu D, Ren T, Gao X. Cationic transfection lipids. Current medicinal chemistry. 2003;10(14):1307-15. Epub 2003/04/08.

91. Simões S, Filipe A, Faneca H, Mano M, Penacho N, Düzgünes N, et al. Cationic liposomes for gene delivery. Expert opinion on drug delivery. 2005;2(2):237-54.

92. Martin B, Sainlos M, Aissaoui A, Oudrhiri N, Hauchecorne M, Vigneron JP, et al. The design of cationic lipids for gene delivery. Current pharmaceutical design. 2005;11(3):375-94. Epub 2005/02/23.

93. Zhang XX, McIntosh TJ, Grinstaff MW. Functional lipids and lipoplexes for improved gene delivery. Biochimie. 2012;94(1):42-58. Epub 2011/05/31.

94. Tiera MJ, Shi Q, Winnik FM, Fernandes JC. Polycation-based gene therapy: current knowledge and new perspectives. Current gene therapy. 2011;11(4):288-306. Epub 2011/04/02.

95. Lungwitz U, Breunig M, Blunk T, Göpferich A. Polyethylenimine-based non-viral gene delivery systems. European Journal of Pharmaceutics and Biopharmaceutics. 2005;60(2):247-66.

96. Neu M, Fischer D, Kissel T. Recent advances in rational gene transfer vector design based on poly(ethylene imine) and its derivatives. The journal of gene medicine. 2005;7(8):992-1009.

97. Saranya N, Moorthi A, Saravanan S, Devi MP, Selvamurugan N. Chitosan and its derivatives for gene delivery. International Journal of Biological Macromolecules. 2011;48(2):234-8.

98. Saccardo P, Villaverde A, González-Montalbán N. Peptide-mediated DNA condensation for non-viral gene therapy. Biotechnology Advances. 2009;27(4):432-8.

99. Kleemann E, Neu M, Jekel N, Fink L, Schmehl T, Gessler T, et al. Nano-carriers for DNA delivery to the lung based upon a TAT-derived peptide covalently coupled to PEG–PEI. Journal of Controlled Release. 2005;109(1–3):299-316.

100. Mishra S, Webster P, Davis ME. PEGylation significantly affects cellular uptake and intracellular trafficking of non-viral gene delivery particles. European Journal of Cell Biology. 2004;83(3):97-111.

101. Hughes JA, Rao GA. Targeted polymers for gene delivery. Expert opinion on drug delivery. 2005;2(1):145-57. Epub 2005/11/22.

102. Molas M, Gomez-Valades AG, Vidal-Alabro A, Miguel-Turu M, Bermudez J, Bartrons R, et al. Receptor-mediated gene transfer vectors: progress towards genetic pharmaceuticals. Current gene therapy. 2003;3(5):468-85. Epub 2003/10/08.

103. Ferrer-Miralles N, Vázquez E, Villaverde A. Membrane-active peptides for non-viral gene therapy: making the safest easier. Trends in Biotechnology. 2008;26(5):267-75.

104. Badylak SF, Gilbert TW. Immune response to biologic scaffold materials. Seminars in Immunology. 2008;20(2):109-16.

105. Anderson JM, Rodriguez A, Chang DT. Foreign body reaction to biomaterials. Seminars in Immunology. 2008;20(2):86-100.

106. Jang JH, Houchin TL, Shea LD. Gene delivery from polymer scaffolds for tissue engineering. Expert review of medical devices. 2004;1(1):127-38. Epub 2005/11/19.

107. Bleiziffer O, Eriksson E, Yao F, Horch RE, Kneser U. Gene transfer strategies in tissue engineering. Journal of cellular and molecular medicine. 2007;11(2):206-23. Epub 2007/05/10.

108. Heyde M, Partridge KA, Oreffo RO, Howdle SM, Shakesheff KM, Garnett MC. Gene therapy used for tissue engineering applications. The Journal of pharmacy and pharmacology. 2007;59(3):329-50. Epub 2007/03/03.

109. Bengali Z, Pannier AK, Segura T, Anderson BC, Jang JH, Mustoe TA, et al. Gene delivery through cell culture substrate adsorbed DNA complexes. Biotechnology and bioengineering. 2005;90(3):290-302. Epub 2005/04/01.

110. Ziauddin J, Sabatini DM. Microarrays of cells expressing defined cDNAs. Nature. 2001;411(6833):107-10. Epub 2001/05/03.

111. Wang C-HK, Pun SH. Substrate-mediated nucleic acid delivery from self-assembled monolayers. Trends in Biotechnology. 2011;29(3):119-26.

112. Adler AF, Speidel AT, Christoforou N, Kolind K, Foss M, Leong KW. High-throughput screening of microscale pitted substrate topographies for enhanced nonviral transfection efficiency in primary human fibroblasts. Biomaterials. 2011;32(14):3611-9. Epub 2011/02/22.

113. Adler AF, Leong KW. Emerging links between surface nanotechnology and endocytosis: impact on nonviral gene delivery. Nano today. 2010;5(6):553-69. Epub 2011/03/09.

114. Yoshikawa T, Uchimura E, Kishi M, Funeriu DP, Miyake M, Miyake J. Transfection microarray of human mesenchymal stem cells and on-chip siRNA gene knockdown. Journal of controlled release : official journal of the Controlled Release Society. 2004;96(2):227-32. Epub 2004/04/15.

115. Bengali Z, Rea JC, Shea LD. Gene expression and internalization following vector adsorption to immobilized proteins: dependence on protein identity and density. The journal of gene medicine. 2007;9(8):668-78. Epub 2007/05/30.

116. Gersbach CA, Coyer SR, Le Doux JM, Garcia AJ. Biomaterial-mediated retroviral gene transfer using self-assembled monolayers. Biomaterials. 2007;28(34):5121-7. Epub 2007/08/19.

117. Sottile J, Chandler J. Fibronectin matrix turnover occurs through a caveolin-1-dependent process. Molecular biology of the cell. 2005;16(2):757-68. Epub 2004/11/26.

118. Rejman J, Bragonzi A, Conese M. Role of clathrin- and caveolae-mediated endocytosis in gene transfer mediated by lipo- and polyplexes. Molecular therapy : the journal of the American Society of Gene Therapy. 2005;12(3):468-74. Epub 2005/06/21.

119. Rea JC, Gibly RF, Barron AE, Shea LD. Self-assembling peptide-lipoplexes for substrate-mediated gene delivery. Acta biomaterialia. 2009;5(3):903-12. Epub 2008/11/08.

120. Stachelek SJ, Song C, Alferiev I, Defelice S, Cui X, Connolly JM, et al. Localized gene delivery using antibody tethered adenovirus from polyurethane heart valve cusps and intra-aortic implants. Gene therapy. 2004;11(1):15-24. Epub 2003/12/19.

121. Blocker KM, Kiick KL, Sullivan MO. Surface Immobilization of Plasmid DNA with a Cell-Responsive Tether for Substrate-Mediated Gene Delivery. Langmuir : the ACS journal of surfaces and colloids. 2011. Epub 2011/02/18.

122. Tang Z, Wang Y, Podsiadlo P, Kotov NA. Biomedical Applications of Layer-by-Layer Assembly: From Biomimetics to Tissue Engineering. Advanced Materials. 2006;18(24):3203-24.

123. De Geest BG, Sanders NN, Sukhorukov GB, Demeester J, De Smedt SC. Release mechanisms for polyelectrolyte capsules. Chemical Society reviews. 2007;36(4):636-49. Epub 2007/03/28.

124. Jewell CM, Lynn DM. Multilayered polyelectrolyte assemblies as platforms for the delivery of DNA and other nucleic acid-based therapeutics. Advanced drug delivery reviews. 2008;60(9):979-99. Epub 2008/04/09.

125. Decher G, Hong JD, Schmitt J. Buildup of ultrathin multilayer films by a self-assembly process: III. Consecutively alternating adsorption of anionic and cationic polyelectrolytes on charged surfaces. Thin Solid Films. 1992;210–211, Part 2(0):831-5.

126. Schmitt J, Gruenewald T, Decher G, Pershan PS, Kjaer K, Loesche M. Internal structure of layer-by-layer adsorbed polyelectrolyte films: a neutron and x-ray reflectivity study. Macromolecules. 1993;26(25):7058-63.

127. Decher G. Fuzzy Nanoassemblies: Toward Layered Polymeric Multicomposites. Science. 1997;277(5330):1232-7.

128. Chiarelli PA, Johal MS, Holmes DJ, Casson JL, Robinson JM, Wang H-L. Polyelectrolyte Spin-Assembly. Langmuir : the ACS journal of surfaces and colloids. 2001;18(1):168-73.

129. Jiang C, Markutsya S, Tsukruk VV. Compliant, Robust, and Truly Nanoscale Free-Standing Multilayer Films Fabricated Using Spin-Assisted Layer-by-Layer Assembly. Advanced Materials. 2004;16(2):157-61.

130. Vozar S, Poh YC, Serbowicz T, Bachner M, Podsiadlo P, Qin M, et al. Automated spin-assisted layer-by-layer assembly of nanocomposites. The Review of scientific instruments. 2009;80(2):023903. Epub 2009/03/05.

131. Schlenoff JB, Dubas ST, Farhat T. Sprayed Polyelectrolyte Multilayers. Langmuir : the ACS journal of surfaces and colloids. 2000;16(26):9968-9.

132. Izquierdo A, Ono SS, Voegel JC, Schaaf P, Decher G. Dipping versus Spraying: Exploring the Deposition Conditions for Speeding Up Layer-by-Layer Assembly. Langmuir : the ACS journal of surfaces and colloids. 2005;21(16):7558-67.

133. Porcel CH, Izquierdo A, Ball V, Decher G, Voegel JC, Schaaf P. Ultrathin Coatings and (Poly(glutamic acid)/Polyallylamine) Films Deposited by Continuous and Simultaneous Spraying. Langmuir : the ACS journal of surfaces and colloids. 2004;21(2):800-2.

134. Neff PA, Naji A, Ecker C, Nickel B, v. Klitzing R, Bausch AR. Electrical Detection of Self-Assembled Polyelectrolyte Multilayers by a Thin Film Resistor. Macromolecules. 2005;39(2):463-6.

135. Bucur CB, Sui Z, Schlenoff JB. Ideal Mixing in Polyelectrolyte Complexes and Multilayers: Entropy Driven Assembly. Journal of the American Chemical Society. 2006;128(42):13690-1.

136. Schlenoff JB, Rmaile AH, Bucur CB. Hydration Contributions to Association in Polyelectrolyte Multilayers and Complexes: Visualizing Hydrophobicity. Journal of the American Chemical Society. 2008;130(41):13589-97.

137. Kotov NA. Layer-by-layer self-assembly: The contribution of hydrophobic interactions. Nanostructured Materials. 1999;12(5–8):789-96.

138. Quinn JF, Johnston APR, Such GK, Zelikin AN, Caruso F. Next generation, sequentially assembled ultrathin films: beyond electrostatics. Chemical Society reviews. 2007;36(5):707-18.

139. Such GK, Johnston APR, Caruso F. Engineered hydrogen-bonded polymer multilayers: from assembly to biomedical applications. Chemical Society reviews. 2011;40(1):19-29.

140. Serizawa T, Hashiguchi S, Akashi M. Stepwise Assembly of Ultrathin Poly(vinyl alcohol) Films on a Gold Substrate by Repetitive Adsorption/Drying Processes. Langmuir : the ACS journal of surfaces and colloids. 1999;15(16):5363-8.

141. Serizawa T, Hamada K-i, Kitayama T, Fujimoto N, Hatada K, Akashi M. Stepwise Stereocomplex Assembly of Stereoregular Poly(methyl methacrylate)s on a Substrate. Journal of the American Chemical Society. 2000;122(9):1891-9.

142. Shimazaki Y, Nakamura R, Ito S, Yamamoto M. Molecular Weight Dependence of Alternate Adsorption through Charge-Transfer Interaction. Langmuir : the ACS journal of surfaces and colloids. 2000;17(3):953-6.

143. Hatzor A, Moav T, Cohen H, Matlis S, Libman J, Vaskevich A, et al. Coordination-Controlled Self-Assembled Multilayers on Gold. Journal of the American Chemical Society. 1998;120(51):13469-77.

144. Lvov Y, Ariga K, Ichinose I, Kunitake T. Layer-by-layer architectures of concanavalin A by means of electrostatic and biospecific interactions. Journal of the Chemical Society, Chemical Communications. 1995(22):2313-4.

145. Cassier T, Lowack K, Decher G. Layer-by-layer assembled protein/polymer hybrid films: nanoconstruction via specific recognition. Supramolecular Science. 1998;5(3–4):309-15.

146. Rauf S, Zhou D, Abell C, Klenerman D, Kang D-J. Building three-dimensional nanostructures with active enzymes by surface templated layer-by-layer assembly. Chemical Communications. 2006(16):1721-3.

147. Johnston APR, Mitomo H, Read ES, Caruso F. Compositional and Structural Engineering of DNA Multilayer Films. Langmuir : the ACS journal of surfaces and colloids. 2006;22(7):3251-8.

148. Schwarz S, Eichhorn KJ, Wischerhoff E, Laschewsky A. Polyelectrolyte adsorption onto planar surfaces: a study by streaming potential and ellipsometry measurements. Colloids and Surfaces A: Physicochemical and Engineering Aspects. 1999;159(2–3):491-501.

149. Ladam G, Schaad P, Voegel JC, Schaaf P, Decher G, Cuisinier F. In Situ Determination of the Structural Properties of Initially Deposited Polyelectrolyte Multilayers. Langmuir : the ACS journal of surfaces and colloids. 1999;16(3):1249-55.

150. Picart C, Lavalle P, Hubert P, Cuisinier FJG, Decher G, Schaaf P, et al. Buildup Mechanism for Poly(l-lysine)/Hyaluronic Acid Films onto a Solid Surface. Langmuir : the ACS journal of surfaces and colloids. 2001;17(23):7414-24.

151. Adamczyk Z, Zembala M, Warszyński P, Jachimska B. Characterization of Polyelectrolyte Multilayers by the Streaming Potential Method. Langmuir : the ACS journal of surfaces and colloids. 2004;20(24):10517-25.

152. Sukhorukov GB, Möhwald H, Decher G, Lvov YM. Assembly of polyelectrolyte multilayer films by consecutively alternating adsorption of polynucleotides and polycations. Thin Solid Films. 1996;284–285(0):220-3.

153. Lvov Y, Ariga K, Ichinose I, Kunitake T. Assembly of Multicomponent Protein Films by Means of Electrostatic Layer-by-Layer Adsorption. Journal of the American Chemical Society. 1995;117(22):6117-23.

154. Anzai J-i, Kobayashi Y, Nakamura N, Nishimura M, Hoshi T. Layer-by-Layer Construction of Multilayer Thin Films Composed of Avidin and Biotin-Labeled Poly(amine)s. Langmuir : the ACS journal of surfaces and colloids. 1998;15(1):221-6.

155. Tronin A, Lvov Y, Nicolini C. Ellipsometry and x-ray reflectometry characterization of self-assembly process of polystyrenesulfonate and polyallylamine. Colloid Polym Sci. 1994;272(10):1317-21.

156. Kim DK, Han SW, Kim CH, Hong JD, Kim K. Morphology of multilayers assembled by electrostatic attraction of oppositely charged model polyelectrolytes. Thin Solid Films. 1999;350(1–2):153-60.

157. Picart C, Ladam G, Senger B, Voegel JC, Schaaf P, Cuisinier FJG, et al. Determination of structural parameters characterizing thin films by optical methods: A comparison between scanning angle reflectometry and optical waveguide lightmode spectroscopy. The Journal of Chemical Physics. 2001;115(2):1086-94.

158. Boulmedais F, Ball V, Schwinte P, Frisch B, Schaaf P, Voegel J-C. Buildup of Exponentially Growing Multilayer Polypeptide Films with Internal Secondary Structure. Langmuir : the ACS journal of surfaces and colloids. 2002;19(2):440-5.

159. Richert L, Lavalle P, Payan E, Shu XZ, Prestwich GD, Stoltz JF, et al. Layer by layer buildup of polysaccharide films: physical chemistry and cellular adhesion aspects. Langmuir : the ACS journal of surfaces and colloids. 2004;20(2):448-58. Epub 2005/03/04.

160. Schoeler B, Kumaraswamy G, Caruso F. Investigation of the Influence of Polyelectrolyte Charge Density on the Growth of Multilayer Thin Films Prepared by the Layer-by-Layer Technique. Macromolecules. 2001;35(3):889-97.

161. Baba A, Park M-K, Advincula RC, Knoll W. Simultaneous Surface Plasmon Optical and Electrochemical Investigation of Layer-by-Layer Self-Assembled

Conducting Ultrathin Polymer Films. Langmuir : the ACS journal of surfaces and colloids. 2002;18(12):4648-52.

162. Pei R, Cui X, Yang X, Wang E. Assembly of Alternating Polycation and DNA Multilayer Films by Electrostatic Layer-by-Layer Adsorption. Biomacromolecules. 2001;2(2):463-8.

163. Lvov Y, Onda M, Ariga K, Kunitake T. Ultrathin films of charged polysaccharides assembled alternately with linear polyions. Journal of Biomaterials Science, Polymer Edition. 1998;9(4):345-55.

164. Notley SM, Eriksson M, Wågberg L. Visco-elastic and adhesive properties of adsorbed polyelectrolyte multilayers determined in situ with QCM-D and AFM measurements. Journal of colloid and interface science. 2005;292(1):29-37.

165. Marx KA. Quartz Crystal Microbalance: A Useful Tool for Studying Thin Polymer Films and Complex Biomolecular Systems at the Solution−Surface Interface. Biomacromolecules. 2003;4(5):1099-120.

166. Sauerbrey G. Verwendung von Schwingquarzen zur Wägung dünner Schichten und zur Mikrowägung. Zeitschrift für Physik A Hadrons and Nuclei. 1959;155(2):206-22.

167. Zhang J, Senger B, Vautier D, Picart C, Schaaf P, Voegel J-C, et al. Natural polyelectrolyte films based on layer-by layer deposition of collagen and hyaluronic acid. Biomaterials. 2005;26(16):3353-61.

168. Croll TI, O'Connor AJ, Stevens GW, Cooper-White JJ. A Blank Slate? Layer-by-Layer Deposition of Hyaluronic Acid and Chitosan onto Various Surfaces. Biomacromolecules. 2006;7(5):1610-22.

169. Voinova MV, Rodahl M, Jonson M, Kasemo B. Viscoelastic Acoustic Response of Layered Polymer Films at Fluid-Solid Interfaces: Continuum Mechanics Approach. Physica Scripta. 1999;59(5):391.

170. Voinova MV, Jonson M, Kasemo B. Missing mass effect in biosensor's QCM applications. Biosensors & bioelectronics. 2002;17(10):835-41. Epub 2002/09/24.

171. Lvov Y, Decher G, Haas H, Möhwald H, Kalachev A. X-ray analysis of ultrathin polymer films self-assembled onto substrates. Physica B: Condensed Matter. 1994;198(1–3):89-91.

172. Kellogg GJ, Mayes AM, Stockton WB, Ferreira M, Rubner MF, Satija SK. Neutron Reflectivity Investigations of Self-Assembled Conjugated Polyion Multilayers. Langmuir : the ACS journal of surfaces and colloids. 1996;12(21):5109-13.

173. Lösche M, Schmitt J, Decher G, Bouwman WG, Kjaer K. Detailed Structure of Molecularly Thin Polyelectrolyte Multilayer Films on Solid Substrates as Revealed by Neutron Reflectometry. Macromolecules. 1998;31(25):8893-906.

174. Shiratori SS, Rubner MF. pH-Dependent Thickness Behavior of Sequentially Adsorbed Layers of Weak Polyelectrolytes. Macromolecules. 2000;33(11):4213-9.

175. McAloney RA, Sinyor M, Dudnik V, Goh MC. Atomic Force Microscopy Studies of Salt Effects on Polyelectrolyte Multilayer Film Morphology. Langmuir : the ACS journal of surfaces and colloids. 2001;17(21):6655-63.

176. Lobo RFM, Pereira-da-Silva MA, Raposo M, Faria RM, Jr ONO. The morphology of layer-by-layer films of polymer/polyelectrolyte studied by atomic force microscopy. Nanotechnology. 2003;14(1):101.

177. Siedlecki CA, Marchant RE. Atomic force microscopy for characterization of the biomaterial interface. Biomaterials. 1998;19(4–5):441-54.

178. Mermut O, Lefebvre J, Gray DG, Barrett CJ. Structural and Mechanical Properties of Polyelectrolyte Multilayer Films Studied by AFM. Macromolecules. 2003;36(23):8819-24.

179. Pavoor PV, Bellare A, Strom A, Yang D, Cohen RE. Mechanical Characterization of Polyelectrolyte Multilayers Using Quasi-Static Nanoindentation. Macromolecules. 2004;37(13):4865-71.

180. Richert L, Engler AJ, Discher DE, Picart C. Elasticity of native and cross-linked polyelectrolyte multilayer films. Biomacromolecules. 2004;5(5):1908-16. Epub 2004/09/14.

181. Thompson MT, Berg MC, Tobias IS, Rubner MF, Van Vliet KJ. Tuning compliance of nanoscale polyelectrolyte multilayers to modulate cell adhesion. Biomaterials. 2005;26(34):6836-45. Epub 2005/06/24.

182. Caruso F, Niikura K, Furlong DN, Okahata Y. 1. Ultrathin Multilayer Polyelectrolyte Films on Gold: Construction and Thickness Determination. Langmuir : the ACS journal of surfaces and colloids. 1997;13(13):3422-6.

183. Nazaran P, Bosio V, Jaeger W, Anghel DF, v. Klitzing R. Lateral Mobility of Polyelectrolyte Chains in Multilayers†. The Journal of Physical Chemistry B. 2007;111(29):8572-81.

184. Picart C, Mutterer J, Richert L, Luo Y, Prestwich GD, Schaaf P, et al. Molecular basis for the explanation of the exponential growth of polyelectrolyte multilayers. Proceedings of the National Academy of Sciences of the United States of America. 2002;99(20):12531-5. Epub 2002/09/19.

185. Collin D, Lavalle P, Garza JM, Voegel J-C, Schaaf P, Martinoty P. Mechanical Properties of Cross-Linked Hyaluronic Acid/Poly-(l-lysine) Multilayer Films. Macromolecules. 2004;37(26):10195-8.

186. Lavalle P, Picart C, Mutterer J, Gergely C, Reiss H, Voegel J-C, et al. Modeling the Buildup of Polyelectrolyte Multilayer Films Having Exponential Growth✗. The Journal of Physical Chemistry B. 2003;108(2):635-48.

187. Laugel N, Betscha C, Winterhalter M, Voegel J-C, Schaaf P, Ball V. Relationship between the Growth Regime of Polyelectrolyte Multilayers and the Polyanion/Polycation Complexation Enthalpy. The Journal of Physical Chemistry B. 2006;110(39):19443-9.

188. Xu L, Pristinski D, Zhuk A, Stoddart C, Ankner JF, Sukhishvili SA. Linear versus Exponential Growth of Weak Polyelectrolyte Multilayers: Correlation with Polyelectrolyte Complexes. Macromolecules. 2012;45(9):3892-901.

189. Porcel C, Lavalle P, Ball V, Decher G, Senger B, Voegel J-C, et al. From Exponential to Linear Growth in Polyelectrolyte Multilayers. Langmuir : the ACS journal of surfaces and colloids. 2006;22(9):4376-83.

190. Dubas ST, Schlenoff JB. Factors Controlling the Growth of Polyelectrolyte Multilayers. Macromolecules. 1999;32(24):8153-60.

191. Izumrudov V, Kharlampieva E, Sukhishvili SA. Salt-Induced Multilayer Growth: Correlation with Phase Separation in Solution. Macromolecules. 2004;37(22):8400-6.

192. Boddohi S, Killingsworth CE, Kipper MJ. Polyelectrolyte Multilayer Assembly as a Function of pH and Ionic Strength Using the Polysaccharides Chitosan and Heparin. Biomacromolecules. 2008;9(7):2021-8.

193. Voigt U, Jaeger W, Findenegg GH, Klitzing Rv. Charge Effects on the Formation of Multilayers Containing Strong Polyelectrolytes. The Journal of Physical Chemistry B. 2003;107(22):5273-80.

194. Glinel K, Moussa A, Jonas AM, Laschewsky A. Influence of Polyelectrolyte Charge Density on the Formation of Multilayers of Strong Polyelectrolytes at Low Ionic Strength. Langmuir : the ACS journal of surfaces and colloids. 2002;18(4):1408-12.

195. Poptoshev E, Schoeler B, Caruso F. Influence of Solvent Quality on the Growth of Polyelectrolyte Multilayers. Langmuir : the ACS journal of surfaces and colloids. 2004;20(3):829-34.

196. Steitz R, Leiner V, Siebrecht R, v. Klitzing R. Influence of the ionic strength on the structure of polyelectrolyte films at the solid/liquid interface. Colloids and Surfaces A: Physicochemical and Engineering Aspects. 2000;163(1):63-70.

197. Salomäki M, Tervasmäki P, Areva S, Kankare J. The Hofmeister Anion Effect and the Growth of Polyelectrolyte Multilayers. Langmuir : the ACS journal of surfaces and colloids. 2004;20(9):3679-83.

198. Ghimici L, Dragan S. Behaviour of cationic polyelectrolytes upon binding of electrolytes: effects of polycation structure, counterions and nature of the solvent. Colloid Polym Sci. 2002;280(2):130-4.

199. Kujawa P, Moraille P, Sanchez J, Badia A, Winnik FM. Effect of Molecular Weight on the Exponential Growth and Morphology of Hyaluronan/Chitosan Multilayers: A Surface Plasmon Resonance Spectroscopy and Atomic Force Microscopy Investigation. Journal of the American Chemical Society. 2005;127(25):9224-34.

200. Stevens MM, George JH. Exploring and Engineering the Cell Surface Interface. Science. 2005;310(5751):1135-8.

201. Tryoen-Toth P, Vautier D, Haikel Y, Voegel JC, Schaaf P, Chluba J, et al. Viability, adhesion, and bone phenotype of osteoblast-like cells on polyelectrolyte multilayer films. Journal of biomedical materials research. 2002;60(4):657-67. Epub 2002/04/12.

202. Salloum DS, Olenych SG, Keller TC, Schlenoff JB. Vascular smooth muscle cells on polyelectrolyte multilayers: hydrophobicity-directed adhesion and growth. Biomacromolecules. 2005;6(1):161-7. Epub 2005/01/11.

203. Richert L, Lavalle P, Vautier D, Senger B, Stoltz JF, Schaaf P, et al. Cell interactions with polyelectrolyte multilayer films. Biomacromolecules. 2002;3(6):1170-8. Epub 2002/11/12.

204. Richert L, Boulmedais F, Lavalle P, Mutterer J, Ferreux E, Decher G, et al. Improvement of stability and cell adhesion properties of polyelectrolyte multilayer films by chemical cross-linking. Biomacromolecules. 2004;5(2):284-94. Epub 2004/03/09.

205. Mendelsohn JD, Yang SY, Hiller J, Hochbaum AI, Rubner MF. Rational design of cytophilic and cytophobic polyelectrolyte multilayer thin films. Biomacromolecules. 2003;4(1):96-106. Epub 2003/01/14.

206. Ren K, Crouzier T, Roy C, Picart C. Polyelectrolyte multilayer films of controlled stiffness modulate myoblast cells differentiation. Advanced functional materials. 2008;18(9):1378-89. Epub 2008/10/09.

207. Wittmer CR, Phelps JA, Lepus CM, Saltzman WM, Harding MJ, Van Tassel PR. Multilayer nanofilms as substrates for hepatocellular applications. Biomaterials. 2008;29(30):4082-90. Epub 2008/07/26.

208. Schneider A, Richert L, Francius G, Voegel JC, Picart C. Elasticity, biodegradability and cell adhesive properties of chitosan/hyaluronan multilayer films. Biomedical materials. 2007;2(1):S45-51. Epub 2008/05/07.

209. Wittmer CR, Phelps JA, Saltzman WM, Van Tassel PR. Fibronectin terminated multilayer films: protein adsorption and cell attachment studies. Biomaterials. 2007;28(5):851-60. Epub 2006/10/24.

210. Berg MC, Yang SY, Hammond PT, Rubner MF. Controlling Mammalian Cell Interactions on Patterned Polyelectrolyte Multilayer Surfaces. Langmuir : the ACS journal of surfaces and colloids. 2004;20(4):1362-8.

211. Picart C, Elkaim R, Richert L, Audoin F, Arntz Y, Da Silva Cardoso M, et al. Primary Cell Adhesion on RGD-Functionalized and Covalently Crosslinked Thin Polyelectrolyte Multilayer Films. Advanced functional materials. 2005;15(1):83-94.

212. Wagner VE, Koberstein JT, Bryers JD. Protein and bacterial fouling characteristics of peptide and antibody decorated surfaces of PEG-poly(acrylic acid) co-polymers. Biomaterials. 2004;25(12):2247-63. Epub 2004/01/27.

213. Kidambi S, Chan C, Lee I. Tunable Resistive m-dPEG Acid Patterns on Polyelectrolyte Multilayers at Physiological Conditions: Template for Directed Deposition of Biomacromolecules. Langmuir : the ACS journal of surfaces and colloids. 2007;24(1):224-30.

214. Boulmedais F, Frisch B, Etienne O, Lavalle P, Picart C, Ogier J, et al. Polyelectrolyte multilayer films with pegylated polypeptides as a new type of anti-microbial protection for biomaterials. Biomaterials. 2004;25(11):2003-11. Epub 2004/01/27.

215. Mansouri S, Fatisson J, Miao Z, Merhi Y, Winnik FM, Tabrizian M. Silencing red blood cell recognition toward Anti-A antibody by means of polyelectrolyte layer-by-layer assembly in a two-dimensional model system. Langmuir : the ACS journal of surfaces and colloids. 2009;25(24):14071-8. Epub 2009/08/26.

216. Mansouri S, Merhi Y, Winnik FM, Tabrizian M. Investigation of layer-by-layer assembly of polyelectrolytes on fully functional human red blood cells in suspension for attenuated immune response. Biomacromolecules. 2011;12(3):585-92. Epub 2011/02/11.

217. Tan Q, Ji J, Barbosa MA, Fonseca C, Shen J. Constructing thromboresistant surface on biomedical stainless steel via layer-by-layer deposition anticoagulant. Biomaterials. 2003;24(25):4699-705. Epub 2003/09/03.

218. Ji J, Tan Q, Fan DZ, Sun FY, Barbosa MA, Shen J. Fabrication of alternating polycation and albumin multilayer coating onto stainless steel by electrostatic layer-by-layer adsorption. Colloids and surfaces B, Biointerfaces. 2004;34(3):185-90. Epub 2004/07/21.

219. Fu J, Ji J, Yuan W, Shen J. Construction of anti-adhesive and antibacterial multilayer films via layer-by-layer assembly of heparin and chitosan. Biomaterials. 2005;26(33):6684-92. Epub 2005/06/11.

220. Thierry B, Winnik FM, Merhi Y, Silver J, Tabrizian M. Bioactive coatings of endovascular stents based on polyelectrolyte multilayers. Biomacromolecules. 2003;4(6):1564-71. Epub 2003/11/11.

221. Schwinte P, Ball V, Szalontai B, Haikel Y, Voegel JC, Schaaf P. Secondary structure of proteins adsorbed onto or embedded in polyelectrolyte multilayers. Biomacromolecules. 2002;3(6):1135-43. Epub 2002/11/12.

222. Peyratout CS, Dahne L. Tailor-made polyelectrolyte microcapsules: from multilayers to smart containers. Angewandte Chemie. 2004;43(29):3762-83. Epub 2004/07/20.

223. Leguen E, Chassepot A, Decher G, Schaaf P, Voegel JC, Jessel N. Bioactive coatings based on polyelectrolyte multilayer architectures functionalized by embedded proteins, peptides or drugs. Biomolecular engineering. 2007;24(1):33-41. Epub 2006/07/25.

224. Ren K, Ji J, Shen J. Tunable DNA release from cross-linked ultrathin DNA/PLL multilayered films. Bioconjugate chemistry. 2006;17(1):77-83. Epub 2006/01/19.

225. Etienne O, Schneider A, Taddei C, Richert L, Schaaf P, Voegel JC, et al. Degradability of polysaccharides multilayer films in the oral environment: an in vitro and in vivo study. Biomacromolecules. 2005;6(2):726-33. Epub 2005/03/15.

226. Benkirane-Jessel N, Lavalle P, Hübsch E, Holl V, Senger B, Haïkel Y, et al. Short-Time Tuning of the Biological Activity of Functionalized Polyelectrolyte Multilayers. Advanced functional materials. 2005;15(4):648-54.

227. Antipov AA, Sukhorukov GB, Leporatti S, Radtchenko IL, Donath E, Möhwald H. Polyelectrolyte multilayer capsule permeability control. Colloids and Surfaces A: Physicochemical and Engineering Aspects. 2002;198–200(0):535-41.

228. Sukhorukov GB, Antipov AA, Voigt A, Donath E, Möhwald H. pH-Controlled Macromolecule Encapsulation in and Release from Polyelectrolyte Multilayer Nanocapsules. Macromolecular Rapid Communications. 2001;22(1):44-6.

229. Déjugnat C, Haložan D, Sukhorukov GB. Defined Picogram Dose Inclusion and Release of Macromolecules using Polyelectrolyte Microcapsules. Macromolecular Rapid Communications. 2005;26(12):961-7.

230. Wood KC, Boedicker JQ, Lynn DM, Hammond PT. Tunable Drug Release from Hydrolytically Degradable Layer-by-Layer Thin Films. Langmuir : the ACS journal of surfaces and colloids. 2005;21(4):1603-9.

231. Fredin NJ, Zhang J, Lynn DM. Surface Analysis of Erodible Multilayered Polyelectrolyte Films: Nanometer-Scale Structure and Erosion Profiles. Langmuir : the ACS journal of surfaces and colloids. 2005;21(13):5803-11.

232. Quinn JF, Caruso F. Facile Tailoring of Film Morphology and Release Properties Using Layer-by-Layer Assembly of Thermoresponsive Materials. Langmuir : the ACS journal of surfaces and colloids. 2003;20(1):20-2.

233. Quinn JF, Caruso F. Thermoresponsive Nanoassemblies: Layer-by-Layer Assembly of Hydrophilic−Hydrophobic Alternating Copolymers. Macromolecules. 2005;38(8):3414-9.

234. Volodkin DV, Madaboosi N, Blacklock J, Skirtach AG, Möhwald H. Surface-Supported Multilayers Decorated with Bio-active Material Aimed at Light-Triggered Drug Delivery†. Langmuir : the ACS journal of surfaces and colloids. 2009;25(24):14037-43.

235. Mertz D, Hemmerle J, Boulmedais F, Voegel J-C, Lavalle P, Schaaf P. Polyelectrolyte multilayer films under mechanical stretch. Soft Matter. 2007;3(11):1413-20.

236. Mertz D, Vogt C, Hemmerle J, Mutterer J, Ball V, Voegel J-C, et al. Mechanotransductive surfaces for reversible biocatalysis activation. Nature materials. 2009;8(9):731-5.

237. Recksiedler CL, Deore BA, Freund MS. A Novel Layer-by-Layer Approach for the Fabrication of Conducting Polymer/RNA Multilayer Films for Controlled Release. Langmuir : the ACS journal of surfaces and colloids. 2006;22(6):2811-5.

238. Wood KC, Zacharia NS, Schmidt DJ, Wrightman SN, Andaya BJ, Hammond PT. Electroactive controlled release thin films. Proceedings of the National Academy of Sciences. 2008;105(7):2280-5.

239. Manna U, Patil S. Glucose-Triggered Drug Delivery from Borate Mediated Layer-by-Layer Self-Assembly. ACS Applied Materials & Interfaces. 2010;2(5):1521-7.

240. Qiu X, Leporatti S, Donath E, Möhwald H. Studies on the Drug Release Properties of Polysaccharide Multilayers Encapsulated Ibuprofen Microparticles. Langmuir : the ACS journal of surfaces and colloids. 2001;17(17):5375-80.

241. Pargaonkar N, Lvov YM, Li N, Steenekamp JH, de Villiers MM. Controlled Release of Dexamethasone from Microcapsules Produced by Polyelectrolyte Layer-by-Layer Nanoassembly. Pharmaceutical research. 2005;22(5):826-35.

242. Anal AK, Stevens WF. Chitosan-alginate multilayer beads for controlled release of ampicillin. International journal of pharmaceutics. 2005;290(1-2):45-54. Epub 2005/01/25.

243. Agarwal A, Lvov Y, Sawant R, Torchilin V. Stable nanocolloids of poorly soluble drugs with high drug content prepared using the combination of sonication and layer-by-layer technology. Journal of controlled release : official journal of the Controlled Release Society. 2008;128(3):255-60. Epub 2008/05/16.

244. Zheng J, Yue X, Dai Z, Wang Y, Liu S, Yan X. Novel iron-polysaccharide multilayered microcapsules for controlled insulin release. Acta biomaterialia. 2009;5(5):1499-507. Epub 2009/02/24.

245. Zhao J, Cui Y, Wang A, Fei J, Yang Y, Li J. Side effect reduction of encapsulated hydrocortisone crystals by insulin/alginate shells. Langmuir : the ACS journal of surfaces and colloids. 2011;27(4):1499-504. Epub 2010/11/12.

246. Nadiri A, Kuchler-Bopp S, Mjahed H, Hu B, Haikel Y, Schaaf P, et al. Cell apoptosis control using BMP4 and noggin embedded in a polyelectrolyte multilayer film. Small. 2007;3(9):1577-83. Epub 2007/08/21.

247. Dierich A, Le Guen E, Messaddeq N, Stoltz JF, Netter P, Schaaf P, et al. Bone Formation Mediated by Synergy-Acting Growth Factors Embedded in a Polyelectrolyte Multilayer Film. Advanced Materials. 2007;19(5):693-7.

248. Haidar ZS, Tabrizian M, Hamdy RC. A hybrid rhOP-1 delivery system enhances new bone regeneration and consolidation in a rabbit model of distraction osteogenesis. Growth factors. 2010;28(1):44-55. Epub 2009/12/02.

249. Jessel N, Oulad-Abdelghani M, Meyer F, Lavalle P, Haikel Y, Schaaf P, et al. Multiple and time-scheduled in situ DNA delivery mediated by beta-cyclodextrin embedded in a polyelectrolyte multilayer. Proceedings of the National Academy of Sciences of the United States of America. 2006;103(23):8618-21. Epub 2006/06/01.

250. Meyer F, Ball V, Schaaf P, Voegel JC, Ogier J. Polyplex-embedding in polyelectrolyte multilayers for gene delivery. Biochimica et biophysica acta. 2006;1758(3):419-22. Epub 2006/01/18.

251. Dimitrova M, Arntz Y, Lavalle P, Meyer F, Wolf M, Schuster C, et al. Adenoviral Gene Delivery from Multilayered Polyelectrolyte Architectures. Advanced functional materials. 2007;17(2):233-45.

252. Zhang J, Chua LS, Lynn DM. Multilayered thin films that sustain the release of functional DNA under physiological conditions. Langmuir : the ACS journal of surfaces and colloids. 2004;20(19):8015-21. Epub 2004/09/08.

253. Jewell CM, Zhang J, Fredin NJ, Lynn DM. Multilayered polyelectrolyte films promote the direct and localized delivery of DNA to cells. Journal of controlled release : official journal of the Controlled Release Society. 2005;106(1-2):214-23. Epub 2005/06/28.

254. Jewell CM, Zhang J, Fredin NJ, Wolff MR, Hacker TA, Lynn DM. Release of plasmid DNA from intravascular stents coated with ultrathin multilayered polyelectrolyte films. Biomacromolecules. 2006;7(9):2483-91. Epub 2006/09/12.

255. Cai K, Hu Y, Wang Y, Yang L. Build up of multilayered thin films with chitosan/DNA pairs on poly(D,L-lactic acid) films: physical chemistry and sustained

release behavior. Journal of biomedical materials research Part A. 2008;84(2):516-22. Epub 2007/07/10.

256. Cai K, Hu Y, Luo Z, Kong T, Lai M, Sui X, et al. Cell-specific gene transfection from a gene-functionalized poly(d,l-lactic acid) substrate fabricated by the layer-by-layer assembly technique. Angewandte Chemie. 2008;47(39):7479-81. Epub 2008/08/21.

257. Lu ZZ, Wu J, Sun TM, Ji J, Yan LF, Wang J. Biodegradable polycation and plasmid DNA multilayer film for prolonged gene delivery to mouse osteoblasts. Biomaterials. 2008;29(6):733-41. Epub 2007/11/13.

258. Blacklock J, You YZ, Zhou QH, Mao G, Oupicky D. Gene delivery in vitro and in vivo from bioreducible multilayered polyelectrolyte films of plasmid DNA. Biomaterials. 2009;30(5):939-50. Epub 2008/11/18.

259. Saurer EM, Yamanouchi D, Liu B, Lynn DM. Delivery of plasmid DNA to vascular tissue in vivo using catheter balloons coated with polyelectrolyte multilayers. Biomaterials. 2011;32(2):610-8. Epub 2010/10/12.

260. Zhu H, Ji J, Barbosa MA, Shen J. Protein electrostatic self-assembly on poly(DL-lactide) scaffold to promote osteoblast growth. Journal of biomedical materials research Part B, Applied biomaterials. 2004;71(1):159-65. Epub 2004/09/16.

261. Zhu H, Ji J, Shen J. Osteoblast growth promotion by protein electrostatic self-assembly on biodegradable poly(lactide). Journal of biomaterials science Polymer edition. 2005;16(6):761-74. Epub 2005/07/21.

262. Gong Y, Zhu Y, Liu Y, Ma Z, Gao C, Shen J. Layer-by-layer assembly of chondroitin sulfate and collagen on aminolyzed poly(L-lactic acid) porous scaffolds to enhance their chondrogenesis. Acta biomaterialia. 2007;3(5):677-85. Epub 2007/06/20.

263. Yamanlar S, Sant S, Boudou T, Picart C, Khademhosseini A. Surface functionalization of hyaluronic acid hydrogels by polyelectrolyte multilayer films. Biomaterials. 2011;32(24):5590-9. Epub 2011/05/17.

264. Lee J, Shanbhag S, Kotov NA. Inverted colloidal crystals as three-dimensional microenvironments for cellular co-cultures. Journal of Materials Chemistry. 2006;16(35):3558-64.

265. Sakai S, Yamada Y, Yamaguchi T, Ciach T, Kawakami K. Surface immobilization of poly(ethyleneimine) and plasmid DNA on electrospun poly(L-lactic acid) fibrous mats using a layer-by-layer approach for gene delivery. Journal of biomedical materials research Part A. 2009;88(2):281-7. Epub 2008/02/09.

266. Macdonald ML, Samuel RE, Shah NJ, Padera RF, Beben YM, Hammond PT. Tissue integration of growth factor-eluting layer-by-layer polyelectrolyte multilayer coated implants. Biomaterials. 2011;32(5):1446-53. Epub 2010/11/19.

267. Doroski DM, Brink KS, Temenoff JS. Techniques for biological characterization of tissue-engineered tendon and ligament. Biomaterials. 2007;28(2):187-202. Epub 2006/09/20.

268. Georgakoudi I, Rice WL, Hronik-Tupaj M, Kaplan DL. Optical spectroscopy and imaging for the noninvasive evaluation of engineered tissues. Tissue engineering Part B, Reviews. 2008;14(4):321-40. Epub 2008/10/11.

269. Smith LE, Smallwood R, Macneil S. A comparison of imaging methodologies for 3D tissue engineering. Microscopy research and technique. 2010;73(12):1123-33. Epub 2010/10/29.

270. Kiernan JA. Histological and histochemical methods : theory and practice. 3rd ed. Oxford ; Boston: Butterworth Heinemann; 1999. x, 502 p. p.

271. Bancroft JD, Stevens A. Theory and practice of histological techniques. 3rd ed. Edinburgh ; New York: Churchill Livingstone; 1990. xiv, 726 p. p.

272. Garcia Y, Breen A, Burugapalli K, Dockery P, Pandit A. Stereological methods to assess tissue response for tissue-engineered scaffolds. Biomaterials. 2007;28(2):175-86. Epub 2006/09/12.

273. Nehal KS, Gareau D, Rajadhyaksha M. Skin imaging with reflectance confocal microscopy. Seminars in cutaneous medicine and surgery. 2008;27(1):37-43. Epub 2008/05/20.

274. Huzaira M, Rius F, Rajadhyaksha M, Anderson RR, Gonzalez S. Topographic variations in normal skin, as viewed by in vivo reflectance confocal microscopy. The Journal of investigative dermatology. 2001;116(6):846-52. Epub 2001/06/16.

275. Theer P, Hasan MT, Denk W. Two-photon imaging to a depth of 1000 microm in living brains by use of a Ti:Al2O3 regenerative amplifier. Optics letters. 2003;28(12):1022-4. Epub 2003/07/03.

276. Helmchen F, Denk W. Deep tissue two-photon microscopy. Nature methods. 2005;2(12):932-40. Epub 2005/11/22.

277. So PT, Dong CY, Masters BR, Berland KM. Two-photon excitation fluorescence microscopy. Annual review of biomedical engineering. 2000;2:399-429. Epub 2001/11/10.

278. Masters BR, So PT, Gratton E. Multiphoton excitation microscopy of in vivo human skin. Functional and morphological optical biopsy based on three-dimensional imaging, lifetime measurements and fluorescence spectroscopy. Annals of the New York Academy of Sciences. 1998;838:58-67. Epub 1998/03/25.

279. Squirrell JM, Schramm RD, Paprocki AM, Wokosin DL, Bavister BD. Imaging mitochondrial organization in living primate oocytes and embryos using multiphoton

microscopy. Microscopy and microanalysis : the official journal of Microscopy Society of America, Microbeam Analysis Society, Microscopical Society of Canada. 2003;9(3):190-201. Epub 2003/06/17.

280. Schenke-Layland K. Non-invasive multiphoton imaging of extracellular matrix structures. Journal of biophotonics. 2008;1(6):451-62. Epub 2009/04/04.

281. Ho ST, Hutmacher DW. A comparison of micro CT with other techniques used in the characterization of scaffolds. Biomaterials. 2006;27(8):1362-76. Epub 2005/09/22.

282. Pawley J. The development of field-emission scanning electron microscopy for imaging biological surfaces. Scanning. 1997;19(5):324-36. Epub 1997/08/01.

283. Pesez M, Bartos J. Colorimetric and fluorimetric analysis of organic compounds and drugs. New York: M. Dekker; 1974. xiv, 672 p. p.

284. Quant-it PicoGreen dsDNA reagent and kits. In: Molecular Probes I, editor. 2008.

285. Hoescht stains In: Molecular Probes I, editor. 2005.

286. Park JC, Hwang YS, Suh H. Viability evaluation of engineered tissues. Yonsei medical journal. 2000;41(6):836-44. Epub 2001/02/24.

287. Mosmann T. Rapid colorimetric assay for cellular growth and survival: Application to proliferation and cytotoxicity assays. Journal of Immunological Methods. 1983;65(1–2):55-63.

288. Marshall NJ, Goodwin CJ, Holt SJ. A critical assessment of the use of microculture tetrazolium assays to measure cell growth and function. Growth regulation. 1995;5(2):69-84.

289. Paull KD, Shoemaker RH, Boyd MR, Parsons JL, Risbood PA, Barbera WA, et al. The synthesis of XTT: A new tetrazolium reagent that is bioreducible to a water-soluble formazan. Journal of Heterocyclic Chemistry. 1988;25(3):911-4.

290. Ishiyama M, Sasamoto K, Shiga M, Ohkura Y, Ueno K, Nishiyama K, et al. Novel disulfonated tetrazolium salt that can be reduced to a water-soluble formazan and its application to the assay of lactate dehydrogenase. The Analyst. 1995;120(1):113-6.

291. LIVE/DEAD viability/cytotoxicity kit for mammalian cells. In: Molecular Probes I, editor. 2005.

292. Kaneshiro ES, Wyder MA, Wu Y-P, Cushion MT. Reliability of calcein acetoxy methyl ester and ethidium homodimer or propidium iodide for viability assessment of microbes. Journal of Microbiological Methods. 1993;17(1):1-16.

293. Gratzner HG. Monoclonal Antibody to 5-Bromo- and 5-Iododeoxyuridine: A New Reagent for Detection of DNA Replication. Science. 1982;218(4571):474-5.

294. Li X, Darzynkiewicz Z. Labelling DNA strand breaks with BrdUTP. Detection of apoptosis and cell proliferation. Cell Proliferation. 1995;28(11):571-9.

295. Gavrieli Y, Sherman Y, Ben-Sasson SA. Identification of programmed cell death in situ via specific labeling of nuclear DNA fragmentation. The Journal of Cell Biology. 1992;119(3):493-501.

296. Gorczyca W, Gong J, Darzynkiewicz Z. Detection of DNA Strand Breaks in Individual Apoptotic Cells by the in Situ Terminal Deoxynucleotidyl Transferase and Nick Translation Assays. Cancer Research. 1993;53(8):1945-51.

297. Alberts B. Molecular biology of the cell. 5th ed. New York: Garland Science; 2008.

298. Van Dilla MA, Truiullo TT, Mullaney PF, Coultex JR. Cell Microfluorometry: A Method for Rapid Fluorescence Measurement. Science. 1969;163(3872):1213-4.

299. Hulett HR, Bonner WA, Barrett J, Herzenberg LA. Cell Sorting: Automated Separation of Mammalian Cells as a Function of Intracellular Fluorescence. Science. 1969;166(3906):747-9.

300. Steiner G, Koch E. Trends in Fourier transform infrared spectroscopic imaging. Analytical and Bioanalytical Chemistry. 2009;394(3):671-8.

301. Swain RJ, Stevens MM. Raman microspectroscopy for non-invasive biochemical analysis of single cells. Biochemical Society transactions. 2007;35(Pt 3):544-9. Epub 2007/05/22.

302. Krafft C, Dietzek B, Popp J. Raman and CARS microspectroscopy of cells and tissues. The Analyst. 2009;134(6):1046-57. Epub 2009/05/29.

303. Pezacki JP, Blake JA, Danielson DC, Kennedy DC, Lyn RK, Singaravelu R. Chemical contrast for imaging living systems: molecular vibrations drive CARS microscopy. Nature chemical biology. 2011;7(3):137-45. Epub 2011/02/16.

304. Lasch P, Chiriboga L, Yee H, Diem M. Infrared spectroscopy of human cells and tissue: detection of disease. Technology in cancer research & treatment. 2002;1(1):1-7. Epub 2003/03/05.

305. Boskey AL, Mendelsohn R. Infrared spectroscopic characterization of mineralized tissues. Vibrational Spectroscopy. 2005;38(1-2):107-14. Epub 2006/05/13.

306. Moore DJ, Rerek ME. Insights into the molecular organization of lipids in the skin barrier from infrared spectroscopy studies of stratum corneum lipid models. Acta dermato-venereologica Supplementum. 2000;208:16-22. Epub 2000/07/08.

307. Walsh MJ, Hammiche A, Fellous TG, Nicholson JM, Cotte M, Susini J, et al. Tracking the cell hierarchy in the human intestine using biochemical signatures derived by mid-infrared microspectroscopy. Stem Cell Research. 2009;3(1):15-27.

308. Diem M, Chiriboga L, Yee H. Infrared spectroscopy of human cells and tissue. VIII. Strategies for analysis of infrared tissue mapping data and applications to liver tissue. Biopolymers. 2000;57(5):282-90. Epub 2000/08/25.

309. Ou-Yang H, Paschalis EP, Mayo WE, Boskey AL, Mendelsohn R. Infrared microscopic imaging of bone: spatial distribution of CO3(2-). Journal of bone and mineral research : the official journal of the American Society for Bone and Mineral Research. 2001;16(5):893-900. Epub 2001/05/09.

310. Wood BR, Bambery KR, Evans CJ, Quinn MA, McNaughton D. A three-dimensional multivariate image processing technique for the analysis of FTIR spectroscopic images of multiple tissue sections. BMC medical imaging. 2006;6:12. Epub 2006/10/04.

311. Matthaus C, Boydston-White S, Miljkovic M, Romeo M, Diem M. Raman and infrared microspectral imaging of mitotic cells. Applied spectroscopy. 2006;60(1):1-8. Epub 2006/02/04.

312. Kazanci M, Roschger P, Paschalis EP, Klaushofer K, Fratzl P. Bone osteonal tissues by Raman spectral mapping: orientation-composition. Journal of structural biology. 2006;156(3):489-96. Epub 2006/08/26.

313. Brackmann C, Esguerra M, Olausson D, Delbro D, Krettek A, Gatenholm P, et al. Coherent anti-Stokes Raman scattering microscopy of human smooth muscle cells in bioengineered tissue scaffolds. Journal of biomedical optics. 2011;16(2):021115. Epub 2011/03/03.

314. Brackmann C, Zaborowska M, Sundberg J, Gatenholm P, Enejder A. In situ imaging of collagen synthesis by osteoprogenitor cells in microporous bacterial cellulose scaffolds. Tissue engineering Part C, Methods. 2012;18(3):227-34. Epub 2011/10/21.

315. Wegener J, Keese CR, Giaever I. Electric cell-substrate impedance sensing (ECIS) as a noninvasive means to monitor the kinetics of cell spreading to artificial surfaces. Experimental cell research. 2000;259(1):158-66. Epub 2000/08/16.

316. Arndt S, Seebach J, Psathaki K, Galla HJ, Wegener J. Bioelectrical impedance assay to monitor changes in cell shape during apoptosis. Biosensors & bioelectronics. 2004;19(6):583-94. Epub 2003/12/20.

317. Keese CR, Wegener J, Walker SR, Giaever I. Electrical wound-healing assay for cells in vitro. Proceedings of the National Academy of Sciences of the United States of America. 2004;101(6):1554-9. Epub 2004/01/30.

318. Luong JH, Habibi-Rezaei M, Meghrous J, Xiao C, Male KB, Kamen A. Monitoring motility, spreading, and mortality of adherent insect cells using an impedance sensor. Analytical chemistry. 2001;73(8):1844-8. Epub 2001/05/08.

319. De Blasio BF, Laane M, Walmann T, Giaever I. Combining optical and electrical impedance techniques for quantitative measurement of confluence in MDCK-I cell cultures. BioTechniques. 2004;36(4):650-4, 6, 8 passim. Epub 2004/04/20.

320. Bagnaninchi PO, Drummond N. Real-time label-free monitoring of adipose-derived stem cell differentiation with electric cell-substrate impedance sensing. Proceedings of the National Academy of Sciences of the United States of America. 2011;108(16):6462-7. Epub 2011/04/06.

321. Hilber W, Lornejad-Schäfer MR, Schäfer C, Lederer T, Schröder K, Jakoby B. Impedance Spectroscopy of a Human Hepatic 3D Cell Model in-Vitro: A Comparative Study with Differently Shaped Electrodes. Procedia Engineering. 2011;25(0):1000-3.

322. Hildebrandt C, Buth H, Cho S, Impidjati, Thielecke H. Detection of the osteogenic differentiation of mesenchymal stem cells in 2D and 3D cultures by electrochemical impedance spectroscopy. Journal of biotechnology. 2010;148(1):83-90. Epub 2010/01/21.

323. Metherall P, Barber DC, Smallwood RH, Brown BH. Three-dimensional electrical impedance tomography. Nature. 1996;380(6574):509-12. Epub 1996/04/11.

324. Tidswell AT, Gibson A, Bayford RH, Holder DS. Electrical impedance tomography of human brain activity with a two-dimensional ring of scalp electrodes. Physiological measurement. 2001;22(1):167-75. Epub 2001/03/10.

325. Zou Y, Guo Z. A review of electrical impedance techniques for breast cancer detection. Medical engineering & physics. 2003;25(2):79-90. Epub 2003/01/23.

326. Borsic A, Halter R, Wan Y, Hartov A, Paulsen KD. Sensitivity study and optimization of a 3D electric impedance tomography prostate probe. Physiological measurement. 2009;30(6):S1-18. Epub 2009/06/06.

327. Tully-Dartez S, Cardenas HE, Sit PF. Pore characteristics of chitosan scaffolds studied by electrochemical impedance spectroscopy. Tissue engineering Part C, Methods. 2010;16(3):339-45. Epub 2009/07/08.

328. Bagnaninchi PO, Dikeakos M, Veres T, Tabrizian M. Towards on-line monitoring of cell growth in microporous scaffolds: Utilization and interpretation of complex permittivity measurements. Biotechnology and bioengineering. 2003;84(3):343-50. Epub 2003/09/12.

329. Dziong D, Bagnaninchi PO, Kearney RE, Tabrizian M. Nondestructive online in vitro monitoring of pre-osteoblast cell proliferation within microporous polymer scaffolds. IEEE transactions on nanobioscience. 2007;6(3):249-58. Epub 2007/10/12.

330. Daoud J, Asami K, Rosenberg L, Tabrizian M. Dielectric spectroscopy for non-invasive monitoring of epithelial cell differentiation within three-dimensional scaffolds. Physics in medicine and biology. 2012;57(16):5097-112. Epub 2012/07/28.

331. Mizutani R, Suzuki Y. X-ray microtomography in biology. Micron. 2012;43(2–3):104-15.

332. Bertoldi S, Farè S, Tanzi MC. Assessment of scaffold porosity: the new route of micro-CT. Journal of applied biomaterials & biomechanics : JABB. 2011;9(3):165-75.

333. Barbetta A, Bedini R, Pecci R, Dentini M. Role of X-ray microtomography in tissue engineering. Annali dell'Istituto superiore di sanita. 2012;48(1):10-8. Epub 2012/03/30.

334. Bonse U, Busch F. X-ray computed microtomography (μCT) using synchrotron radiation (SR). Progress in Biophysics and Molecular Biology. 1996;65(1–2):133-69.

335. Weiss P, Obadia L, Magne D, Bourges X, Rau C, Weitkamp T, et al. Synchrotron X-ray microtomography (on a micron scale) provides three-dimensional imaging representation of bone ingrowth in calcium phosphate biomaterials. Biomaterials. 2003;24(25):4591-601. Epub 2003/09/03.

336. Jones AC, Arns CH, Sheppard AP, Hutmacher DW, Milthorpe BK, Knackstedt MA. Assessment of bone ingrowth into porous biomaterials using MICRO-CT. Biomaterials. 2007;28(15):2491-504. Epub 2007/03/06.

337. Morris DE, Mather ML, Simon CG, Jr., Crowe JA. Time-optimized X-ray micro-CT imaging of polymer based scaffolds. Journal of biomedical materials research Part B, Applied biomaterials. 2011. Epub 2011/11/25.

338. Jones JR, Tsigkou O, Coates EE, Stevens MM, Polak JM, Hench LL. Extracellular matrix formation and mineralization on a phosphate-free porous bioactive glass scaffold using primary human osteoblast (HOB) cells. Biomaterials. 2007;28(9):1653-63. Epub 2006/12/19.

339. Rockwood DN, Gil ES, Park SH, Kluge JA, Grayson W, Bhumiratana S, et al. Ingrowth of human mesenchymal stem cells into porous silk particle reinforced silk composite scaffolds: An in vitro study. Acta biomaterialia. 2011;7(1):144-51. Epub 2010/07/27.

340. Kruger EA, Im DD, Bischoff DS, Pereira CT, Huang W, Rudkin GH, et al. In vitro mineralization of human mesenchymal stem cells on three-dimensional type I collagen versus PLGA scaffolds: a comparative analysis. Plastic and reconstructive surgery. 2011;127(6):2301-11. Epub 2011/05/28.

341. Bentley MD, Rodriguez-Porcel M, Lerman A, Sarafov MH, Romero JC, Pelaez LI, et al. Enhanced renal cortical vascularization in experimental hypercholesterolemia. Kidney international. 2002;61(3):1056-63. Epub 2002/02/19.

342. Rai B, Oest ME, Dupont KM, Ho KH, Teoh SH, Guldberg RE. Combination of platelet-rich plasma with polycaprolactone-tricalcium phosphate scaffolds for segmental bone defect repair. Journal of biomedical materials research Part A. 2007;81(4):888-99. Epub 2007/01/20.

343. Patel V, Hoffmann KR, Ionita CN, Keleshis C, Bednarek DR, Rudin S. Rotational micro-CT using a clinical C-arm angiography gantry. Medical physics. 2008;35(10):4757-64. Epub 2008/11/04.

344. Watling CP, Lago N, Benmerah S, FitzGerald JJ, Tarte E, McMahon S, et al. Novel use of X-ray micro computed tomography to image rat sciatic nerve and integration into scaffold. Journal of neuroscience methods. 2010;188(1):39-44. Epub 2010/02/09.

345. Xu H, Othman SF, Magin RL. Monitoring tissue engineering using magnetic resonance imaging. Journal of bioscience and bioengineering. 2008;106(6):515-27. Epub 2009/01/13.

346. Kuperman V. Magnetic resonance imaging : physical principles and applications. San Diego: Academic Press; 2000. xiii, 182 p. p.

347. Laule C, Kozlowski P, Leung E, Li DKB, MacKay AL, Moore GRW. Myelin water imaging of multiple sclerosis at 7 T: Correlations with histopathology. NeuroImage. 2008;40(4):1575-80.

348. Xu H, Othman SF, Hong L, Peptan IA, Magin RL. Magnetic resonance microscopy for monitoring osteogenesis in tissue-engineered construct in vitro. Physics in medicine and biology. 2006;51(3):719-32. Epub 2006/01/21.

349. Chesnick IE, Avallone FA, Leapman RD, Landis WJ, Eidelman N, Potter K. Evaluation of bioreactor-cultivated bone by magnetic resonance microscopy and FTIR microspectroscopy. Bone. 2007;40(4):904-12.

350. Major JL, Meade TJ. Bioresponsive, cell-penetrating, and multimeric MR contrast agents. Accounts of chemical research. 2009;42(7):893-903. Epub 2009/06/23.

351. Washburn NR, Weir M, Anderson P, Potter K. Bone formation in polymeric scaffolds evaluated by proton magnetic resonance microscopy and X-ray microtomography. Journal of biomedical materials research Part A. 2004;69(4):738-47. Epub 2004/05/27.

352. Novotny JE, Turka CM, Jeong C, Wheaton AJ, Li C, Presedo A, et al. Biomechanical and magnetic resonance characteristics of a cartilage-like equivalent generated in a suspension culture. Tissue engineering. 2006;12(10):2755-64. Epub 2007/05/24.

353. Ramaswamy S, Gurkan I, Sharma B, Cascio B, Fishbein KW, Spencer RG. Assessment of tissue repair in full thickness chondral defects in the rabbit using magnetic

resonance imaging transverse relaxation measurements. Journal of biomedical materials research Part B, Applied biomaterials. 2008;86(2):375-80. Epub 2007/12/29.

354. Cheng HL, Islam SS, Loai Y, Antoon R, Beaumont M, Farhat WA. Quantitative magnetic resonance imaging assessment of matrix development in cell-seeded natural urinary bladder smooth muscle tissue-engineered constructs. Tissue engineering Part C, Methods. 2010;16(4):643-51. Epub 2009/09/24.

355. Stuckey DJ, Ishii H, Chen QZ, Boccaccini AR, Hansen U, Carr CA, et al. Magnetic resonance imaging evaluation of remodeling by cardiac elastomeric tissue scaffold biomaterials in a rat model of myocardial infarction. Tissue engineering Part A. 2010;16(11):3395-402. Epub 2010/06/10.

356. Miyagi Y, Zeng F, Huang XP, Foltz WD, Wu J, Mihic A, et al. Surgical ventricular restoration with a cell- and cytokine-seeded biodegradable scaffold. Biomaterials. 2010;31(30):7684-94. Epub 2010/07/28.

357. Welsch GH, Mamisch TC, Zak L, Blanke M, Olk A, Marlovits S, et al. Evaluation of cartilage repair tissue after matrix-associated autologous chondrocyte transplantation using a hyaluronic-based or a collagen-based scaffold with morphological MOCART scoring and biochemical T2 mapping: preliminary results. The American journal of sports medicine. 2010;38(5):934-42. Epub 2010/03/26.

358. Othman SF, Curtis ET, Plautz SA, Pannier AK, Butler SD, Xu H. MR elastography monitoring of tissue-engineered constructs. NMR in biomedicine. 2012;25(3):452-63. Epub 2011/03/10.

359. Muthupillai R, Ehman RL. Magnetic resonance elastography. Nature medicine. 1996;2(5):601-3. Epub 1996/05/01.

360. Othman SF, Xu H, Royston TJ, Magin RL. Microscopic magnetic resonance elastography (microMRE). Magnetic resonance in medicine : official journal of the Society of Magnetic Resonance in Medicine / Society of Magnetic Resonance in Medicine. 2005;54(3):605-15. Epub 2005/08/10.

361. Abarrategi A, Fernandez-Valle ME, Desmet T, Castejon D, Civantos A, Moreno-Vicente C, et al. Label-free magnetic resonance imaging to locate live cells in three-dimensional porous scaffolds. Journal of the Royal Society, Interface / the Royal Society. 2012;9(74):2321-31. Epub 2012/03/24.

362. Huang D, Swanson EA, Lin CP, Schuman JS, Stinson WG, Chang W, et al. Optical coherence tomography. Science. 1991;254(5035):1178-81. Epub 1991/11/22.

363. Fujimoto JG, Brezinski ME, Tearney GJ, Boppart SA, Bouma B, Hee MR, et al. Optical biopsy and imaging using optical coherence tomography. Nature medicine. 1995;1(9):970-2. Epub 1995/09/01.

364. Schmitt JM, Knuttel A, Yadlowsky M, Eckhaus MA. Optical-coherence tomography of a dense tissue: statistics of attenuation and backscattering. Physics in medicine and biology. 1994;39(10):1705.

365. Aguirre AD, Hsiung P, Ko TH, Hartl I, Fujimoto JG. High-resolution optical coherence microscopy for high-speed, in vivo cellular imaging. Optics letters. 2003;28(21):2064-6. Epub 2003/11/01.

366. Choma MA, Ellerbee AK, Yang C, Creazzo TL, Izatt JA. Spectral-domain phase microscopy. Optics letters. 2005;30(10):1162-4. Epub 2005/06/11.

367. Liang X, Graf BW, Boppart SA. Imaging engineered tissues using structural and functional optical coherence tomography. Journal of biophotonics. 2009;2(11):643-55. Epub 2009/08/13.

368. Yang Y, Bagnaninchi PO, Ahearne M, Wang RK, Liu KK. A novel optical coherence tomography-based micro-indentation technique for mechanical characterization of hydrogels. Journal of the Royal Society, Interface / the Royal Society. 2007;4(17):1169-73. Epub 2007/05/03.

369. Yang Y, Dubois A, Qin XP, Li J, El Haj A, Wang RK. Investigation of optical coherence tomography as an imaging modality in tissue engineering. Physics in medicine and biology. 2006;51(7):1649-59. Epub 2006/03/23.

370. Bagnaninchi PO, Yang Y, Zghoul N, Maffulli N, Wang RK, Haj AJ. Chitosan microchannel scaffolds for tendon tissue engineering characterized using optical coherence tomography. Tissue engineering. 2007;13(2):323-31. Epub 2007/05/24.

371. Tan W, Oldenburg AL, Norman JJ, Desai TA, Boppart SA. Optical coherence tomography of cell dynamics in three-dimensional tissue models. Optics express. 2006;14(16):7159-71. Epub 2006/08/07.

372. Ko HJ, Tan W, Stack R, Boppart SA. Optical coherence elastography of engineered and developing tissue. Tissue engineering. 2006;12(1):63-73. Epub 2006/02/28.

373. Patil CA, Kalkman J, Faber DJ, Nyman JS, van Leeuwen TG, Mahadevan-Jansen A. Integrated system for combined Raman spectroscopy-spectral domain optical coherence tomography. Journal of biomedical optics. 2011;16(1):011007. Epub 2011/02/02.

374. Bagnaninchi PO, Holmes C, Drummond N, Daoud J, Tabrizian M. Two-dimensional and three-dimensional viability measurements of adult stem cells with optical coherence phase microscopy. Journal of biomedical optics. 2011;16(8):086003. Epub 2011/09/08.

375. Dunkers JP, Lee YJ, Chatterjee K. Single cell viability measurements in 3D scaffolds using in situ label free imaging by optical coherence microscopy. Biomaterials. 2012;33(7):2119-26. Epub 2011/12/24.

376. Thierry B, Kujawa P, Tkaczyk C, Winnik FM, Bilodeau L, Tabrizian M. Delivery platform for hydrophobic drugs: prodrug approach combined with self-assembled multilayers. Journal of the American Chemical Society. 2005;127(6):1626-7. Epub 2005/02/11.

377. Shi C, Zhu Y, Ran X, Wang M, Su Y, Cheng T. Therapeutic potential of chitosan and its derivatives in regenerative medicine. The Journal of surgical research. 2006;133(2):185-92. Epub 2006/02/07.

378. Hillberg AL, Holmes CA, Tabrizian M. Effect of genipin cross-linking on the cellular adhesion properties of layer-by-layer assembled polyelectrolyte films. Biomaterials. 2009;30(27):4463-70. Epub 2009/06/13.

379. Miao Z, Tardif K, Cloutier I, Lemieux C, Tanguay JF, Winnik FM, editors. Stem-cell growth on a phosphorylcholine-modif led chitosan-based matrix. Proceedings of the ACS Division of Polymeric Materials: Science & Engineering 2008; New Orleans, Louisiana, USA.

380. Son YJ, Jang JS, Cho YW, Chung H, Park RW, Kwon IC, et al. Biodistribution and anti-tumor efficacy of doxorubicin loaded glycol-chitosan nanoaggregates by EPR effect. Journal of controlled release : official journal of the Controlled Release Society. 2003;91(1-2):135-45. Epub 2003/08/23.

381. Yoo HS, Lee JE, Chung H, Kwon IC, Jeong SY. Self-assembled nanoparticles containing hydrophobically modified glycol chitosan for gene delivery. Journal of controlled release : official journal of the Controlled Release Society. 2005;103(1):235-43. Epub 2005/02/16.

382. Amsden BG, Sukarto A, Knight DK, Shapka SN. Methacrylated glycol chitosan as a photopolymerizable biomaterial. Biomacromolecules. 2007;8(12):3758-66. Epub 2007/11/23.

383. Knight DK, Shapka SN, Amsden BG. Structure, depolymerization, and cytocompatibility evaluation of glycol chitosan. Journal of biomedical materials research Part A. 2007;83(3):787-98. Epub 2007/06/15.

384. Huang YC, Simmons C, Kaigler D, Rice KG, Mooney DJ. Bone regeneration in a rat cranial defect with delivery of PEI-condensed plasmid DNA encoding for bone morphogenetic protein-4 (BMP-4). Gene therapy. 2005;12(5):418-26. Epub 2005/01/14.

385. Kim K, Luu YK, Chang C, Fang D, Hsiao BS, Chu B, et al. Incorporation and controlled release of a hydrophilic antibiotic using poly(lactide-co-glycolide)-based electrospun nanofibrous scaffolds. Journal of controlled release : official journal of the Controlled Release Society. 2004;98(1):47-56. Epub 2004/07/13.

386. Landers R, Hubner U, Schmelzeisen R, Mulhaupt R. Rapid prototyping of scaffolds derived from thermoreversible hydrogels and tailored for applications in tissue engineering. Biomaterials. 2002;23(23):4437-47. Epub 2002/09/27.

387. Landers R, Pfister A, Hübner U, John H, Schmelzeisen R, Mülhaupt R. Fabrication of soft tissue engineering scaffolds by means of rapid prototyping techniques. Journal of Materials Science. 2002;37(15):3107-16.

388. Ai H, Jones SA, Lvov YM. Biomedical applications of electrostatic layer-by-layer nano-assembly of polymers, enzymes, and nanoparticles. Cell biochemistry and biophysics. 2003;39(1):23-43. Epub 2003/07/02.

389. Picart C. Polyelectrolyte multilayer films: from physico-chemical properties to the control of cellular processes. Current medicinal chemistry. 2008;15(7):685-97. Epub 2008/03/14.

390. Kujawa P, Schmauch G, Viitala T, Badia A, Winnik FM. Construction of viscoelastic biocompatible films via the layer-by-layer assembly of hyaluronan and phosphorylcholine-modified chitosan. Biomacromolecules. 2007;8(10):3169-76. Epub 2007/09/14.

391. Brandrup J, Immergut EH, Grulke EA, Abe A, Bloch DR. Polymer Handbook (4th Edition). John Wiley & Sons.

392. Noh H, Vogler EA. Volumetric interpretation of protein adsorption: mass and energy balance for albumin adsorption to particulate adsorbents with incrementally increasing hydrophilicity. Biomaterials. 2006;27(34):5801-12. Epub 2006/08/25.

393. Washburn NR, Yamada KM, Simon CG, Jr., Kennedy SB, Amis EJ. High-throughput investigation of osteoblast response to polymer crystallinity: influence of nanometer-scale roughness on proliferation. Biomaterials. 2004;25(7-8):1215-24. Epub 2003/12/04.

394. Eisenbarth E, Velten D, Muller M, Thull R, Breme J. Nanostructured niobium oxide coatings influence osteoblast adhesion. Journal of biomedical materials research Part A. 2006;79(1):166-75. Epub 2006/06/22.

395. Lee JH, Khang G, Lee JW, Lee HB. Interaction of Different Types of Cells on Polymer Surfaces with Wettability Gradient. Journal of colloid and interface science. 1998;205(2):323-30. Epub 1998/12/16.

396. Wilson CJ, Clegg RE, Leavesley DI, Pearcy MJ. Mediation of biomaterial-cell interactions by adsorbed proteins: a review. Tissue engineering. 2005;11(1-2):1-18. Epub 2005/03/02.

397. Yamauchi F, Kato K, Iwata H. Layer-by-layer assembly of poly(ethyleneimine) and plasmid DNA onto transparent indium-tin oxide electrodes for temporally and

spatially specific gene transfer. Langmuir : the ACS journal of surfaces and colloids. 2005;21(18):8360-7. Epub 2005/08/24.

398. Bengali Z, Rea JC, Gibly RF, Shea LD. Efficacy of immobilized polyplexes and lipoplexes for substrate-mediated gene delivery. Biotechnology and bioengineering. 2009;102(6):1679-91. Epub 2009/01/17.

399. Brito LA, Chandrasekhar S, Little SR, Amiji MM. In vitro and in vivo studies of local arterial gene delivery and transfection using lipopolyplexes-embedded stents. Journal of biomedical materials research Part A. 2010;93(1):325-36. Epub 2009/07/02.

400. Zhang Q, Cheng SX, Zhang XZ, Zhuo RX. Water soluble polymer protected lipofectamine 2000/DNA complexes for solid-phase transfection. Macromolecular bioscience. 2009;9(12):1262-71. Epub 2009/11/12.

401. Yamauchi F, Koyamatsu Y, Kato K, Iwata H. Layer-by-layer assembly of cationic lipid and plasmid DNA onto gold surface for stent-assisted gene transfer. Biomaterials. 2006;27(18):3497-504. Epub 2006/02/21.

402. Holmes CA, Tabrizian M. Enhanced MC3T3 preosteoblast viability and adhesion on polyelectrolyte multilayer films composed of glycol-modified chitosan and hyaluronic acid. Journal of biomedical materials research Part A. 2011. Epub 2011/11/30.

403. Son KK, Tkach D, Patel DH. Zeta potential of transfection complexes formed in serum-free medium can predict in vitro gene transfer efficiency of transfection reagent. Biochimica et biophysica acta. 2000;1468(1-2):11-4. Epub 2000/10/06.

404. Srinivasan C, Burgess DJ. Optimization and characterization of anionic lipoplexes for gene delivery. Journal of controlled release : official journal of the Controlled Release Society. 2009;136(1):62-70. Epub 2009/04/01.

405. Hsu CY, Uludag H. Effects of size and topology of DNA molecules on intracellular delivery with non-viral gene carriers. BMC biotechnology. 2008;8:23. Epub 2008/03/04.

406. Ye L, Haider H, Tan R, Su L, Law PK, Zhang W, et al. Angiomyogenesis using liposome based vascular endothelial growth factor-165 transfection with skeletal myoblast for cardiac repair. Biomaterials. 2008;29(13):2125-37. Epub 2008/02/19.

407. Candiani G, Frigerio M, Viani F, Verpelli C, Sala C, Chiamenti L, et al. Dimerizable redox-sensitive triazine-based cationic lipids for in vitro gene delivery. ChemMedChem. 2007;2(3):292-6. Epub 2006/12/28.

408. Decastro M, Saijoh Y, Schoenwolf GC. Optimized cationic lipid-based gene delivery reagents for use in developing vertebrate embryos. Developmental dynamics : an official publication of the American Association of Anatomists. 2006;235(8):2210-9. Epub 2006/06/21.

409. Michel M, Vautier D, Voegel JC, Schaaf P, Ball V. Layer by layer self-assembled polyelectrolyte multilayers with embedded phospholipid vesicles. Langmuir : the ACS journal of surfaces and colloids. 2004;20(12):4835-9. Epub 2005/06/30.

410. Drexler W, Morgner U, Ghanta RK, Kartner FX, Schuman JS, Fujimoto JG. Ultrahigh-resolution ophthalmic optical coherence tomography. Nature medicine. 2001;7(4):502-7. Epub 2001/04/03.

411. Boppart SA, Bouma BE, Pitris C, Southern JF, Brezinski ME, Fujimoto JG. In vivo cellular optical coherence tomography imaging. Nature medicine. 1998;4(7):861-5. Epub 1998/07/14.

412. Fujimoto JG. Optical coherence tomography for ultrahigh resolution in vivo imaging. Nature biotechnology. 2003;21(11):1361-7. Epub 2003/11/05.

413. Ahearne M, Bagnaninchi PO, Yang Y, El Haj AJ. Online monitoring of collagen fibre alignment in tissue-engineered tendon by PSOCT. Journal of tissue engineering and regenerative medicine. 2008;2(8):521-4. Epub 2008/10/29.

414. Jeong K, Turek JJ, Nolte DD. Volumetric motility-contrast imaging of tissue response to cytoskeletal anti-cancer drugs. Optics express. 2007;15(21):14057-64. Epub 2007/10/17.

415. Nolte DD, An R, Turek J, Jeong K. Holographic tissue dynamics spectroscopy. Journal of biomedical optics. 2011;16(8):087004. Epub 2011/09/08.

416. Luo D, Saltzman WM. Enhancement of transfection by physical concentration of DNA at the cell surface. Nature biotechnology. 2000;18(8):893-5. Epub 2000/08/10.

417. Shea LD, Smiley E, Bonadio J, Mooney DJ. DNA delivery from polymer matrices for tissue engineering. Nature biotechnology. 1999;17(6):551-4. Epub 1999/06/29.

418. Huang YC, Connell M, Park Y, Mooney DJ, Rice KG. Fabrication and in vitro testing of polymeric delivery system for condensed DNA. Journal of biomedical materials research Part A. 2003;67(4):1384-92. Epub 2003/11/19.

419. Fang J, Zhu YY, Smiley E, Bonadio J, Rouleau JP, Goldstein SA, et al. Stimulation of new bone formation by direct transfer of osteogenic plasmid genes. Proceedings of the National Academy of Sciences of the United States of America. 1996;93(12):5753-8. Epub 1996/06/11.

420. Luu YK, Kim K, Hsiao BS, Chu B, Hadjiargyrou M. Development of a nanostructured DNA delivery scaffold via electrospinning of PLGA and PLA-PEG block copolymers. Journal of controlled release : official journal of the Controlled Release Society. 2003;89(2):341-53. Epub 2003/04/25.

421. Chun KW, Cho KC, Kim SH, Jeong JH, Park TG. Controlled release of plasmid DNA from biodegradable scaffolds fabricated using a thermally-induced phase-separation method. Journal of biomaterials science Polymer edition. 2004;15(11):1341-53. Epub 2005/01/15.

422. Jang JH, Shea LD. Controllable delivery of non-viral DNA from porous scaffolds. Journal of controlled release : official journal of the Controlled Release Society. 2003;86(1):157-68. Epub 2002/12/20.

423. Levy RJ, Song C, Tallapragada S, DeFelice S, Hinson JT, Vyavahare N, et al. Localized adenovirus gene delivery using antiviral IgG complexation. Gene therapy. 2001;8(9):659-67. Epub 2001/06/15.

424. Zhang J, Lynn DM. Multilayered Films Fabricated from Combinations of Degradable Polyamines: Tunable Erosion and Release of Anionic Polyelectrolytes. Macromolecules. 2006;39(26):8928-35.

425. Yousefi A-M, Gauvin C, Sun L, DiRaddo RW, Fernandes J. Design and fabrication of 3D-plotted polymeric scaffolds in functional tissue engineering. Polymer Engineering & Science. 2007;47(5):608-18.

426. Filion MC, Phillips NC. Toxicity and immunomodulatory activity of liposomal vectors formulated with cationic lipids toward immune effector cells. Biochimica et Biophysica Acta (BBA) - Biomembranes. 1997;1329(2):345-56.

427. Filion MC, Phillips NC. Major limitations in the use of cationic liposomes for DNA delivery. International journal of pharmaceutics. 1998;162(1–2):159-70.

428. Sekar TV, Foygel K, Willmann JK, Paulmurugan R. Dual-therapeutic reporter genes fusion for enhanced cancer gene therapy and imaging. Gene therapy. 2012. Epub 2012/08/24.

429. Suzuki E, Nakayama M. The mammalian Ced-1 ortholog MEGF10/KIAA1780 displays a novel adhesion pattern. Experimental cell research. 2007;313(11):2451-64. Epub 2007/05/15.

430. Schmidt MH, Furnari FB, Cavenee WK, Bogler O. Epidermal growth factor receptor signaling intensity determines intracellular protein interactions, ubiquitination, and internalization. Proceedings of the National Academy of Sciences of the United States of America. 2003;100(11):6505-10. Epub 2003/05/08.

431. He C-X, Li N, Hu Y-L, Zhu X-M, Li H-J, Han M, et al. Effective Gene Delivery to Mesenchymal Stem Cells Based on the Reverse Transfection and Three-Dimensional Cell Culture System. Pharmaceutical research. 2011;28(7):1577-90.

432. Whittlesey KJ, Shea LD. Nerve growth factor expression by PLG-mediated lipofection. Biomaterials. 2006;27(11):2477-86. Epub 2005/12/01.

433. Lei P, Padmashali RM, Andreadis ST. Cell-controlled and spatially arrayed gene delivery from fibrin hydrogels. Biomaterials. 2009;30(22):3790-9. Epub 2009/04/28.

434. Holladay C, Keeney M, Greiser U, Murphy M, O'Brien T, Pandit A. A matrix reservoir for improved control of non-viral gene delivery. Journal of Controlled Release. 2009;136(3):220-5.

435. Wieland JA, Houchin-Ray TL, Shea LD. Non-viral vector delivery from PEG-hyaluronic acid hydrogels. Journal of Controlled Release. 2007;120(3):233-41.

436. Picart C, Schneider A, Etienne O, Mutterer J, Schaaf P, Egles C, et al. Controlled Degradability of Polysaccharide Multilayer Films In Vitro and In Vivo. Advanced functional materials. 2005;15(11):1771-80.

437. Hoogeveen NG, Cohen Stuart MA, Fleer GJ, Böhmer MR. Formation and Stability of Multilayers of Polyelectrolytes. Langmuir : the ACS journal of surfaces and colloids. 1996;12(15):3675-81.

438. Kim J, Kim G, Cremer PS. Investigations of Polyelectrolyte Adsorption at the Solid/Liquid Interface by Sum Frequency Spectroscopy: Evidence for Long-Range Macromolecular Alignment at Highly Charged Quartz/Water Interfaces. Journal of the American Chemical Society. 2002;124(29):8751-6.

439. Lee D, Nolte AJ, Kunz AL, Rubner MF, Cohen RE. pH-Induced Hysteretic Gating of Track-Etched Polycarbonate Membranes: Swelling/Deswelling Behavior of Polyelectrolyte Multilayers in Confined Geometry. Journal of the American Chemical Society. 2006;128(26):8521-9.

440. Alem H, Blondeau F, Glinel K, Demoustier-Champagne S, Jonas AM. Layer-by-Layer Assembly of Polyelectrolytes in Nanopores. Macromolecules. 2007;40(9):3366-72.

441. DeRocher JP, Mao P, Han J, Rubner MF, Cohen RE. Layer-by-Layer Assembly of Polyelectrolytes in Nanofluidic Devices. Macromolecules. 2010;43(5):2430-7.

442. Lazzara TD, Lau KHA, Abou-Kandil AI, Caminade A-M, Majoral J-P, Knoll W. Polyelectrolyte Layer-by-Layer Deposition in Cylindrical Nanopores. ACS Nano. 2010;4(7):3909-20.

443. Schneider A, Vodouhe C, Richert L, Francius G, Le Guen E, Schaaf P, et al. Multifunctional polyelectrolyte multilayer films: combining mechanical resistance, biodegradability, and bioactivity. Biomacromolecules. 2007;8(1):139-45. Epub 2007/01/09.

444. He C-X, Tabata Y, Gao J-Q. Non-viral gene delivery carrier and its three-dimensional transfection system. International journal of pharmaceutics. 2010;386(1–2):232-42.

# Appendix 1: Examining Cellular Adhesion Kinetics on Glycol-Chitosan/Hyaluronic Acid Films

Electric cell impedance sensing (ECIS) analysis allows for the real-time analysis of cellular adhesion, proliferation, differentiation and apoptosis on 2D electrode surfaces. Generally, as cell attachment and spreading on electrode surfaces increases, normalized capacitance measurements at frequencies around 40 kHz decrease fairly linearly (315). Monitoring of electrode capacitance can thus be used to study cellular adhesion kinetics on 2D electrode surfaces.

In order to examine NIH3T3 or MC3T3 cellular adhesion kinetics on our Glyc-CHI/HA multilayer films, a commercial ECIS system (ECIS Zθ, Applied Biophysics) was used to monitor the capacitance of coated and uncoated microelectrode arrays at 32 kHz. ECIS electrode arrays consisting of one or forty 250 μm gold microelectrodes per well (8W1E or 8W10+; Applied Biophysics) were coated with $[\text{Glyc-CHI/HA}]_{10}$Glyc-CHI films, corresponding films composed of unmodified chitosan, or were left uncoated. Experiments examining adhesion kinetics at a high cellular density were performed using single-electrode arrays and a seeding density of $5 \times 10^4$ cells/well. Studies examining adhesion and proliferation at a lower cellular density were conducted using forty-electrode arrays and a seeding density of $1 \times 10^4$ cells/well. Measurements were performed directly in the appropriate cell culture media, allowing real-time monitoring, in an incubator with high humidity at 37 °C and 5% $CO_2$.

ECIS analysis revealed that both NIH3T3 and MC3T3 cellular adhesion is delayed on Glyc-CHI films (Figs. A1.1-A1.4). However, in all cases, cellular adhesion eventually reaches levels similar to tissue culture plastic controls, with the rate of surface adhesion being dependent upon the cell seeding density employed. Electrodes were also coated with corresponding films composed of unmodified chitosan and HA, however, cells did not adhere (data not shown).

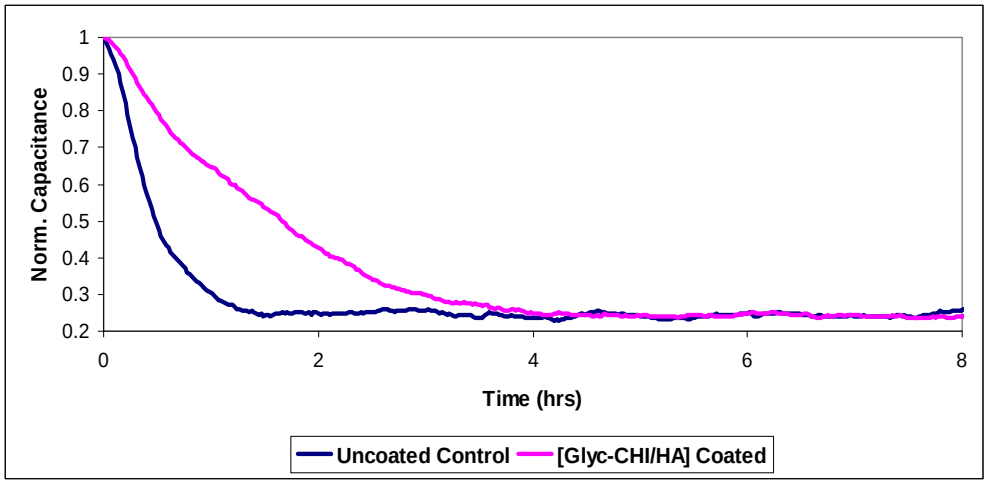


**FIGURE A.1.1: Representative electric cell-substrate impedance sensing (ECIS) plot of NIH3T3 cell attachment at high seeding density on uncoated electrodes (blue) and electrodes coated in $[Glyc\text{-}CHI/HA]_{10}$Glyc-CHI films (magenta). Normalized capacitance analyzed at 32 kHz.**

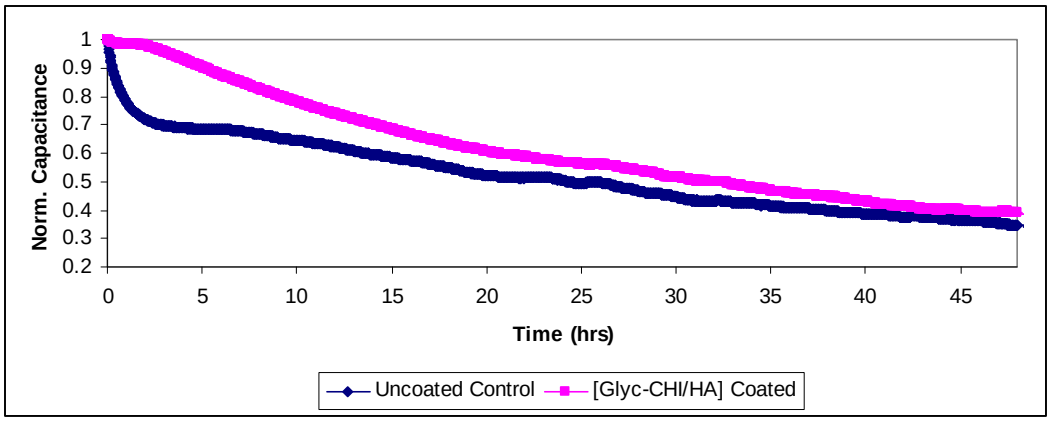


**FIGURE A.1.2: Representative electric cell-substrate impedance sensing (ECIS) plot of NIH3T3 cell attachment and proliferation at low seeding density on uncoated electrodes (blue) and electrodes coated in [Glyc-CHI/HA]$_{10}$Glyc-CHI films (magenta). Normalized capacitance analyzed at 32 kHz.**

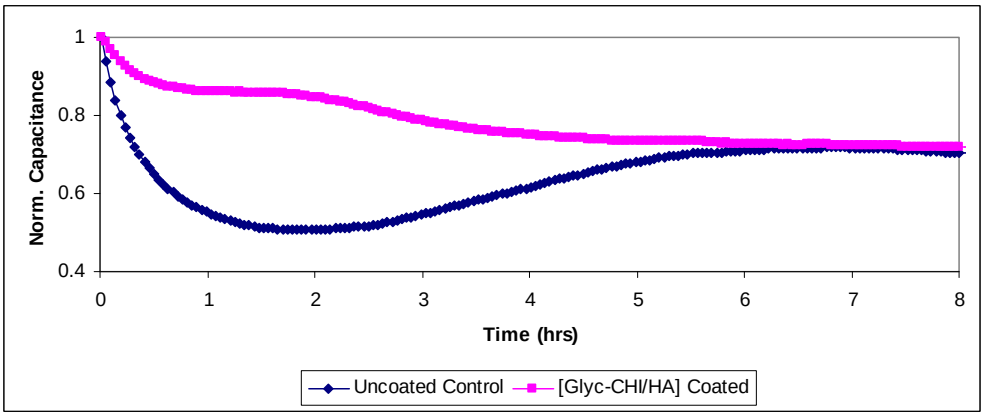


**FIGURE A.1.3: Representative electric cell-substrate impedance sensing (ECIS) plot of MC3T3 cell attachment at high seeding density on uncoated electrodes (blue) and electrodes coated in [Glyc-CHI/HA]$_{10}$Glyc-CHI films (magenta). Normalized capacitance analyzed at 32 kHz.**

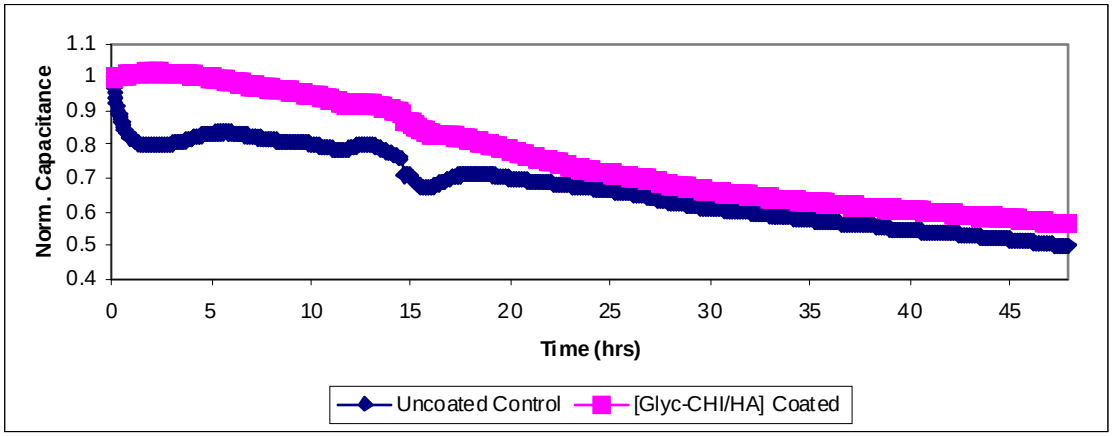


**FIGURE A.1.4: Representative electric cell-substrate impedance sensing (ECIS) plot of MC3T3 cell attachment and proliferation at low seeding density on uncoated electrodes (blue) and electrodes coated in [Glyc-CHI/HA]$_{10}$Glyc-CHI films (magenta). Normalized capacitance analyzed at 32 kHz.**

# Appendix 2: Glycol-Chitosan/Hyaluronic Acid Films with Embedded Gene Delivery Polyplexes Exhibit Low *In Vitro* Transfection Efficiencies

In order to enhance transfection efficiencies from our LbL-films, we originally proposed to use polyethylemine (PEI), one of the most efficient and widely studied polymeric transfection reagents, as our gene carrier vector. PEI-based polyplexes have been used to transfect many different cell lines, in numerous scaffold-based gene delivery designs (384), and have also been explored for 2D gene delivery from PE multilayer films (250), thus making them an attractive candidate for our studies. We thus began by examining *in vitro* transfection from Glyc-CHI/HA polyelectrolyte mulilayers with incorporated PEI-based gene delivery polyplexes.

Gene delivery polyplexes were formed by complexing linear PEI with a molecular weight of ~ 25 kDa and various amounts of plasmid DNA encoding the fluorescent marker gene EGFP at various N:P ratios. Prior to embedding, the size and surface charge of the resulting polyplexes were characterized via dynamic light scattering and zeta potential analysis, respectively (Table A.2.1).

| Amount of DNA (ug) | Avg. Particle Diameter (nm) | Avg. Zeta Potential (mV) | Avg. Polydispersity Index |
|---|---|---|---|
| 2 | 426 ± 44 | 20 ± 2 | 0.24 ± 0.01 |
| 4 | 570 ± 61 | 20 ± 1 | 0.27 ± 0.02 |
| 6 | 626 ± 84 | 22 ± 3 | 0.26 ± 0.02 |

**Table A.2.1: Physical characterization of pEGFP containing polyplexes (PEI). Polyplexes were formed with linear 25 kDa PEI at an N:P ratio of 24. The size and polydispersity of the resulting complexes were determined via low angle dynamic light scattering (DLS), while particle surface charge was characterized via zeta potential measurement. Data presented is from 3 separate experiments (n=9).**

The resulting gene delivery polyplexes were then adsorbed on top of, or within, Glyc-CHI/HA LbL films of varying architectures. The *in vitro* transfection efficiency of the resulting films was then tested in NIH3T3 cells via FACS analysis (Table A.2.2). Results indicated lower than desired transfection efficiencies (less than 5%) in all studies, thus, we switched our delivery vector to lipid-based Lipofectamine2000$^{TM}$.

| | % GFP + | | | | % PI + | | | |
|---|---|---|---|---|---|---|---|---|
| | "4 ug" Films | | "8 ug" Films | | "4 ug" Films | | "8 ug" Films | |
| N:P | 2 billayers | 4 billayers | 2 billayers | 4 billayers | 2 billayers | 4 billayers | 2 billayers | 4 billayers |
| 12 | 0.26 ± 0.16 | 0.98 ± 0.41 | 1.5 ± 0.46 | 2.9 ± 0.75 | 3.25 ± 0.93 | 3.98 ± 1.45 | 3.67 ± 1.83 | 3.81 ± 1.11 |
| 24 | 0.41 ± 0.30 | 1.62 ± 1.20 | 1.61 ± 1.04 | 2.81 ± 2.44 | 4.00 ± 2.30 | 4.60 ± 2.15 | 3.10 ± 1.33 | 3.76 ± 2.45 |
| 48 | 0.39 ± 0.21 | 1.84 ± 0.16 | 0.48 ± 0.10 | 0.13 ± 0.08 | 5.78 ± 0.87 | 4.92 ± 0.80 | 2.07 ± 0.23 | 2.55 ± 1.28 |

**Table A.2.2 NIH3T3 transfection efficiency and death after 48 hrs of growth on [Glyc-CHI/HA]$_5$- Poly-[HA/ Glyc-CHI]$_N$ films, where N=2 or 4. Film embedded polyplexes were formed from polyethylimine (PEI) and the indicated amount of pEGFP at the listed N:P ratios. Data presented represent the mean percentage of GFP-expressing (%GFP+) or PI-staining (%PI+) cells, as determined via fluorescent activated cell sorting, ± STD for 2, or 3 separate experiments. (n=6, or 9).**

# Appendix 3: HEK293 cells Adhered Poorly to LbL Coated and Uncoated PLGA Scaffolds

HEK293 human embryonic kidney cells are one of the most widely employed model cell lines in transfection assessment studies. However, HEK293 cells are also known to be weakly adherent to many material surfaces (428-430). In order to non-invasively assess HEK293 cell seeding and growth on our LbL-coated PLGA scaffold system we performed optical coherence phase microscopy (OCPM) imaging. HEK293 cells were seeded on uncoated control scaffolds or scaffolds coated with either [Glyc-CHI/HA]$_5$Glyc-CHI films or [Glyc-CHI/HA]$_5$Glyc-CHI-Lipo-[Glyc-CHI/HA]$_2$Glyc-CHI films, where lipoplexes were formed using 4 μg of plasmid DNA and 8 μL of Lipofectamine2000$^{TM}$.

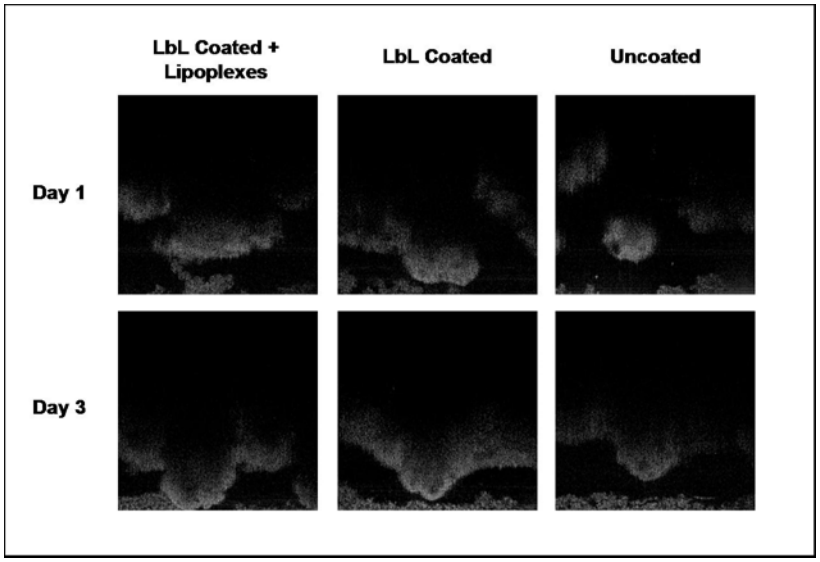


**FIGURE A.3.1: Representative optical coherence phase microscopy (OCPM) cross-sectional images of HEK293 cell growth on LbL-coated scaffolds, with (left) and without (center) embedded gene delivery lipoplexes, and on uncoated control scaffolds (right) at the time points indicated. All images are of a small representative 1mm x 1mm region within the scaffold, and represent an imaging penetration depth of 1mm.**

Representative cross-sectional images of overall construct morphology on days one and three for each scaffold system are presented in Fig. A.3.1. The polymeric scaffold strands are evident within the OCPM intensity images as large, optically dense structures. OCPM images for all scaffold systems at both time points clearly indicate that many HEK293 cells are non-adherent, appearing as unattached clusters or layers of cells at the bottom well surface. Cells remaining within the scaffolds were hard to distinguish from the scaffold strands on which they were growing. Overall, HEK293 cells were poorly adherent on both uncoated and LbL-coated PLGA scaffolds.